University of Alberta Library
0 1620 2669964 3

91-156

Ex libris
universitatis
albertaensis

UNIVERSITY OF ALBERTA

RELEASE FORM

NAME OF AUTHOR	Pushp K. Trikha
TITLE OF THESIS	Improvement of the Radiation Pattern of a $9m$ Radio Telescope Antenna at 408 MHz.
DEGREE	Master of Science
YEAR THIS DEGREE GRANTED	Spring 1991

Permission is hereby granted to the University of Alberta library to reproduce single copies of this thesis and to lend or sell such copies for private, scholarly or scientific research purposes only.

The author reserves other publication rights, and neither the thesis nor extensive extracts from it may be printed or otherwise reproduced without the author's written permission.

[redacted]

Date:.....April 5.....1991

UNIVERSITY OF ALBERTA

FACULTY OF GRADUATE STUDIES AND RESEARCH

THE UNDERSIGNED CERTIFY THAT THEY HAVE READ, AND

RECOMMEND TO THE FACULTY OF GRADUATE STUDIES AND RESEARCH FOR ACCEPTANCE, A THESIS

ENTITLED "IMPROVEMENT OF THE RADIATION PATTERN OF A $9m$ RADIO TELESCOPE ANTENNA AT 408 MHz."

SUBMITTED BY PUSHP K. TRIKHA

IN PARTIAL FULFILMENT OF THE REQUIREMENTS FOR THE DEGREE OF MASTER OF SCIENCE.

[redacted]

Date: April 15 1991

To my mother and father

Abstract

The Synthesis Telescope at D.R.A.O. operates simultaneously at 408 MHz and 1420 MHz. The reflector antennas (paraboloids) used in the telescope have high sidelobes at 408 MHz, which degrade the telescope performance at this frequency.

The radiation pattern of one of the antennas was measured at 408 MHz and shows evidence of the high sidelobes. The pattern was measured by using a remote controlled transmitter and a computer controlled data collection system to record the receiver power level and the antenna position.

The existing reflector feed is optimized for 1420 MHz operation. As a result, the performance of the feed at 408 MHz suffers, and other feed problems exist in addition to the high sidelobe levels caused by the broad beam in the feed pattern.

Four possible solutions to the feed problems were designed and tested, and some other feed modifications were simulated using a software program. It was shown that it was not possible to make the 408 MHz feed pattern significantly narrower without increasing the aperture blockage and affecting the 1420 MHz pattern. On the other hand, it was possible to solve several other feed problems using one of the four solutions. The best solution consisted of four slots backed by a common coaxial cavity. Better isolation between the adjacent elements of the antenna, better isolation between the receiving ports of the hybrid network, better polarization performance, and better radiation efficiency were achieved.

Acknowledgements

I would like to thank the following people at D.R.A.O. for their valuable input into the project: First, I thank Ron Casorso for his technical advice on the design of the remote controlled transmitter. Next, I am grateful to Ed Danallanko for giving me some basic training in the machine shop and for constructing various components of the antennas and to Roman Lipiecki, a machinist in the Electrical Engineering department at the University of Alberta, for constructing one of the scale models of the slot excited feed horns. I am also grateful to Geoff Croes, Walter Wyslousil, and Gary Hovey for some advice in logging the antenna pattern data. I would like to thank Ev Sheehan and Rod Stuart for their advice on constructing some components of the antennas and other circuits. In addition, I would like to thank Rick Smegal for various discussions concerning antennas and antenna measurements. Also, I would like to thank Brent Carlson and Tom Burgess for introducing me to computer drafting. In the Administration department, I am grateful to Bette Jones for her valuable librarian services and to Erika Rohner for ordering any of the necessary parts. Finally, I would like to thank my supervisors Tom Landecker, Dave Routledge, and Fred Vaneldik for their patience, encouragement, technical advice and discussions throughout the project, and I would like to thank the Director, Lloyd Higgs, for allowing me to do the project at the Radio Observatory.

Table of Contents

Page

1.0 Introduction 1

1.1 The Antennas of the Synthesis Telescope 1
1.2 Basic Antenna Parameters 1
1.3 The Radiation Pattern of a Paraboloid 7
1.4 The Sidelobe Problem 9
1.5 The Sidelobes and Telescope Performance 13
1.6 What has been done to solve the Sidelobe Problem 18
1.7 Topics of this thesis 20

2.0 Measuring the 408 MHz Radiation Pattern 23

2.01 The Antenna Range 23
2.02 The Transmitting Antenna 25
2.03 The Transmitter 27
2.04 The Crystal Oscillator 29
2.05 The Multiplier 35
2.06 The High Power 408 MHz Oscillator 37
2.07 Injection Locking 41
2.08 The Remote Control 44
2.09 The Receiver 47
2.10 Data Logging and The Delay Correction 47
2.11 Sampling period and Further Computer Processing 52

3.0 The Measured Reflector Antenna Pattern 55

3.1 Analysing the Measured Pattern 55
3.2 Comparison with the Software Prediction 59
3.3 Verification of the Measured Pattern 65
3.4 Comparing the 408 MHz and 1420 MHz Radiation Patterns . 67

4.0 The Feed of the Synthesis Telescope 71

4.1 Feed Operation at 1420 MHz and 408 MHz 71
4.2 Feed Problems at 408 MHz 85
4.3 Electrical Characteristics at 408 MHz 100
4.4 Design Constraints 101
4.5 Feed Pattern Measurements 101

5.0 Feed Modifications 105

5.1 The Microstrip Antenna Solution 106

5.1.1 Theory and Design Details 106
5.1.2 The Advantages and Disadvantages 111
5.1.3 Corrective Measures 115
5.2 The Annular Slot Solution 121
5.2.1 Design Details 121
5.2.2 Results and Discussion 124
5.3 Rectangular Slots backed by Rectangular Cavities 131
5.3.1 Design Details 131
5.3.2 Exciting the Slots 133
5.3.3 Scale Model Construction 136
5.3.4 Results and Discussion 137
5.3.5 Antenna Losses 143
5.4 Rectangular Slots backed by a Coaxial Cavity 146
5.4.1 Design Details 146
5.4.2 Matching and Tuning the Slots 148
5.4.3 Results from the Scale Model 152
5.4.4 Working at 408 MHz 161
5.4.5 Increasing the Bandwidth and Reducing Tuning Errors 162
5.4.6 Effect on 1420 MHz Performance 164
5.5 Sharpening the Beam at 408 MHz 170
5.5.1 Method of Moments 170
5.5.2 Software Simulations 174
5.6 The Middle Ground Option 181

6.0 Conclusions 185

7.0 References 189

List of Figures

FIGURE Page

1.01 Dimensions of the Synthesis Telescope Antenna 2
1.02 Typical Radiation Pattern of a Paraboloid 2
1.03 The Co-ordinate System for Calculating the Radiation Pattern . . . 3
1.04 Sources of Sidelobes 11
1.05 Surface Roughness 11
1.06 Aperture Blockage 11
1.07 Strut Scatter 12
1.08 Spillover 12
1.09 Sources of Antenna Temperature 15
1.10 Example of Solar Interference 15
1.11 Source of Grating Rings 16
1.12 Example of Grating Ring 17
1.13 Triangular Feed Strut 19
1.14 Cylindrical Shroud 19

2.01 Antenna Range 24
2.02 Receiving Antenna 24
2.03 Transmitting Antenna 26
2.04 Block Diagram of Transmitter 28
2.05(a) Crystal Oscillator 32
2.05(b) Small Signal Circuit 33
2.06 Printed Circuit Layout 34
2.07 Multiplier 36
2.08(a) High Power Oscillator 39
2.08(b) Small Signal Circuit 40
2.09 Injection Locking 43
2.10 Remote–Tone–Detector Block Diagram 45
2.11 Remote Control Circuit 46
2.12 The Receiver 49
2.13 Data Logging System 50
2.14 Delay Correction 51

3.01 408 MHz Radiation Pattern 57
3.02 Major Sidelobe Groups at 408 MHz 58
3.03 Software Structured Diagram 60
3.04 Comparison of Measured Pattern with Predicted Pattern 63
3.05 1420 MHz Radiation Pattern 69
3.06 Feed Patterns at 408 MHz and 1420 MHz 70

4.01 Feed Dimensions 72
4.02 Reflector Illumination and Feed Aperture Distribution 73
4.03 Major Sections of the Feed 75

4.04 Present Feed Approximation 76
4.05 Feed Pattern and the Number of Rings 77
4.06 1420 MHz Feed Patterns 78
4.07 Location of 408 MHz Probes 81
4.08 Details of the 408 MHz Probe 82
4.09 408 MHz Feed Patterns 83
4.10 6−Port Hybrid Network 84
4.11 Polarization Pattern at 408 MHz 86
4.12 Input Return Loss 88
4.13 Determining the Cross Polarization Level 90
4.14 Calculated Cross Polarization Level 91
4.15 Geometry for the Primary Beam Pointing Error 93
4.16 Primary Beam Pointing Error 94
4.17 Reflector Cross Polarization Level for ϕ=45^o. 95
4.18 Secondary Effects of Primary Beam Pointing Error 96
4.19 Algebraic Calculation of the Radiation Efficiency 99
4.20 Design Constraints 103
4.21 The Antenna Range 104

5.1.1 Microstrip Patch Orientation 107
5.1.2 Rectangular Patch 107
5.1.3 Radiation from the Rectangular Patch 109
5.1.4 Circuit Model for the Rectangular Patch 110
5.1.5 Short Cicuit Patch 113
5.1.6 Multilayer Patches (the triple decker) 117
5.1.7 Other Patch Shapes 120

5.2.1 Annular Slot Feed Horn 123
5.2.2 Annular Slot Feed Pattern at 408 MHz 125
5.2.3 Existing and Annular Slot Feed Patterns at 408 MHz 126
5.2.4 TE_{11} and TM_{11} Modes at 408 MHz 127
5.2.5 Effect on 1420 MHz 128
5.2.6 Top Loading the Probe 130

5.3.1 Dielectric Filled Cavities 132
5.3.2 Coaxial line to Slot Transitions 135
5.3.3 Calculating the Offset Distance 135
5.3.4 Isolation Levels for Probes and Slots 138
5.3.5 Feed Patterns for the Slot Excited Feed Horn 139
5.3.6 Input Return Loss Measurement 141
5.3.7 Cutoff Frequencies for Possible TE modes 142

5.4.1 Scale Model Design 147
5.4.2 Printed Circuit Layout for Ring Hybrid 149
5.4.3 Antenna Matching Circuit 149
5.4.4 Isolation Levels between Opposing and Adjacent Ports 153
5.4.5 Return Loss at the Ring Hybrid Input 154
5.4.6 VSWR Measuring Arrangement 155

5.4.7 Feed Patterns for the Slot Excited Feed Horn 157
5.4.8 Measured Polarization Pattern 158
5.4.9 Replacing the Probes with a Printed Circuit 163
5.4.10 Isolation versus Opposite Probe Length Difference 163
5.4.11 Predicting the Effect on 1420 MHz Performance 165
5.4.12 Measuring the Effect on 1420 MHz Performance 167

5.5.1 Geometry for Deriving the Integral Equation 171
5.5.2 Simulations and Results 175
5.5.3(a) Predicted Effect of "45° Flange" at 1420 MHz 176
5.5.3(b) Predicted Effect of "0° Flange" at 1420 MHz 178
5.5.3(c) Predicted Effect of "Extra Ring" at 1420 MHz 179

5.6.1 The Middle Ground Option 182
5.6.2 Predicted Edge Illumination and Aperture Blockage 184

6.01 Comparison of the feed modifications 187

List of Photographic Plates

PLATE Page

1 The Synthesis Telescope 21

2 The 408 MHz Transmitter 53

3 Feed Modifications 168

1. INTRODUCTION

1.1 The Antennas of the Synthesis Telescope

The antennas used in the Synthesis Telescope (ST) are paraboloids. A photograph of the ST showing the antennas is shown in plate 1. A cross-section of the antenna with the critical dimensions is shown in fig 1.01. Paraboloids are used in the ST because they are highly directive; that is, most of the radiation received by the antenna comes from a small angle. The highly directional property is essential for better sensitivity in receiving weak radio emission. A paraboloid will focus incoming parallel rays to a point. Another antenna structure, known as the feed, is located at this point and collects the converging rays. The feed of the ST consists of a coaxial horn and monopoles. The feed will be described in more detail in chapter 4.

1.2 Basic Antenna Parameters

The performance of an antenna can be determined by calculating various antenna parameters. Parameters that best determine the performance for a reflector antenna include the solid angle, directivity, gain, and aperture efficiency.

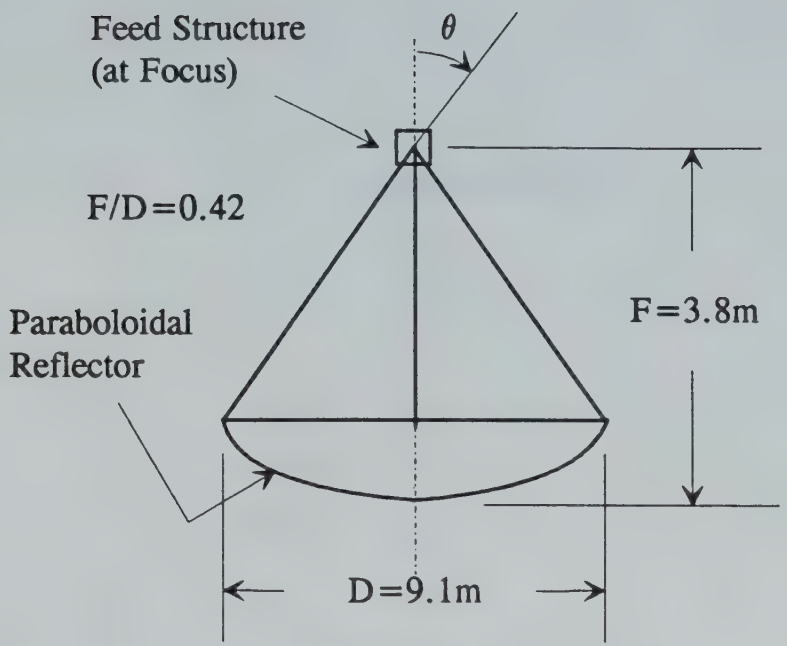

Figure 1.01 The Critical Dimensions of the Synthesis Telescope Reflector Antenna.

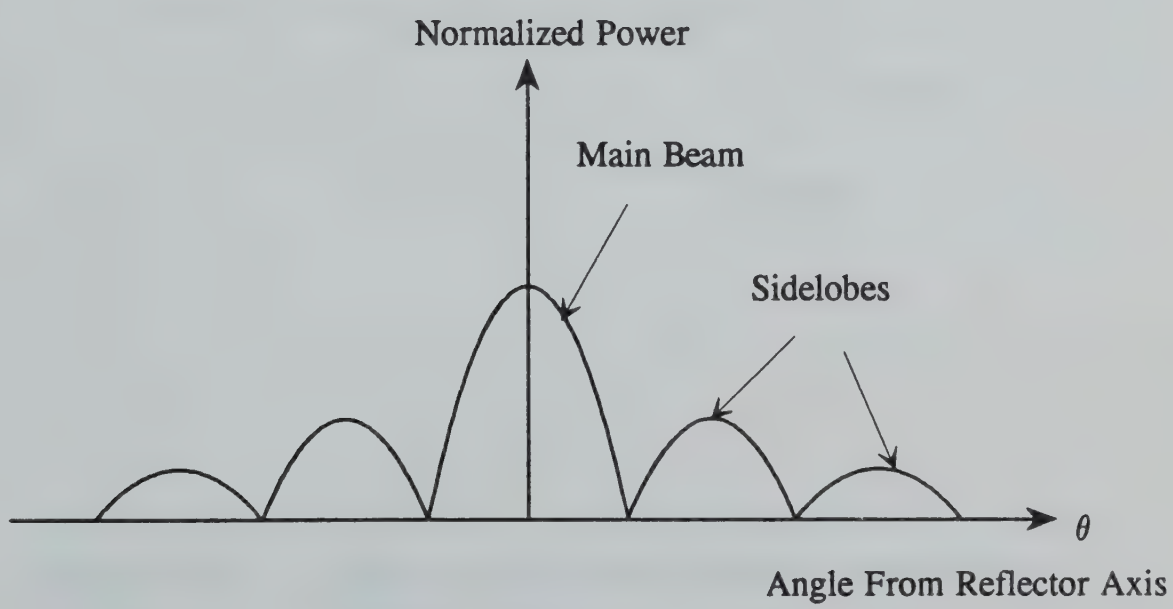

Figure 1.02 A Typical Radiation Pattern of a Paraboloid.

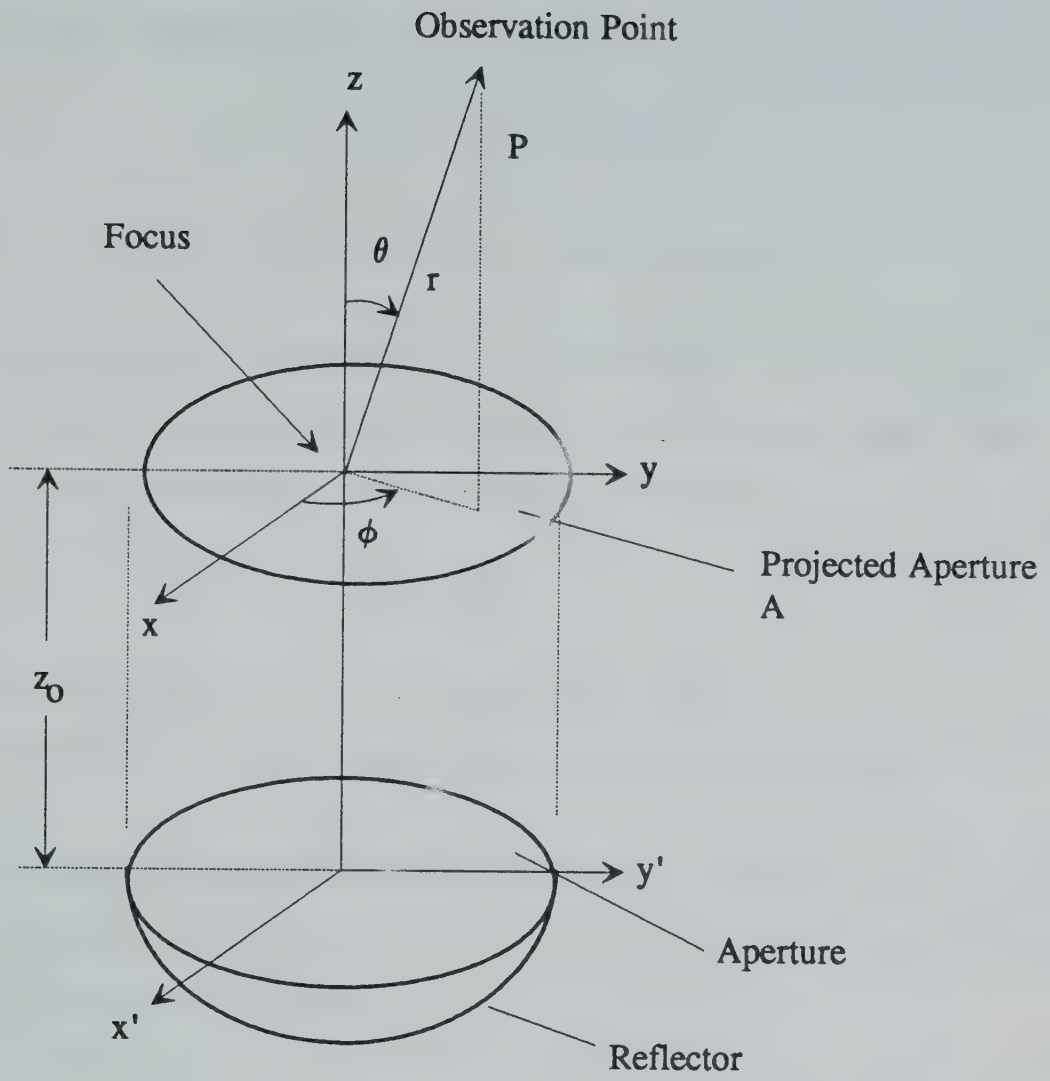

Figure 1.03 The Co-ordinate System used for Calculating the Radiation Pattern.

The first parameter is the antenna solid angle. The antenna solid angle is the angle through which all the power from an antenna would flow if the power were constant over this angle and equal to the maximum value (Kraus, 1986). Using the co-ordinate system in fig. 1.03, the antenna solid angle, Ω_a, can be expressed as

$$\Omega_a = \int_0^{2\pi} \int_0^{\pi} P_n(\theta, \phi) sin\theta d\theta d\phi,$$

where $P_n(\theta, \phi)$ is the normalized antenna power pattern.

The second antenna parameter is the directivity, D. It is defined as the ratio of the maximum power density to the average power density. Equivalently, the directivity can be expressed as follows:

$$D = \frac{4\pi}{\Omega_a}.$$

A good reflector antenna has a high directivity because most of the power transmitted from the antenna flows through a small solid angle.

A third antenna parameter is the antenna gain, G. The antenna gain will have the same value as the directivity as long as there are no ohmic losses on the reflector. Otherwise,

$$G = kD,$$

where k is the efficiency factor that depends on the ohmic losses on the reflector.

A fourth parameter is the aperture efficiency. The aperture efficiency, ε_{ap}, is defined as the ratio of the effective aperture, A_e, to the physical aperture, A_p, or

$$\varepsilon_{ap} = \frac{A_e}{A_p}, \qquad \text{where } 0 < \varepsilon_{ap} < 1.0.$$

The physical aperture is the area of the reflector aperture. Assuming matched polarization, the effective aperture is the ratio of the power received at the feed antenna terminals to the power density of the incident plane wave. A reflector that makes good use of its physical aperture will have a high aperture efficiency. The gain of an antenna is related to the aperture efficiency as follows:

$$G = \frac{\varepsilon_{ap} 4\pi A_p}{\lambda^2},$$

where λ is the operating wavelength. The aperture efficiency includes both the ohmic efficiency of the reflector and the feed efficiency. The feed efficiency is the efficiency with which the feed illuminates the reflector.

Other antenna parameters can be calculated that best describe the performance of the feed rather than of the reflector antenna. These parameters include the radiation efficiency, bandwidth, quality factor, and cross polarization.

The first parameter is the radiation efficiency. The radiation efficiency, η, is the ratio of the radiated power, P_r, to the input power. The input power includes the radiated power and the dissipated power, P_l. The dissipated power is caused by non-radiation losses that consist of both losses in the feed network and ohmic losses in the feed structure. The radiation efficiency can be expressed as follows:

$$\eta = \frac{P_r}{P_r + P_l}.$$

A feed will have a low radiation efficiency if the non-radiation losses are comparable to the radiation losses.

The second parameter is the antenna bandwidth. The antenna bandwidth is defined as the frequency range for which the antenna exhibits certain characteristics. Some characteristics include the voltage standing wave ratio (VSWR), return loss (RL), input impedance, and radiation pattern. For example, the bandwidth could be defined as the frequency range for which the VSWR is less than 2.

A third parameter, that is related to the bandwidth, is the antenna quality factor, Q. The half-power bandwidth, BW, is defined as follows:

$$BW = \frac{f_o}{Q}$$

where f_o is the operating frequency. The antenna Q can be expressed in terms of the total energy stored per cycle, E_{stored}, and the average power dissipated per cycle. The power dissipated includes both the power dissipated due to the ohmic losses, P_o, and the power radiated. The antenna Q can be expressed mathematically as follows (Gardiol, 1984):

$$Q = \frac{2\pi f_o E_{stored}}{P_r + P_o}.$$

From the formula, it can be seen that reducing the stored energy lowers the antenna Q and therefore broadens the bandwidth.

A fourth parameter is the feed cross polarization level, CPL. In the transmitting situation, an ideal circularly polarized feed will produce a rotating electrical field vector, which is equal in magnitude for all orientations. However, in a non-ideal feed, the rotating electrical field vector will trace out an ellipse. The axial ratio, AR, is defined as the ratio of the major axis to the minor axis of the polarization ellipse. The cross polarization level can be determined from the axial ratio as follows (Mott, 1986):

$$CPL = \frac{AR - 1}{AR + 1}.$$

The polarization ellipse can also be expressed as the sum of a right hand circularly polarized signal R and a left hand circularly polarized signal L. If R is being received, the cross-polarization level is also defined as follows (Mott, 1986):

$$CPL = \frac{L}{R}.$$

An ideal circularly polarized feed will have $AR = 1$ and $CPL = 0$.

1.3 The Radiation Pattern of a Paraboloid

The radiation pattern of a paraboloid consists of a main beam and sidelobes as shown in fig 1.02. Using the co-ordinate system in fig. 1.03, the far field pattern is obtained as follows. First, the principles of Geometrical Optics (GO) such as the law of reflection and the principle of equality of path length are used to compute the fields in the aperture from the given feed pattern. The fields in the projected aperture are the fields in the aperture multiplied by a constant phase term of $exp(-jkz_o)$, where z_o is the projected distance. The electric field in the projected aperture, $\mathbf{E}_A$, is

$$E_x \mathbf{a_x} + E_y \mathbf{a_y}.$$

The far field radiation pattern is obtained by integrating the electric field over the projected aperture as follows (Balanis, 1982):

$$\mathbf{E}(\theta,\phi) = \frac{jke^{-jkr}}{4\pi r}(1+cos\theta)\int\int_A \mathbf{F}(\theta,\phi)e^{j(kxsin\theta cos\phi + kysin\theta sin\phi)}dxdy,$$

where

$$\mathbf{F}(\theta,\phi) = [(cos\phi\,\mathbf{a}_\theta - sin\phi\,\mathbf{a}_\phi)E_x + (sin\phi\,\mathbf{a}_\theta + cos\phi\,\mathbf{a}_\phi)]E_y,$$

and $\mathbf{a_x}$, $\mathbf{a_y}$, $\mathbf{a_\theta}$, and $\mathbf{a_\phi}$ are unit vectors. The result states that the far field pattern is proportional to the Fourier transform of the electric field in the aperture. The width of the main beam and the peak sidelobe level depend on the functional form of the aperture field distribution (Kraus, 1988). The pattern obtained using the Fourier transform is predicted accurately only for angles covering the main beam and the first few sidelobes. To predict the radiation pattern accurately for the remaining angles, the Geometrical Theory of Diffraction (GTD) (Keller, 1962) must be used.

The GTD supplements GO by including the law of diffraction. The diffracted field is obtained by multiplying the incident field by a diffraction coefficient and a spatial attenuation factor in much the same way as a reflected field is obtained by multiplying the incident field by a reflection coefficient. The diffraction coefficient depends on the type of discontinuity, the angle of incidence, and the position of the observation point. Some discontinuities, for which diffraction coefficients are accurately known, include edges of a flat plate, curved edges, and corners. The spatial attenuation factor depends on whether the incident wave is a plane wave or a spherical wave.

The incident fields on the reflector rim are first found from the given feed pattern. The diffracted fields from the rim are then calculated and form the sidelobe pattern for the remaining angles in the radiation pattern.

1.4 The Sidelobe Problem

The sidelobe levels observed in practical situations are higher than the levels predicted by the Fourier transform and the GTD. The main causes for the higher sidelobes are surface roughness, aperture blockage, strut scatter, and spillover. (See fig. 1.04.)

Looking at surface roughness, if any part of a parabolic surface deviates slightly from the desired surface, the rays of the incoming plane wave do not all meet at the focus. Instead, some rays from a direction slightly off boresight reflect into the focus as shown in fig. 1.05. From another point of view, the surface irregularities cause the phase of the electric field in the aperture to deviate from nominal values. Taking the Fourier transform of the aperture field with these phase errors results in a loss in gain and higher near sidelobes. The loss in gain or the gain loss factor, GL, can be predicted as follows (Ruze, 1952):

$$GL = exp[-(\frac{4\pi\delta}{\lambda})^2],$$

where δ is the rms surface error and λ is the operating wavelength. The higher sidelobe level and loss in gain are significant for large surface deviations.

The feed and struts raise the sidelobe level in the forward hemisphere by causing aperture blockage. Aperture blockage is illustrated in fig. 1.06. Aperture blockage increases the level of the first few sidelobes and lowers the gain. The effect of aperture blockage is calculated by superimposing the fields due to the two aperture distributions (Silver, 1949). The field due to the reflector aperture distribution without the blockage is added to the field due to the blocked aperture distribution; the field in the blocked

area is 180^o out of phase with respect to the original. Aperture blockage also increases the level of the other sidelobes in the forward hemisphere. The feed and struts block a small area of the reflector aperture, and the radiation from the blocked area has a wide extent in angle.

Feed leg or strut scatter and spillover raise the sidelobe level in the region, $\theta = 0^o$ to 120^o. The effects are more significant in the region, $\theta > 90^o$.

The increase in the sidelobe level due to the struts is mainly due to the "scatter cones" formed around the axis of each strut (Rusch et al., 1982). A scatter cone is formed when the plane wave from the reflector is incident on the strut. The plane wave causes a linear phase variation of the induced current along the strut. Viewing the strut as a travelling wave antenna, a radiation cone is produced around the strut in the general direction of the travelling current. As shown in fig. 1.07, this results in scattered radiation on a cone of opening angle 120^o when the feed struts make an angle of 60^o with the reflector axis.

Spillover is direct feed radiation and adds to the level of the far sidelobes. If the edge of the reflector is at $\theta = 120^o$, spillover has a major impact on the sidelobes from $\theta = 90^o$ to 120^o but can also have an impact from $\theta = 0^o$ to 90^o if the beam of the feed is broad. Figure 1.08 illustrates spillover.

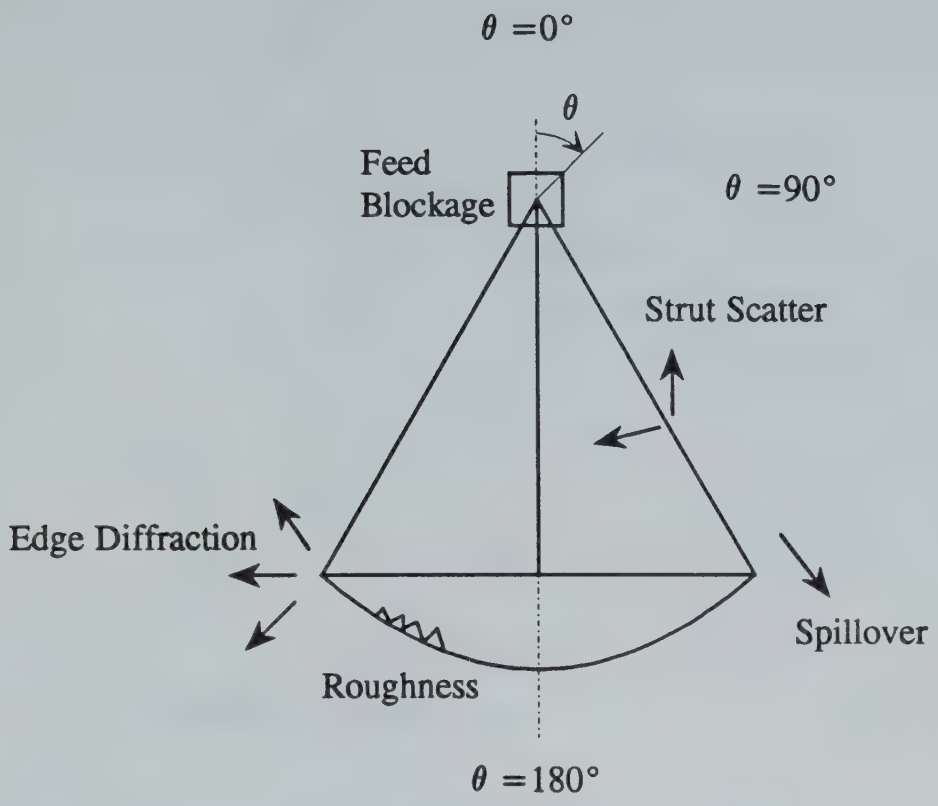

Figure 1.04 The Sources of Sidelobes.

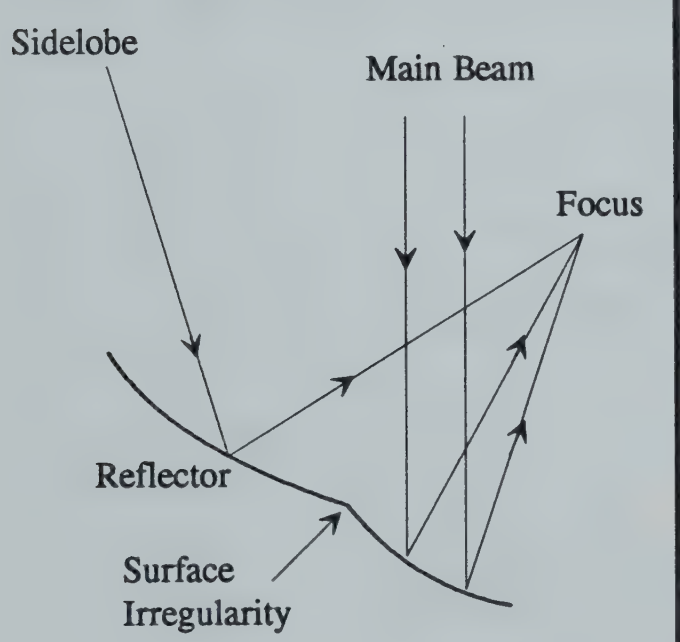

Figure 1.05 Surface Roughness

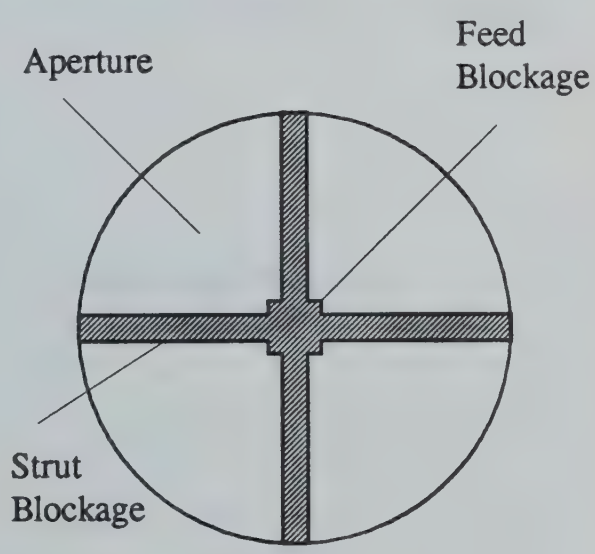

Figure 1.06 Aperture Blockage

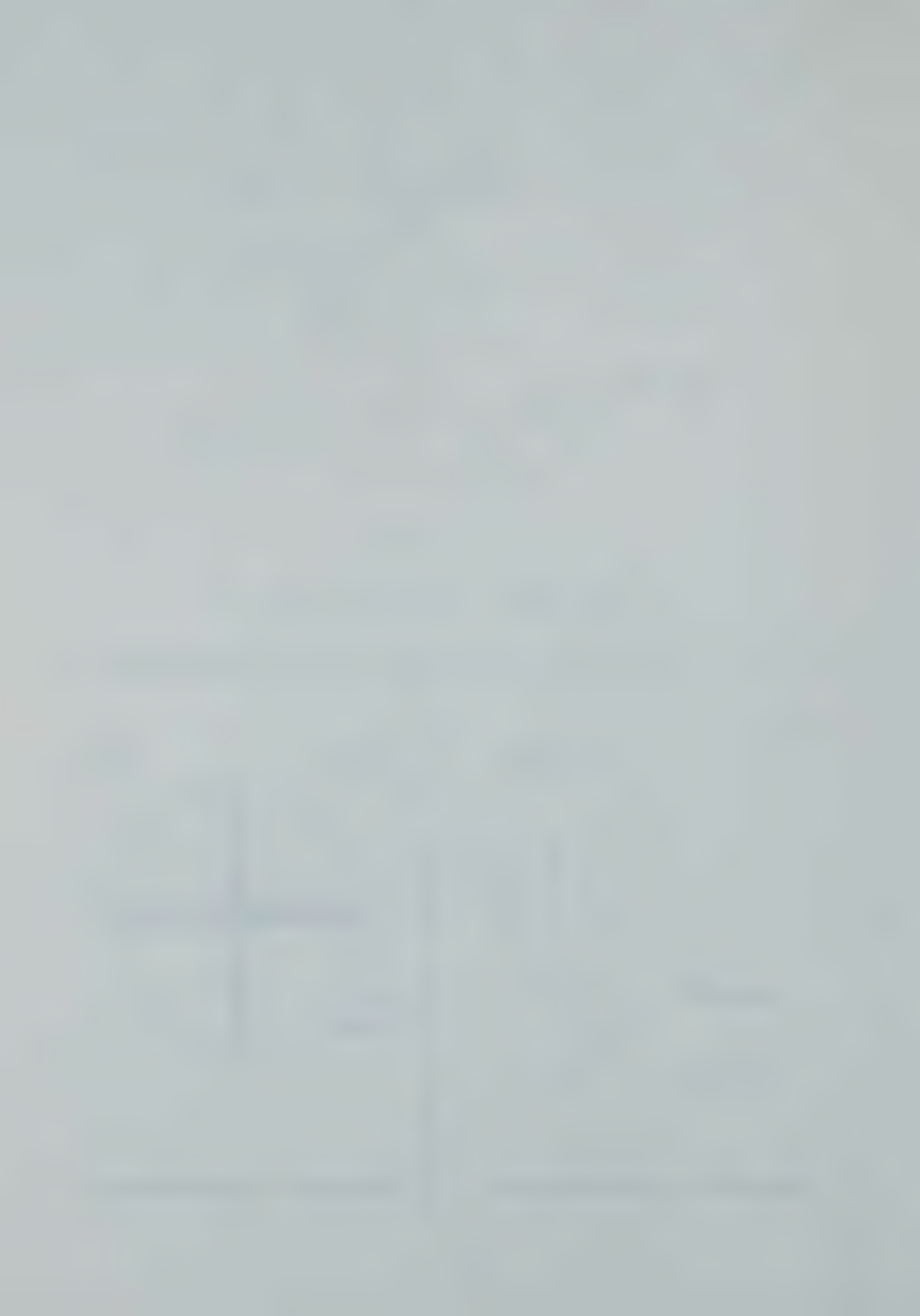

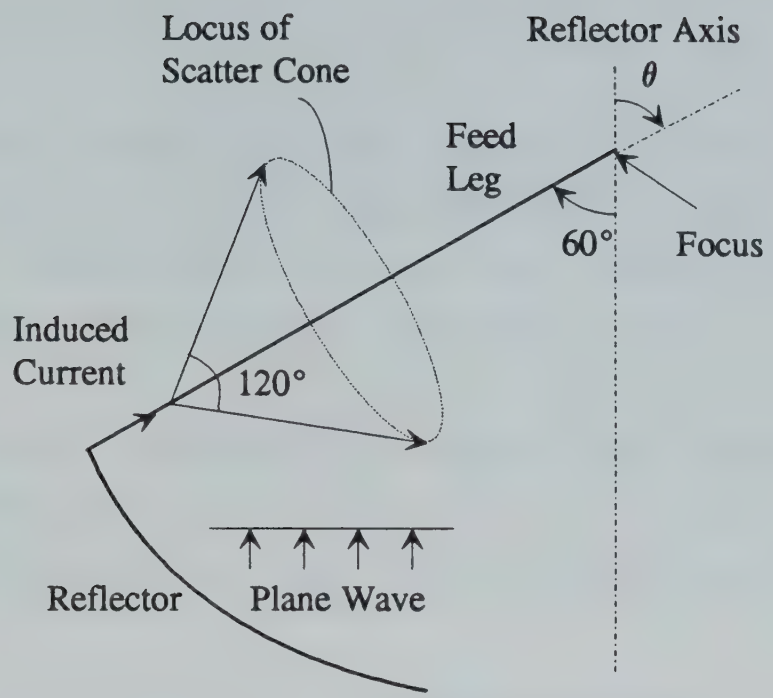

Figure 1.07 The Formation and Location of a Scatter Cone.

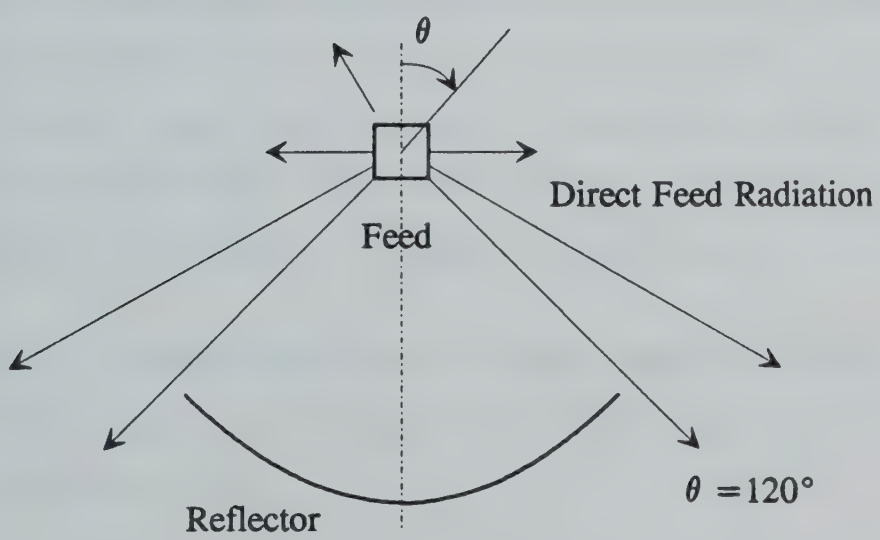

Figure 1.08 Spillover or Direct Feed Radiation.

1.5 The Sidelobes and Telescope Performance

For the two operating frequencies of the synthesis telescope, the sidelobe problem and its effect on telescope performance is more evident at 408 MHz. The high sidelobes affect the system noise temperature, the recorded visibilities, and therefore, the quality of the final image.

The two major components of the system noise temperature, T_S, are the antenna temperature, T_a, and the receiver noise temperature, T_{rx}. Using the co-ordinate system in fig. 1.03, T_a is defined as follows (Kraus, 1988):

$$T_a = \frac{1}{\Omega_a}\int_0^{2\pi}\int_0^{\pi} P_n(\theta,\phi)T(\theta,\phi)sin\theta\, d\theta d\phi,$$

where $T(\theta,\phi)$ is the brightness temperature distribution, and $P_n(\theta,\phi)$ is the normalized antenna power pattern.

From fig. 1.09, if the sidelobes of the antenna are high and point toward a source of high brightness temperature such as the ground (T_g = 200 - 300 K), the Sun ($T_s \geq 7$ x 10^5 K), and other strong sources in the sky, then T_a will be large, and the signal to noise ratio, $\Delta T_a/T_a$, of the observed source will be small. ΔT_a is the increase in antenna temperature when the antenna is pointing at the source being observed.

In addition to the high sidelobes, the ohmic losses in the feed antenna also increase the system noise temperature. The increase in the system temperature is (Kraus, 1988)

$$T_{ap}(\frac{1}{\eta} - 1),$$

where T_{ap} is the physical temperature of the feed (300 K) and η is the radiation efficiency (see section 1.2).

The Sun not only increases the system noise temperature but also affects the output of the interferometer or visibility as shown in fig. 1.10. From the figure, the Sun is so strong that it causes the visibility to deviate appreciably from nominal values even though the signal enters the sidelobes of the antenna. At present, the effect of the Sun is eliminated only by observing at night time.

High sidelobe levels also degrade the final image. The image is affected by the appearance of grating rings. Grating rings are caused by high sidelobes and grating lobes, which appear as a result of the Fourier transform of the sampled visibility function in the u-v plane (Bracewell and Thompson, 1973). A simplified one-dimensional version of the Fourier Transform relationship between the sampled visibility function and the sky brightness distribution is shown in fig. 1.11. From the figure, a grating ring appears in the observed field of view because the grating lobe, which is weighted by a prominent sidelobe of the reflector pattern, passes through an unwanted strong source. This is more evident at 408 MHz than at 1420 MHz because the sidelobes are higher. A good example is shown in fig. 1.12. The ring is due to the source, Cygnus A, whose strength (intensity) exceeds that of any source within the field being observed.

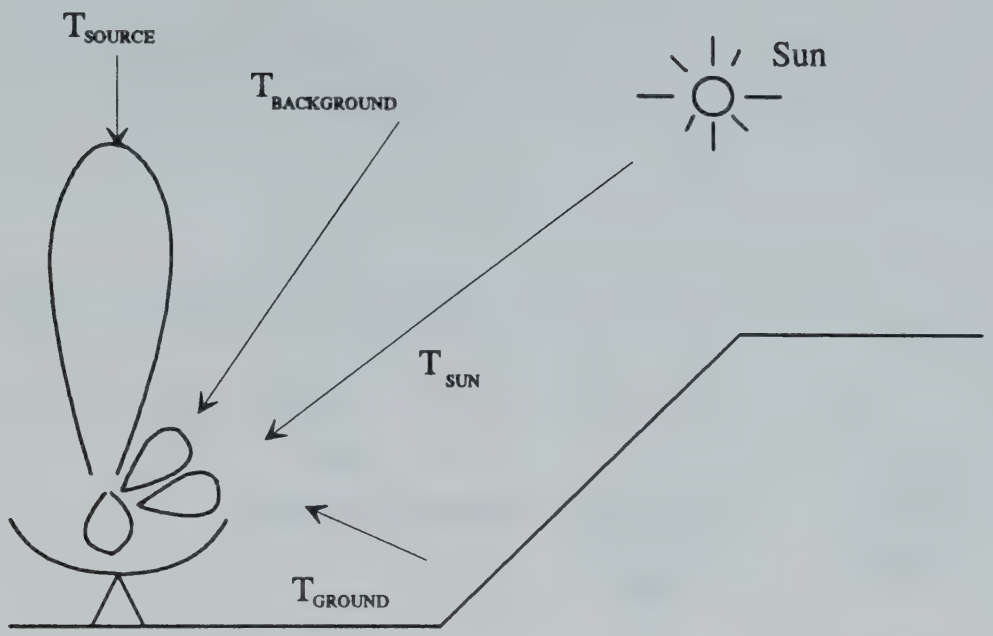

Figure 1.09 Sources of Antenna Temperature.

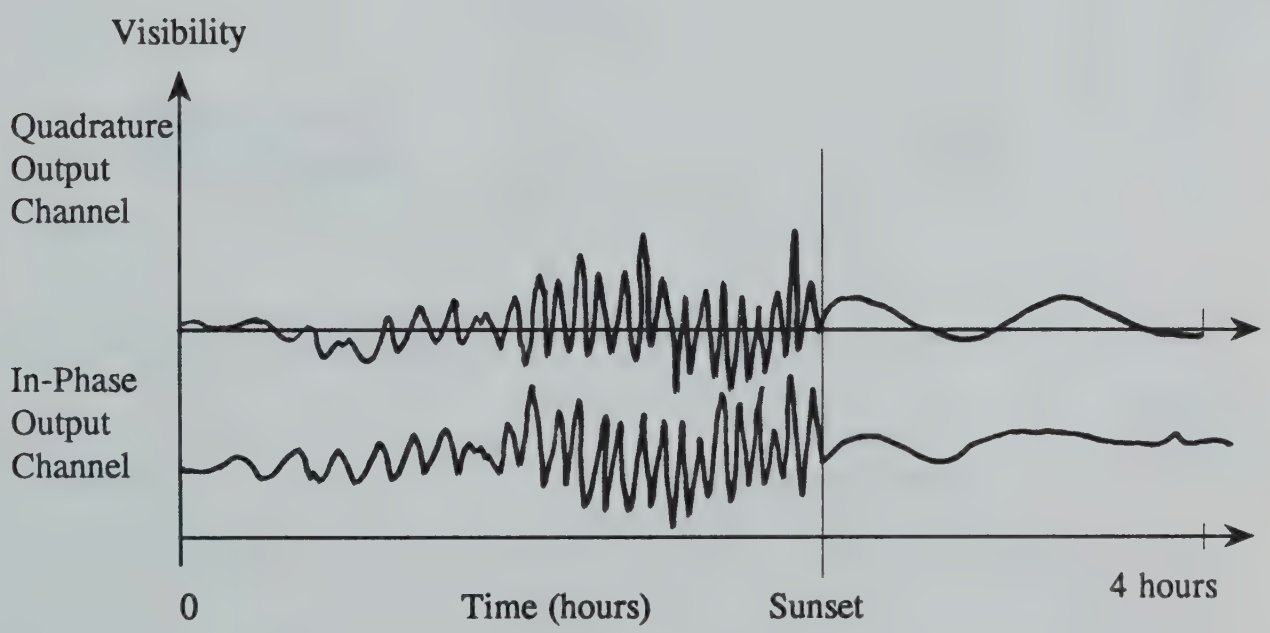

Figure 1.10 An Example of a 408 MHz Interferometer Visibility Record Corrupted by Signals from the Sun. The variation after the time of sunset are the true visibilities due to the source under observation.

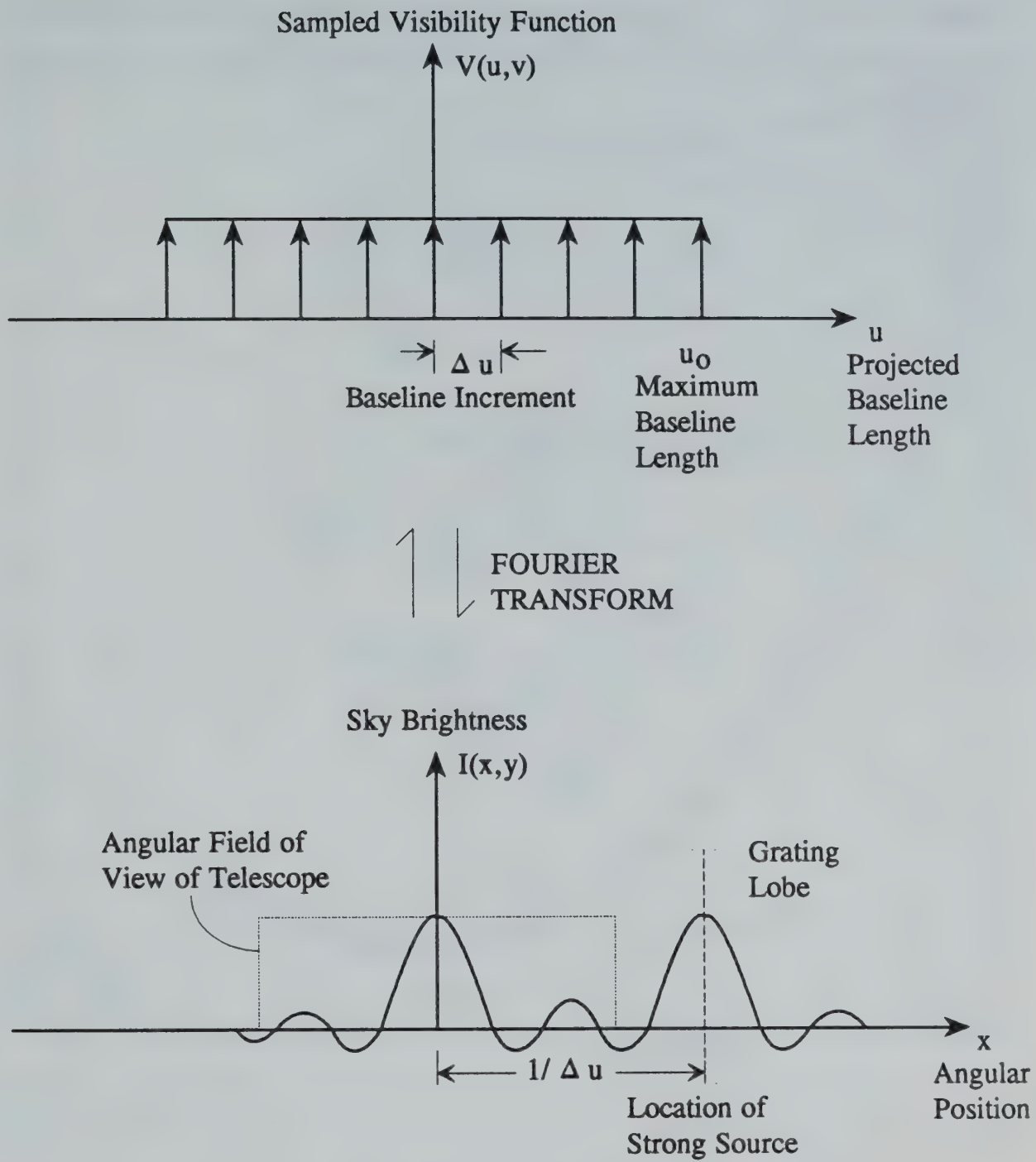

Figure 1.11 A Simplified One-Dimensional Diagram of the Fourier Transform Relationship between the Sky Brightness and the Sampled Visibility Function. If a grating lobe is weigthed by a high sidelobe of the reflector, a strong grating ring will appear to pass through the observed field of view.

Figure 1.12 An Example of a Grating Ring. The grating ring was formed when a high sidelobe was pointing at the source Cygnus A.

1.6 What has been done to solve the Sidelobe Problem at 408 MHz and 1420 MHz.

It is important to reduce the far sidelobes of a radio telescope antenna because, as shown in sections 1.4 and 1.5, these sidelobes affect the system noise temperature. So far, strut and rim modifications have been shown in the literature to reduce the far sidelobes.

Strut modifications reduce the far sidelobes by redirecting feed leg scatter. The most effective method of reducing the peak sidelobe level of the scatter cones (see section 1.4) is changing the shape of the strut from circular to triangular (Satoh et al., 1984). A triangular feed strut is shown in fig. 1.13. The apex of the triangle faces the reflector, and the strut, therefore, redirects the incident plane wave to other directions that are less likely to strike the ground when the antenna is pointed at the zenith. The scattered radiation redirected from the ground to regions in the forward hemisphere results in a lower ground temperature contribution to the system noise temperature (Landecker et al, 1991). Of course, the price paid is higher near sidelobes due to the redirected radiation.

Rim modifications can also reduce the far sidelobes. An effective rim modification is a cylindrical shroud placed around the reflector as shown in fig. 1.14 (Narasimhan et al., 1983). It is attractive because the shroud prevents direct feed radiation (spillover) from intercepting the ground. This results in a lower system noise temperature for antenna pointings near the zenith. An experiment was performed at DRAO using one of the $9m$ paraboloids of the Synthesis Telescope with a $1m$ high fence or shroud attached to the rim. The fence was shown to reduce the system noise temperature at 1420 MHz (Anderson, 1990). The addition of the fence seems promising if an increase in the near sidelobe levels can be tolerated. Other effects such as reflector cross polarization must be considered as well.

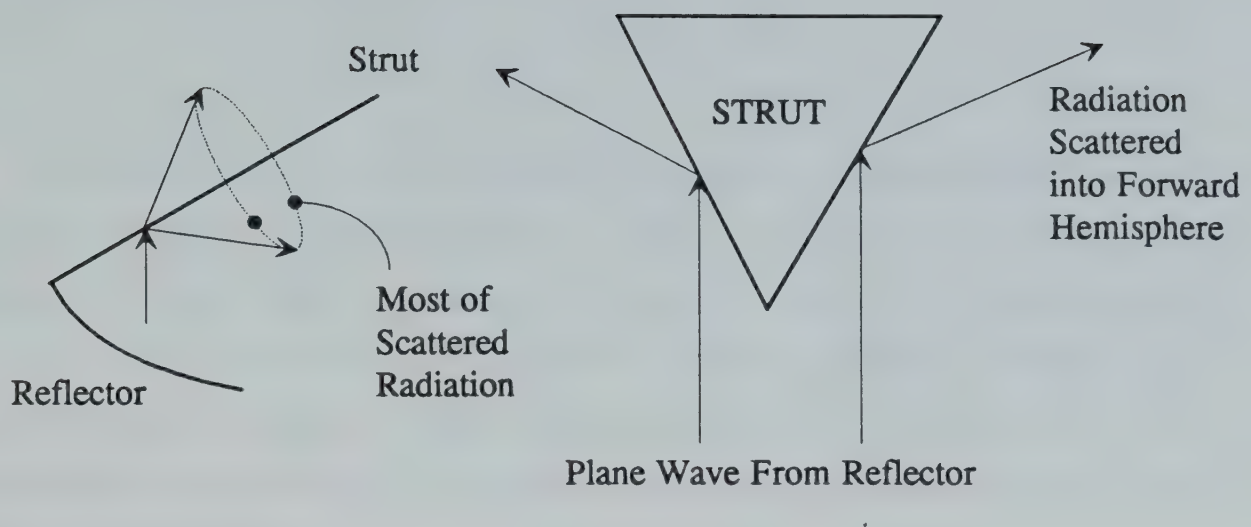

Figure 1.13 A Triangular Feed Strut. Most of the radiation scattered from the triangular strut ends up in the forward hemisphere.

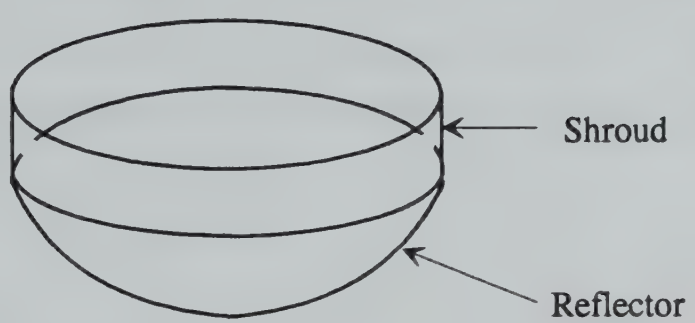

Figure 1.14 The Cylindrical Shroud. The shroud prevents the intense portion of the direct feed radiation from intercepting the ground when the antenna is pointed at the zenith.

1.7 Topics of this thesis

As shown in section 1.5, the high sidelobes at 408 MHz affect the performance of the Synthesis Telescope (*ST*). To assess the severity of the sidelobes at 408 MHz, the radiation pattern of one of the antennas used in the *ST* was measured. Measuring the pattern required a suitable transmitter, antenna range, and data logging system. The details of measuring the pattern are discussed in chapter 2, and the measured pattern is presented in chapter 3.

The analysis of the measured pattern in chapter 3 shows that the feed is partly responsible for the high sidelobes at 408 MHz. The feed of the Synthesis Telescope operates at 1420 MHz and 408 MHz simultaneously, but is optimized for 1420 MHz. The optimization at 1420 MHz creates other problems at 408 MHz in addition to the high sidelobes. The existing feed and its problems at 408 MHz, and the electrical characteristics of the feed at 408 MHz are discussed in chapter 4. Possible modifications to solve the feed problems at 408 MHz are discussed in chapter 5. The design constraints for the feed modifications are discussed in section 4.4.

Plate 1

This photograph shows the Synthesis Telescope at D.R.A.O. The Telescope consists of an array of seven $9m$ paraboloidal antennas. The antenna whose radiation pattern at 408 MHz was measured is located at the further end of the array, closest to the hill in the background.

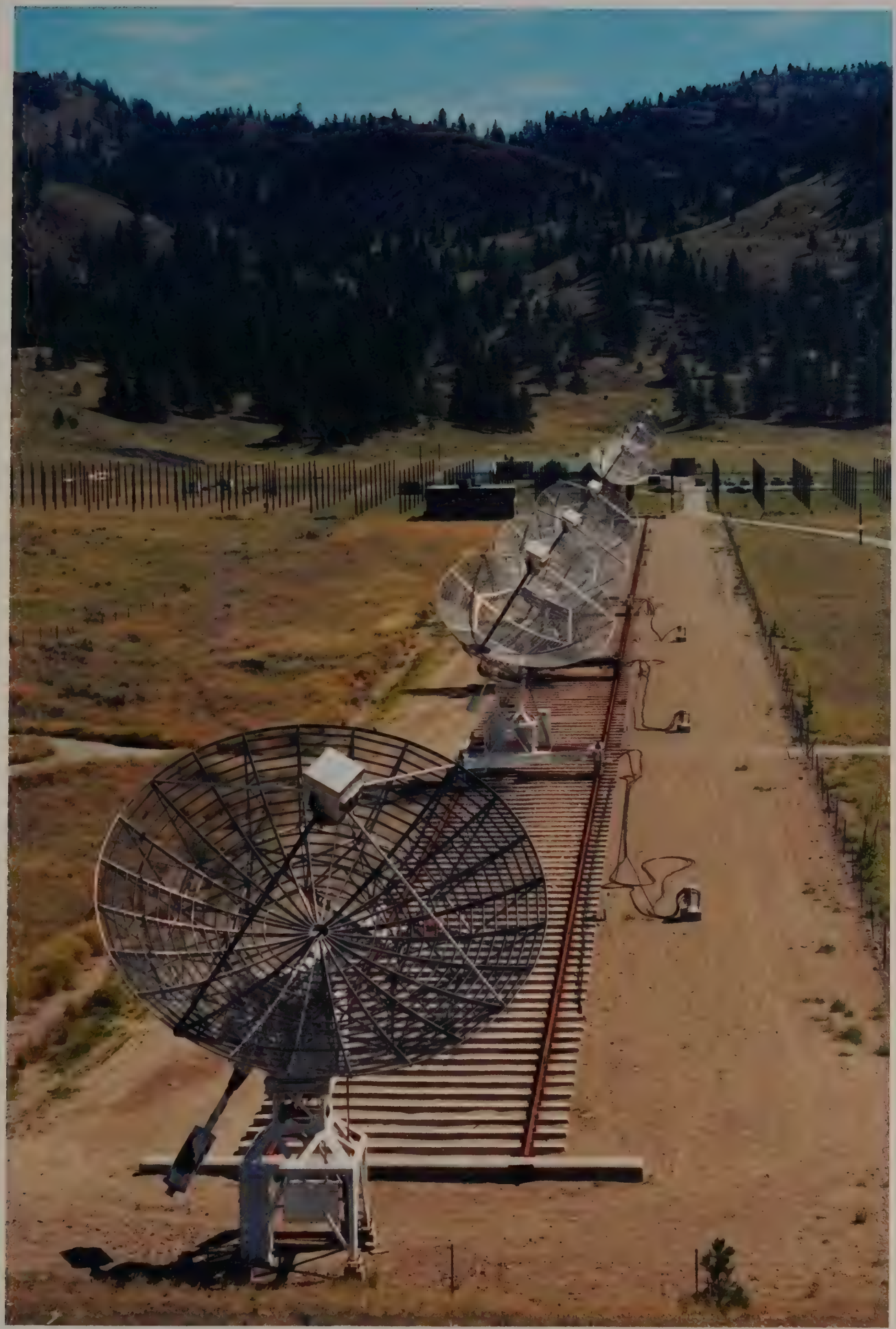

2. MEASURING THE 408 MHz RADIATION PATTERN

To establish the magnitude of the sidelobe problem at 408 MHz, the radiation pattern of one of the antennas of the Synthesis Telescope was measured. The measurement apparatus consisted of an antenna range, a transmitting antenna, a transmitter, a receiver, and a data logging system. The measurement and the apparatus are described in this chapter.

2.1 The Antenna Range

The antenna range is shown in fig. 2.01. The transmitter and its antenna were placed on top of a hill. The transmitter was activated by remote control from the receiver location. The receiving antenna (test antenna) was a 9m paraboloid, steerable in hour angle and declination. The paraboloid is shown in fig. 2.02. The power level at the receiver and the position of the antenna were recorded by a computer as the test antenna was steered.

The distance between the transmitting and receiving antennas was $800m$. By using the relation

$$r \geq \frac{2D^2}{\lambda},$$

where D is the diameter of the test antenna ($9m$), λ is the operating wavelength ($0.7353m$), and r is the distance between the transmitting and receiving antennas, it can be shown that the distance of $800m$ is in the far field of the test antenna. A far field pattern measurement of the test antenna can thus be made.

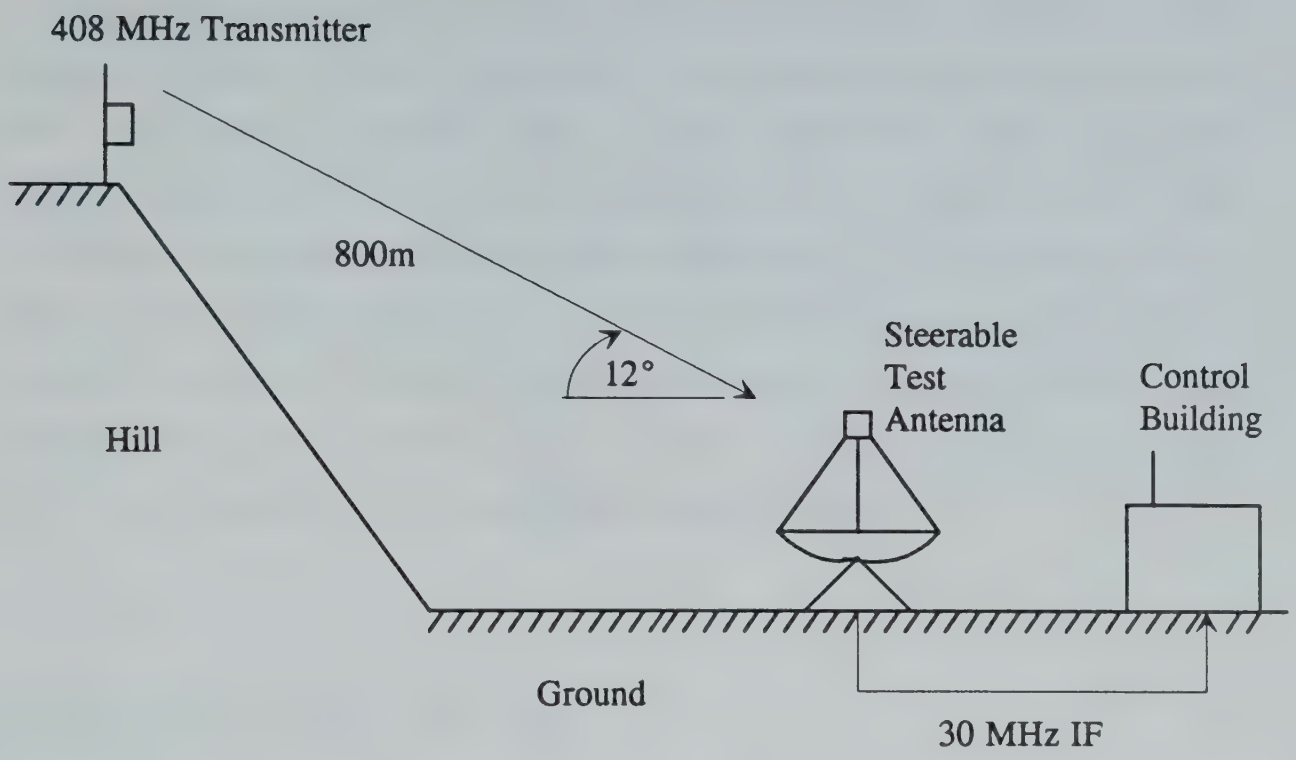

Figure 2.01 The Antenna Range.

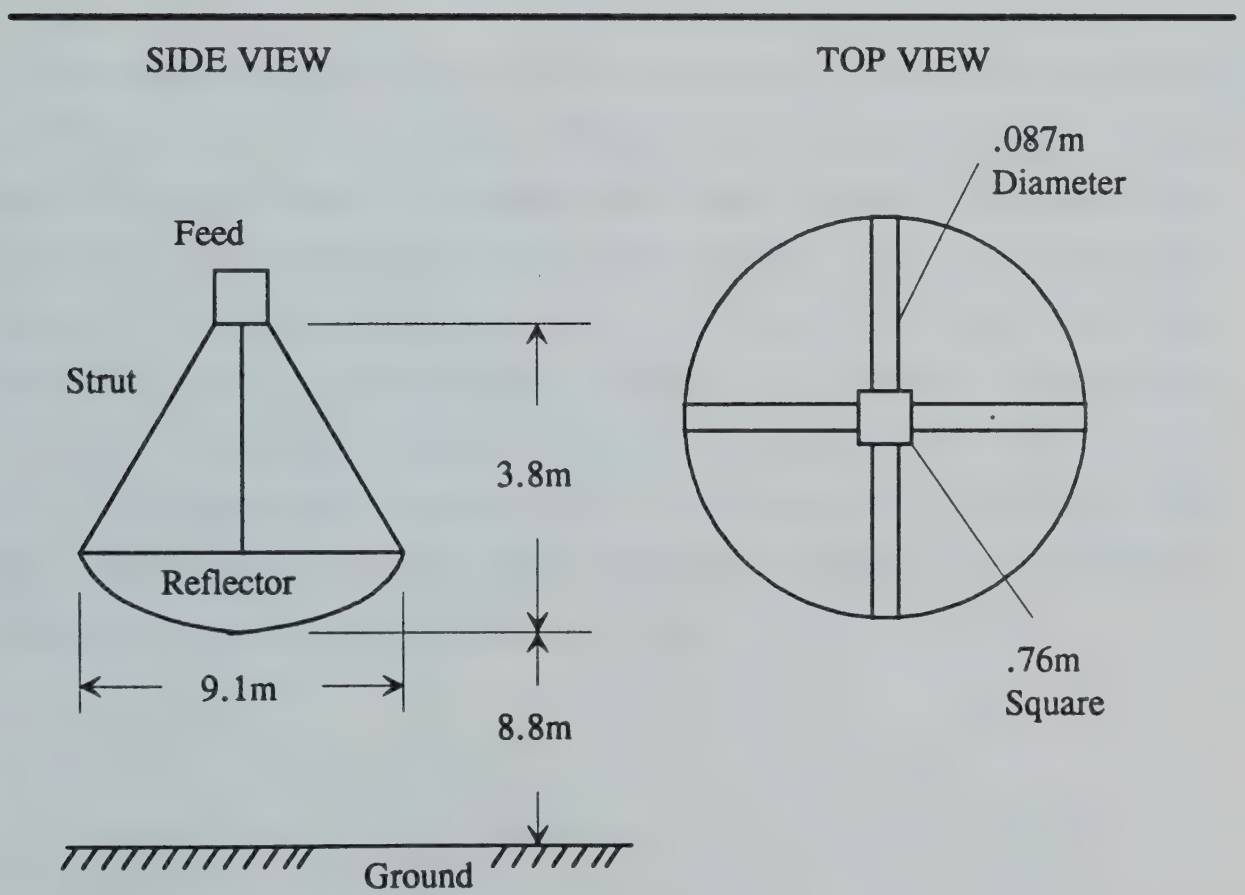

Figure 2.02 The Receiving or Test Antenna.

To minimize the ground wave reflected between the transmitting and receiving antennas, vertical polarization was chosen for the transmitting antenna. At the low elevation angle of the transmitter (12^o), the ground reflection coefficient for vertical polarization, Γ_V, is much smaller than the reflection coefficient for horizontal polarization, Γ_H. For instance, the ground of the measurement site may be approximated as a ground of rich clay soil for which $|\Gamma_V| \approx 0.1$ and $|\Gamma_H| \approx 0.9$ for an elevation angle of 12^o (Kraus, 1988 p.717). Because $|\Gamma_V|$ is small, the direct propagation wave will be much greater than the reflected ground wave.

2.2 The Transmitting Antenna

The transmitting antenna is shown in fig 2.03. The antenna consists of a half-wave dipole and a square reflector ground plane. The one-λ square ground plane was placed $\lambda/4$ behind the dipole to ensure maximum directivity toward the test antenna. With the help of a quarter-wave balun, the two arms of the dipole were fed 180^o out of phase from a 50 ohm coaxial line. The gain of the transmitting antenna was calculated approximately as follows. A resonant half-wave dipole in free space has a gain of about 1.6. The ground plane restricts most of the radiation to the forward half space, and the gain is approximately doubled to about 3. A photograph of the transmitting antenna is shown in plate 2.

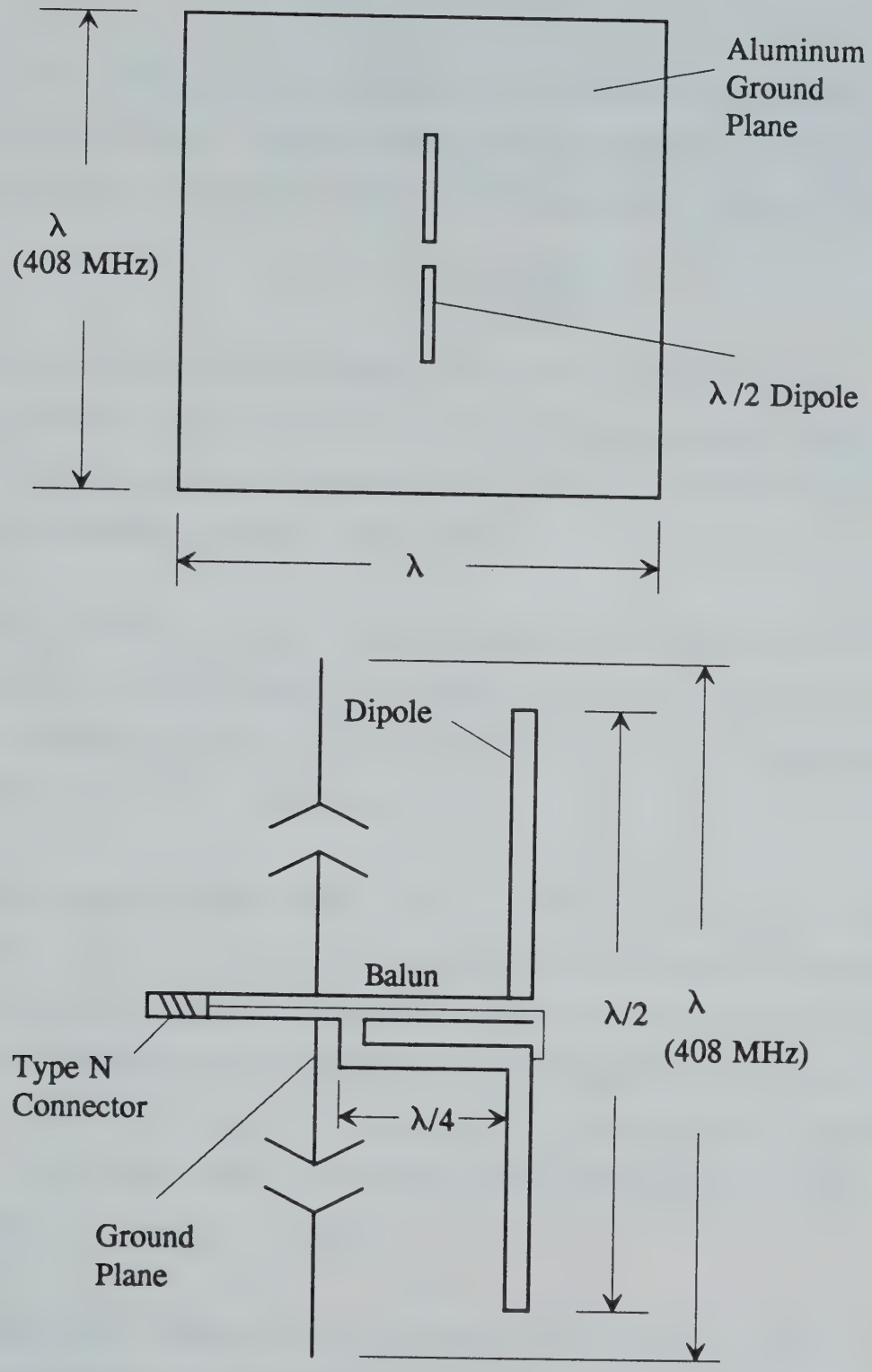

Figure 2.03 The Transmitting Antenna.

2.3 The Transmitter

Before designing and building the transmitter, the power required to achieve a specified dynamic range at the receiver had to calculated. This was done with the help of the Friis Transmission formula (Kraus, 1988):

$$P_r = \frac{P_t G_t A_{er}}{4\pi r^2},$$

where P_r is the received power, P_t is the transmitted power, r is the distance between the transmitting and receiving antennas ($800m$), G_t is the gain of the transmitting antenna (3.0), and A_{er} is the effective area of the receiving antenna ($39.4m^2$; Veidt, 1985).

The formula is valid as long as the direct wave is much stronger than the reflected ground wave. As shown in section 2.1, the ground reflection coefficient is small for vertical polarization, and therefore, the reflected ground wave can be neglected.

The required power level at the receiver is calculated as follows: The dynamic range required for an adequate measurement of the sidelobes is about 60 dB. With the transmitter off and the receiving antenna pointing at the transmitting site, the noise level measured at the receiver was about -100 dBm. Thus, the power received, P_r, at the antenna should be $-100+60 = -40$ dBm. Using the formula, the minimum transmitted power, P_t required is 4.5 mW (6.5 dBm).

The block diagram for the transmitter is shown in fig. 2.04. The major components of the transmitter consist of a high power oscillator, a low power crystal oscillator, and a multiplier. A photograph of the complete transmitter unit is shown in plate 2. Frequency stability at the transmitter output is achieved by injection locking the high power oscillator with

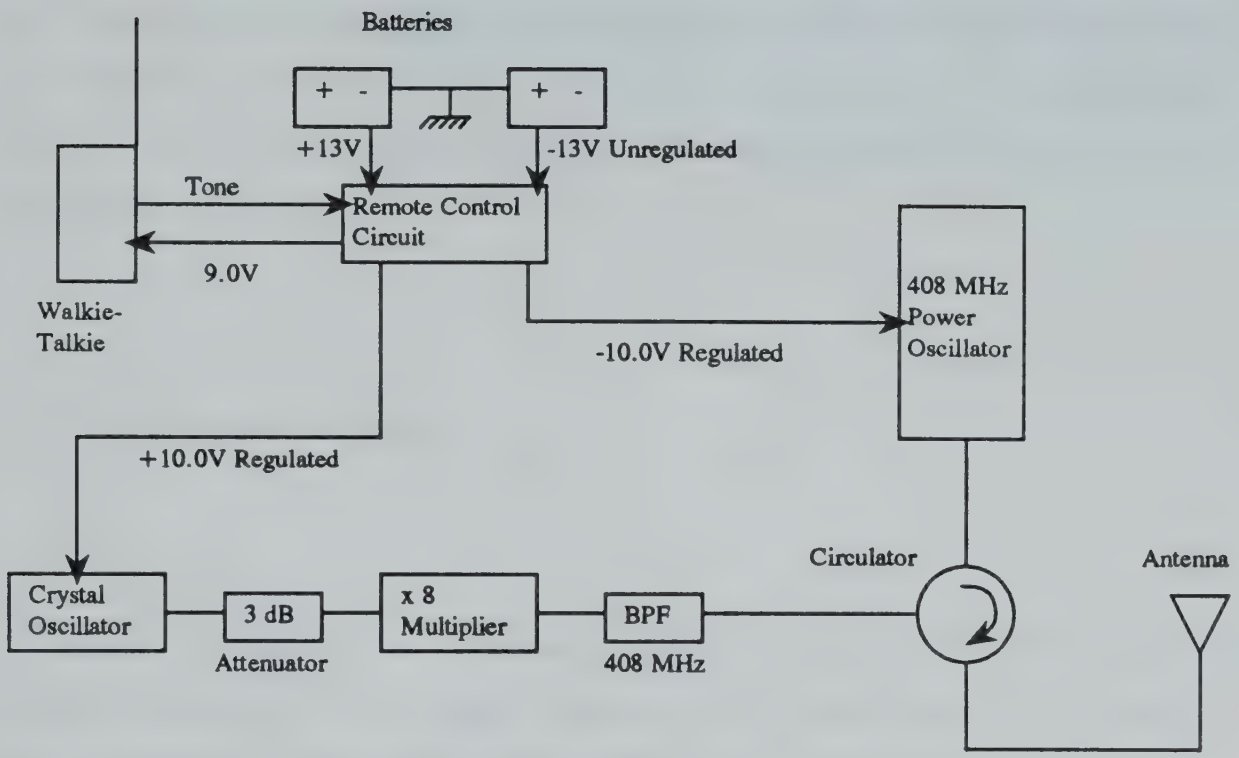

Figure 2.04 Block Diagram of the Transmitter.

a low power reference signal. The filtered output of the 8 times multiplier, which multiplies the output of the 51.0 MHz crystal oscillator, is the reference signal. Amplitude stability is improved by regulating the supply voltages to the oscillators. The power level of the transmitter output was monitored and recorded at regular intervals just in case there were any amplitude variations. Any slight variations would probably be caused by changes in temperature during the day. The major components of the transmitter and the method of injection locking are discussed in detail in the following paragraphs.

2.4 The Crystal Oscillator

The 51.0 MHz crystal oscillator is shown in fig. 2.05(a). Resistors R_1, R_2, R_E and the RF choke bias transistor Q_1. Capacitors C_1, C_2, and C_3 and inductance L_1 form the tuned circuit that resonates at the crystal frequency. Oscillation is possible if the small signal loop gain is greater than unity. The small signal circuit is shown in fig. 2.05(b). A small voltage at the collector, v_c, produces a voltage drop across the equivalent tuned circuit load because of the voltage divider action of C_1, C_2, and C_3. This voltage divider action also results in a voltage, v_x, which, in turn, produces an emitter voltage, v_e, because of the voltage divider action of R_E, h_{ib}, and r_x. The transistor operates as a common base amplifier, and the emitter voltage is amplified to produce a collector voltage, v_c. Feedback is thus established, and the loop is completed. The approximate small signal loop gain, A_L, is calculated as follows: For the calculation, the circuit is broken between the collector and the capacitor, C_1.

$$A_L = (\frac{v_x}{v_{c'}})(\frac{v_e}{v_x})(\frac{v_c}{v_e}),$$

where

$$\frac{v_x}{v_{c'}} = \frac{n_2}{n_1 + n_2}, \quad \frac{v_e}{v_x} = \frac{(h_{ib} \| R_E)}{(h_{ib} \| R_E) + r_x}, \quad \text{and} \quad \frac{v_c}{v_e} = \frac{R'_c}{h_{ib}}.$$

The turns ratios n_1, n_2, and n_3 due to the voltage divider consisting of C_1, C_2, and C_3 are calculated as follows:

$$n_1 = \frac{C_2 C_3}{C_1 C_2 + C_2 C_3 + C_1 C_3} = 0.768$$

$$n_2 = \frac{C_1 C_3}{C_1 C_2 + C_2 C_3 + C_1 C_3} = 0.063$$

$$n_3 = \frac{C_1 C_2}{C_1 C_2 + C_2 C_3 + C_1 C_3} = 0.169$$

The resistance "seen" looking into the emitter or h_{ib} is calculated as follows:

$$h_{ib} = \frac{26mV}{I_E \ (mA)} = 3.8 \ \Omega.$$

The DC emitter current, I_E, is 6.8 mA from DC circuit analysis. The equivalent resistance that loads the collector is R'_c and is calculated as follows:

$$R'_c = (\frac{(h_{ib} \| R_E) + r_x}{{n_2}^2} \ \| \ Q^2 r \ \| \ \frac{R_L}{{n_3}^2})(n_1 + n_2)^2,$$

where Q is the quality factor of coil L_1, r is the resistance of coil L_1, r_x is the crystal resistance at 51.0 MHz, and R_L is the load resistance of the crystal oscillator. The measured values are listed in fig. 2.05(b). Substituting values, R'_c is 676 Ω, and the loop gain is 1.48. Since the loop gain is greater than one, the small signal will keep growing until the amplitude is limited by the nonlinearity of the transistor. The transistor causes the effective loop gain to equal one, which is the condition required for oscillation.

The crystal oscillator was constructed on double sided printed circuit board. The artwork for the printed circuit layout is shown in fig. 2.06. The desired oscillating frequency is obtained by shorting the leads of the crystal and fine tuning the coil L_1 until the oscillating frequency is approximately equal to the crystal frequency. The short circuit is then removed, and the circuit will oscillate at the crystal frequency. For this oscillator, 72 mW of DC power is required for 20 mW (+13 dBm) of RF power into a 50 ohm load. A photograph of the crystal oscillator is shown in plate 2.

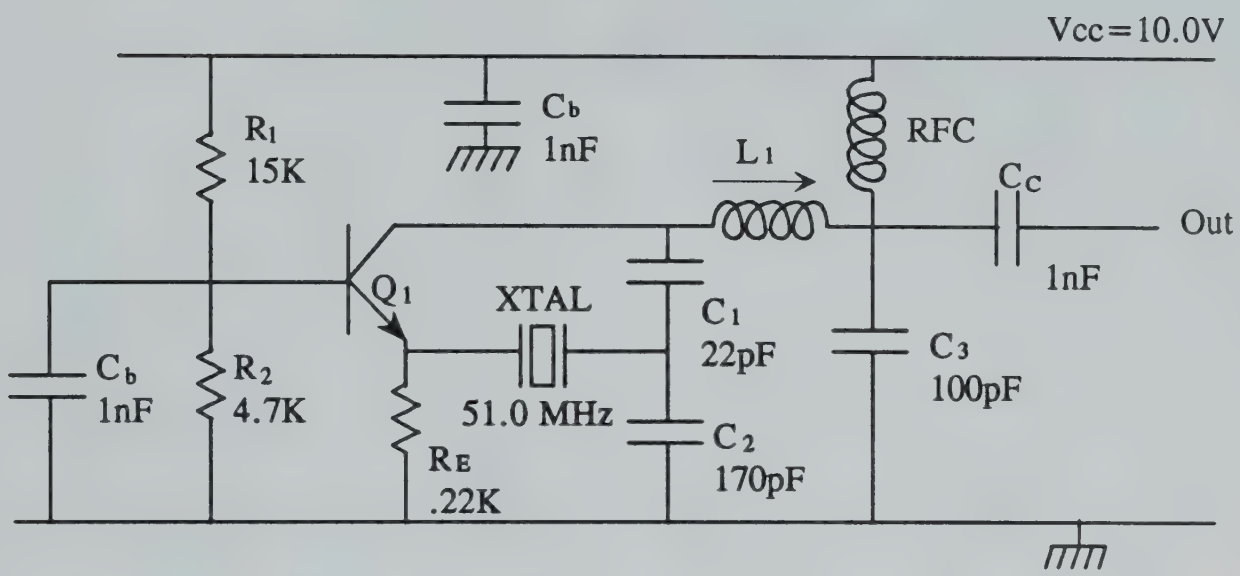

Notes: Q_1 is 2N918
L_1 is 12 Turns of #28 Wire

Figure 2.05(a) The 51.0 MHz Crystal Oscillator

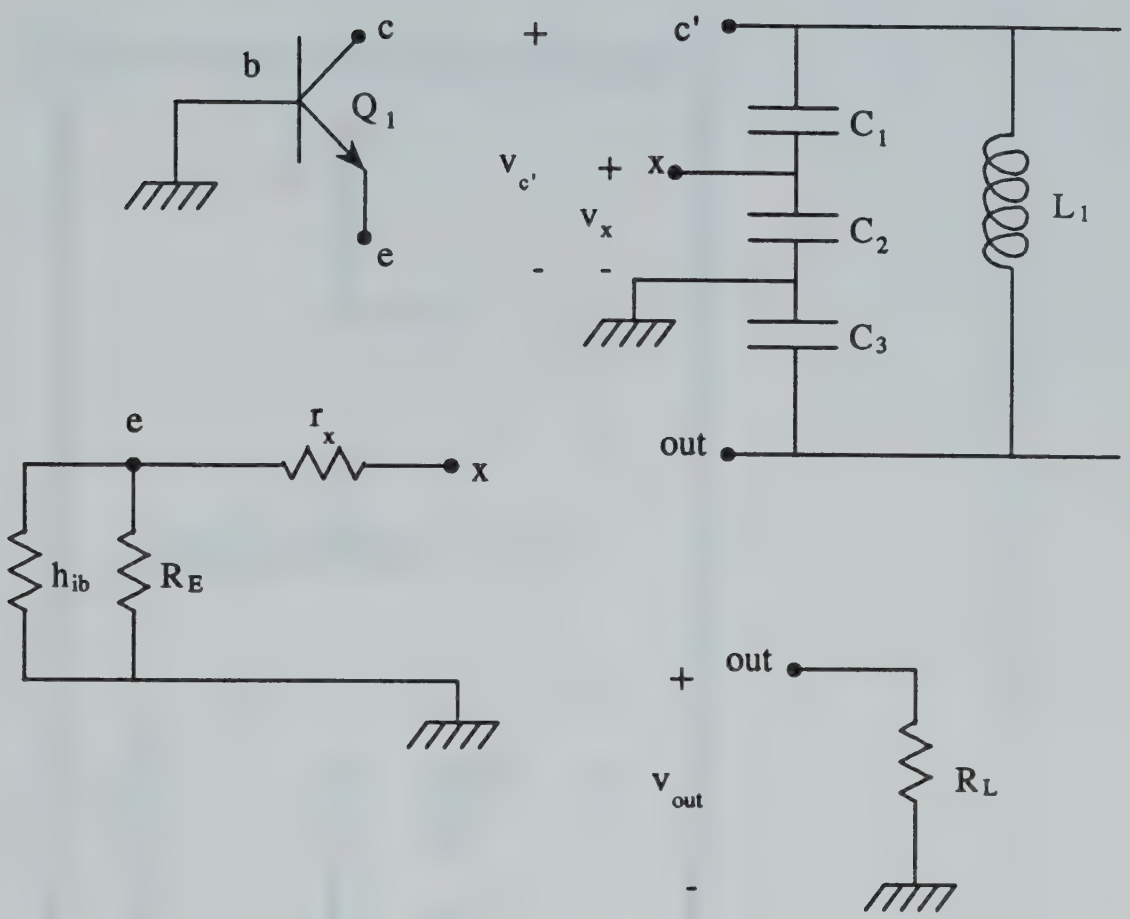

Notes: $Q_{L_1} = 100$ (Boonton 160-A Q-Meter)

$r_{L_1} = 0.3$ ohms

$r_x = 30$ ohms (West Crystal Co.; Kelowna)

$R_L = 50$ ohms

Figure 2.05(b) The Small Signal Circuit.

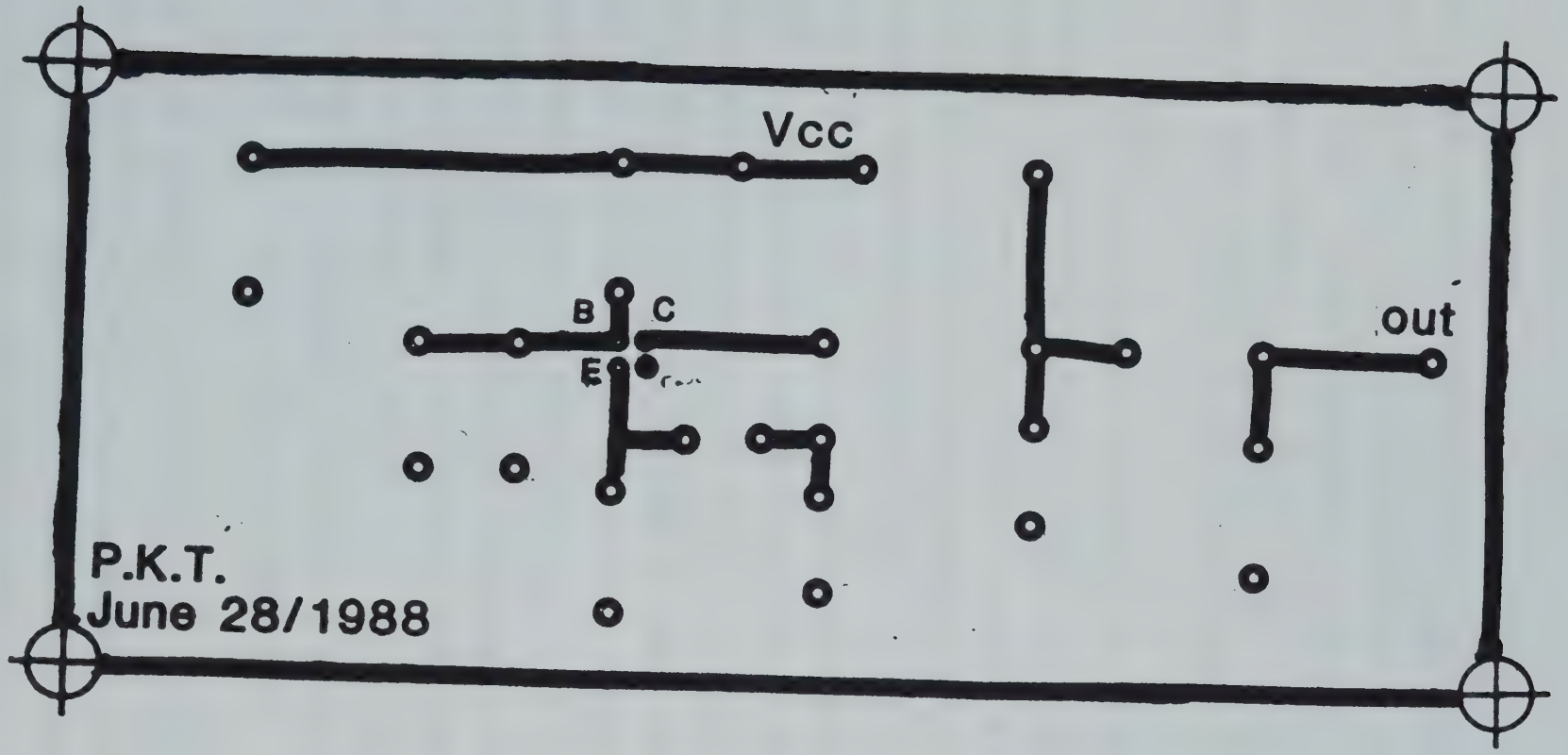

Figure 2.06 Printed Circuit Layout for the 51 MHz Crystal Oscillator.

2.5 The Frequency Multiplier

The operating principle of the multiplier is to generate a series of impulses that have the frequency of the input waveform. In the frequency domain, the impulses are a series of harmonics of the input frequency. An output resonant network filters out and passes the desired harmonic. In the frequency domain, most of the power is concentrated in the desired harmonic, and therefore, minimum power is lost through the multiplier.

The 8 times multiplier circuit is shown in fig. 2.07 (HP Application Note 920). In the circuit diagram, L_m and C_m represent the input matching network. C_t and L are tuned to the input frequency and generate the impulses with the help of the step recovery diodes. When the input voltage is positive, the diodes are forward biased, and the large forward capacitance of the diodes is being charged. When the input voltage is negative, the diodes are switched hard into reverse, and the energy switches back and forth between the inductance L and the diode reverse capacitance. This action produces the impulse followed by some damped ringing due to the output resonant network. L_n, C_n, and C_c constitute the output resonant network, which causes the impulse to ring at the desired output frequency. The reverse capacitance determines the height of the impulse and therefore the output power of the multiplier. Two diodes supply the necessary power. The capacitors, C_n and C_c, were fine tuned to minimize the power loss through the multiplier. The maximum power obtained at the multiplier output was -10 dBm into a 50 ohm load.

A 3 dB attenuator is placed before the multiplier to reduce the effect of the reactive loading on the crystal oscillator. A 408 MHz bandpass filter is placed at the multiplier output to select the desired harmonic. The multiplier circuit was also constructed on double-sided printed circuit board. A photograph of the multiplier is shown in plate 2.

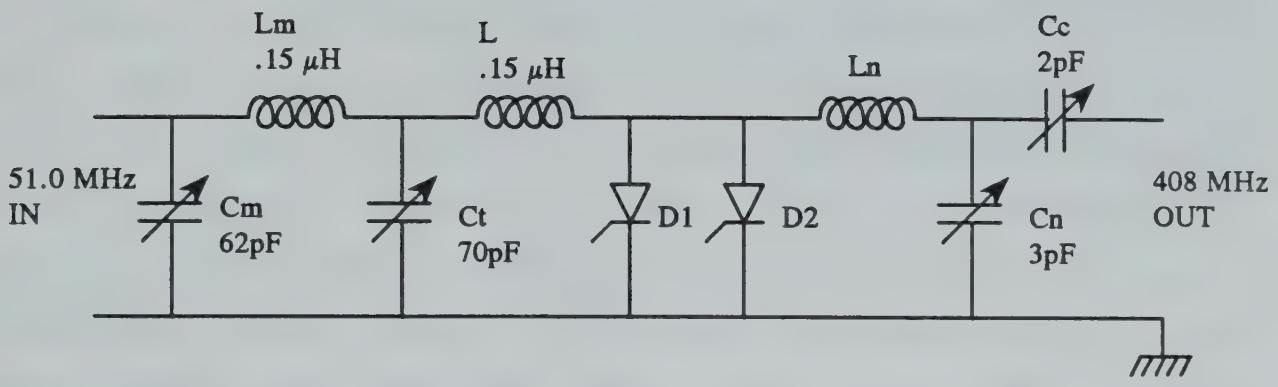

Notes: Ln is 1.5 in. of solid tinned wire.
D1,D2 are HP5082-0112 Step Recovery Diodes.

Figure 2.07 The 8 - Times Frequency Multiplier.

2.6 The High Power 408 MHz Oscillator

The physical and electrical circuits of the high power oscillator are shown in fig. 2.08(a). The design is based on the 700 MHz oscillator used in the Synthesis Telescope at D.R.A.O. (Vaneldik, 1981). The cavity, post, and tuning screw represent the tuned LC circuit. The lengths of the screw and the post set the cavity inductance, L_{cav}. The cavity capacitance, C_{cav}, is set by the distance between the screw and the post. Therefore, frequency tuning is achieved by changing the position of the screw. Coupling to the cavity is achieved through a coupling capacitor C_c connected to the base of a high power 2N3866 transistor. The transistor is specially built for oscillation purposes. The small signal circuit is shown in fig. 2.08(b). A small voltage at the emitter produces a voltage drop across the equivalent tuned circuit load because of the voltage divider action of C_{be} and C_{ce}. This voltage drop produces a base voltage, v_b, because of the same voltage divider. The transistor operates as an emitter follower, and thus the emitter voltage, v_e, "follows" the base voltage. Feedback is established, and the loop is completed. The approximate small signal loop gain, A_L, is calculated as follows:

$$A_L = (\frac{v_e}{v_b})(\frac{v_{b'}}{v_e})$$

$$= (\frac{R'_e}{R'_e + h_{ib}})(\frac{n_1}{n_2}),$$

where R'_e is the equivalent resistance that loads the emitter, and n_1, n_2 are the turns ratios for the voltage divider that consists of C_{be} and C_{ce}. The formulas for n_1, n_2, and R'_e are shown below:

$$n_1 = \frac{C_{ce}}{C_{be} + C_{ce}} \text{ and } n_2 = \frac{C_{be}}{C_{be} + C_{ce}}.$$

$$R'_e = (\frac{\beta h_{ib}}{{n_1}^2} \| Q^2 r \| \frac{R_L}{{n_3}^2})(n_2)^2,$$

where β is the small signal current gain of the transistor, Q is the quality factor of the cavity, r is the equivalent resistance for the losses in the cavity, R_L is the load resistance (50 ohms), and n_3 is the coupling from the cavity to the load. If A_L is greater than one, the small signal will keep growing until the effective loop gain is equal to one, which is the condition required for oscillation. The values of the circuit parameters are only crudely known, and therefore, the loop gain calculation is left at the algebraic stage; however, it is useful for conceptual understanding. The biasing circuit is shown in Fig. 2.08(a); its values were chosen for minimum base drive and a good DC to RF conversion efficiency. A DC input power of 300 mW was required for an RF output power of 100 mW into a 50 ohm load, resulting in a conversion efficiency of 33 %.

The cavity enclosure for the oscillator was made out of aluminum and the tuning screw and the post were made out of brass. The biasing circuit was built into a small box, which was mounted on the side of the cavity enclosure. The transistor was embedded inside the wall of the aluminum cavity. A photograph of the high power oscillator is shown in plate 2.

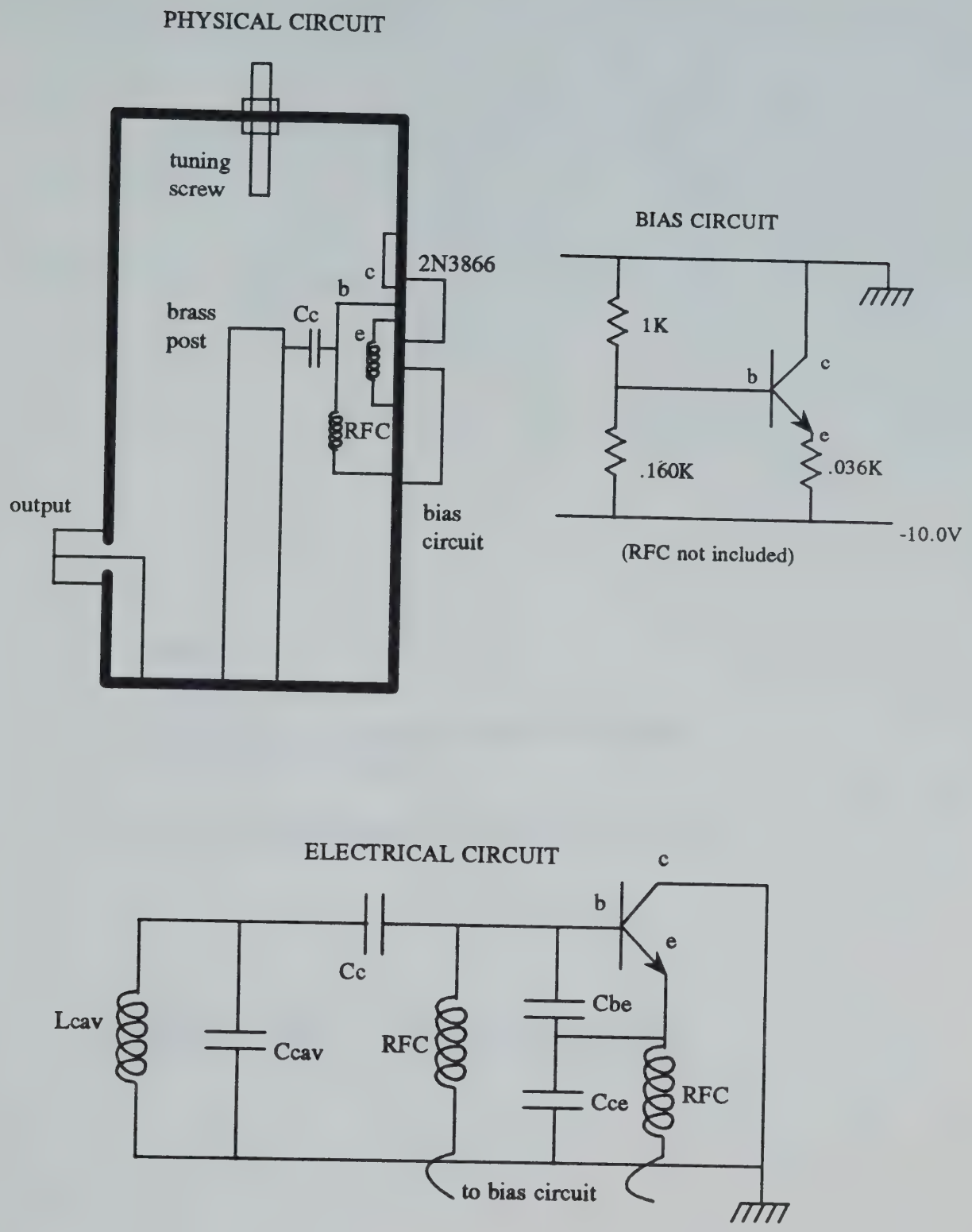

Figure 2.08(a) The 408 MHz High Power Oscillator.

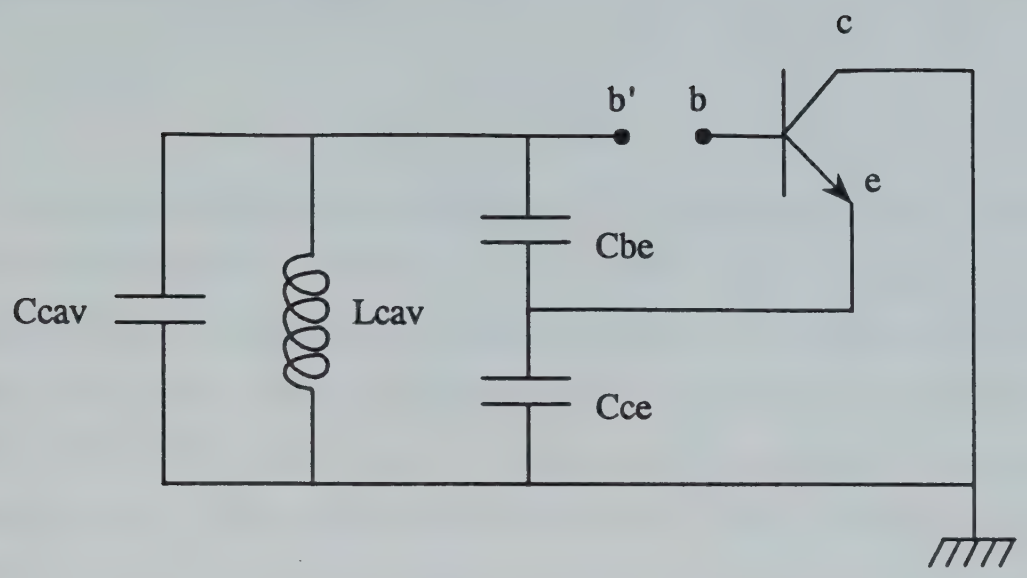

Notes:

The values of Cbe and Cce may be found from the transistor data sheets.

b'-b is the break point for the loop gain analysis.

Figure 2.08(b) The Small Signal Circuit.

2.7 Injection Locking

Injection locking is a method of forcing one oscillator to operate at the frequency of another oscillator. In our case, a low Q oscillator is forced to operate at the frequency of a high Q oscillator. As shown in the block diagram in fig. 2.09, the signal of the high Q oscillator is injected into a port of the low Q oscillator, and the output of this oscillator is fed back to the injection port. The output signal is locked when the frequency difference between the two oscillator signals is zero. From the circuit diagram in fig. 2.09, the high Q oscillator is the output of the frequency multiplier. The low Q oscillator is the free running 408 MHz power oscillator. The circulator provides a means of injecting a signal and also completes the feedback loop from the output port to the injection port.

The injection lock circuit is governed by the following differential equation (Paciorek, 1965):

$$\frac{d\theta}{dt} = \Delta\omega_o - \frac{\omega_o}{2Q} \cdot \frac{E_L}{E_O} \cdot \frac{sin\theta}{1 + \frac{E_L}{E_O} cos\theta},$$

where θ is the phase difference between the output signal and the injected signal, $\Delta\omega_o$ is the unlocked frequency difference between the two signals, $\Delta\omega_{o\ max}$ is the locking range, Q is the quality factor of the free-running oscillator, E_L is the injected voltage, E_O is the output voltage, and ω_o is the instantaneous frequency of the high power oscillator.

Locking occurs when the phase difference is constant or when $d\theta/dt = 0$, and the locking range occurs when $d\Delta\omega_o/d\theta = 0$. This gives

$$\Delta\omega_{o\ max} = \frac{\omega_o}{2Q} \cdot \frac{E_L}{E_O} \cdot \frac{1}{\sqrt{1 - (\frac{E_L}{E_O})^2}}.$$

Usually, E_L/E_O is much smaller than one, and

$$\Delta\omega_{o\ max} = \frac{\omega_o}{2Q}\cdot\frac{E_L}{E_O} = \frac{\omega_o}{2Q}\cdot\sqrt{\frac{P_L}{P_O}}.$$

Locking will be successful if the unlocked frequency difference is less than the locking range. From the formula, the locking range is proportional to the square root of the ratio of the injected power to the output power. Therefore, the injected power must be sufficient for a good locking range. In the circuit, the power output of the high power oscillator is 20 dBm, and an injected power of -10 dBm is required for a locking range of 200 KHz. Thus, to ensure locking when DC power is applied to the oscillators, the frequency of the high power oscillator, which is loaded by the circulator, is tuned to a frequency of 408 $\pm$ 0.1 MHz.

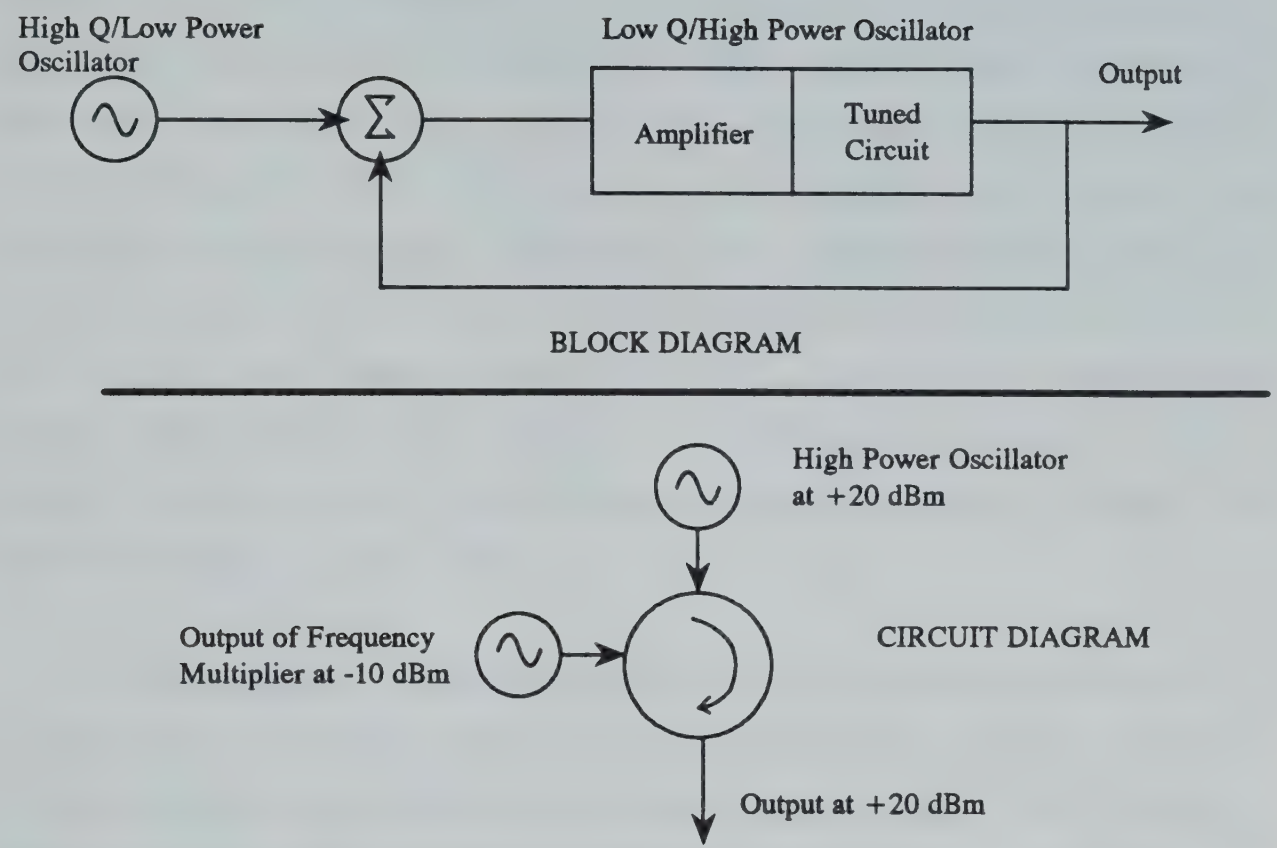

Figure 2.09 Injection Locking

2.8 The Remote Control

The transmitter was remotely located on a hillside and a circuit was devised to turn the transmitter on and off from the receiving antenna station. This was achieved by sending a 1 KHz tone by means of a walkie-talkie for a duration of two seconds. Two seconds was chosen to prevent accidental triggering. The block diagram of the circuitry used to detect the tone and supply the regulated voltages to the oscillators in the transmitter is shown in fig. 2.10. The detailed circuit diagrams are shown in Fig. 2.11. The type 567 tone decoder detects the 1 KHz tone from the walkie-talkie receiver. The type 555 timer activates the flip-flop after the tone has been detected for two seconds. The flip-flop energizes the relays to supply the regulated voltages to the oscillators.

Unfortunately, the complete transmitter unit consumed a small amount of power while on standby. Two 24 amp-hour batteries were used, and one of the batteries was dedicated to the high power oscillator. This oscillator consumed 30 mA while operating, meaning that the battery could last 100 days if used for measurements 8 hours a day. The other battery, however, was used for everything else. The crystal oscillator and multiplier consumed 100 mA while operating. On standby or with both oscillators turned off, the remote control circuit consumed 50mA. Therefore, it was possible to make measurements for only 12 days at 8 hours a day. However, 12 days was satisfactory since it took only 3 days to measure the full radiation pattern.

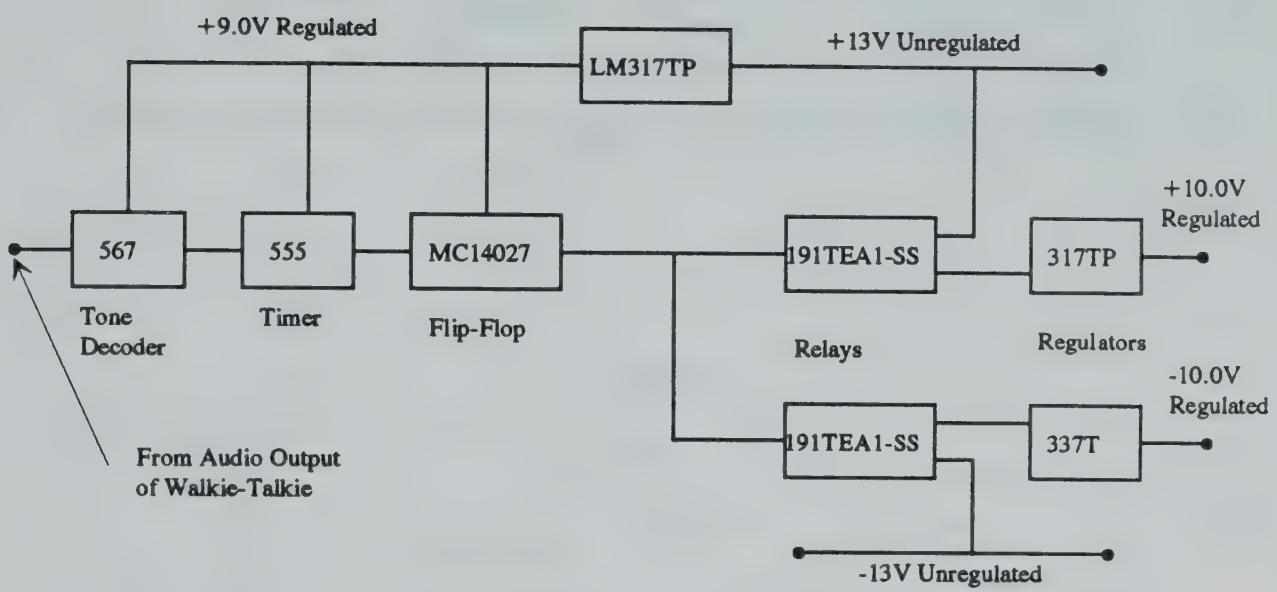

Figure 2.10 Remote Tone Detector Block Diagram.

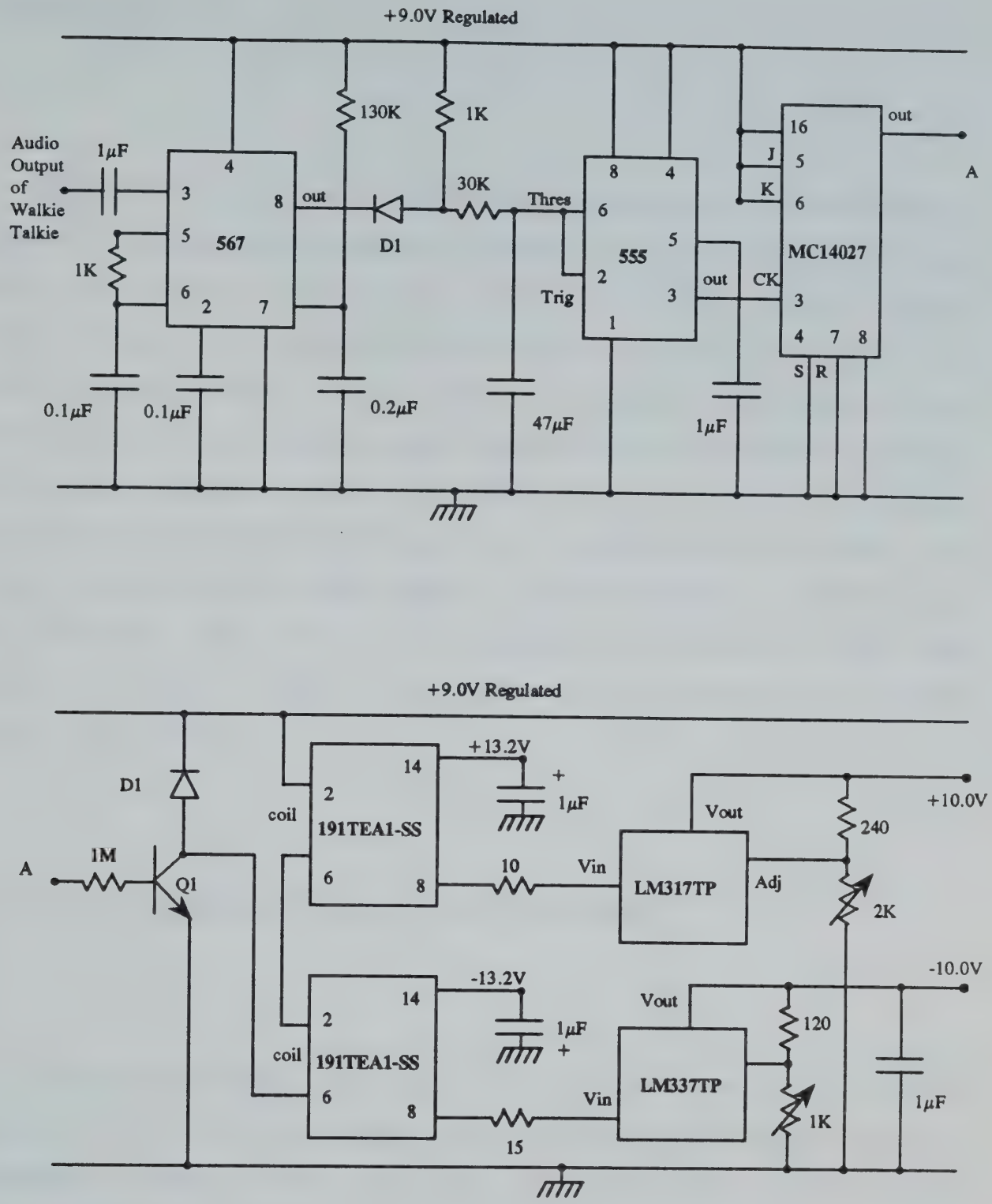

Figure 2.11 Detailed Circuit Diagram for the Remote Tone Detector.

2.9 The Receiver

The receiver used for the pattern measurement was the same receiver used for the Synthesis Telescope at 408 MHz. A block diagram of a section of the receiver is shown in fig. 2.12. The 408 MHz signal at the antenna terminals was amplified by a low noise amplifier and filtered by a 4 MHz bandpass filter. A large signal was present at the antenna terminals because a large dynamic range was required for an adequate measurement of the radiation pattern. Therefore, the second stage pre-amplifier was bypassed to prevent saturating the IF amplifier after the mixer. The mixer converted the 408 MHz signal at the filter output to a 30 MHz signal, which was sent to the control building by underground cables. The power level at the 30 MHz IF output in the control building was recorded for the measurement.

2.10 Data Logging and The Delay Correction

The measured data were logged into an IBM compatible Personal Computer (PC). The block diagram for the system used to record the measurements is shown in fig. 2.13. The measured output of the receiver was monitored by a TEK494P spectrum analyser and sent to the IBM PC via a GPIB interface. The spectrum analyser was used instead of an ordinary power meter because the spectrum analyser had a GPIB port. It was possible, therefore, to establish communication between the spectrum analyser and the computer. The antenna position was displayed on synchro dials in hour angle and declination. The analog voltages on the

synchros (120VAC signals whose phases corresponded to the antenna position) were converted to digital signals by a Synchro to Digital Interface card that was designed and built at D.R.A.O.. The digital signals were processed by a 68000 microprocessor and sent to the IBM PC via the RS-232 port. The software for the 68000 Microprocessor was written by Dobby Lam, a D.R.A.O. summer student in 1988. A Basic program for the PC was written by the author to read the present position of the antenna and then immediately record the power level from the spectrum analyser. An error in the data was caused by the time delay between reading the position and sampling the receiver output power level. Most of the time delay was caused by the section of the Basic program that was written for communications between the spectrum analyser and the computer. The time delay caused by the spectrum analyser itself was insignificant because a wide receiving bandwidth was chosen for its input bandpass filter. The time delay was measured and corrected for as follows:
At a fixed declination,

1) Scan East and record power levels as a function of position.

2) Repeat 1) by scanning West.

The delay can be deduced from the misalignment between the two data sets as shown in fig. 2.14.

For subsequent scans, East or West:

3) Add or subtract an offset value in position depending on the direction travelled as shown in fig. 2.14.

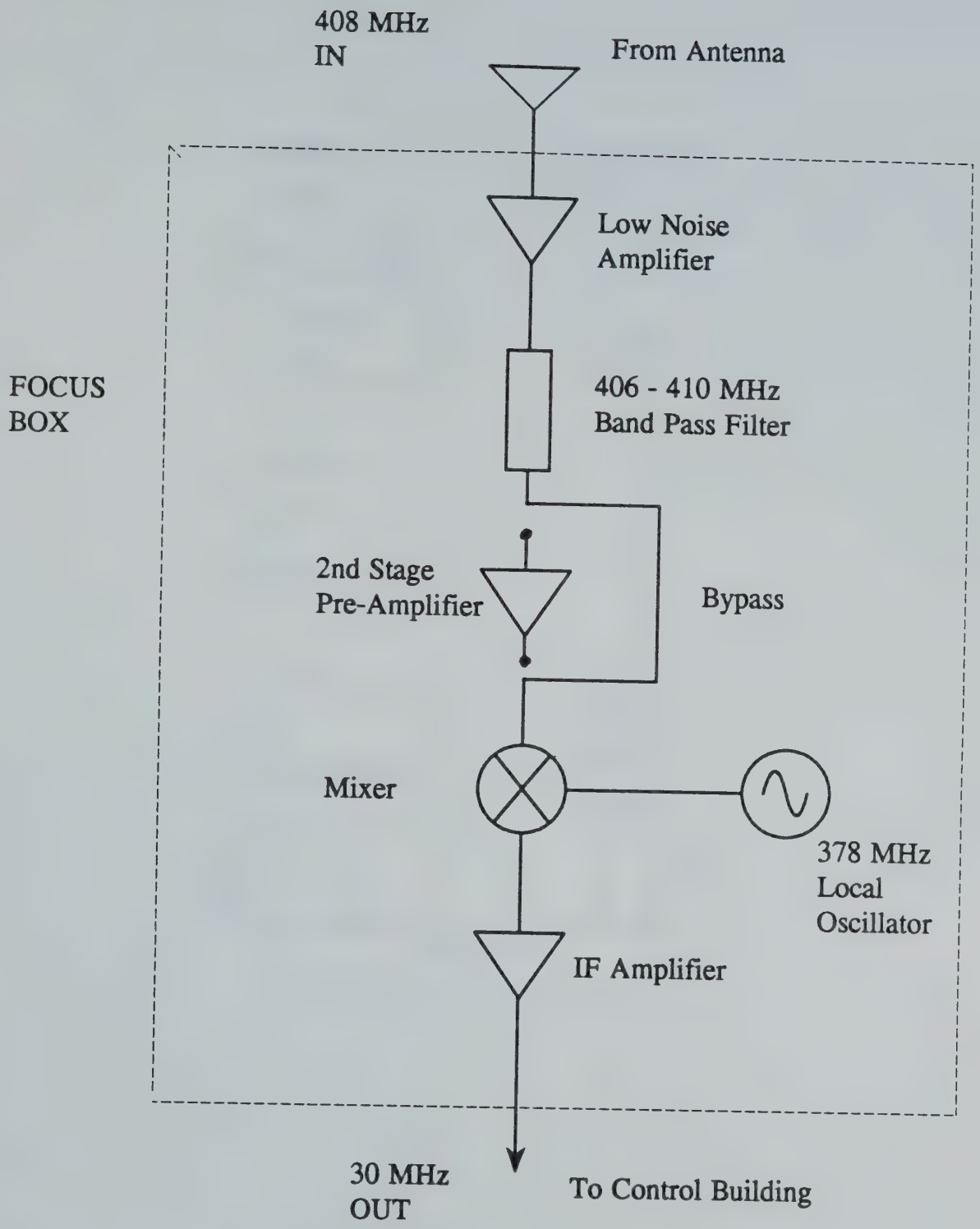

Figure 2.12 Block Diagram of a Section of the 408 MHz Receiver.

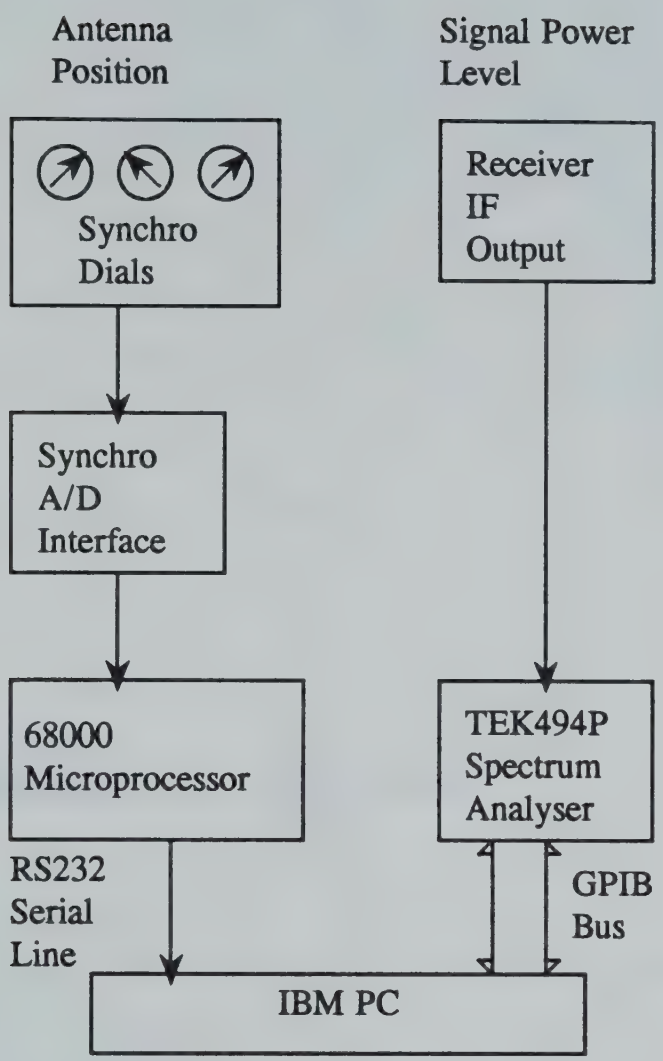

Figure 2.13 Data Logging Block Diagram.

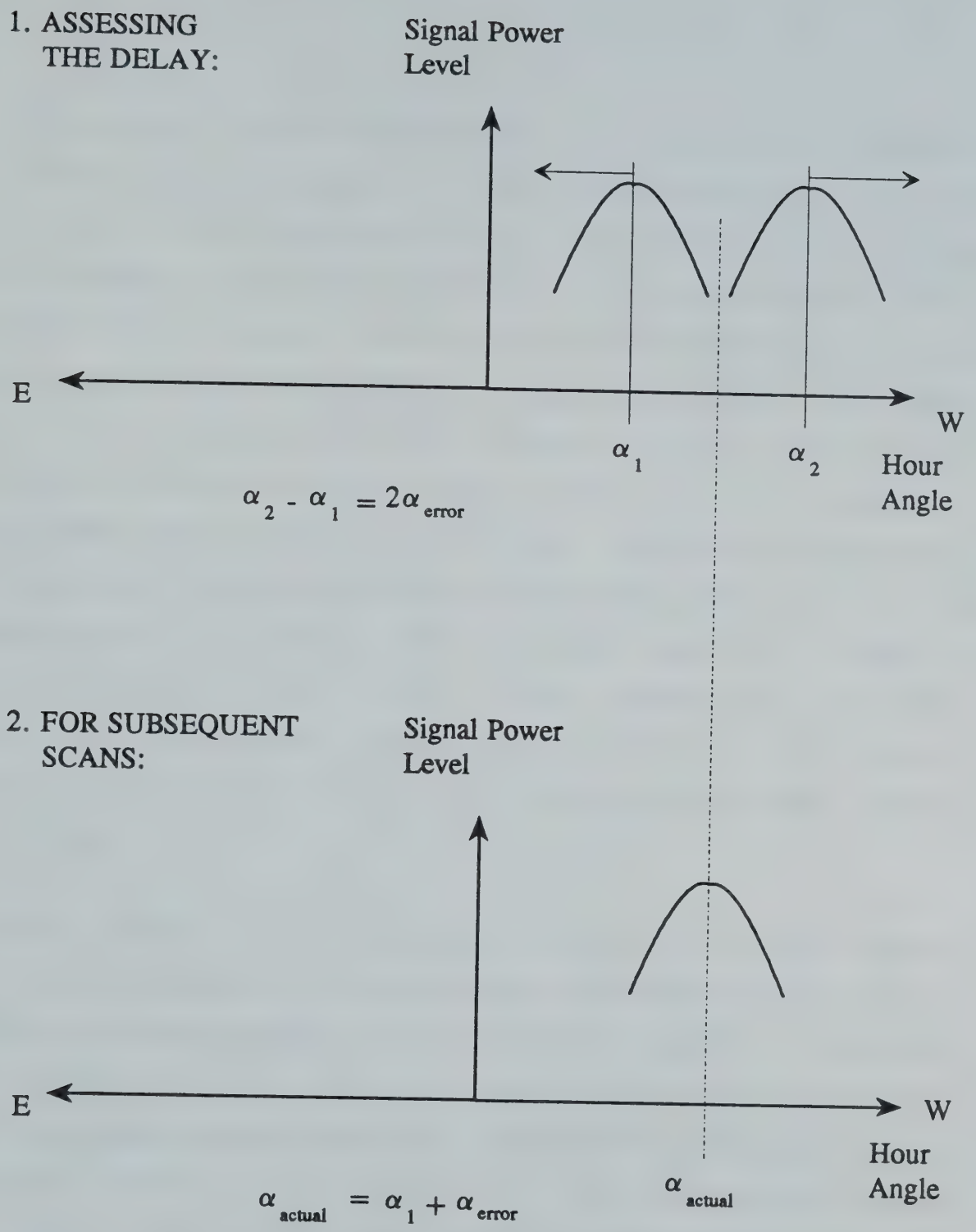

Figure 2.14 Delay Correction Procedure.

2.11 Sampling Period and Further Computer Processing

The receiver IF output was monitored only at discrete time intervals, and therefore care was required to ensure adequate sampling of the radiation pattern. The limiting factor for the time interval was that it could not be too large to cause loss of information in the antenna pattern. Thus, the upper limit was chosen to be no more than the time taken for the antenna to scan one-half of the half power beamwidth (HPBW). The HPBW for the 9m paraboloid at 408 MHz is approximately 5^o. No lower limit was necessary because the large number of data points was processed by the computer after all the data were received. The lower limit was set by the time taken to measure the power level at the receiver, 0.67 sec. The antenna scanned at a speed of 0.75^o/sec in hour angle (HA) so that the minimum sampling interval was 0.5^o. A safe sampling time was chosen, which was the time required for the antenna to scan 2^o in HA. The declination (DEC) was fixed for each scan in HA; the declination sampling interval was 1.5^o.

After applying the delay correction in section 2.10, further computer processing was necessary. The object was to transform the data from the HA-DEC co-ordinate system into the more easily readable θ-ϕ co-ordinate system shown in fig. 1.03. This was done by first interpolating the sampled data onto a uniform 360^o (HA) x 130^o (DEC) grid using a gaussian interpolation function with a FWHM of 2^o. The result was then interpolated onto a uniform 180^o x 360^o θ-ϕ grid and then plotted on a polar 180^o x 360^o θ-ϕ grid. The interpolation programs were written by Lloyd Higgs, and the software for plotting the data in polar form was written by Marc Anderson in 1987.

Plate 2

These photographs show the major components of the transmitter that was used for measuring the radiation pattern at 408 MHz. The photographs in the first row from left to right show the side view and the front view of the transmitting antenna. The 51.0 MHz crystal oscillator is shown in the second row on the left, and the 8–times frequency multiplier is shown in the same row on the right. The high power oscillator is shown in the third row on the left, and the complete transmitter unit is shown in the same row on the right.

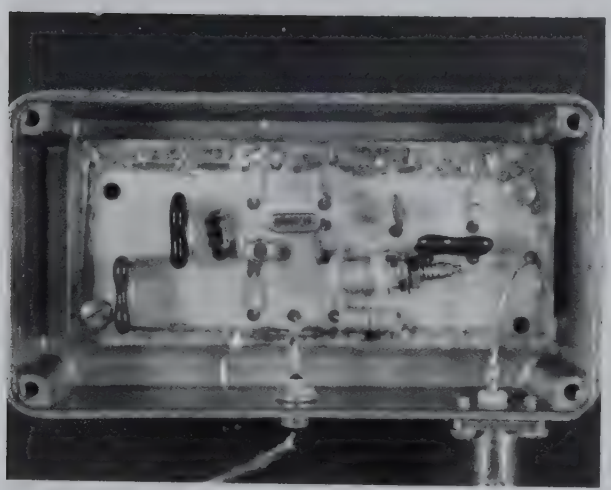

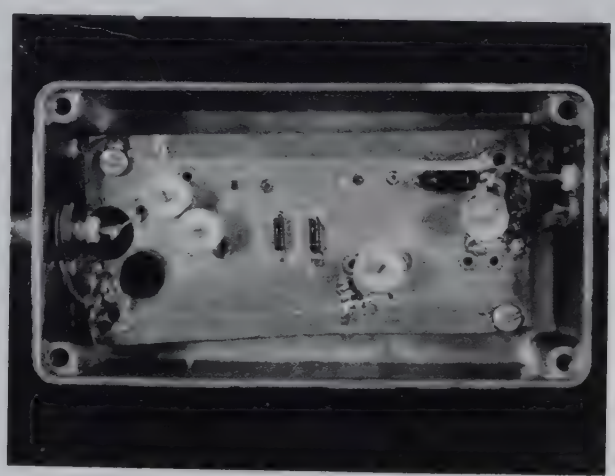

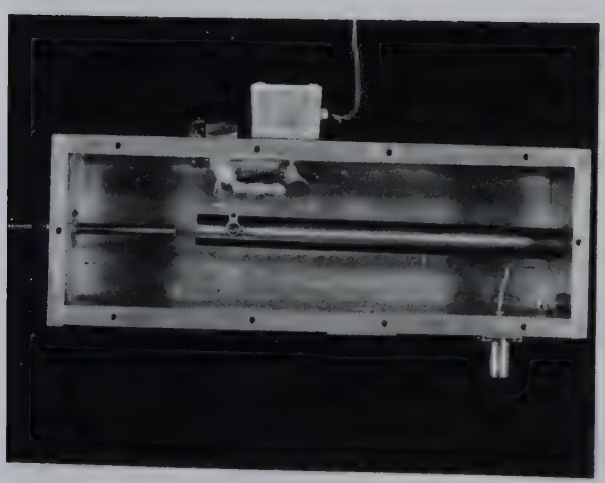

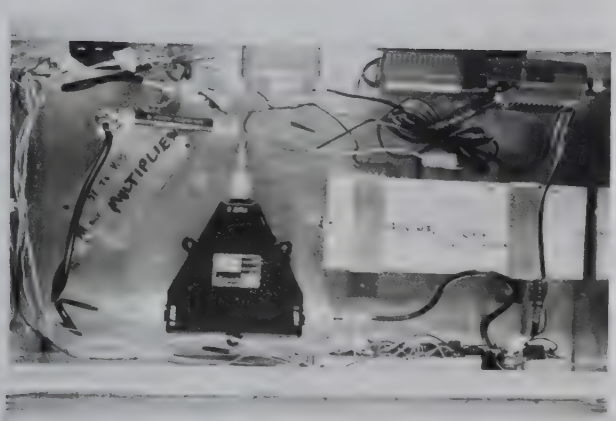
MULTIPLIER

3.0 THE MEASURED REFLECTOR ANTENNA PATTERN

In this chapter, the measured radiation pattern at 408 MHz is presented for the antenna shown in fig. 2.02. First, the measured pattern is analysed. Second, a software program is used to predict the radiation pattern; the result is compared to the measured pattern. Third, a validity check is performed on the measured pattern. Finally, the measured pattern at 408 MHz is compared to the measured pattern at 1420 MHz.

3.1 Analysing the Measured Pattern

The measured radiation pattern at 408 MHz of the 9m paraboloid using the θ-ϕ co-ordinate system is shown in fig. 3.01. The whole radiation pattern could not be measured because the antenna was restricted to positions that ranged from DEC $= -40^o$ to DEC $= 90^o$, and the HA coverage decreased as DEC decreased. However, despite the missing data, the main features are still evident. The main beam is located at the center of the plot and is indicated by the black area. The darkened areas surrounding the main beam in the form of rings are the ringlobes. The ringlobes can be predicted by taking the Fourier transform of the field distribution in the circular aperture. Other darkened areas that stand out from the general sidelobe background are the major sidelobe groups, known as the spillover lobes and the scatter cones. The radiation pattern in fig 3.01 is replotted in fig. 3.02 to emphasize these major sidelobe groups.

The first major group of sidelobes is the spillover lobes. Spillover lobes are caused by direct feed radiation and are located between $\theta = 90^o$ and $\theta = 120^o$. (See explanation in section 1.4.) A quick check of the level of the spillover lobes can be made as follows: First, the gain of the feed, G_f, is calculated (Peters, 1965):

$$G_f = \frac{41253}{\gamma_H \gamma_E},$$

where γ_E and γ_H are the 3 dB beamwidths in degrees of the principal E and H planes respectively. From fig. 3.06, $\gamma_E = \gamma_H = 60^o$, and therefore, G_f is approximately 12 or 11 dB. Since the gain of an isotropic radiator is 0 dB, G_f is 11 dBi or 11 dB with respect to isotropic. Secondly, at the edge of the dish, the feed radiation level is down 10 dB to 1 dBi. Assuming that the direct feed radiation is much greater than any other contributions to the sidelobes in this region, and knowing that the gain of the reflector is 30 dBi (see section 3.3), the level of the spillover lobes with respect to the main beam can be calculated to be $= 1 - 30 = -29$ dB. This is comparable to the level of the spillover lobes obtained from the plot.

The second major group of sidelobes shown on the plot is the scatter cones that are a result of plane wave radiation from the aperture being scattered from the feed legs. (See explanation in section 1.4.) The theoretical loci of the scatter cones are marked by the small circles on the plot. The measured scatter cones lie very close to these predicted cones. The most prominent section of one of the scatter cones observed is the one located between $\phi = 180^o$ and $\phi = 210^o$. Some scatter cones are more evident than others, and the intensity varies along the cone itself. This is because the radiation of the scatter cone is elliptically polarized with the major axis of the polarization ellipse being parallel to the strut, while the feed of the Synthesis Telescope is circularly polarized.

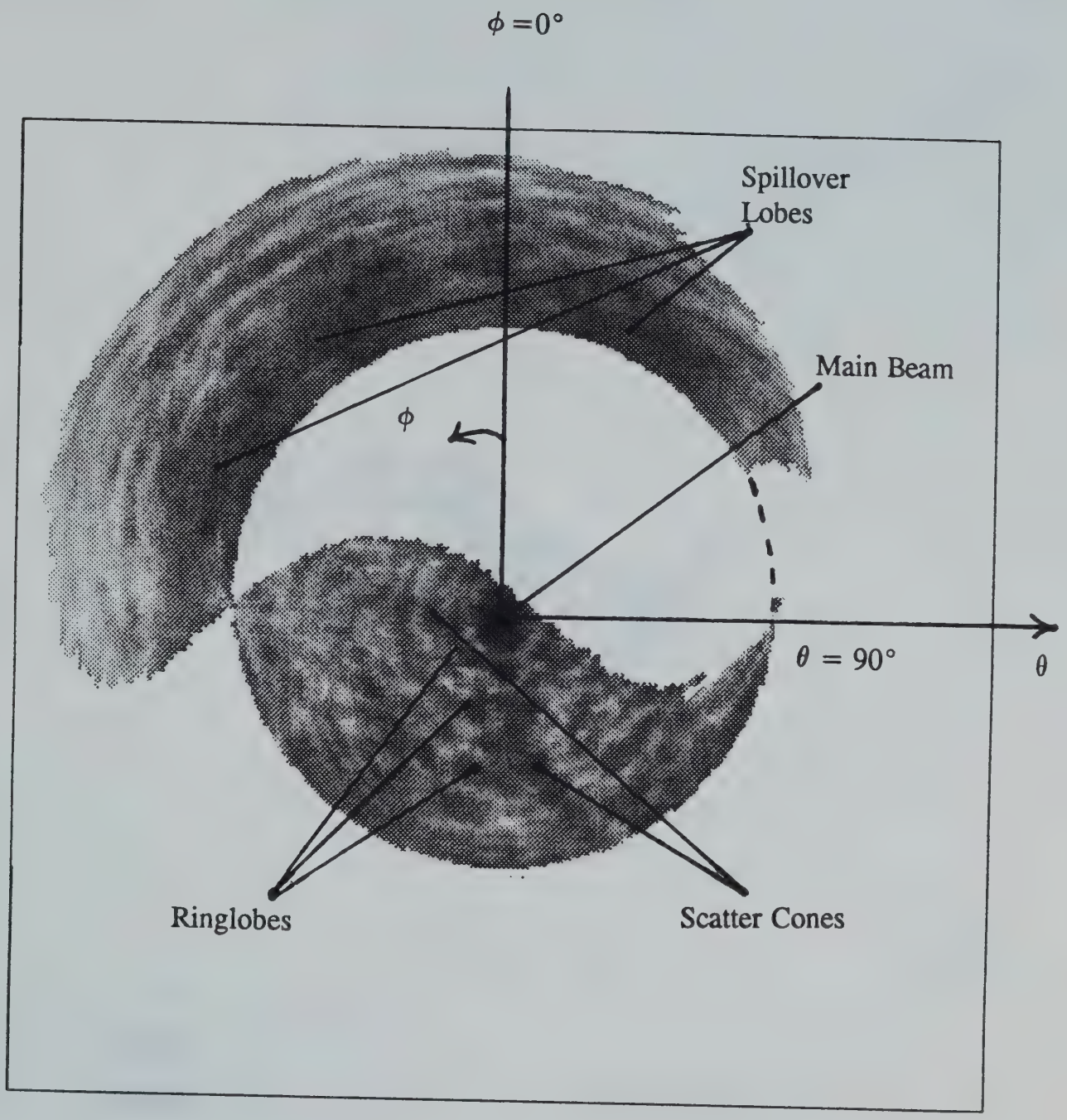

Figure 3.01 The 408 MHz Radiation Pattern of a 9m Paraboloid fed by the Existing Probe Excited Feed. This is a qualitative representation, where the darker shadings correspond to higher power levels.

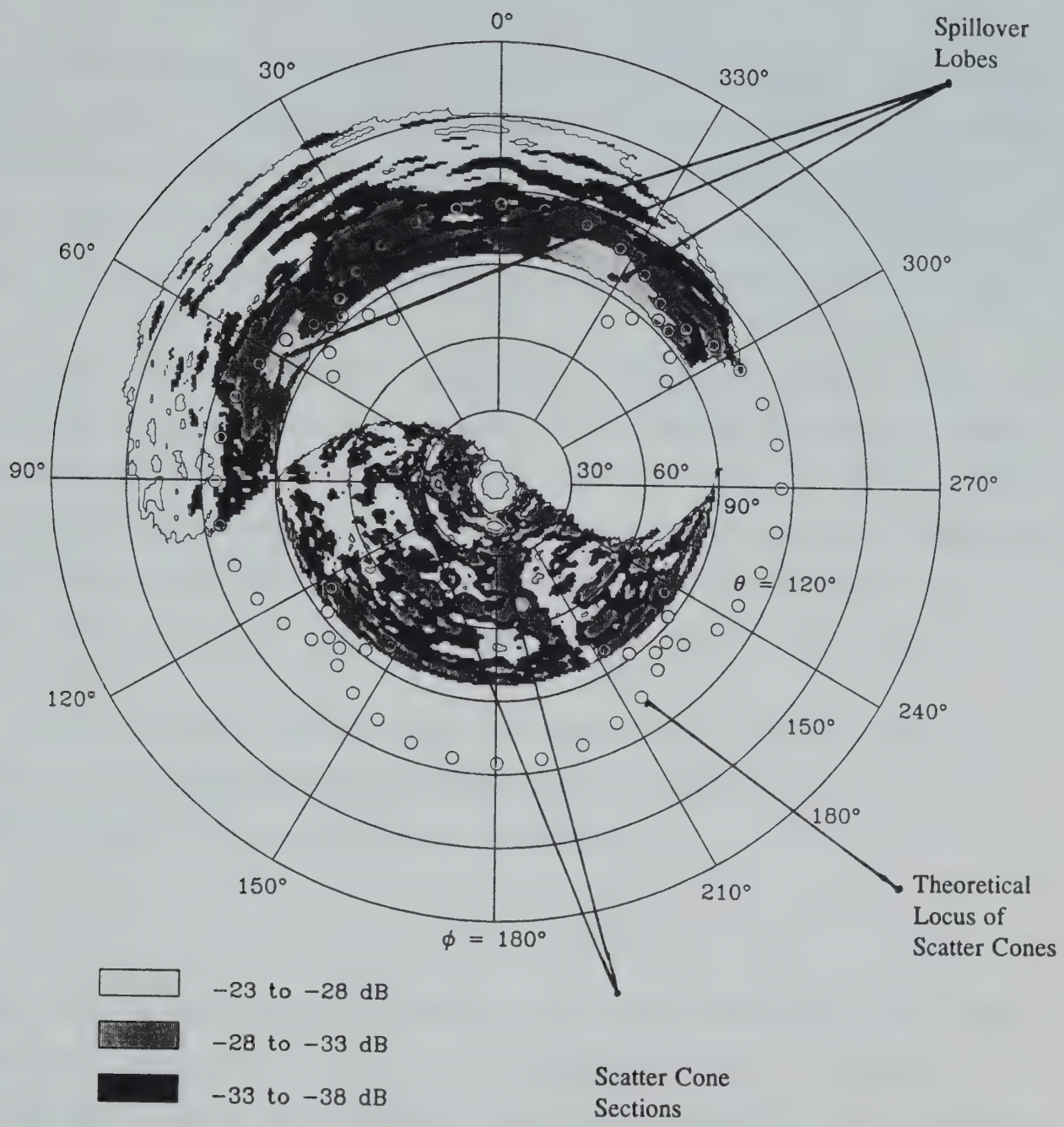

Figure 3.02 The 408 MHz Radiation Pattern plotted to emphasize the Major Sidelobe Groups.

3.2 Comparison with the Software Prediction

The secondary pattern (the pattern of the 9m reflector) can be predicted using the Numerical Electromagnetic Code for Reflector Antennas (NEC-REF) (Rudduck, Chang, 1982). Before comparing the measured pattern with the pattern predicted from the software program, a brief description of how the software calculates the predicted pattern will be presented.

The NEC-REF software computes the radiation pattern using two methods, which are Aperture Integration (AI) and the Geometrical Theory of Diffraction (GTD). The electric field calculated using the GTD is added to the field calculated using AI. The software also computes the effects of strut scatter, feed blockage, and feed spillover. A flowchart that shows how the software computes the total electric field is shown in fig. 3.03.

For the main beam and first few sidelobes, i.e. for the region, $0^o < \theta < \theta_o$, the pattern is predicted most accurately using the AI method. The effect of the GTD is negligible in this region.

$$\theta_o = Sin^{-1}(\frac{1}{\sqrt{D_\lambda}}),$$

where D_λ is the aperture diameter in wavelengths (Rudduck et al., 1982). Aperture Integration is used in the calculation shown in section 1.3, in which the result is proportional to the Fourier transform of the aperture field distribution.

For the remaining angles ($\theta_o < \theta < 180^o$), the radiation pattern is predicted most accurately using the GTD. In this region, the electric field calculated using the AI method is negligible compared to the field calculated using the GTD. The GTD is described briefly in section 1.3. The fields in

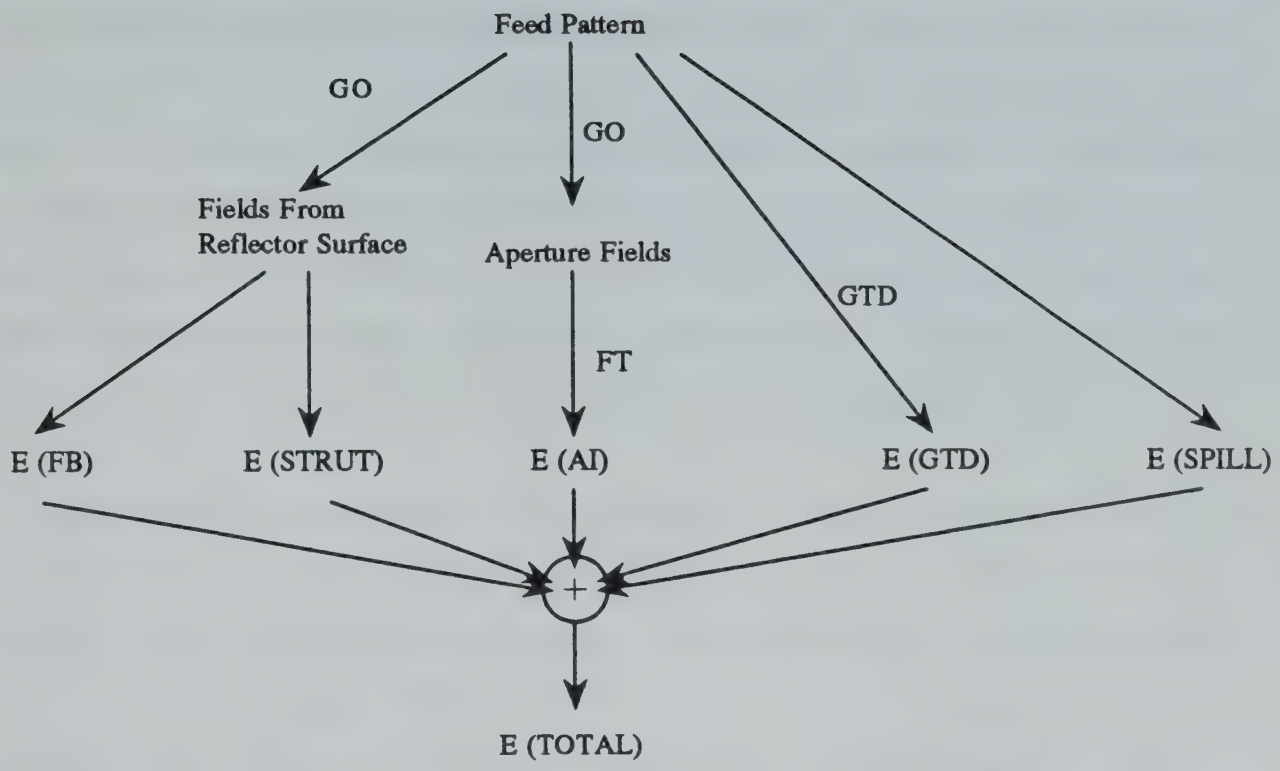

Notes:

SPILL:	Spillover
STRUT:	Strut Blockage
GO:	Geometrical Optics
GTD:	Geometrical Theory of Diffraction
FT:	Fourier Transform
FB:	Feed Blockage
AI:	Aperture Integration

Figure 3.03 A Flowchart Showing How the NEC-REF Software Calculates the Radiation Pattern of a Paraboloid.

this region are a result of the fields diffracted from the reflector rim. The rim is approximated by a number of small linear segments. Each linear segment is the edge of a flat plate that is tangential to the reflector surface. The diffraction coefficient is calculated for the edge of a conducting flat plate, where the diffraction is considered to occur at the centre of each linear segment. The diffraction is also calculated at the corners, where two linear segments are joined. The total diffracted field from the rim is the superposition of the diffracted fields from the edges and the corners.

The effect of strut scatter is also calculated in the software. First, the fields from the reflector surface are calculated using the principles of geometrical optics. These fields constitute a plane wave that is incident on the strut. The strut is then divided into a number of small segments. The field diffracted from each strut segment is calculated by multiplying the field incident on the strut by the diffraction coefficient. The diffraction coefficient is calculated for a circular conducting cylinder. The total strut scatter is the superposition of the diffracted fields from all the strut segments.

The effect of feed spillover is obtained by adding the direct radiation from the feed to the radiation from the reflector.

The effect of feed blockage is also calculated in the software. The feed is modelled as a circular flat plate, and the effect of feed blockage is the field scattered forward from the flat plate with the incident fields being the fields from the reflector surface.

A comparison was made between the predicted pattern and the measured pattern by calculating the average polar pattern cut (i.e. at fixed azimuth) for each case. The predicted average polar pattern cut was obtained by averaging pattern cuts at five different values of ϕ. The measured average cut was obtained as follows: First, the unmeasured portions of the

measured pattern had to be filled in. For each $\theta = \theta_o$, an average of all the measured power levels, $P_n(\theta_o, \phi)$, was taken. The average value was used as a fill value for the unmeasured positions of ϕ at θ_o. In the region, $160^o < \theta < 180^o$, there were no measured data to average. The fill value in this region was chosen to be -35 dB, which was the last measured average value at $\theta = 160^o$. The measured average cut was then just the ϕ-cut with no measured data. (All the values in this cut were averaged values.) The predicted and measured pattern cuts are plotted on the same graph in fig. 3.04. As shown in the figure, some similarities and differences exist between the two pattern cuts.

The first similarity is the general shape of both pattern cuts. The sidelobe envelopes both decrease to a minimum at $\theta \approx 70^o$ and increase to a maximum at $\theta \approx 100^o$, where feed spillover occurs. Both envelopes decrease to another minimum in the shadow region ($120^o < \theta < 180^o$) at $\theta \approx 150^o$ and increase to a maximum at $\theta = 180^o$, where rim diffraction is a maximum.

The second similarity is the angular separation of the sidelobes. This similarity is clearly evident in the region of $0^o < \theta < 50^o$. In this region, the angular separation can be predicted by taking the Fourier transform of the field in the reflector aperture, and the measured pattern verifies this effect. The angular separation of the sidelobes is similar in other regions, but the similarity is not as evident as that in the near sidelobe region.

The most obvious difference between the pattern cuts is the sidelobe level. The largest level differences occur in the regions, $40^o < \theta < 110^o$ and $120^o < \theta < 180^o$. In these regions, the measured sidelobes are 3 to 7 dB higher than the predicted sidelobes. The level discrepancy in the region, $40^o < \theta < 110^o$, may be largely due to surface roughness. Surface roughness is not taken into account in the NEC-REF software. The surface error of the ST antenna is $1cm$ rms. The gain loss factor, GL, is (Ruze, 1952)

$$GL = exp[-(\frac{4\pi\delta}{\lambda})^2],$$

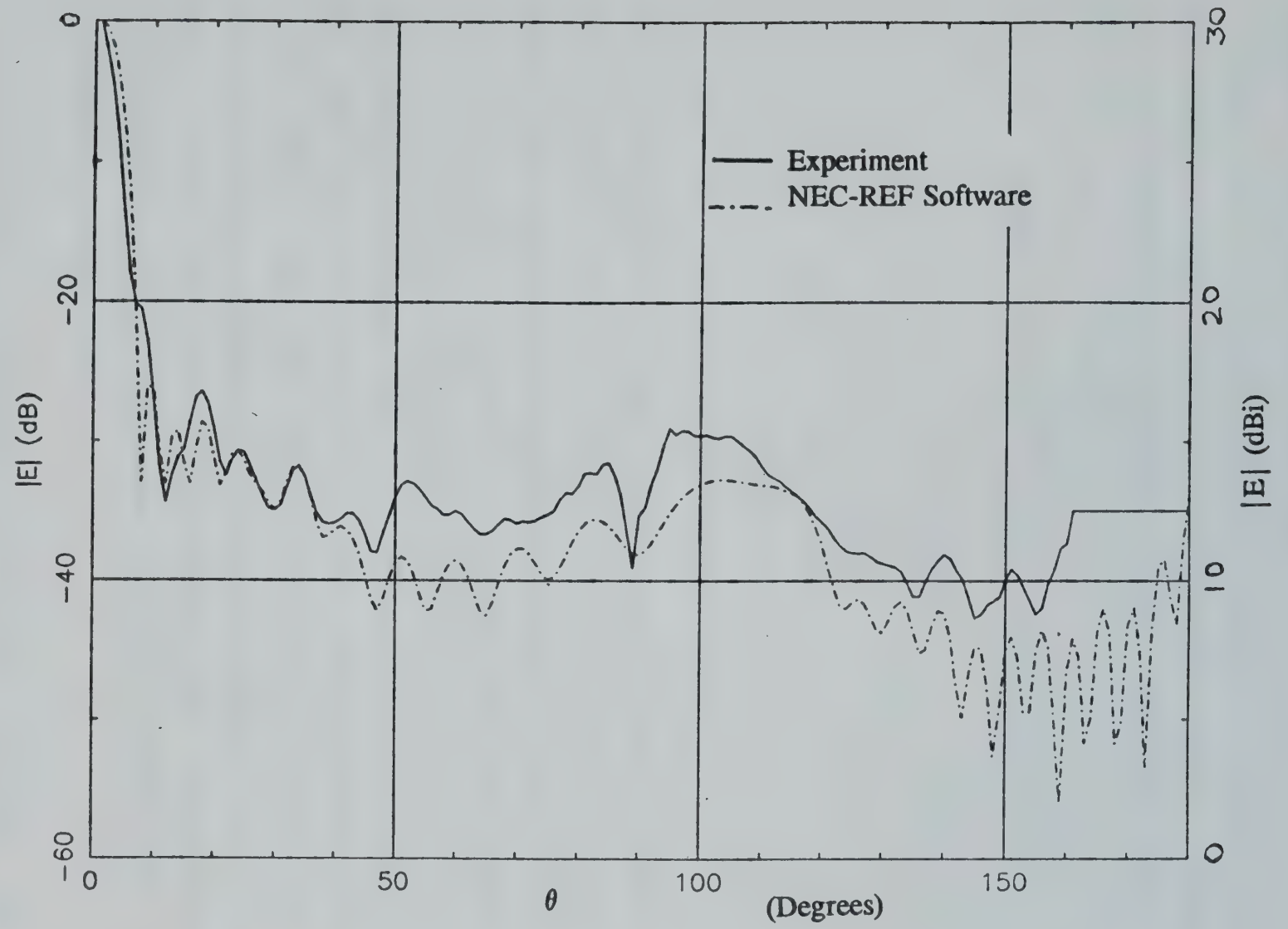

Figure 3.04 The Measured and Predicted Average Pattern Cuts for the 9m Reflector Antenna

where δ is the rms surface error ($1cm$), and λ is the operating wavelength ($73.53cm$). Using the formula, the surface error reduces the gain to 97 % of its ideal value. The gain reduction corresponds to a sidelobe increase in the forward hemisphere, which has a solid angle of 2π sr. Therefore, the level of the sidelobes (due to surface roughness alone) with respect to the main beam may be calculated approximately as follows:

$$\text{sidelobe level} = \frac{\text{power density in sidelobe region}}{\text{maximum power density}}$$

$$= \frac{(1 - GL)/2\pi}{1/\Omega_a}$$

$$= \frac{.03/2\pi}{1/.0132}$$

$$= 6.05 \times 10^{-5}$$

$$= -42dB$$

The sidelobe level with respect to an isotropic radiator is -12 dBi. The predicted sidelobe level without the surface roughness is -10 dBi. Adding the two power levels increases the sidelobe level to -8 dBi or 38 dB below the main beam level. Therefore, in the forward hemisphere, surface roughness may account for a discrepancy of approximately 2 dB. The remaining discrepancy in the region, $40^o < \theta < 110^o$, and the discrepancy in the region, $120^o < \theta < 180^o$, may be due to other effects not taken into account in the software. Such effects could include scattering of direct feed radiation by the struts or diffraction by the rim of radiation scattered from the struts. The rim would then be illuminated at higher radiation levels than before, and this would probably raise the predicted sidelobe level closer to the measured sidelobe level.

The differences in the sidelobe level of the two pattern cuts is also seen in the near region of $10^o < \theta < 20^o$. Here, the measured sidelobes are 1 to 3 dB higher than the predicted sidelobes. Surface roughness and multiple reflections between the feed and the reflector may account for the discrepancy in this region.

3.3 Verification of the Measured Pattern

The pattern measured at 408 MHz was checked by comparing the solid angle obtained from the measurement to the solid angle obtained from other sources such as the NEC-REF software and an observation of the CAS A radio source.

The solid angle obtained from the measured pattern was calculated approximately as follows: (The unmeasured portions of the pattern were filled in by the method described in section 3.2.)

$$\Omega_a \approx \sum_{1}^{360} \sum_{0}^{180} P_n(\theta, \phi) sin\theta \Delta\theta \Delta\phi,$$

where θ, ϕ are in degrees, and $\Delta\theta = \Delta\phi = \pi/180$ radians.

The solid angle obtained from the NEC-REF software was calculated from the maximum directional gain (directivity), which occured at $\theta = 0^o$. The predicted gain, G, at $\theta = 0^o$ was 29.8 dB. By assuming no ohmic losses on the reflector, the solid angle is

$$\Omega_a = \frac{4\pi}{G}$$

The solid angle obtained from the CAS A radio source was calculated by using the result of a previous measurement. The measurement involved measuring the increase in antenna temperature when pointing the antenna at the radio source. The aperture efficiency, ε_{ap}, was then calculated as follows (Kraus, 1988):

$$\varepsilon_{ap} = \frac{2k\Delta T_A}{SA_p},$$

where k is Boltzmann's constant, S is the known source flux density of CAS A, A_p is the physical aperture (aperture area), and ΔT_A is the measured increase in the antenna temperature. The measurement was made by Bruce Veidt (1984), who calculated an aperture efficiency of 60 %. The solid angle was then calculated from the aperture efficiency as follows:

$$\Omega_a = \frac{\lambda^2}{\varepsilon_{ap} A_p},$$

where λ is the wavelength (0.7353m) and A_p is the aperture area ($39.4m^2$). The solid angles obtained using the three methods are summarized below:

Measured data : 1.43×10^{-2} *sr*

CAS A radio source : 1.37×10^{-2} *sr*

NEC-REF software : 1.32×10^{-2} *sr*

The solid angle calculated from the measured data agrees to within 5 % with the solid angle obtained from the CAS A radio source. The discrepancy between the two values results from the fact that nearly half of the measured pattern was estimated, and therefore, the measured pattern is satisfactory.

The solid angle calculated from the NEC-REF software is lower than the solid angles calculated from the measured data and the CAS A radio source. The value predicted from the software is lower because the predicted sidelobe levels are slightly lower than the measured sidelobe levels. As shown in section 3.2, the software does not take into account various effects that would normally raise the sidelobe level. All the solid angle calculations, however, agree to within 8 %.

3.4 Comparing the 408 MHz and 1420 MHz Radiation Patterns

It is worthwhile to compare the measured patterns at 408 MHz and 1420 MHz. The measured 1420 MHz radiation pattern is shown in fig. 3.05 (Anderson, 1990). In the following paragraphs, the measured pattern at 1420 MHz shown in fig. 3.05 is compared to the measured pattern at 408 MHz shown in fig. 3.02.

Similarities between the two patterns include the location of the spillover lobes and scatter cones. In both cases, the most prominent section of the scatter cone is located between $\phi = 180^o$ and $\phi = 210^o$, and the effect of spillover is seen from $\theta = 90^o$ to $\theta = 120^o$.

The major difference between the two patterns is the sidelobe level. The sidelobes at 1420 MHz are about 10 to 15 dB lower. There are two major reasons for the lower sidelobe level. The first is the diameter of the reflector aperture in terms of wavelengths. The reflector aperture is 43 λ wide at 1420 MHz and 12 λ wide at 408 MHz. Therefore, the radiation from the aperture at 408 MHz has a wider extent in angle than the radiation at 1420 MHz. Since the sidelobe level decreases as a function of angle (as predicted by taking the Fourier transform of the aperture distribution) the sidelobe level at any given angle will be lower at 1420 MHz than at 408 MHz. The second reason is the size of the feed. Because the feed is small at 408 MHz, its beam is broad. The measured H-plane feed patterns at 408 MHz and 1420 MHz are shown in fig. 3.06. As shown in the figure, the beam is broader at 408 MHz. The broad beam at 408 MHz results in a reflector illumination with a low edge taper, which raises the level of the near sidelobes as predicted by taking the Fourier transform of the reflector aperture distribution. The high edge illumination also raises the level of the far sidelobes because the diffracted fields from the rim are

stronger. The broad beam also results in high spillover. Again, comparing the radiation pattern in fig. 3.05 to the pattern in fig. 3.02, the level of the spillover lobes range from -23 dB to -28 dB at 408 MHz, and the level ranges from -40 dB to -45 dB at 1420 MHz.

Another difference between the two radiation patterns is the width of the scatter cones. The width of the scatter cones is proportional to the wavelength (Rusch, 1982). The measured 3 dB beamwidth of the most prominent section of the scatter cone at 1420 MHz is approximately 4^o. At 408 MHz, the measured 3 dB width of the most prominent section of the scatter cone is about 14^o; this width is an average value of the scatter cone section from $\theta = 30^o$ to $\theta = 60^o$. The ratio of the two measured widths is 3.5 and confirms the prediction by Rusch.

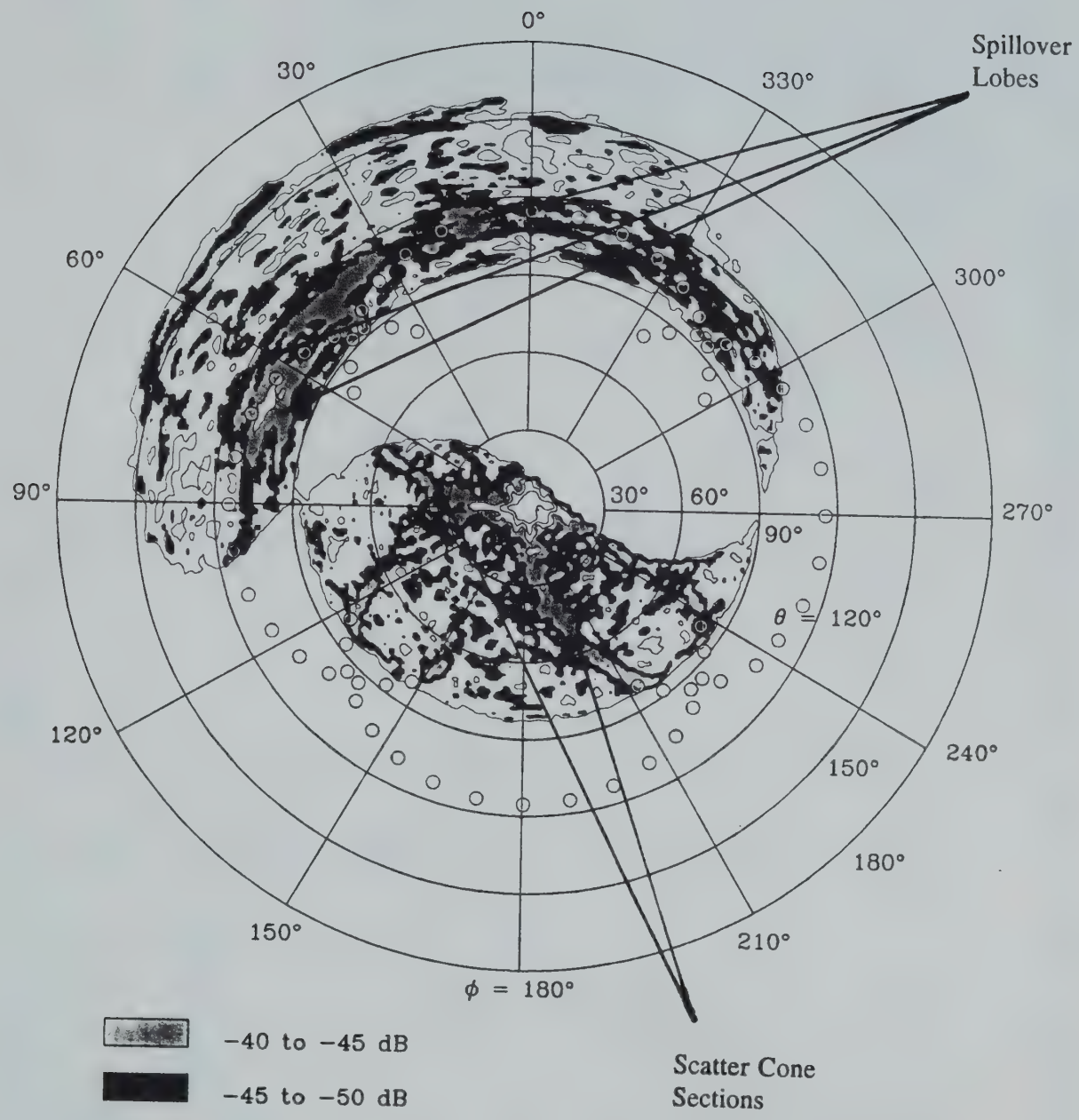

Figure 3.05 The 1420 MHz Radiation Pattern plotted to emphasize the Major Sidelobe Groups (Anderson, 1990).

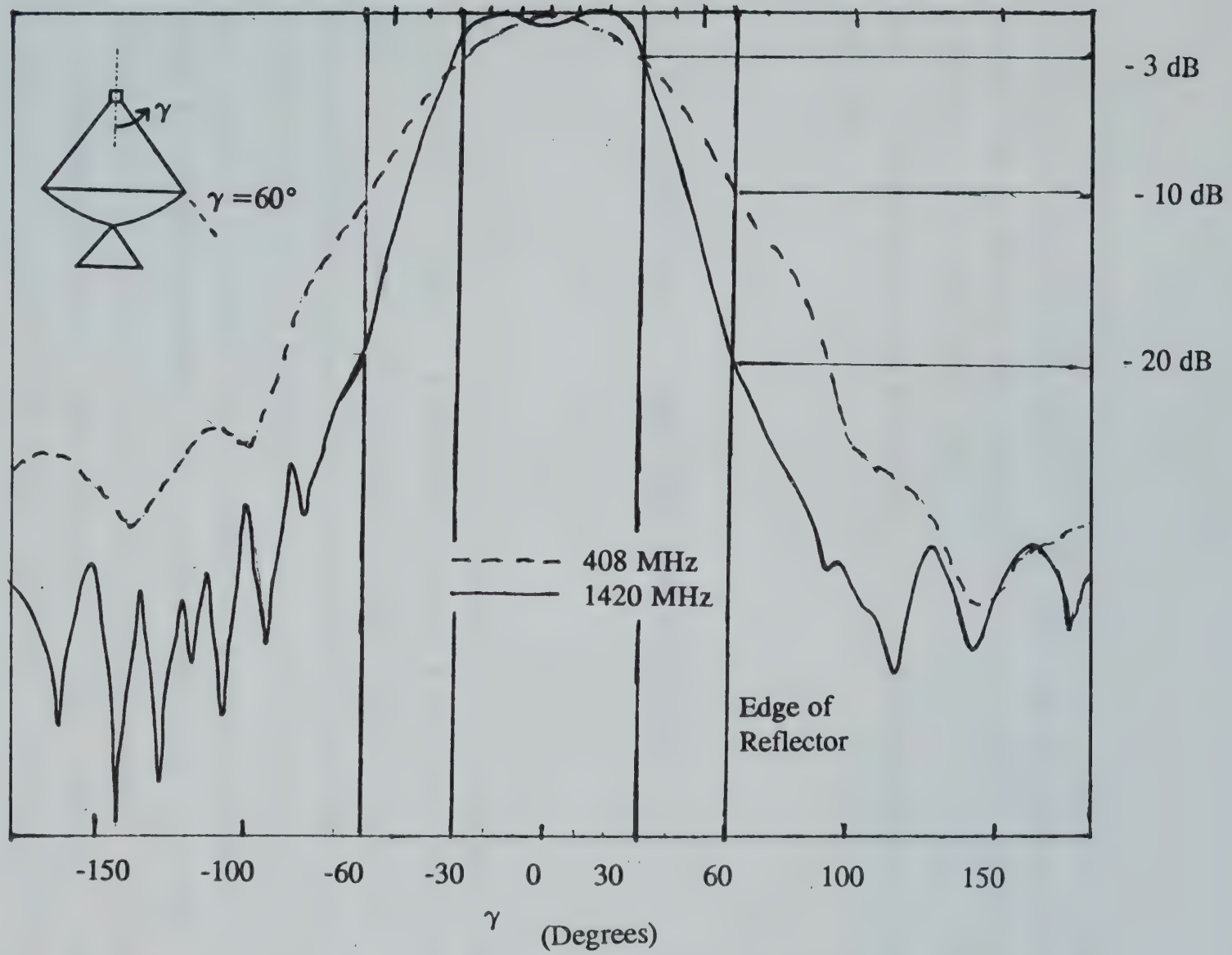

Figure 3.06 The Measured H-Plane Feed Patterns at 408 MHz and 1420 MHz.

4.0 THE FEED OF THE SYNTHESIS TELESCOPE

This chapter describes the existing feed of the Synthesis Telescope. First, the operation of the feed at 1420 MHz and 408 MHz is described. Second, the problems of the existing feed at 408 MHz are described. This is followed by a listing of the electrical specifications at 408 MHz. Finally, a set of design constraints is presented for the feed modifications discussed in chapter 5.

4.1 Feed Operation at 1420 MHz and 408 MHz

A cross section of the existing feed along with its dimensions is shown in fig. 4.01. The feed is a multimode coaxial feed (Koch, 1973; Scheffer, 1971) and is designed and optimized for good reflector illumination (high aperture efficiency) and low cross polarization at 1420 MHz. The highest aperture efficiency for a reflector occurs when the illumination over the circular aperture is uniform, and the illumination is zero elsewhere. This requires a circularly symmetric $2J_1(x)/x$ field distribution in the feed aperture as shown in fig. 4.02 (Christiansen and Högbom, 1985). The variable, x, is proportional to the radial dimension, ρ. The relationship between x and ρ is also shown in the figure. The reflector aperture illumination, which is proportional to the feed pattern, and the feed aperture distribution constitute a Fourier Transform pair.

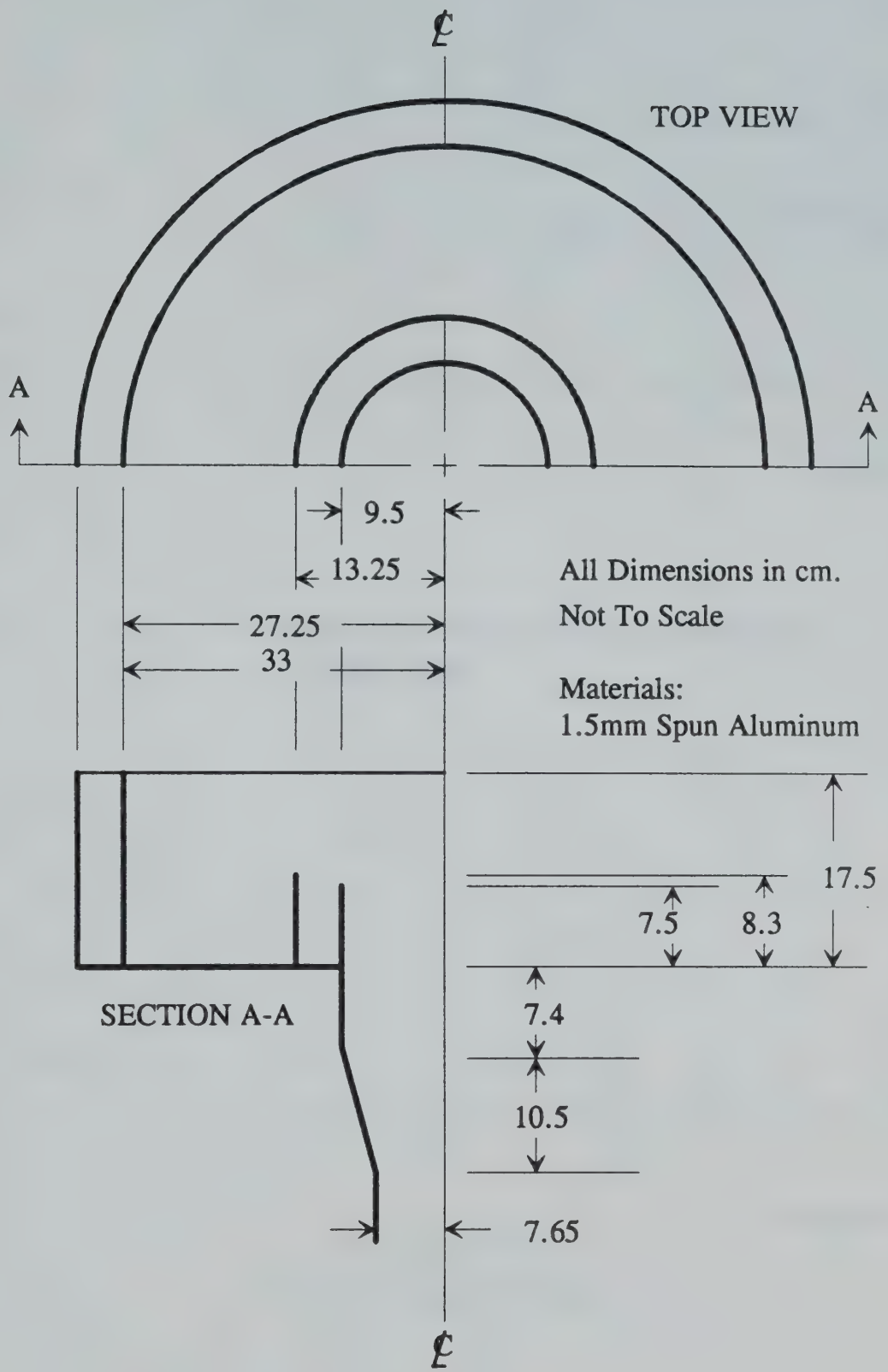

Figure 4.01 The 1420 MHz Feed and Dimensions (Veidt, 1984)

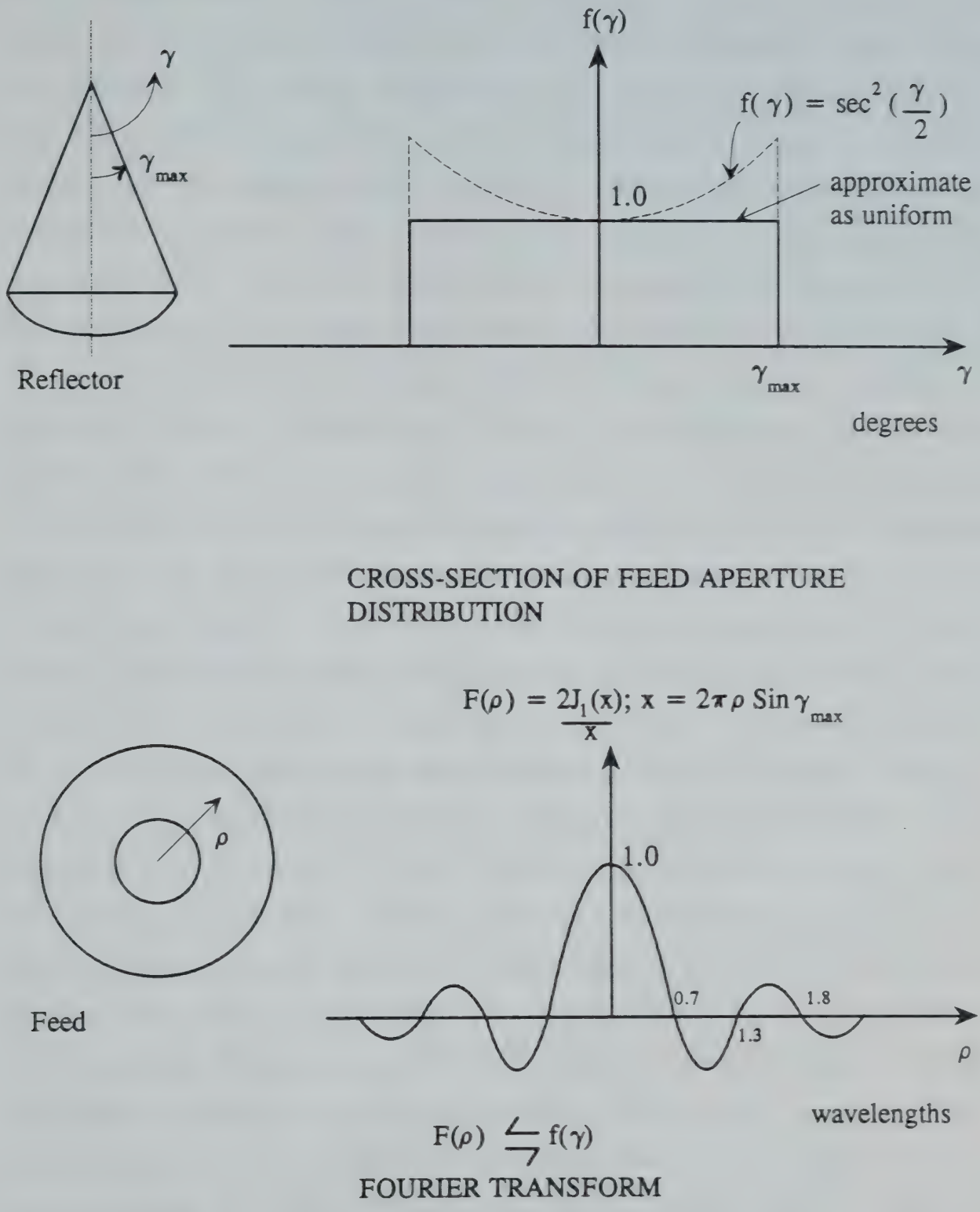

Figure 4.02 The Fourier Transform Relationship between an Ideal Feed Pattern and the Feed Aperture Distribution.

The multimode coaxial feed approximates the $2J_1(x)/x$ field distribution at 1420 MHz as follows (refer to fig. 4.03). From the transmitting point of view, energy propagates up the circular waveguide (region E) in the dominant TE_{11} mode. Even though the waveguide diameter increases just before the opening, most of the energy is still contained in the TE_{11} mode. The two coaxial rings outside the widened circular waveguide enable the front circular section (region B) to support the 1420 MHz circular waveguide TE_{11}, TM_{11}, and TE_{12} modes. The inner choke (region D) couples energy from the circular waveguide to the outer coaxial section (region C) and the front circular section. The outer coaxial section supports the 1420 MHz coaxial waveguide TE_{11} mode. The superposition of the waveguide modes at the feed aperture approximates a truncated version of the $2J_1(x)/x$ feed aperture illumination function shown in fig. 4.04. The figure shows that the radii of the rings approximate the zeroes of the illumination function and that the fields in the inner and outer regions are 180^o out of phase. Improving the reflector illumination requires increasing the number of outer rings. For instance, from fig. 4.04, adding a third ring to include the second lobe in $F(\rho)$ would mean increasing the feed diameter from 2.6λ to 3.6λ. The present feed size (2.6λ in diameter excluding the outer choke) results in a feed pattern in which the feed radiation level at the edge of the reflector is not zero. Instead, there is a roll-off region, and the roll-off rate depends on the number of outer rings used in the feed horn. For example, the graph in fig. 4.05 shows various feed patterns as a function of the number of outer rings. The feed patterns were calculated by taking the Fourier transform of the approximated $2J_1(x)/x$ feed aperture illumination function. It is clear from the graph that as the number of outer rings increases, the reflector illumination for the inner regions ($\gamma < 60^o$) increases, and the slope in the roll-off region ($\gamma > 50^o$) increases. At present only two rings are used with radius values of 0.63λ and 1.31λ. Thus, the roll-off region in the feed pattern has a finite slope, and inevitably, some

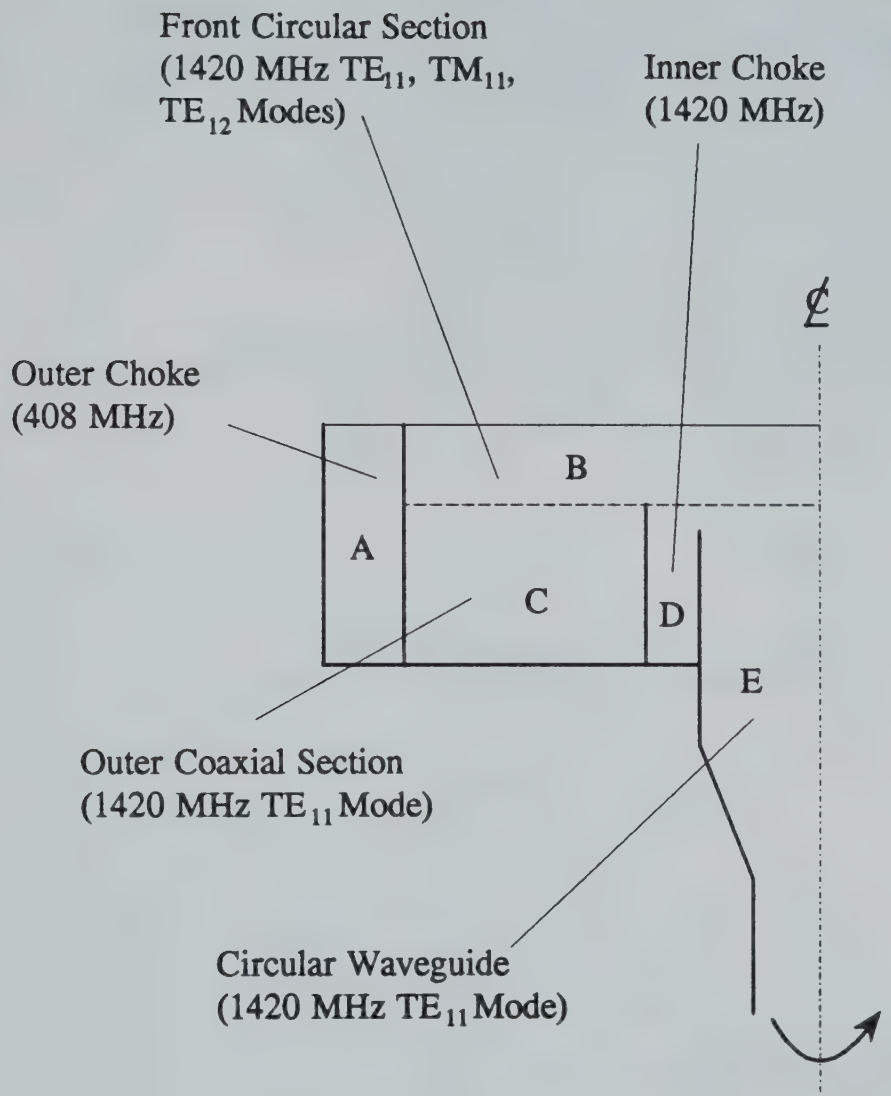

Figure 4.03 The Major Sections of the 1420 MHz Feed and the Location of the 1420 MHz Waveguide Modes.

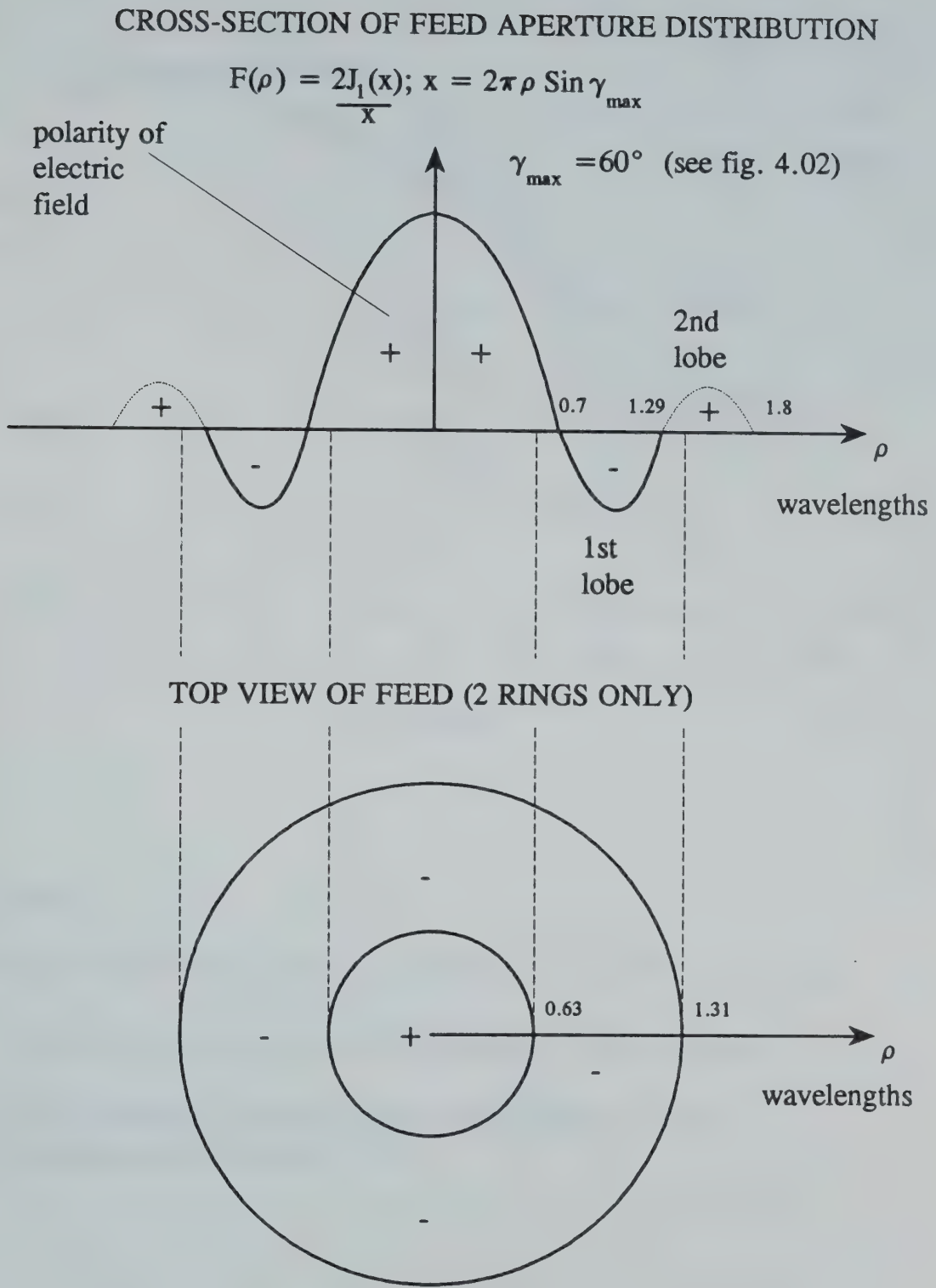

Figure 4.04 The 1420 MHz Feed Approximation. The Ideal feed aperture distribution is only approximated. Note the approximation of the zeroes of the $2J_1(x)/(x)$ function and the radial location of the inner and outer rings. Also note the polarity of the electric field.

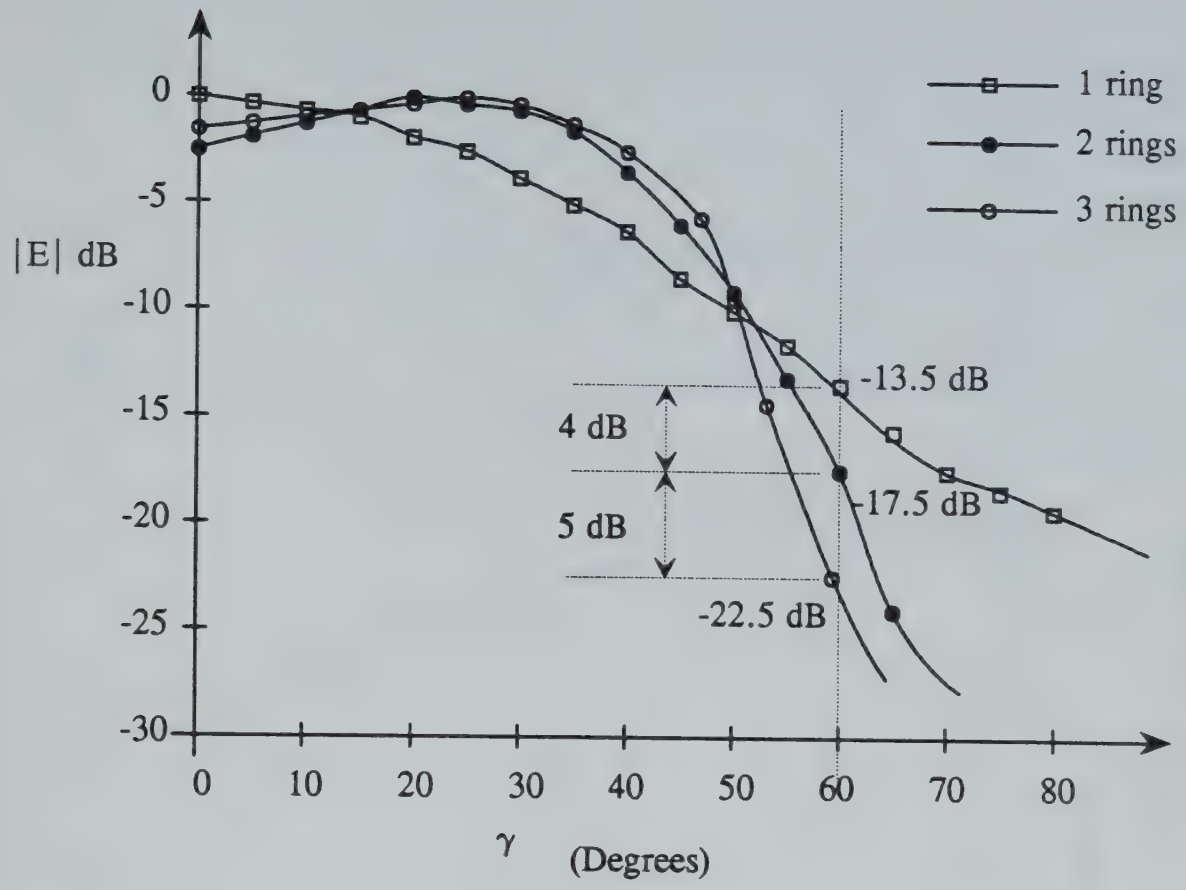

Notes:

The field distribution in the feed aperture is assumed to be $2J_1(x)/x$.

|E| is the Fourier transform of the aperture field distribution.

The calculations were made using equation 2.49, p. 35 in Christiansen and Högbom, 1985.

Figure 4.05 The Feed Pattern as a function of the Number of Outer Rings. The Calculation assumes that the added third ring generates the second lobe of the $2J_1(x)/x$ function in the feed aperture.

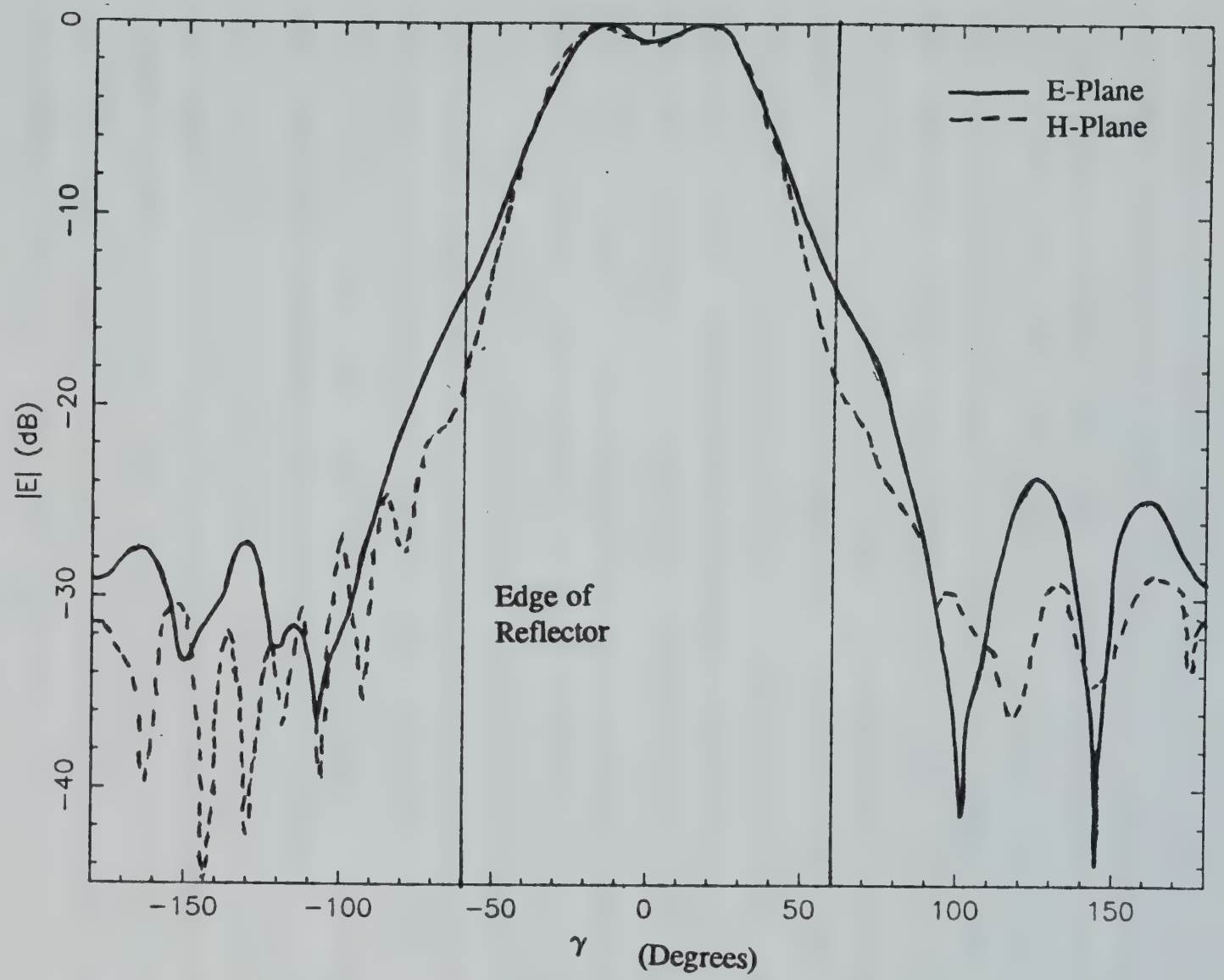

Figure 4.06 The Measured 1420 MHz Feed Pattern.

spillover results. In other words, the illumination is not confined to the reflector. The measured 1420 MHz feed patterns for the Synthesis Telescope are shown in fig. 4.06.

The existing feed is also equipped to receive 408 MHz signals. This is achieved by using 4 monopoles placed near the back wall of the outer coaxial section as shown in fig. 4.07. The 408 MHz probe is shown in fig. 4.08 (Veidt, 1984). The probe is matched to the input feed line with the help of a matching transformer or Gamma match (ARRL, 1988). A series inductance is used to tune out the input reactance of the probe. The probe is then fed away from the base to transform the low input resistance of the probe to 50 ohm coaxial line. The probe is left adjustable to compensate for component and structural variations. From the transmitting point of view, the members of each pair of opposing probes are excited 180^o out of phase and excite the coaxial waveguide TE_{11} mode. At 408 MHz, the front circular section supports the circular waveguide TE_{11} and TM_{11} modes, and therefore, the field distribution in the feed aperture is the superposition of these modes and the direct probe radiation. The measured 408 MHz feed patterns (E and H) are shown in fig. 4.09. Comparing the feed patterns at 408 MHz and 1420 MHz, the beam at 408 MHz is broader (fig. 3.06). The broader beam results in higher spillover and higher edge illumination. To help reduce the spillover, an additional ring (also known as the outer choke) is added. The depth of the ring is approximately 0.25λ at 408 MHz and therefore reduces the outer and edge surface currents, resulting in lower sidelobes at wide angles in the feed pattern. The depth of the choke is 0.83λ or close to 0.75λ at 1420 MHz and approximately acts as a choke at this frequency.

Obtaining circular polarization at 408 MHz is accomplished by a 6 port hybrid network shown in fig. 4.10 (Saleh, 1981). The four probes are connected to ports 1 to 4, and the receiving system is connected to ports 5 and 6. The phasing is 90^o between adjacent probes and is 180^o between opposing probes. The signals at ports 5 and 6 are proportional to the right hand and left hand circular polarized radiation arriving from the $9m$ main reflector.

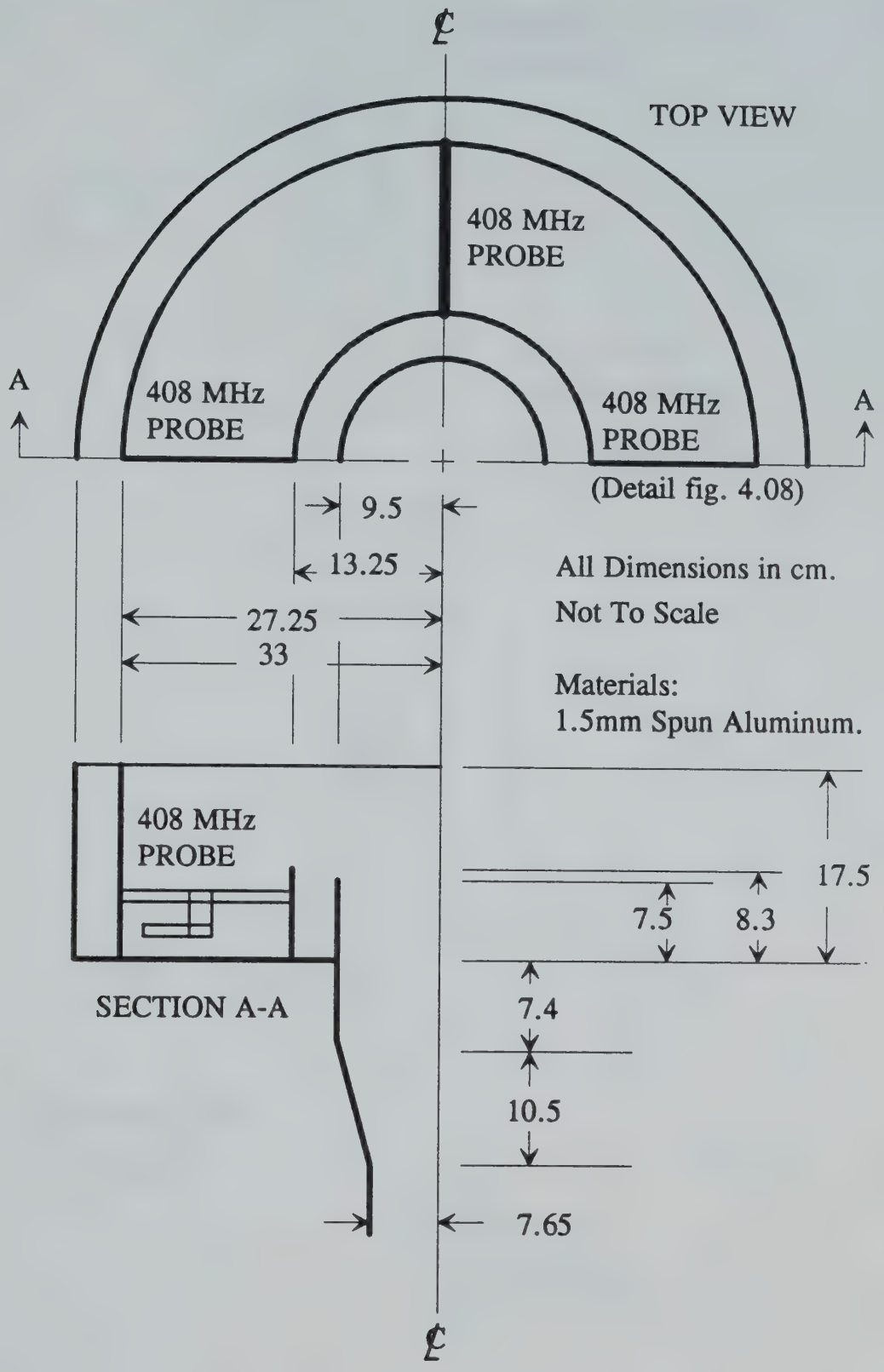

Figure 4.07 The Location of the 408 MHz Probes (Veidt, 1984).

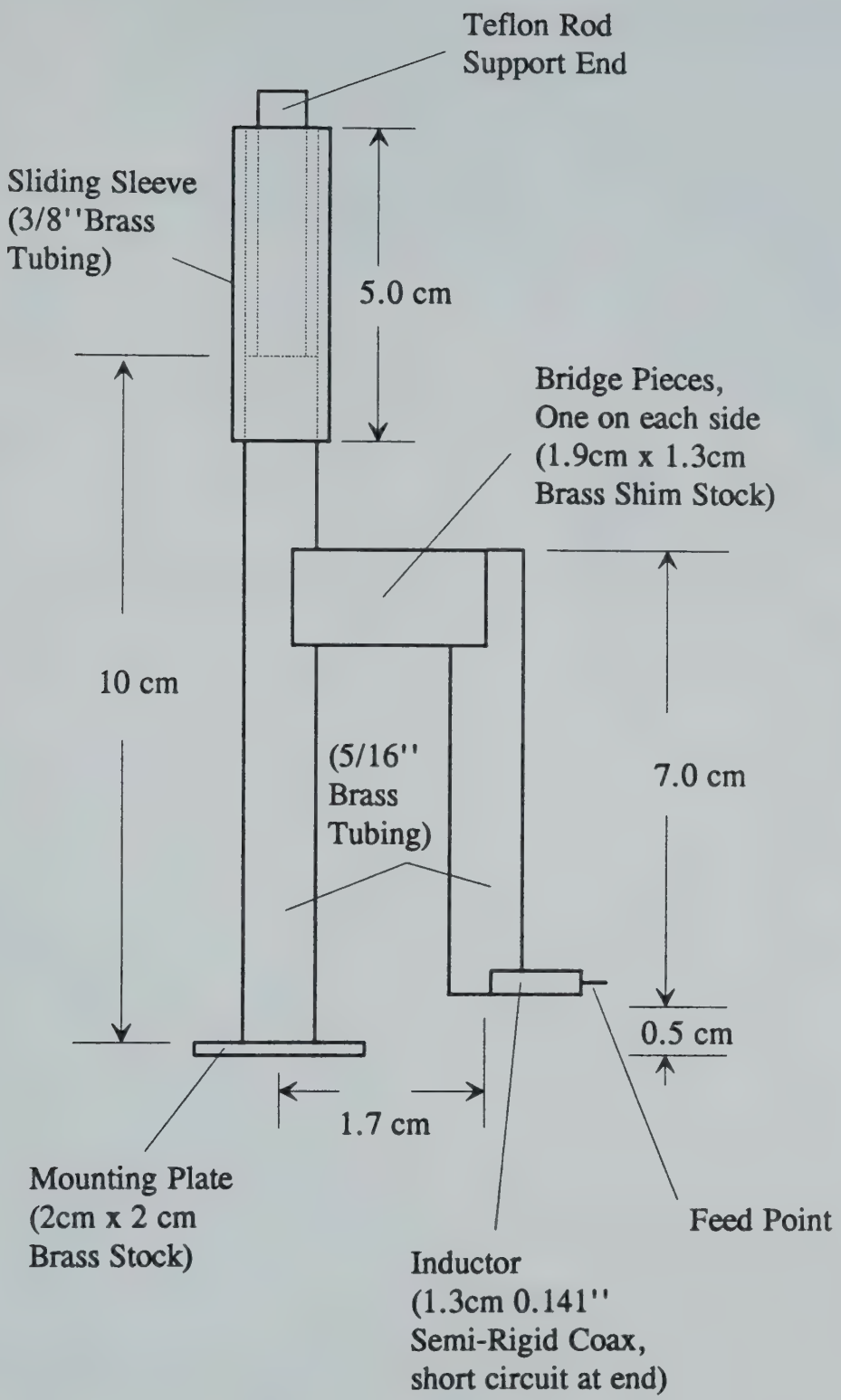

Figure 4.08 Details of the 408 MHz Probe (Veidt, 1984).

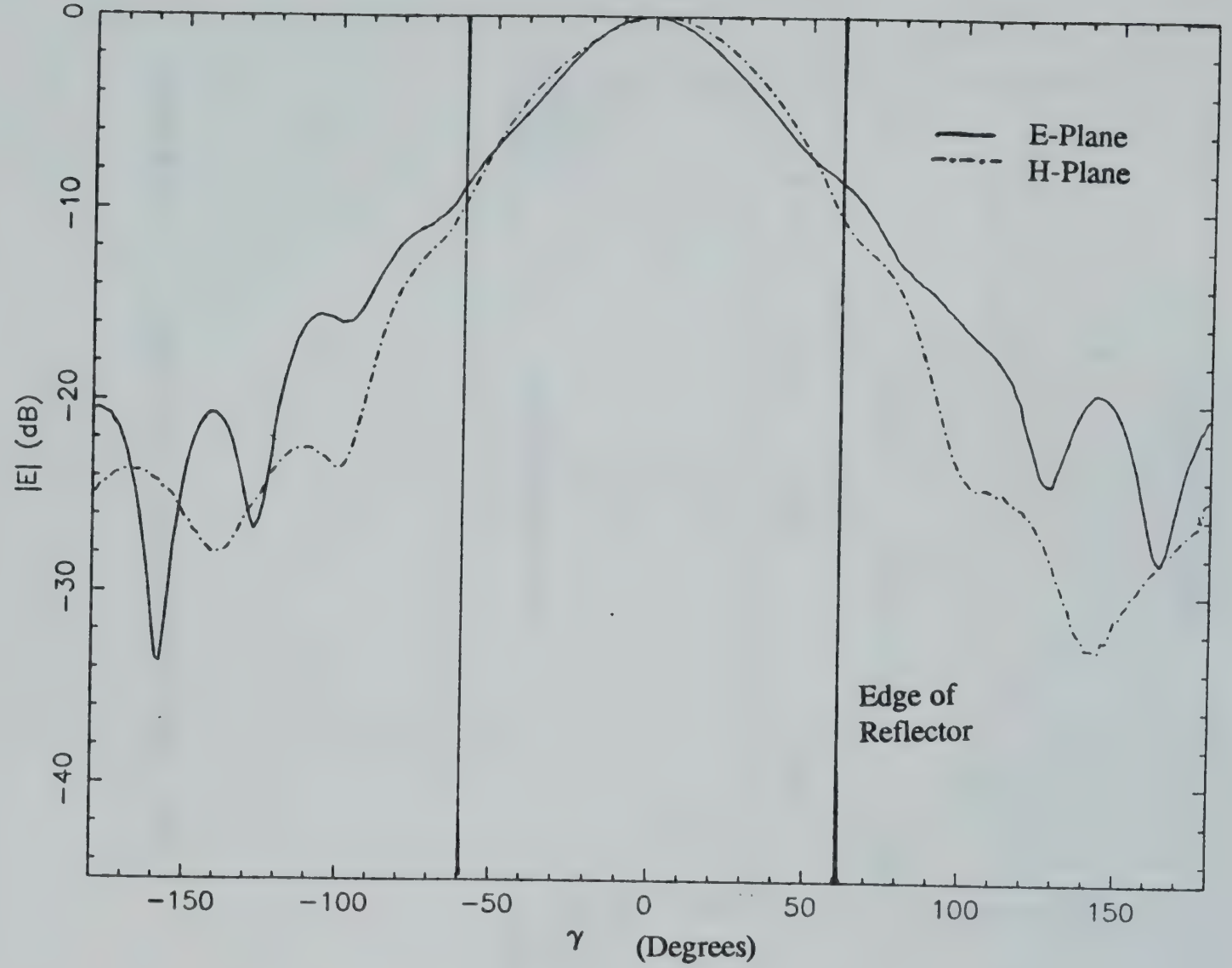

Figure 4.09 The Measured 408 MHz Feed Patterns.

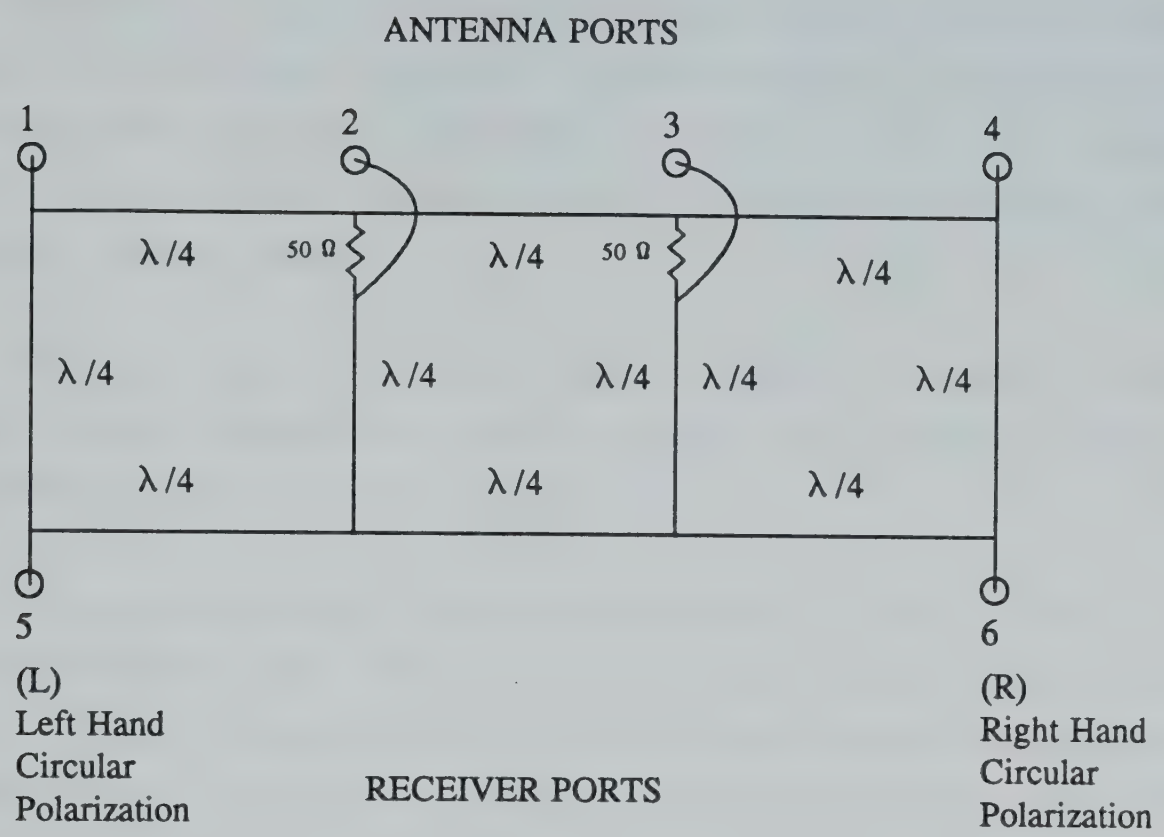

Figure 4.10 The 6 - Port Hybrid Network (Saleh, 1981).

4.2 Feed Problems at 408 MHz

Maintaining optimum feed performance at 1420 MHz creates problems in the feed performance at 408 MHz. These problems are (i) a broad beam, (ii) high cross polarization, (iii) primary beam pointing error, (iv) poor isolation between adjacent antenna ports, (v) low radiation resistance, and (vi) low radiation efficiency.

The first problem is the broad beam. As discussed in section 3.4, the broad beam at 408 MHz is a result of a small feed. Section 3.4 discusses the effects of having a broad primary beam.

The second problem is the cross-polarization. On axis, the measured cross-polarization level (CPL) is -16.8 dB, and the axial ratio (AR) is 1.34. Previous measurements on a different feed of the same design show similar results of a CPL of -17.6 dB and an AR of 1.3 (Kim, 1988). The polarization pattern measured on axis is shown in fig. 4.11. The measurement was made by transmitting a signal (nominally circularly polarized) with the existing feed and measuring the response with a rotating half-wave dipole. If the signal is circularly polarized, the measured response will be the same at all angles. Otherwise, there will be cross-polarization, since the feed will radiate an elliptically polarized signal. The measured response shown in fig. 4.11, however, is not an ellipse, but is proportional to

$$\sqrt{(a\ sin\theta)^2 + (b\ cos\theta)^2},$$

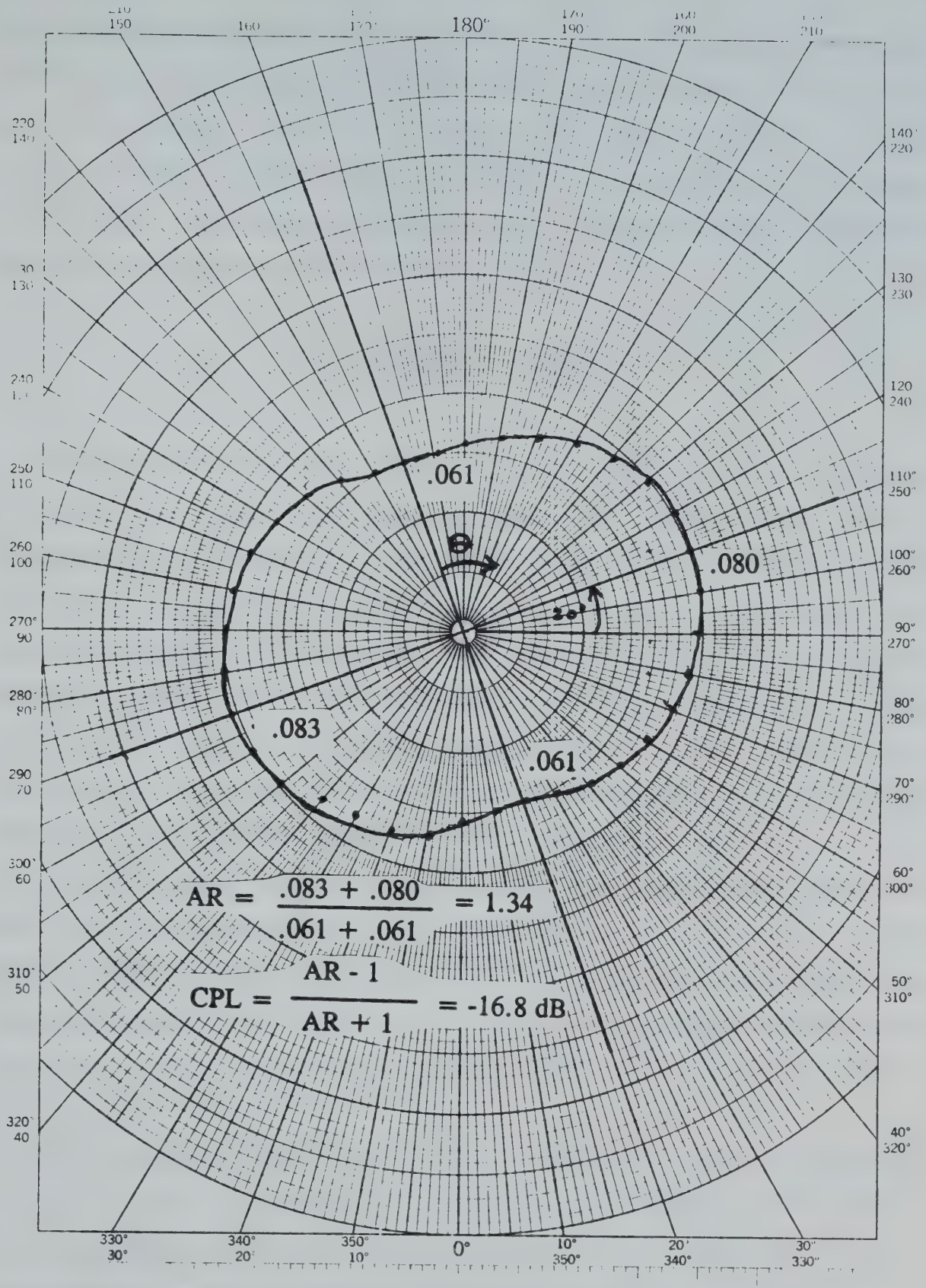

Figure 4.11 The On-Axis Polarization Pattern of the Existing Feed Measured at 408 MHz. The relative response of the horn, when the transmitting dipole is at the angle θ, is indicated by the radial distance of the curve from the origin.

where a is the major axis of the ellipse, b is the minor axis of the ellipse, and θ is the angle between the axis of the rotating dipole and the minor axis of the ellipse. The minor and major axis of the measured curve in fig. 4.11, however, are the same as the minor and major axis of the transmitted ellipse. The transmitted ellipse, that produces the above mentioned response at the receiver, traces out the curve

$$\frac{ab}{\sqrt{(b\ sin\theta)^2 + (a\ cos\theta)^2}}.$$

Cross-polarization results from the probes being fed with amplitudes and phases that deviate from their nominal values. There are two roots to the polarization problem. The first is the small distance between the end of the probe and the central waveguide ring. The second is the small input impedance bandwidth of the probe. The small distance causes the resonant frequency of each probe to become very sensitive to slight length changes. The change in resonant frequency (tuning error) in turn causes a large change in the input impedance of the probe because the input impedance bandwidth of the probe is small. The measured tuning error, Δf, as a function of probe length error, Δx, is 8.8 MHz/mm (Kim, 1988). The input return loss measurement of one of the probes, showing the narrow bandwidth is shown in fig. 4.12. Changes in the probe input impedance from the nominal value of 50 ohms result in errors in the amplitudes and phases feeding the probes. These errors will degrade the polarization performance.

The cross-polarization level, CPL, as a function of the amplitudes, α_i (i = 1, 2, 3, 4), and phases, β_i (i = 1, 2, 3, 4), feeding the probes is derived as follows (refer to fig.4.13). The transmitted electric field, $\mathbf{E}_{tx}$, is

$$[\alpha_1 cos(\omega t + \beta_1) - \alpha_3 cos(\omega t + \beta_3)]\mathbf{a_x} + [\alpha_2 cos(\omega t + \beta_2) - \alpha_4 cos(\omega t + \beta_4)]\mathbf{a_y},$$

or

$$\mathbf{E}_{tx} = a\ cos(\omega t)\mathbf{a_x} - b\ sin(\omega t)\mathbf{a_y} + c\ sin(\omega t)\mathbf{a_x} - d\ cos(\omega t)\mathbf{a_y},$$

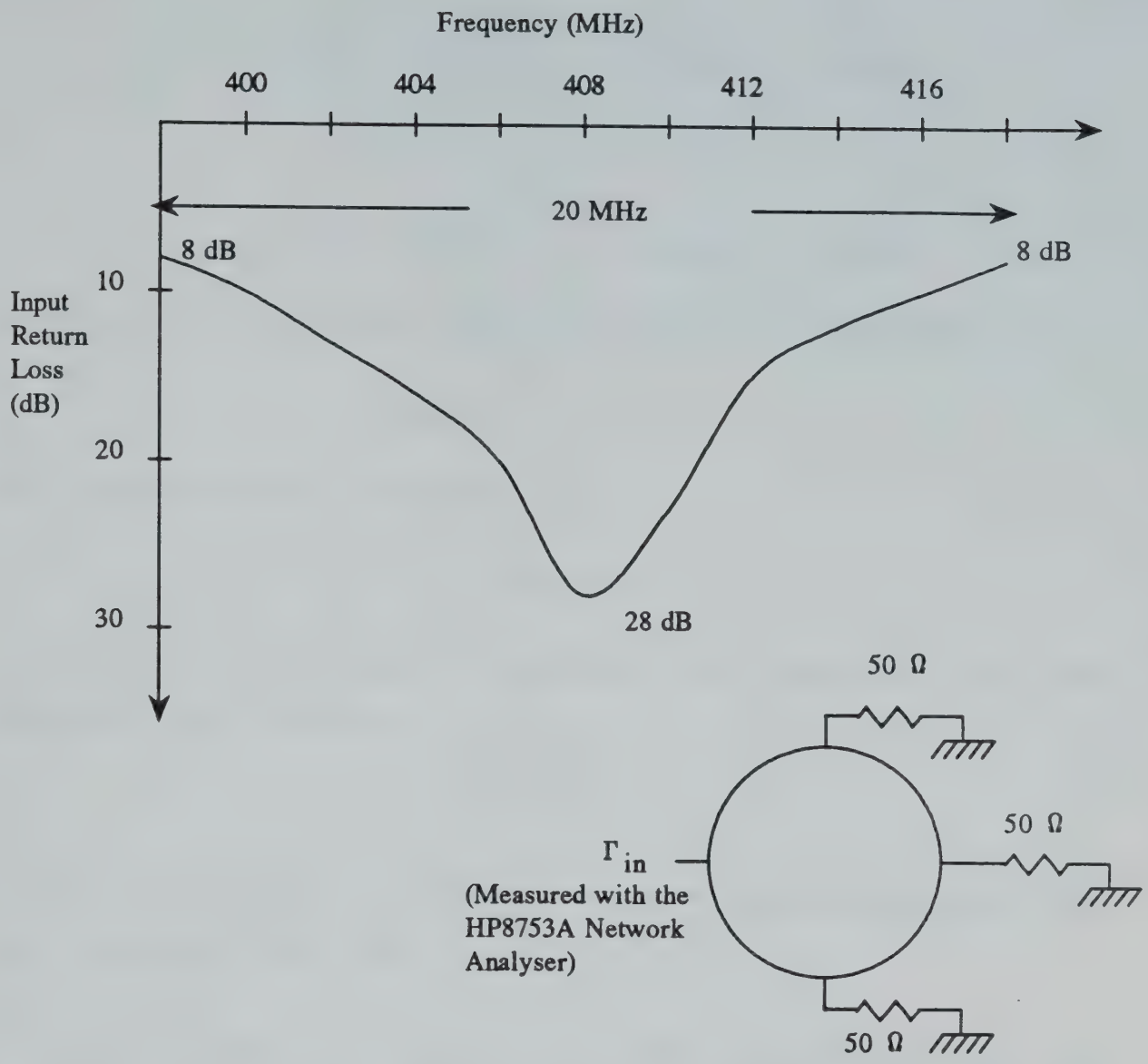

Figure 4.12 The Measured Input Return Loss of one of the probes with the other 3 probes terminated with 50 ohms.

where

$$a = \alpha_1 cos\beta_1 - \alpha_3 cos\beta_3, \qquad b = \alpha_2 sin\beta_2 - \alpha_4 sin\beta_4,$$

$$c = \alpha_3 sin\beta_3 - \alpha_1 sin\beta_1, \qquad d = \alpha_4 cos\beta_4 - \alpha_2 cos\beta_2,$$

and $\mathbf{a_x}$, $\mathbf{a_y}$ are unit vectors. The complex right hand component, R, is

$$\frac{1}{2}[(a+b) + j(c-d)].$$

The complex left hand component, L, is

$$\frac{1}{2}[(c+d) + j(a-b)].$$

If the left hand component is transmitted, the magnitude of the cross-polarization level, $|CPL|$, is

$$\frac{|R|}{|L|}.$$

The cross-polarization level as a function of amplitude error and phase error is plotted in fig. 4.14.

A third problem with the feed at 408 MHz is the primary beam pointing error. Slight amplitude and phase differences between opposing probes lead to primary beam pointing errors. Pointing the feed in a direction off the reflector axis increases the cross-polarization levels for off-axis angles in the reflector pattern (Silver, 1949). This raises the sidelobe level on one side of the reflector pattern, and leads to a slight secondary beam pointing error. In the present feed, the distance between the centers of the two probes in a pair is 55 cm. Assuming that the feed consists of just two isotropic sources symmetrically located about the reflector axis, the point of maximum field strength on a parabolic surface will determine the primary beam pointing error for the given amplitude and phase difference between the two sources.

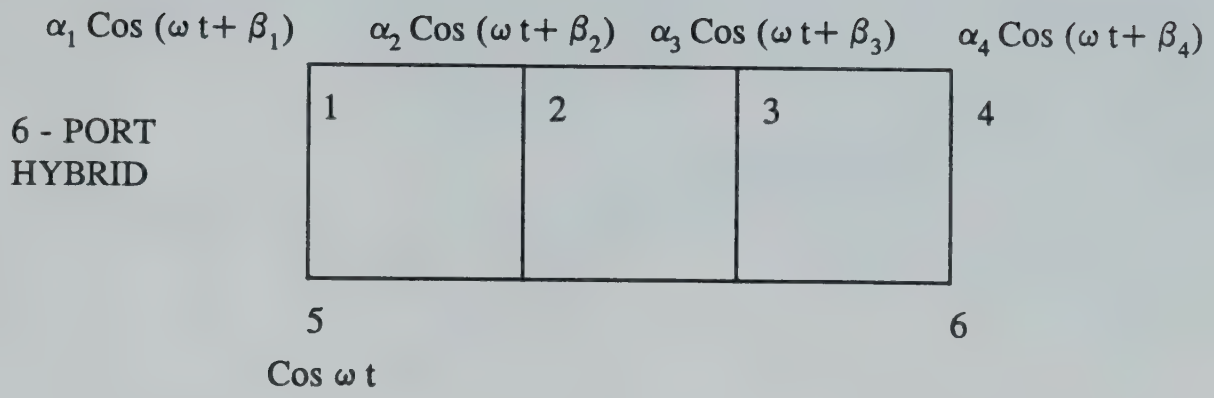

Port 5 is excited with Cos ω t

Nominal Values for (α_i , β_i) i=1,2,3,4 are (½,0°), (½,-90°), (½,-180°), (½,90°) respectively.

Figure 4.13 Determining the Cross Polarization Level at 408 MHz when the antenna ports are being fed with amplitudes and phases that deviate from their nominal values.

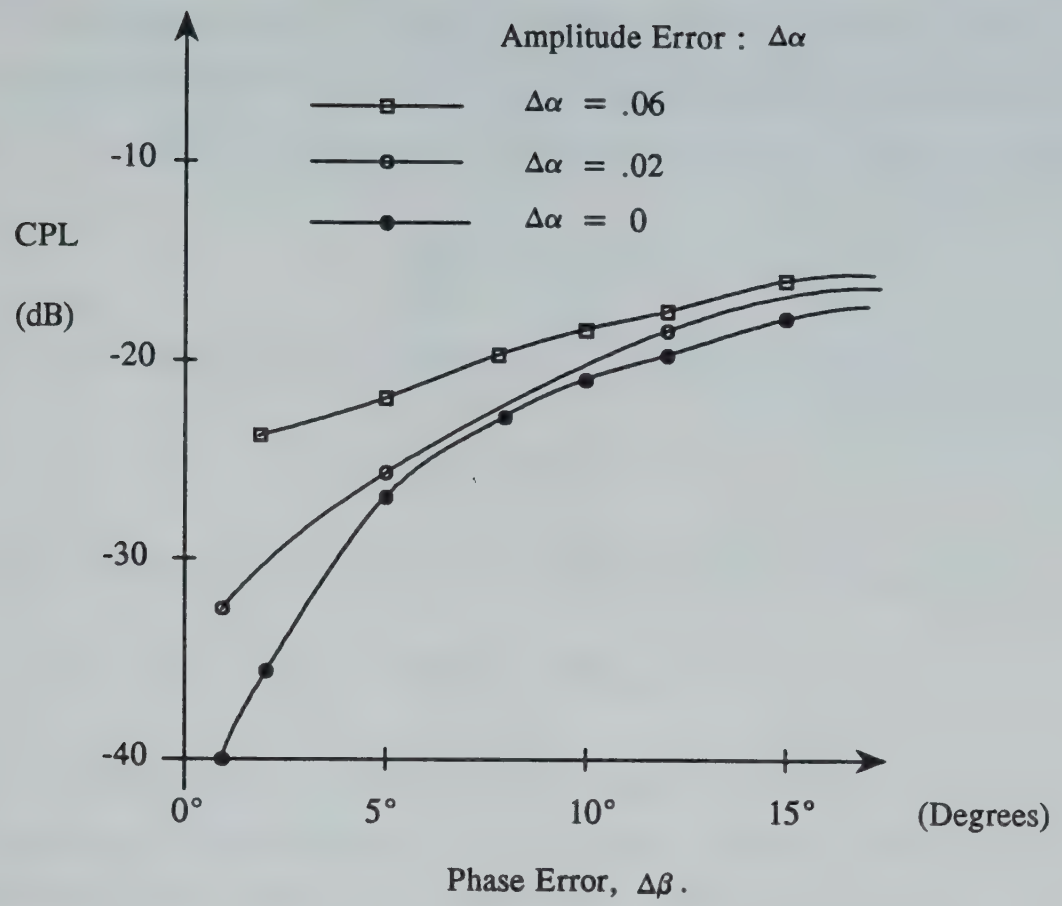

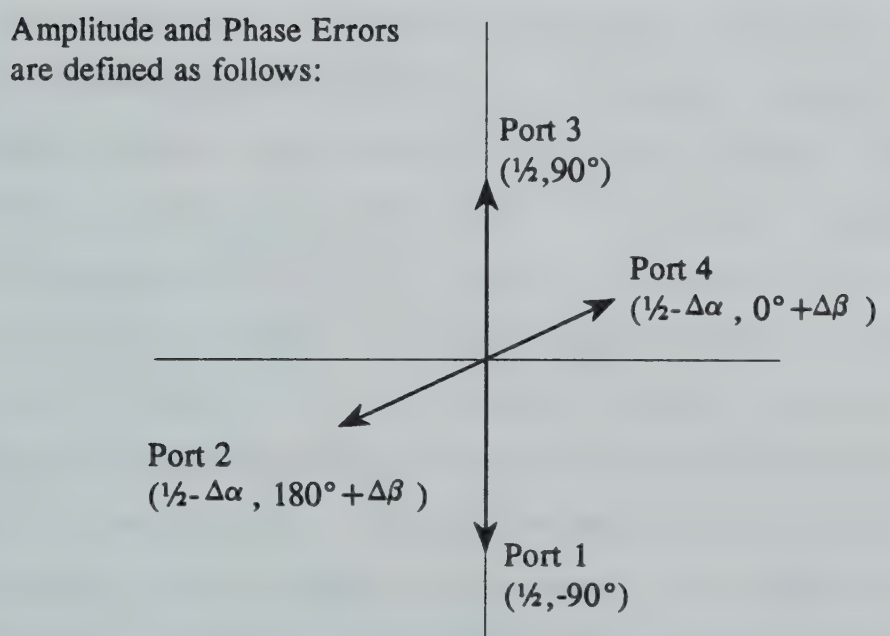

Note: Only Amplitude and Phase Errors between Adjacent Ports are considered.

Figure 4.14 The Cross-Polarization Level as a function of Amplitude and Phase Errors between Adjacent Ports.

The pointing error, γ_e, as a function of the amplitude difference, 2α, and phase difference, $2\beta_e$, between the two sources is derived as follows (refer to fig. 4.15). The electric field due to source 1, E_{P1}, is proportional to

$$\frac{R_o}{R_1}(1+\alpha)e^{j\beta_1}e^{j\beta_e}.$$

The electric field due to source 2, E_{P2}, is proportional to

$$\frac{R_o}{R_2}(1-\alpha)e^{j\beta_2}e^{-j\beta_e}.$$

The total electric field due to both sources, E_P, is proportional to

$$Re[(E_{P1}+E_{P2})e^{j\omega t}].$$

The primary beam is pointed at the angular position, γ_e, where E_P is a maximum. The pointing error is plotted on the graph in fig. 4.16. The figure shows that disconnecting one of the sources ($\alpha = 1.0$) results in a pointing error of 8.6^o. Of course, this is being pessimistic because the feed does not consist of just two probes, and the probes, themselves, are not isotropic sources. Nevertheless, the secondary pattern effects using the NEC-REF software were evaluated for a feed pointing error of 8.6^o. First, increases in cross-polarization levels at angles off boresight are evident. This is shown in fig. 4.17 for the $\phi = 45^o$ pattern cut. At $\theta = \pm 5^o$, the cross-polar levels increase by approximately 20 dB. Secondly, a slight pointing error of about 0.1^o in the reflector pattern appears because the phase of the field in the reflector aperture is no longer symmetrical with respect to the aperture center. Thirdly, the main beam is broader by about 0.3^o because less of the reflector is illuminated, and finally, as expected, the sidelobe levels are higher on one side of the reflector pattern than the other. The beam broadening and the sidelobe changes are shown in fig. 4.18.

GEOMETRY FOR THE PRIMARY BEAM POINTING ERROR

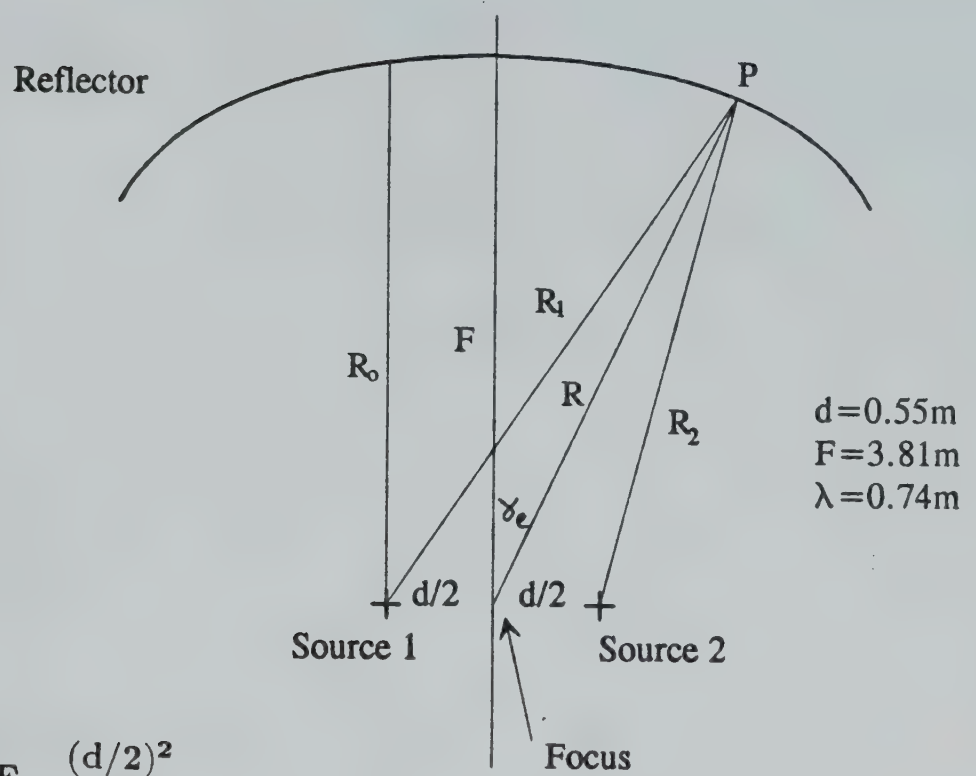

$$R_0 = F - \frac{(d/2)^2}{4F}$$

$$R = \frac{2F}{1 + \mathrm{Cos}\gamma_e}$$

$$R_1^2 = R^2 + (d/2)^2 - Rd \cdot \mathrm{Cos}(\pi/2 + \gamma_e)$$

$$R_2^2 = R^2 + (d/2)^2 - Rd \cdot \mathrm{Cos}(\pi/2 - \gamma_e)$$

$$\beta_1 = \frac{2\pi}{\lambda}(R_1 - R) \qquad \beta_2 = \frac{2\pi}{\lambda}(R_2 - R)$$

Figure 4.15 The Geometry for determining the Primary Beam Pointing Error.

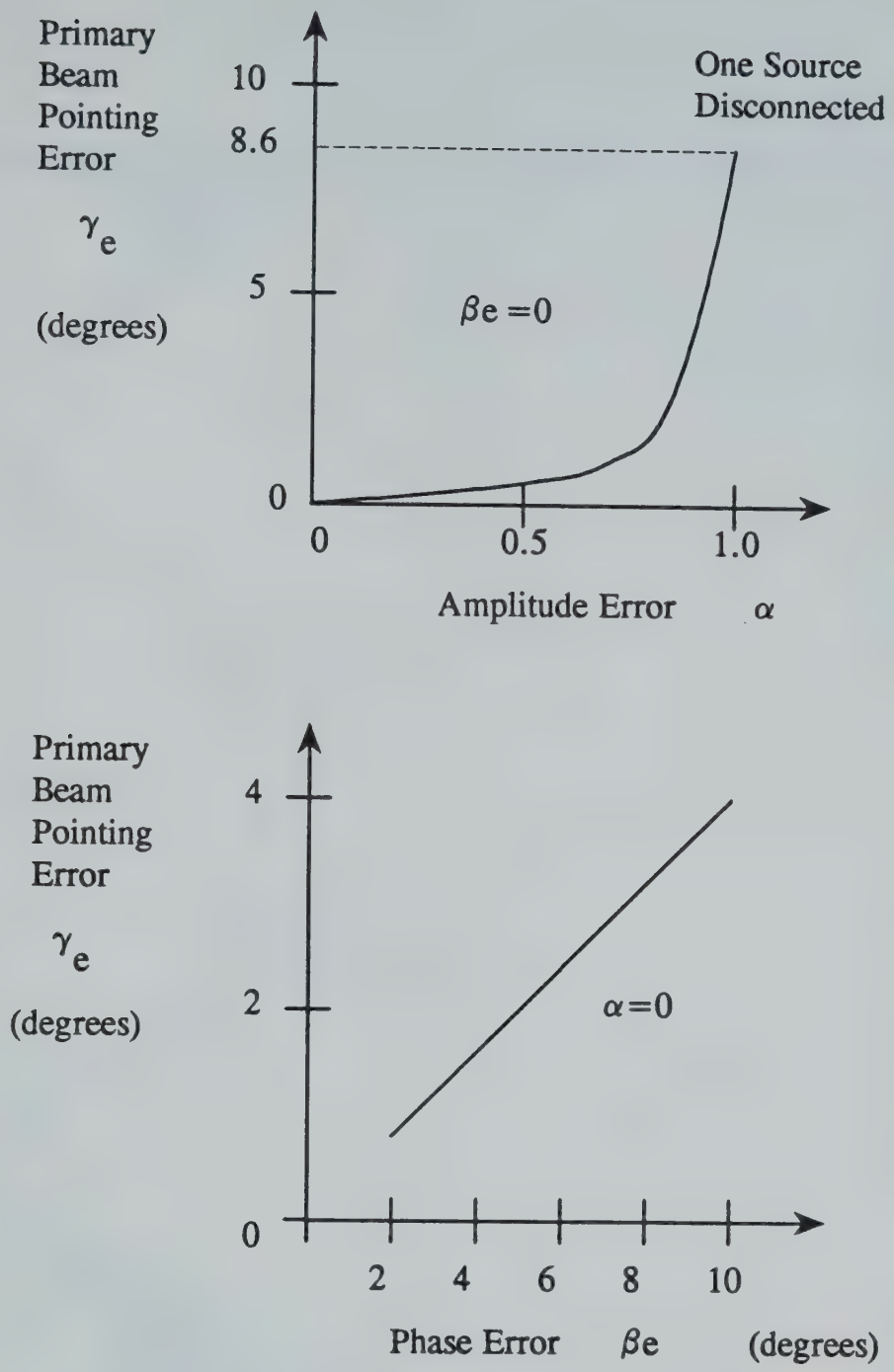

Figure 4.16 The Primary Beam Pointing Error as a function of the Amplitude and Phase Difference between Opposing Elements.

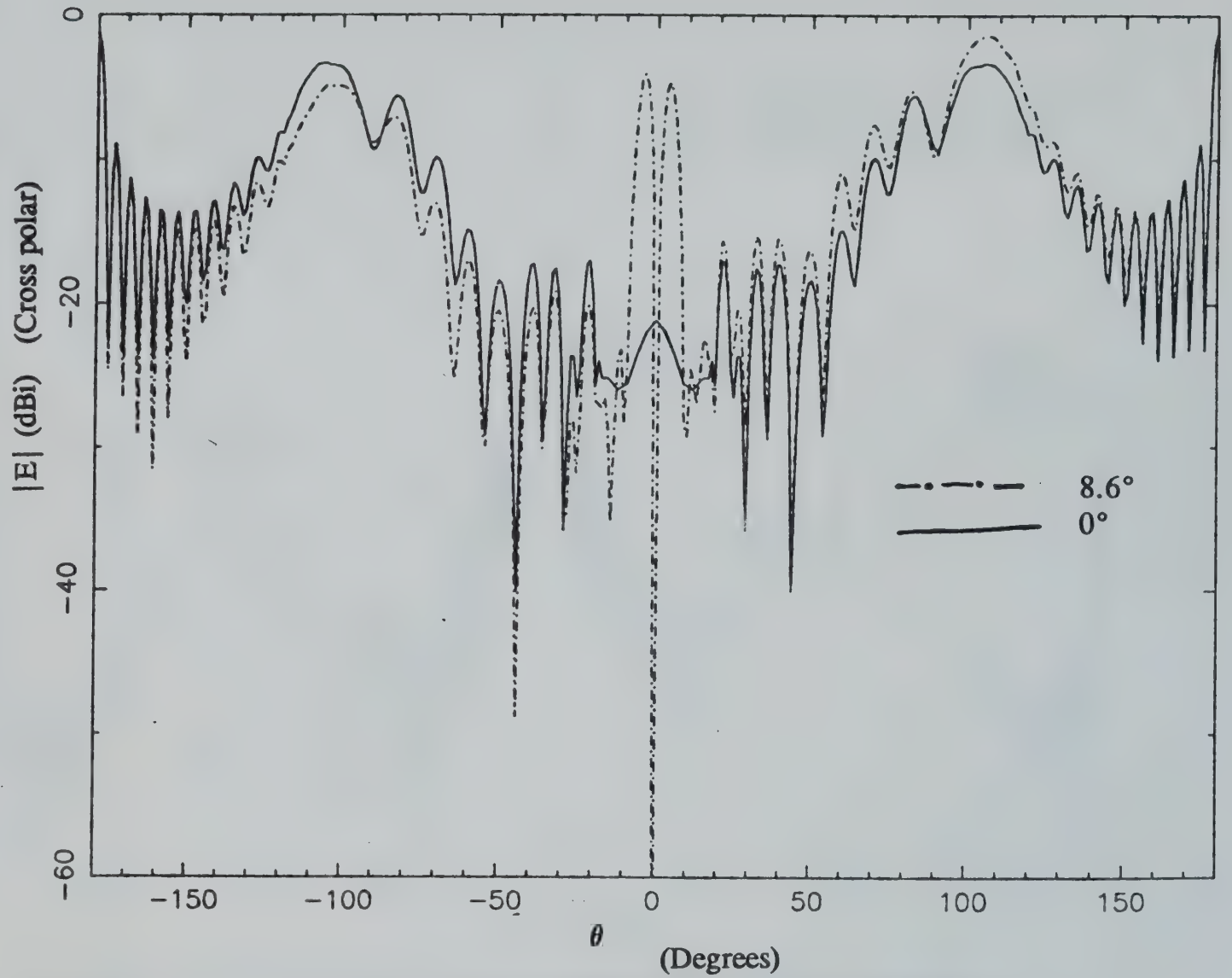

Figure 4.17 The 9m Reflector Cross-Polarization for the ϕ=45° Pattern Cut with a Feed Pointing Error of 8.6°. The pattern cut was calculated using the NEC-REF software.

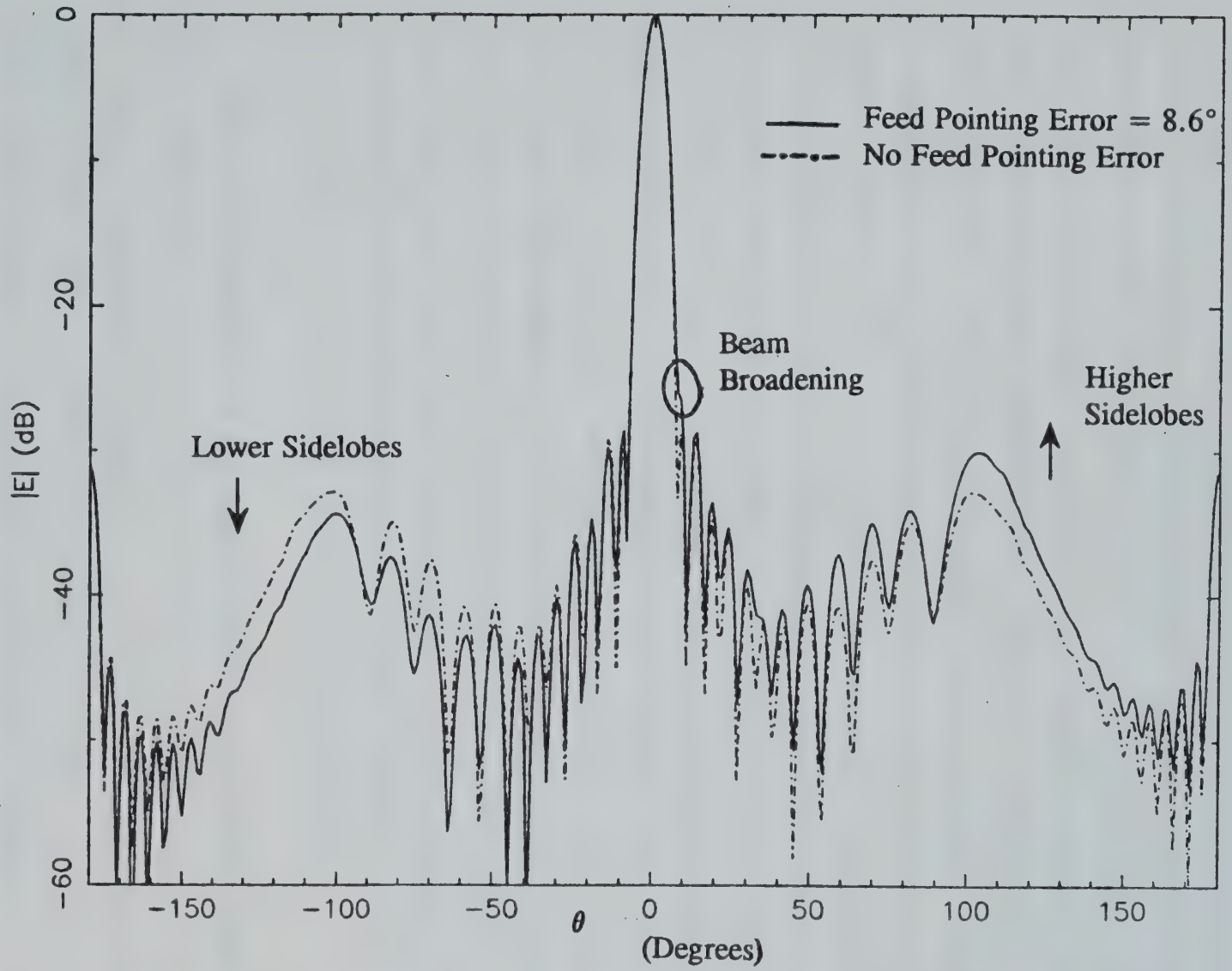

Figure 4.18 The 9m Reflector Patterns with and without the Feed Pointing Error. The patterns were calculated using the NEC-REF software.

Another problem with the feed at 408 MHz is the poor isolation among the four probes. The poor isolation is caused by the low clearance between the end of the probe and the inner conductor (central waveguide ring) of the outer coaxial section. The probes couple to each other via this ring. The isolation is -8 dB between adjacent probes and is -14 dB between opposing probes. The poor isolation between adjacent probes suggests that undesired waveguide modes are excited in the outer coaxial section. A longer waveguide would thus be needed to establish the desired TE_{11} mode in the feed aperture when each of the opposing probes is fed 180^o out of phase. Also the poor isolation between adjacent probes causes a mismatch at the antenna ports, resulting in poor isolation between the receiving ports (L and R). The isolation between the L and R ports is -14 dB at 408 MHz. Therefore, 4 % of the power injected into the R port ends up in the L port. The power leakage from one port to the other will lower the radiation efficiency. For example, some of the power received from a right hand circularly polarized signal at the antenna ports will end up in the L port of the hybrid network instead of all the power ending up in the R port. Furthermore, the antenna is difficult to tune because of the poor isolation between the adjacent probes. Tuning the antenna is an iterative procedure that involves adjusting one set of opposing probes and readjusting the other set of opposing probes. Adjusting one set changes the impedance of the other set due to the high coupling.

The fifth problem with the feed at 408 MHz is the low radiation resistance of the probes. The radiation resistance of the probe can be deduced as follows. The radiation resistance of a $\lambda/2$ dipole located 0.1λ from an infinite ground plane is about 20 ohms (Kraus, 1988). In the existing feed, there is a monopole (not a dipole), the length of the monopole is less than $\lambda/4$, and the distance above the finite ground plane is slightly less than 0.1λ. Therefore, the radiation resistance of the probe is, at most, half the

radiation resistance of the dipole or about 10 ohms. Increasing the distance between the probe and the back wall of the outer coaxial section would increase the radiation resistance, but the feed pattern at 1420 MHz would be affected (Veidt, 1984). Ohmic losses are significant because the radiation resistance is low. The ohmic losses result from the high standing currents that flow in the matching network when transforming the low radiation resistance to 50 ohms.

Finally, the power dissipated due to the ohmic losses and the poor isolation between the L and R ports of the hybrid network lead to a low radiation efficiency. The radiation efficiency can be calculated from these measured characteristics. The algebraic calculation is shown in fig. 4.19. A low radiation efficiency will increase the system noise temperature. The system temperature will increase by (Kraus, 1988)

$$T_{ap}(\frac{1}{\eta_o} - 1) + T_{LN}(\frac{1}{\eta_I} - 1),$$

where T_{ap} is the antenna physical temperature (300 K), T_{LN} is the equivalent noise temperature "seen" at the input of the low noise amplifier from one of the receiving ports of the hybrid network (70 K; Veidt, 1984), η_o is the ohmic efficiency of the feed, and η_I is the isolation efficiency of the hybrid network.

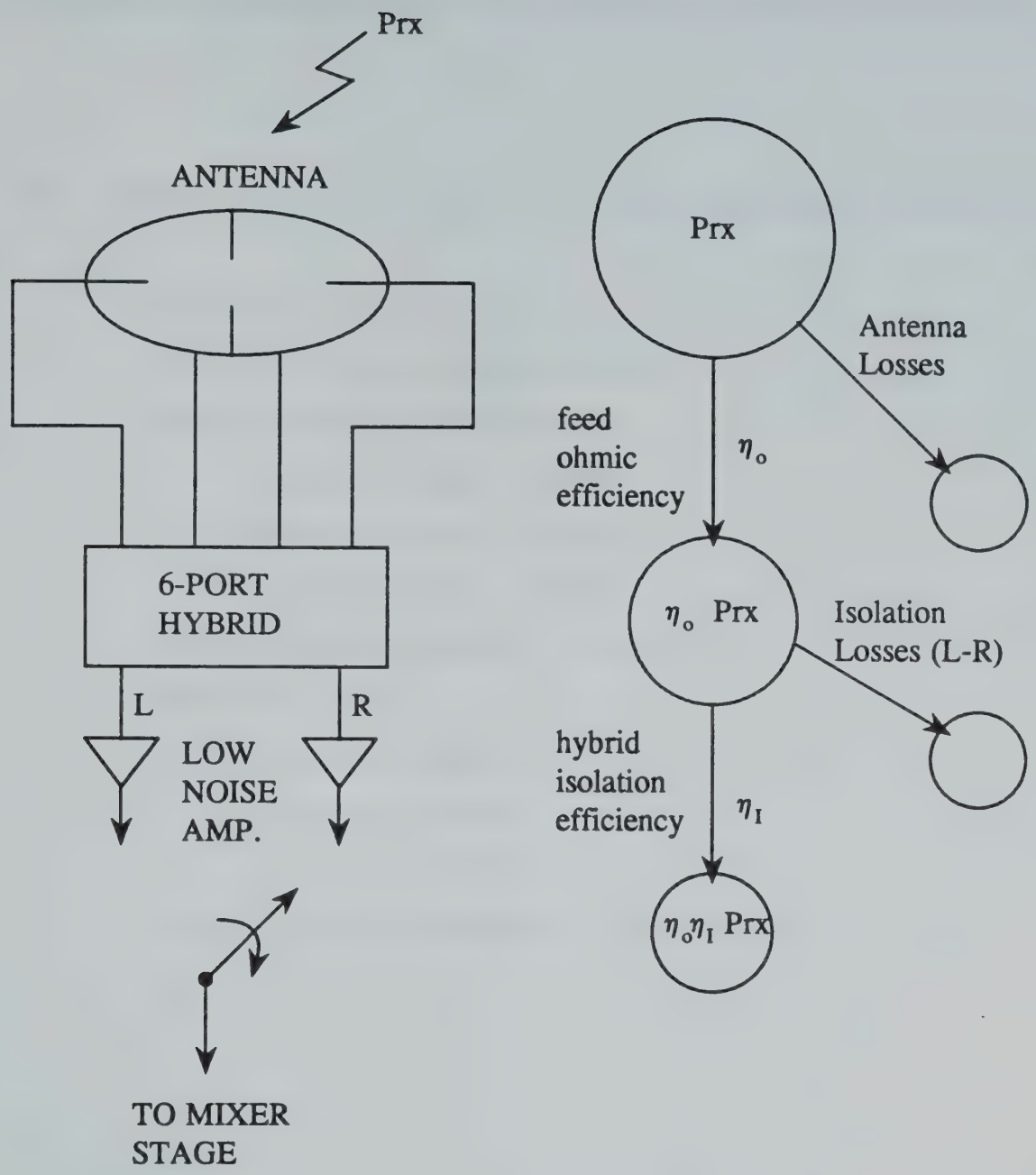

$$\text{EFFICIENCY} = 100\eta_o\eta_I\,\%$$

Figure 4.19 An Algebraic Calculation of the Radiation efficiency.

4.3 Electrical Characteristics of the Existing Feed at 408 MHz

The 408 MHz feed horn electrical characteristics are summarized below:

8 dB Return Loss Bandwidth: 20 MHz

Return Loss at 408 MHz: 30 dB

Isolation levels at 408 MHz

- Adjacent Probes: −8 dB
- Opposing Probes: −14 dB
- L and R Ports: −14 dB

On Axis Cross-Polarization: −16.8 dB

Axial Ratio: 1.34

$\pm$ 60° Radiation Levels

- E - plane: −9 dB
- H - plane: −10 dB

Probe Radiation Resistance: 10 Ω

4.4 Design Constraints

Reducing the reflector sidelobes and solving the feed problems with feed modifications at 408 MHz, without affecting the 1420 MHz performance, requires the set of design constraints shown in fig. 4.20. First, the diameter and depth of the inner and outer rings must remain the same to ensure the correct amplitude and phasing of the 1420 MHz modes at the feed aperture. Second, a short circuit at the back wall of the outer coaxial section must be present so that the 1420 MHz coaxial waveguide TE_{11} mode remains undisturbed. Third, structures for exciting 408 MHz cannot be placed in the front circular section because the resultant of the 1420 MHz field modes in this section would change. Any such structures must be placed in the outer coaxial section at the back, and care must be taken not to disturb the 1420 MHz coaxial TE_{11} mode.

4.5 Feed Pattern Measurements

The feed Patterns were measured using an outdoor antenna range. The feed cross-polarization was also measured using the outdoor range; the cross-polarization measurement was described in section 4.2. The outdoor range is shown in fig. 4.21. The range was designed and built by Richard Smegal, a graduate student at DRAO.

The feed patterns were obtained as follows. A signal was transmitted from the tower, located closest to the control room. The feed under test or the receiving antenna was placed on a turntable, located on top of the receiving tower. The receiving antenna was located in the far field of the transmitting antenna. The ratio of the received signal to the transmitted signal and the turntable position were recorded by a computer as the turntable rotated. The procedure was repeated after changing the orientation of both antennas by 90^o. The principal E-plane and the principal H-plane feed patterns could then be measured.

The measured feed patterns were valid because reflections from the ground and the trailer control room were negligible. The effect of the ground reflections was measured as follows. The measured ratio of the received vertically polarized signal to the transmitted vertically polarized signal was compared to the ratio of the received horizontally polarized signal to the transmitted horizontally polarized signal. The difference between the two ratios was 1 dB at 408 MHz, and therefore, the effect of the ground was negligible. The effect of trailer reflections was negligible because the trailer was not located in the 1st Fresnel zone of the two antennas; that is, the trailer was not high enough to effect the feed radiation levels in the main beam. The trailer affected only the sidelobes in the feed pattern that were greater than 20 dB below the level of the main beam at 408 MHz, and then only on one side of the patterns (indicated by negative angles in the radiation patterns which follow). In summary, the radiation patterns are reliable down to the -20 dB level, and lower measured levels can be believed on one side of the pattern.

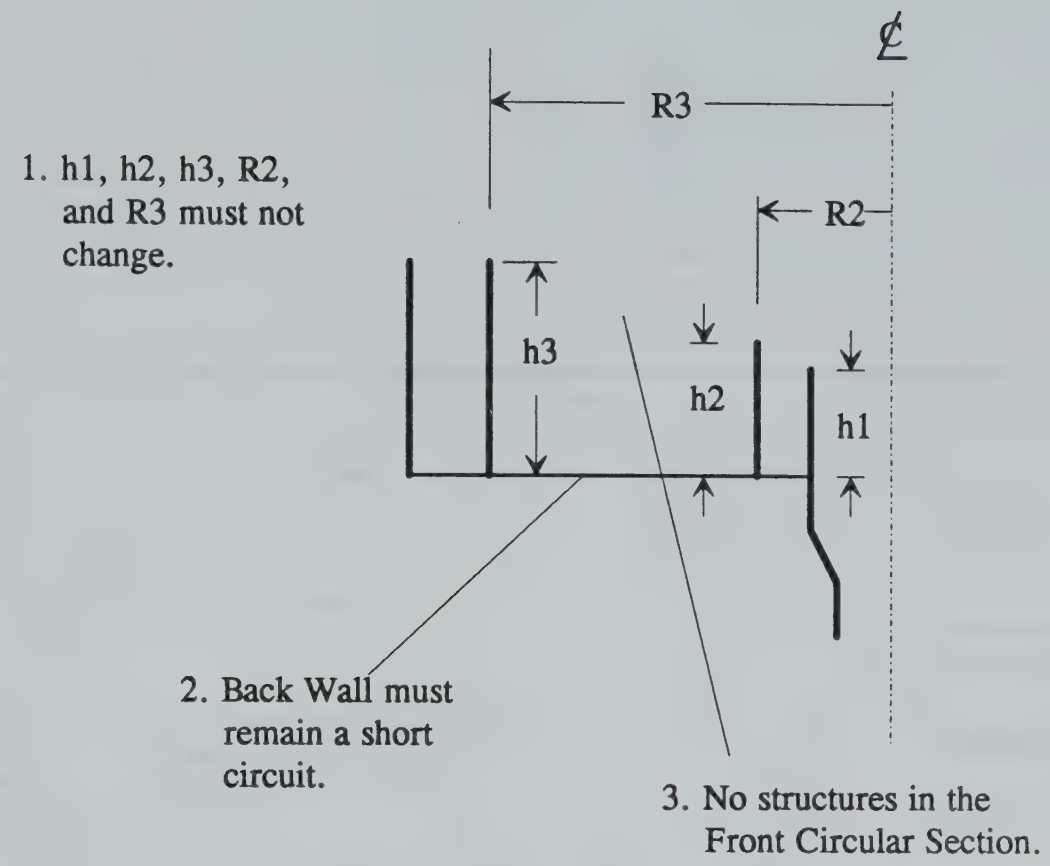

Figure 4.20 The Design Constraints.

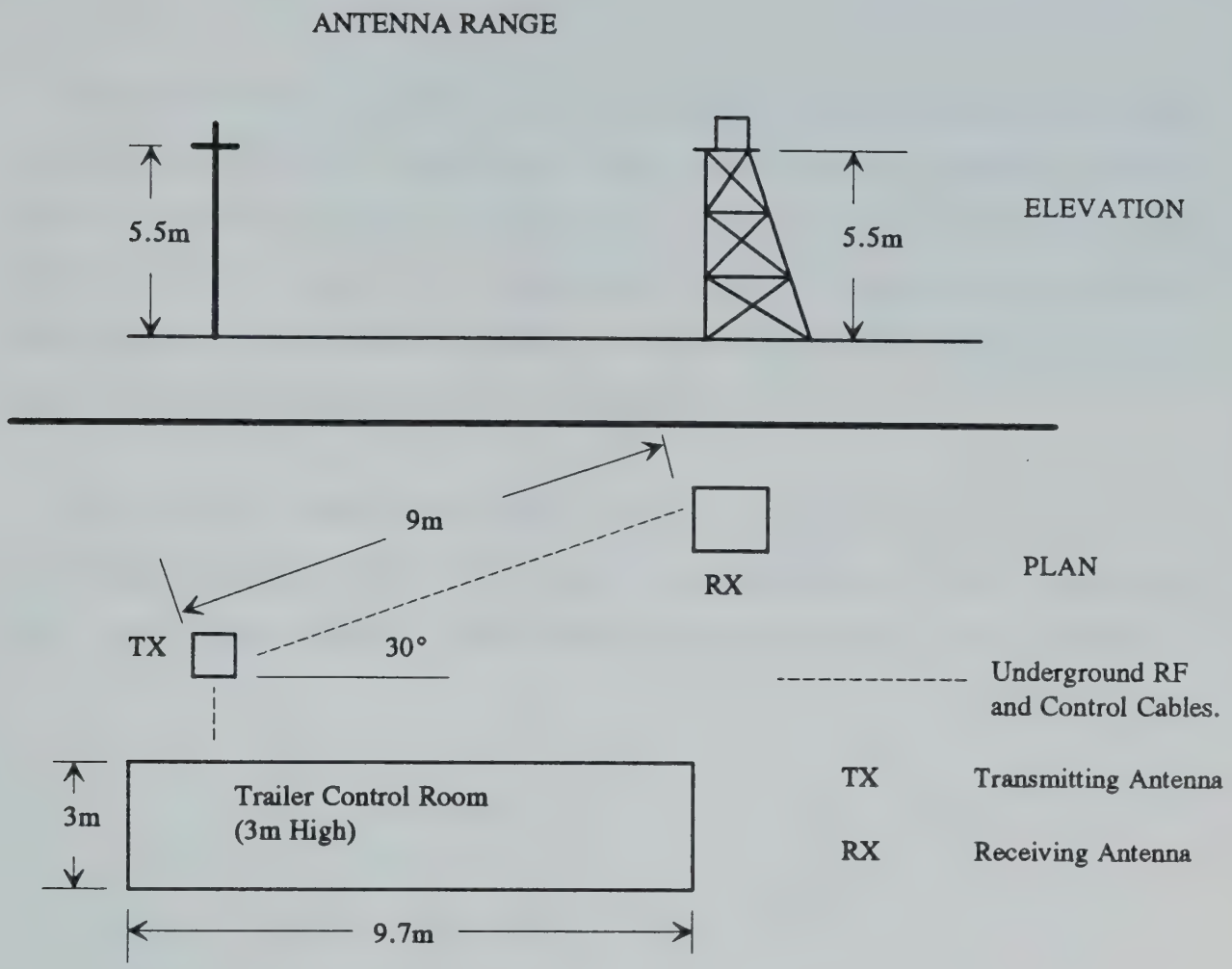

Figure 4.21 The Antenna Range used for Feed Pattern and Polarization Measurements. The Range was designed and built by Richard Smegal, a graduate student at DRAO.

5.0 FEED MODIFICATIONS

Four direct attempts were made to modify the feed design at 408 MHz. For each solution, the theory and design details of the antenna elements and the antenna structure are presented. These are followed by some test results and a discussion. The discussion consists of some advantages and disadvantages of the modified design. Possible corrective measures to overcome the disadvantages are also discussed.

In addition to the four modifications, an attempt was made to sharpen the primary beam at 408 MHz by simulating additional feed modifications using a software program. The results of the simulation are presented.

5.1 The Microstrip Antenna Solution

In the microstrip antenna solution, the individual 408 MHz probes are replaced by microstrip patches as shown in fig 5.1.1. Each patch must be designed for the correct length and width to fit between the inner and outer rings of the outer coaxial section. Before discussing the feasibility of this solution, the theory and design details of the patch will be presented. The design is based on the cavity model (James et al., 1986).

5.1.1 Theory and Design Details

The resonant frequency and the radiation characteristics of the patch can be found by first applying the necessary boundary conditions and solving Maxwell's equations. The patch is shown in fig. 5.1.2, and the boundary conditions are as follows:

$$\mathbf{H} \cdot \mathbf{z} = 0, \quad \mathbf{E} \times \mathbf{z} = 0 \quad \text{(electric conductor)}$$

$$\mathbf{E} \cdot \mathbf{n} = 0, \quad \mathbf{H} \times \mathbf{n} = 0 \quad \text{(magnetic wall)}.$$

If the electric conductor becomes the magnetic wall, and the magnetic wall becomes the electric conductor, the E and H fields in the previous boundary conditions are interchanged, and the results are the conditions for a rectangular waveguide of length h, height b and width a. Thus, for a good first order approximation, the solutions for the E and H fields of the rectangular waveguide are the solutions for the fields of a rectangular microstrip patch with the E and H fields interchanged. The voltage along the patch edge can then be expressed as follows:

$$V = |E_z| \cdot h = V_o cos(\frac{m\pi y}{b}) cos(\frac{n\pi x}{a}).$$

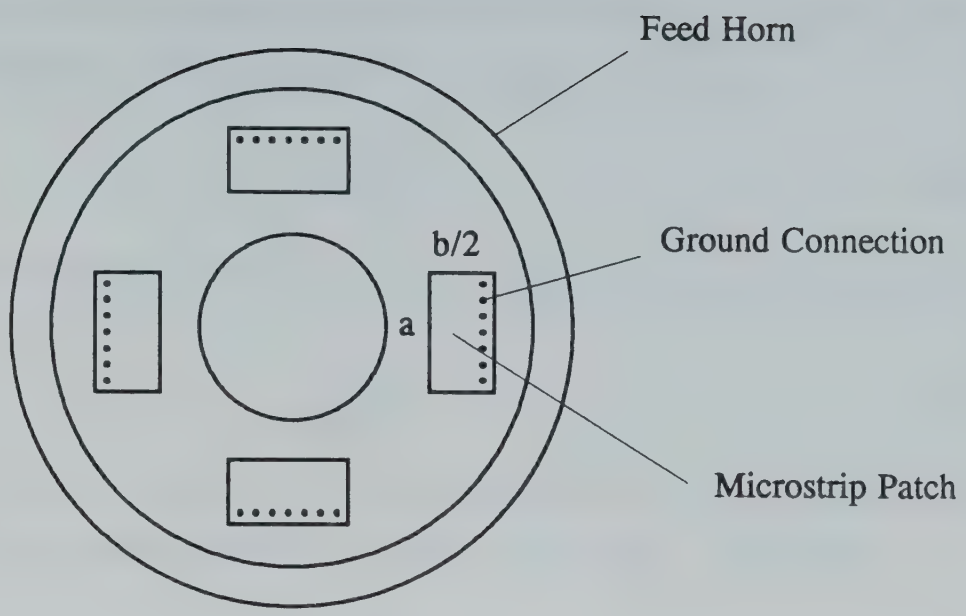

Figure 5.1.1 Microstrip Patch Orientation.

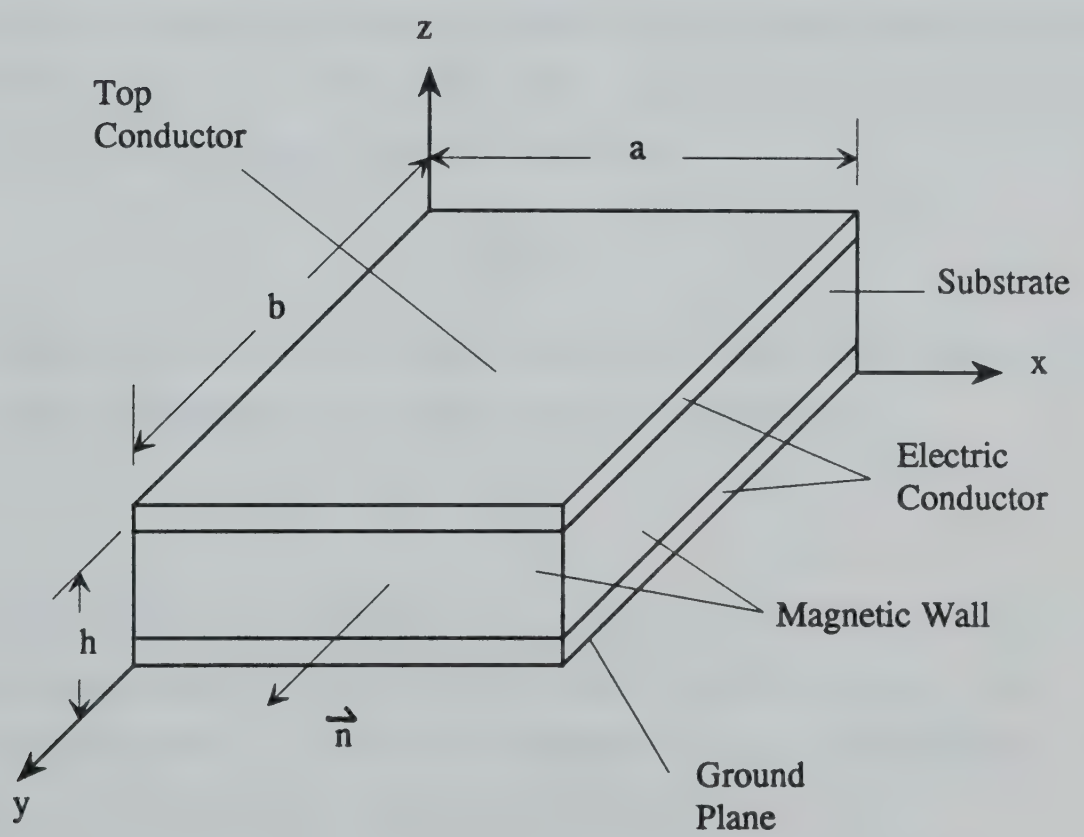

Figure 5.1.2 The Rectangular Patch.

where h is the substrate thickness, b is the patch length, and a is the patch width. For the dominant TE_{10} mode, the voltage reduces to

$$V_o cos(\frac{\pi y}{b}). \tag{1}$$

This voltage standing wave has a dominant mode resonant frequency, f_r, of

$$\frac{c}{2b\sqrt{\epsilon_r}}, \tag{2}$$

where ϵ_r is the relative permittivity of the substrate. The patch length can be obtained by rearranging equation 2 and solving for b. This gives

$$b = \frac{\lambda_o}{2\sqrt{\epsilon_r}},$$

where λ_o is the free space wavelength. At $y = b/2$ the voltage along the patch width is zero, and therefore, connecting this point of the top conductor to the ground plane has no effect on the voltage distribution along the patch length (fig. 5.1.3). The half wavelength patch then becomes a short circuit patch whose length, l_s, is $b/2$ or

$$\frac{\lambda_o}{4\sqrt{\epsilon_r}}.$$

The width of the patch, a, is selected so that only the dominant TE_{10} mode exists. Therefore, the width should be no more than

$$\frac{\lambda_o}{2\sqrt{\epsilon_r}}.$$

The width should not be much smaller than the above value because the radiation conductance will decrease as shown by the equation in fig. 5.1.4. The radiated power, P_r, from the microstrip patch is proportional to the radiation conductance, G_r, and is defined below:

$$P_r = {V_o}^2 G_r.$$

Therefore, the radiated power will decrease as the width is decreased.

3-DIMENSIONAL VIEW

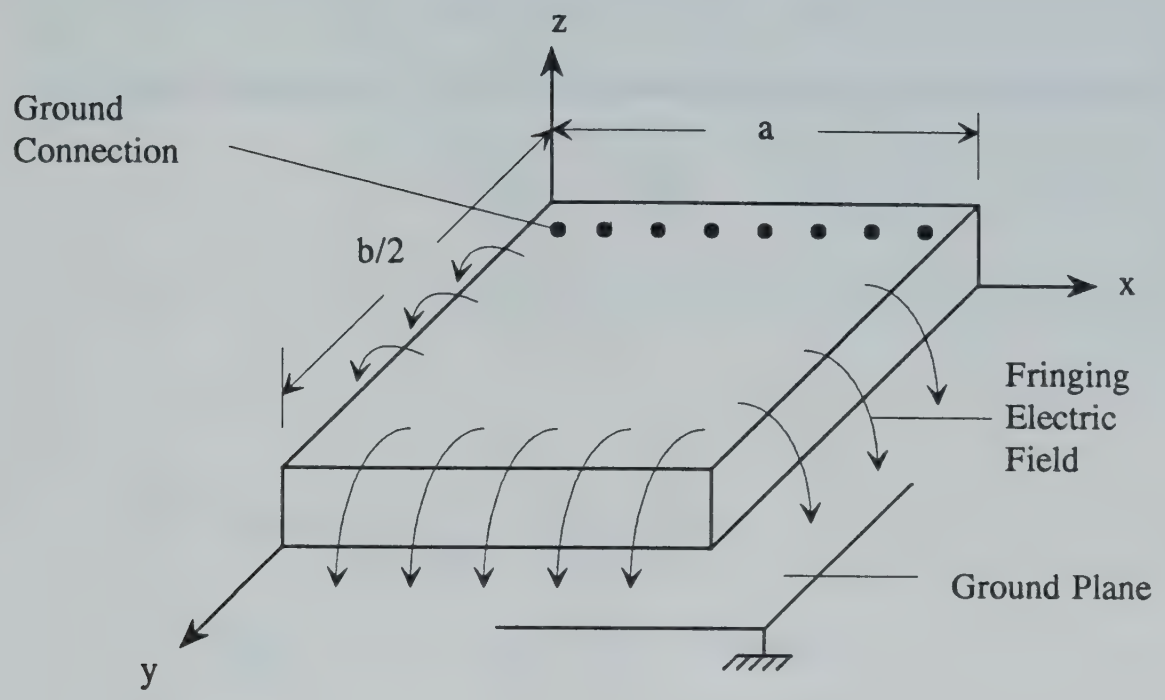

VOLTAGE DISTRIBUTION

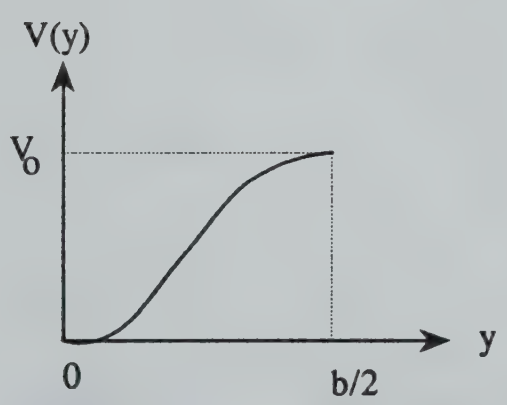

TOP VIEW

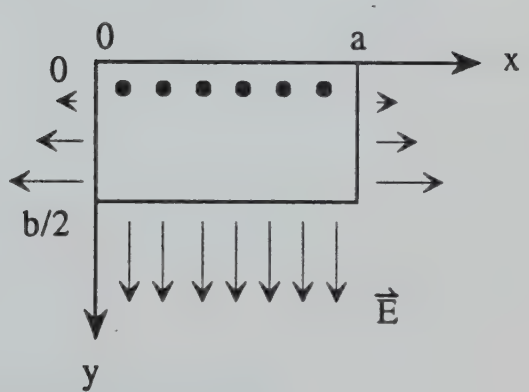

Figure 5.1.3 Radiation from the Rectangular Patch.

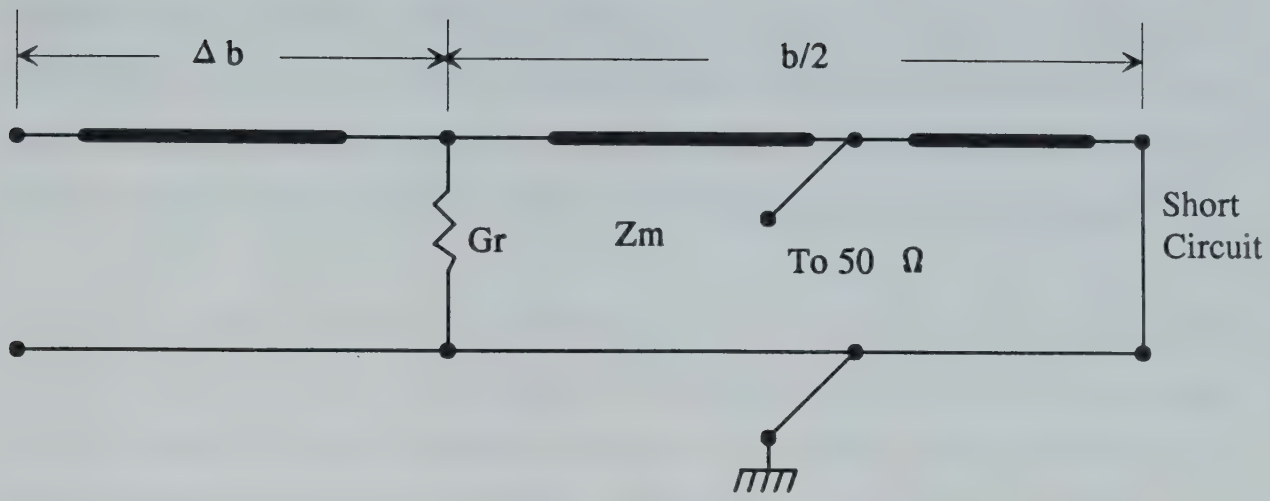

$$\frac{\Delta b}{h} = 0.412 \left(\frac{\varepsilon_e + 0.3}{\varepsilon_e - .258}\right)\left(\frac{a/h + .264}{a/h + .8}\right)$$

$$\lambda_g = \frac{\lambda_o}{\sqrt{\varepsilon_e}} \; ; \varepsilon_e = f(h, a, \varepsilon_r) \; ; \; Zm = f(h, a, \varepsilon_r)$$

$$Gr = \frac{a}{60\,\lambda_o} \quad \text{(Radiation Conductance)}$$

$$b/2 + \Delta b = \frac{\lambda_g}{4}$$

All Equations are from James et al., 1986.

Figure 5.1.4 The Circuit Model for the Rectangular Patch.

The radiation from the microstrip patch comes from the fringing fields as shown in fig. 5.1.3. Looking at the patch from the top, the radiation is y polarized and is due to the fringing fields along the edge $y = b/2$. The radiation from the fringing fields from the two opposite sides, $x = 0$ and $x = a$, cancels out in the far field on the boresight axis (or z axis).

The 50 ohm impedance point for optimum matching to 50 ohm coaxial line is calculated by considering the patch as a wide transmission line. A short circuit is placed at one end ($y = 0$), and a load consisting of a small end capacitance and a radiation resistance is placed at the other end ($y = b/2$). The end capacitance is modelled as a small open circuit transmission line that extends the original line due to the action of the fringing fields. The circuit along with the equations is shown in fig. 5.1.4. The approximate 50 ohm impedance point can be found from transmission line theory. The exact feeding point is determined experimentally because the model and its parameters are approximate.

5.1.2 The Advantages and Disadvantages of the Microstrip Solution

Before using microstrip antennas, the advantages and disadvantages must be considered.

One advantage of replacing the probe with a microstrip patch is that a high radiation resistance can be obtained without affecting the performance at 1420 MHz. As discussed in section 4.2, by using probes, a suitable radiation resistance (e.g. 50 ohms) can only be obtained by moving the probes into the front circular section. Doing this violates one of the

design constraints in section 4.4 and affects the performance at 1420 MHz. Using microstrip patches, the effect on the 1420 MHz performance is minimized. Only a thin sandwich of dielectric material exists between the top conducting layer and the ground plane, which is the back wall of the outer coaxial section. At 1420 MHz, the small structures look like large capacitors and approximate a short circuit between the two conducting layers; this condition only exists if the operating wavelength is more than $2h\sqrt{\epsilon_r}$ (Marcuvitz, 1951). Otherwise, higher order modes or parallel plate modes are introduced. Using the formula in fig. 5.1.4, the radiation resistance for a microstrip patch with width $\lambda_g/2$ and $\epsilon_r = 2.3$ is 185 ohms. The patch can be easily matched to 50 ohm coaxial line as shown in the previous section. To confirm the high radiation resistance and therefore the ease of matching to this resistance, a short-circuited microstrip patch was constructed as shown in fig. 5.1.5. The conducting element was the copper layer of a single-sided printed circuit board. Underneath the copper layer was 1.5mm of epoxy-glass substrate with $\epsilon_r = 3.8$ and 12.5mm of polyethylene substrate with $\epsilon_r = 2.3$. The effective dielectric constant of the combined substrates was about 2.4. The ground plane was aluminum, and the short circuit was approximated by a set of closely spaced screws. The probe was soldered to the copper element at the 50 ohm impedance point, which was calculated using the circuit model in fig. 5.1.4. The measured return loss at this point was 20 dB, and a better return loss could be obtained by a trial and error fine adjustment of the probe position.

Although the microstrip patch is easy to match to 50 ohm coaxial line, losses will still exist due to the large impedance transformation from 185 ohms to 50 ohms. The large impedance transformation will result in a large standing wave along the patch that will give rise to both conductor and dielectric losses.

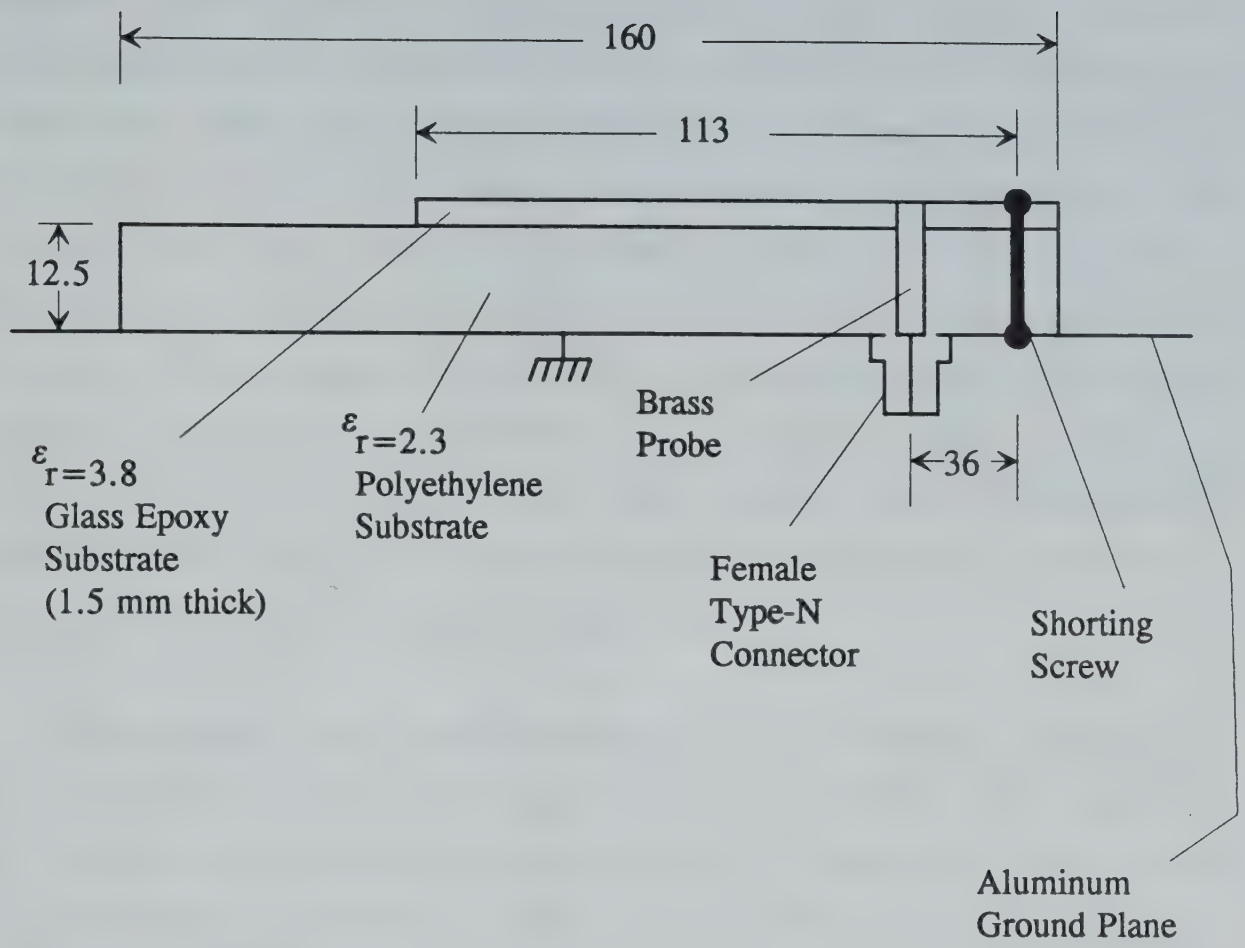

Notes:

All dimensions are in mm.
The patch width is 233mm.
The shorting screws are placed 1.5mm apart.
The resonant frequency is 408 MHz.

Figure 5.15 Details of the Short Circuit Patch.

Another advantage that could be realized with the use of microstrip antennas would be the low coupling between adjacent elements. This condition would exist only for a high dielectric constant of, for example, 10.2. This would make the patch approximately 6 cm long, 12 cm wide, and the distance between the adjacent patches would be slightly greater than 12 cm at 408 MHz. With a high dielectric constant, the fringing electric fields would be confined to a small area that slightly exceeds the area of the patch. The fringing electric field of the unwanted side (the side adjacent to the radiation side) of one patch is then less likely to induce an electric field into the radiation side of the adjacent patch; the potential for coupling between these two sides exists because each of these two sides radiate an electric field of identical polarization.

Unfortunately, there are disadvantages to the microstrip antenna solution. The first is the narrow input impedance bandwidth. The bandwidth for a microstrip patch is proportional to hf/ϵ_r (James et al, 1986), where h is the substrate thickness, f is the operating frequency, and ϵ_r is the relative dielectric constant. A high dielectric constant reduces the bandwidth. For instance, the measured bandwidth, for which the input VSWR $<$ 2, of the patch constructed in fig. 5.1.5, was 15 MHz. A dielectric constant of 10.2 would reduce the bandwidth to 15 x (2.3/10.2) = 3.5 MHz (h and f are constant). The operating bandwidth of the synthesis telescope is 4 MHz, and a return loss of more than 20 dB for at least 4 MHz is desirable. This return loss cannot be achieved with the high dielectric constant, and a high dielectric constant is needed in order for the patches to fit into the outer coaxial section of the feed.

A second disadvantage of the rectangular patch is the spurious radiation. Radiation from the rectangular patch emanates from all sides except the short-circuited side. On boresight, the radiation from the fringing fields of the opposite sides cancel out, but at other angles, the fields do

not cancel, which would result in a higher cross polarization level at these angles. Also, if the probes are replaced by the patches with low dielectric constants, the spurious radiation would increase the potential for coupling between the adjacent patches. With low dielectric constants, the adjacent patches would be closer together, and the fringing electric fields would be larger.

5.1.3 Corrective Measures for the Bandwidth and Spurious Radiation Problems

The bandwidth of the microstrip patches can be increased in two ways. The first method involves increasing the substrate thickness. As shown in the previous section, the bandwidth is proportional to the substrate thickness. By increasing the substrate thickness, the radiated power increases and the stored energy decreases. The radiated power increases because the fringing fields are stronger. The stored energy decreases because the capacitance between the two conducting layers decreases. Therefore, from section 1.2, the antenna Q decreases, and therefore, the bandwidth increases. To confirm that increasing the substrate thickness increases the bandwidth, the substrate thickness of the patch constructed in fig. 5.1.5 was increased from $14mm$ to $26.5mm$. The frequency was kept constant at 408 MHz, and the dielectric constant was kept approximately constant at 2.4 with the addition of another polyethylene layer ($12.5mm$ thick). The bandwidth should increase from 15 MHz to $15 \times (26.5/14) = 28$ MHz. The actual measured bandwidth (for a VSWR < 2) was 30 MHz. If the dielectric constant is increased from 2.4 to 10.2, the bandwidth would decrease from 30 MHz to 7 MHz, and the return loss would not be more than 20 dB over the 4 MHz operating bandwidth of the Synthesis Telescope. Replacing the probes

with even thicker patches would affect the performance at 1420 MHz. For instance, using a dielectric constant of 10.2, each patch would have a sizable conducting area ($6cm \times 12cm = 72cm^2$). The larger substrate thickness would move the top conducting layer toward the front circular section, and effectively, the depth of the outer coaxial section would decrease. The presence of the substrate would also generate higher order 1420 MHz modes or parallel plate modes, which would interfere with the 1420 MHz coaxial TE_{11} mode in the outer coaxial section.

A second method to increase the bandwidth, that does not involve excessive substrate thickness increases, is the use of multilayer patches (Sanford, 1978). To determine the increase in bandwidth, a triple layer microstrip antenna ("the triple decker") was constructed as shown in fig. 5.1.6. All three conducting layers were made of copper. The bottom substrate was polyethylene, and the top two substrates were those used in single sided circuit board. The short circuit was achieved by using high quality RF conducting tape. The probe was electrically connected to the top layer only. Clearance holes were drilled in the other two layers. The copper layers and the substrates were mounted to an aluminum ground plane using four equally spaced plastic screws. The antenna was constructed in the following way: The bottom patch was constructed first. The middle patch was then constructed using the bottom patch as its ground plane. The presence of the middle patch lowered the resonant frequency of the bottom patch. The top patch was then constructed using the middle patch as its ground plane, and the top layer lowered the resonant frequency of the middle patch but not the bottom patch. Multifrequency operation is possible because each patch has its own resonant frequency, and therefore, the antenna can be designed for a wide bandwidth.

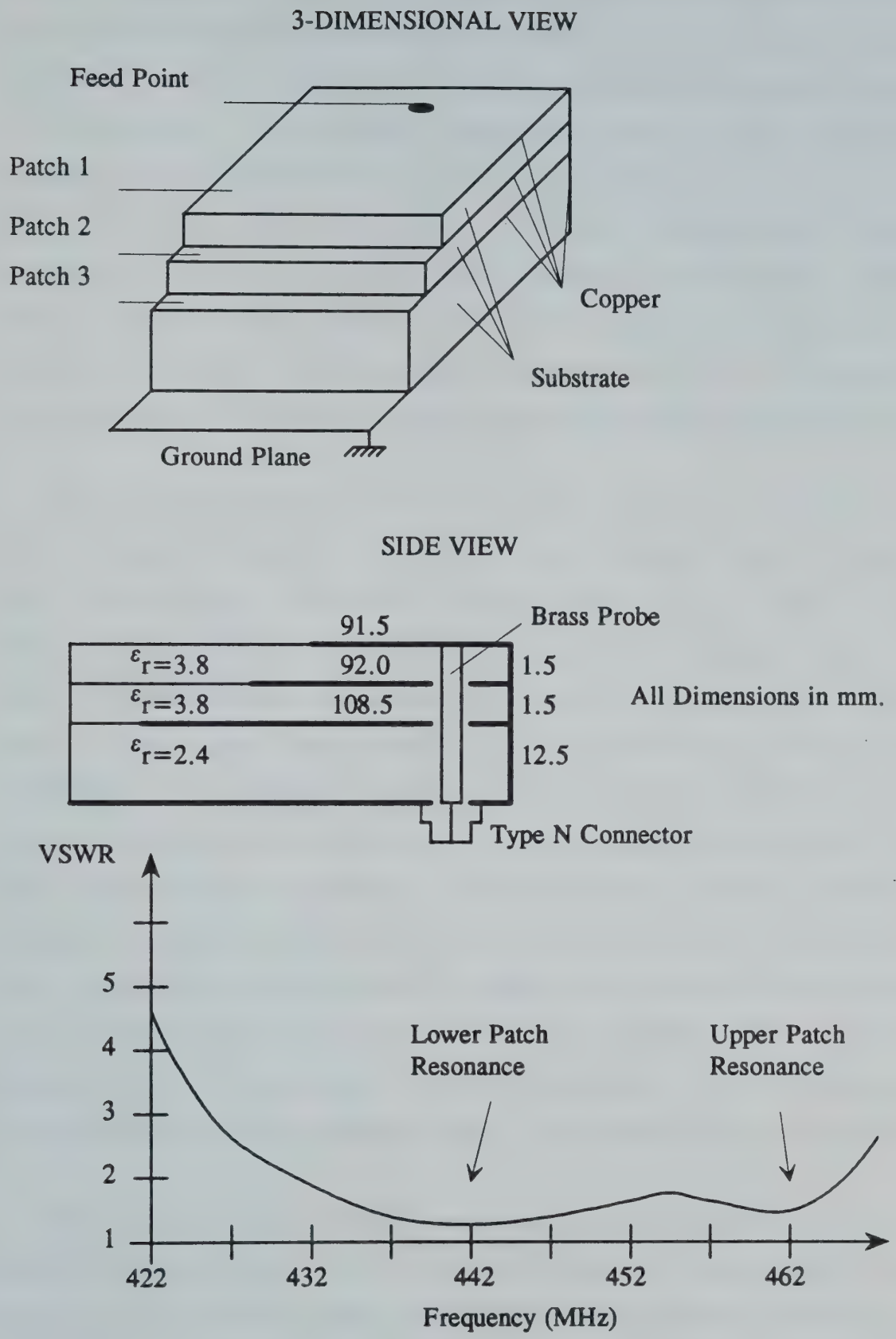

Figure 5.1.6 Multilayer Patches for Bandwidth Improvement- "The Triple Decker".

The design of a multi-layer microstrip antenna is analagous to the design of a multi-pole Chebychev filter. The frequency response of a Chebychev filter contains a ripple in the passband followed by some attenuation in the stopband. The stopband attenuation depends on the magnitude of the ripple and the order of the filter. The number of ripples in the passband equals the order of the filter. Similarly, the frequency response of the input return loss of a multi-layer microstrip antenna also contains a ripple in the operating bandwidth. Here, the number of ripples equals the number of patches. Therefore, the number of poles in a Chebychev filter corresponds to the number of patches in a multi-layer microstrip antenna.

The frequency response of the multi-layer microstrip antenna depends on the number of patches, the length of the patches, and the spacing between the patches. Specifically, the magnitude of the ripple in the desired operating bandwidth and the matching quality depends mainly on the length difference between the individual patches. A small length difference means a small ripple and a good match (return loss) for a fixed operating bandwidth. The resonant frequency of each patch is confined to a small frequency band, and the feed point is optimum for most of the patches. For a fixed number of patches, a wider bandwidth can be obtained at the expense of a larger ripple and a lower return loss. Here, the difference between the length of each patch is larger, and therefore, the resonant freqeuncy of each patch is farther apart. Also, the feed point is placed in a position where a "very average" return loss exists at all the patches instead of a good return loss at one patch and a bad return loss at another patch.

The measured input VSWR as a function of frequency of the "triple-decker" is shown in fig. 5.1.6. For this particular example, the resonant frequency of the middle patch is masked by the resonant frequencies of the other patches, which indicates that this design could be optimized further for a wider bandwidth. The bandwidth achieved for a VSWR < 2 was 44 MHz at 452 MHz, and the best match was VSWR $= 1.2$.

The drawbacks of the triple decker are the complexity and the iterative process involved in tuning the individual elements. Also, if the patches are replaced by the triple deckers, it would be difficult to attain identical input impedances for the four structures, and therefore, as shown in section 4.2, it would be difficult to obtain good polarization performance.

To counteract the problem of spurious radiation, other patch shapes can be considered, such as the annular antenna (Chew, 1982) or the travelling wave antenna (Roscoe, 1989) as shown in fig. 5.1.7. The annular ring patch will fit inside the outer coaxial section of the feed horn only if a dielectric constant of 10.2 is used, and unfortunately, the high dielectric constant would lower the bandwidth. Implementing the travelling wave structure involves the use of a terminating resistor. The resistor represents a noise source and will increase the system noise temperature and therefore reduce the sensitivity. Also, the travelling wave structure can only receive one hand of circular polarization. The Synthesis Telescope must have the capability of receiving two hands (left and right) of circular polarization.

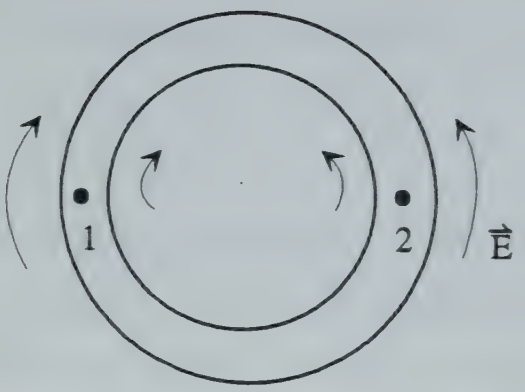

ANNULAR PATCH

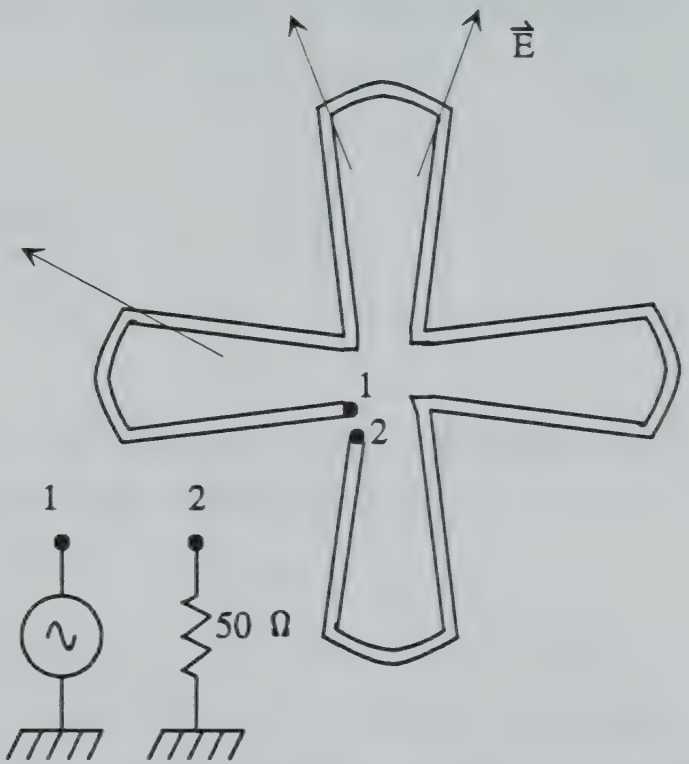

TRAVELLING WAVE PATCH

NOTE: 1,2 ARE FEED POINTS

Figure 5.1.7 Patch Shapes to Correct the Spurious Radiation Problem.

5.2 Annular Slot Solution

This solution consists of an annular slot cut in the back wall of the outer coaxial section. The annular slot is the aperture of a thin coaxial waveguide in which the distance between the inner and outer conductors is the slot width. The feed horn design is shown in fig. 5.2.1. The annular slot modification was built by Ed Danallanko, a machinist at D.R.A.O.. A photograph of the feed modification is shown in plate 3.

5.2.1 Design Details

From fig. 5.2.1, the inner and outer conductor radii, a and b respectively, are chosen such that (Marcuvitz, 1951)

$$(a+b) \geq \frac{c}{\pi f_o},$$

where f_o is the operating frequency, 408 MHz. The slot is centered between the inner and outer rings of the outer coaxial section, and the slot width is 4 cm. The radii, a and b, are 18 cm and 22 cm respectively. There is no constraint on the slot width if the depth of the coaxial waveguide is chosen properly.

The depth of the coaxial guide feeding the slot is chosen to be 40 cm for two reasons. First, the dominant TE_{11} coaxial mode at 408 MHz has to be present at the slot aperture. The coaxial waveguide is excited by short probes, which are located about $\lambda_g/4$ (22.6 cm at 408 MHz) from the backshort, where

$$\lambda_g = \frac{\lambda_o}{\sqrt{1-(\frac{\lambda_0}{\lambda_c})^2}};$$

$$\lambda_c = \pi(a + b),$$

where λ_o is the free space wavelength, and λ_c is the cutoff wavelength of the waveguide. Another $\lambda_g/4$ is sufficient to allow this mode to be established at the aperture. For instance, the next higher order mode is the coaxial TE_{21} mode. This waveguide mode will attenuate by a factor of

$$exp(\ \frac{-2\pi l}{\lambda_o}\sqrt{(\frac{f_c}{f})^2 - 1}\ ),$$

where f_c is the cutoff frequency of the TE_{21} mode (478 MHz), f is the operating frequency (408 MHz), and l is the distance from the probe to the aperture of the waveguide (20 cm). Substituting the values, the attenuation factor is 0.35. Therefore, only a small portion of the TE_{21} mode will be present at the aperture. Secondly, to minimize the effect on the original 1420 MHz pattern, the depth of the thin coaxial waveguide must be an integral number of half wavelengths. This ensures that the 1420 MHz TE_{11} mode in the outer coaxial section will not be disturbed, and a virtual short circuit is seen at the plane of the back wall. For instance, from transmission line theory,

$$Z_{in} = Z_o.\frac{Z_L + jZ_o tan\beta l}{Z_o + jZ_L tan\beta l}$$

If $l = 2\lambda_o$, $Z_{in} = Z_l$. At 1420 MHz, $(\lambda_o/\lambda_c)^2 << 1$, and therefore, $\lambda_g \approx \lambda_o$. The depth of the waveguide was chosen to be 40 cm ($\approx 2\lambda_o$ at 1420 MHz). Therefore, a short circuit is seen at the waveguide aperture, and the TE_{11} mode in the outer coaxial section remains undisturbed.

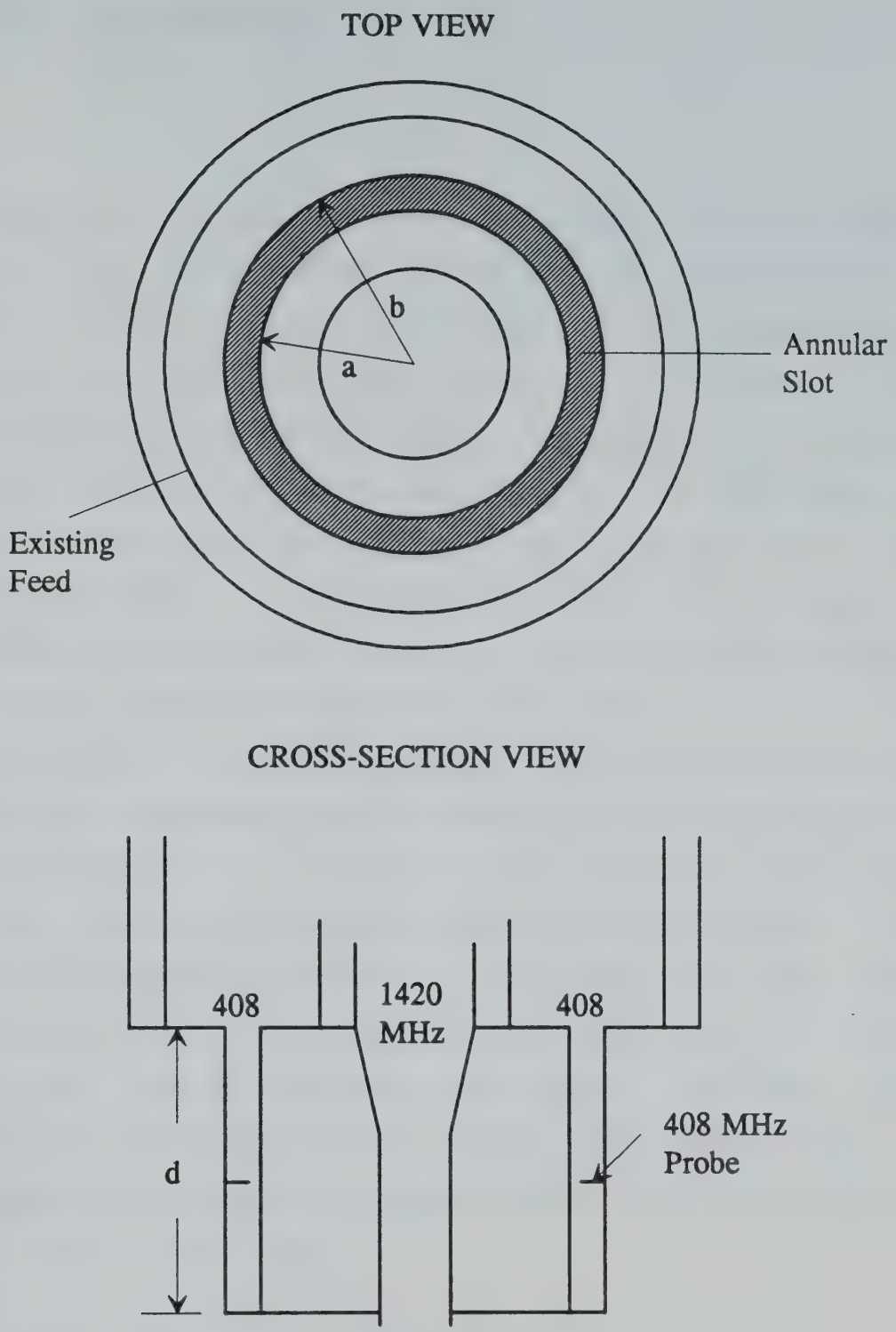

Figure 5.2.1 The Annular Slot Feed Horn.

5.2.2 Results and Discussion

The measured feed pattern using the annular slot modification is shown in fig. 5.2.2. The E and H plane patterns of the annular slot are more similar than the E and H plane patterns of the existing feed (fig. 4.09) because, with the annular slot, the direct probe radiation is eliminated. A comparison between the existing feed pattern and the annular slot feed pattern at 408 MHz is shown in fig. 5.2.3. In the existing feed, the beam is narrow in the E plane and broad in the H plane; the half-wave dipole has a narrow beam in the E plane and a broad beam in the H plane. With the annular slot modification, the front circular section of the feed supports just the 408 MHz TE_{11} and TM_{11} modes and not the direct probe radiation. These modes, along with the cutoff frequencies, and the approximate superposition (vector addition) of these modes at the feed aperture are shown in fig. 5.2.4. The superposition shows that the field strength in the feed aperture is tapered along the x axis and y axis. Therefore, the approximate circular symmetry of the field in the feed aperture should result in a more circular primary beam when applying the Fourier transform. Apart from the similarity of the patterns in the two principal planes, there is no significant reduction in the $\pm$ 60° radiation levels. Because the effective size of the feed remains the same with this modification, the primary beam is still broad.

The measured effect on the performance at 1420 MHz is shown in fig. 5.2.5. As shown from the figure, the effect is minimal and confirms that, using the chosen depth of the waveguide, the slot aperture appears to be a short circuit at 1420 MHz.

The circular feed pattern, and the negligible effect on the original 1420 MHz pattern are advantages, but the annular slot also has disadvantages.

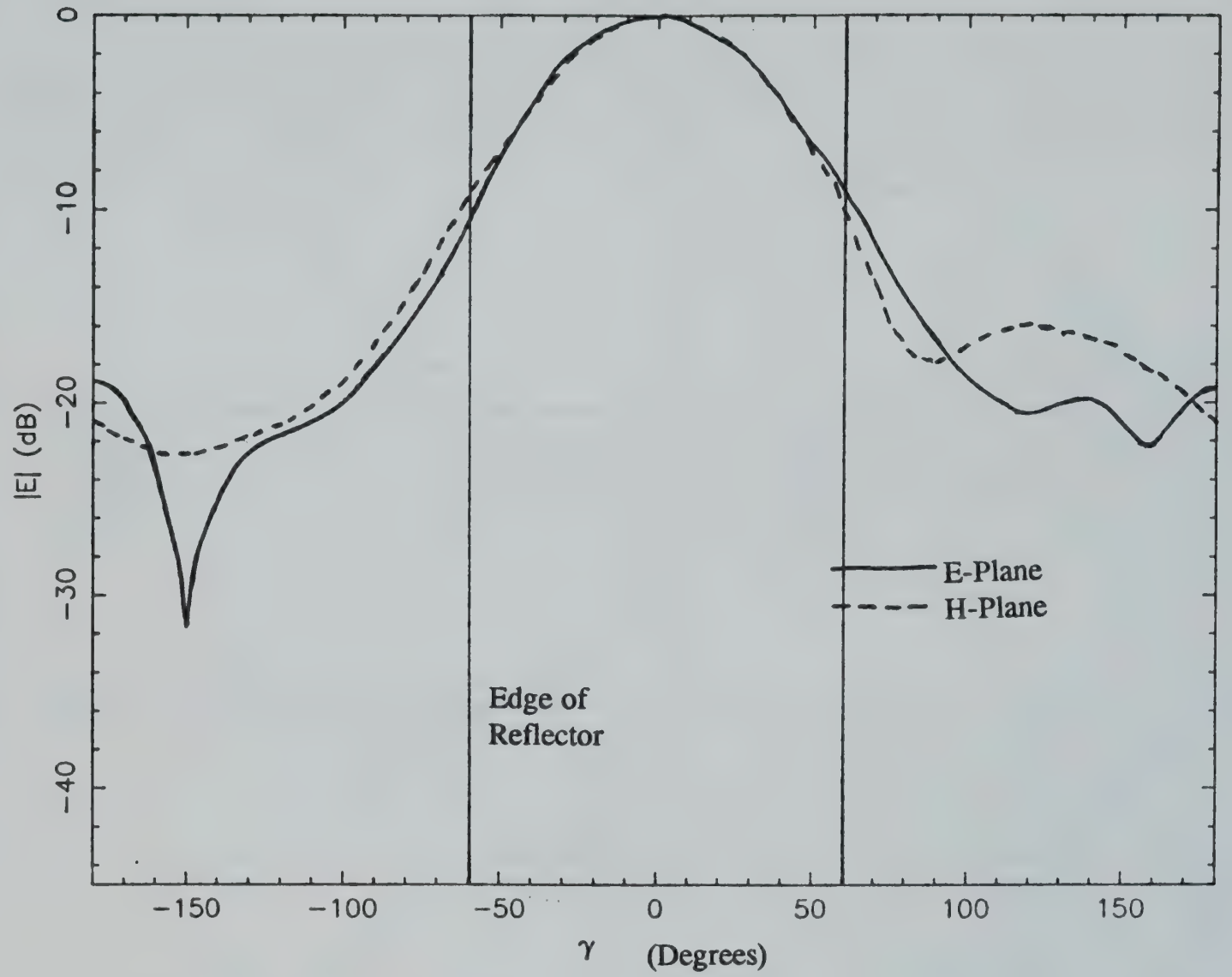

Figure 5.2.2 Measured Feed Patterns for the Annular Slot Excited Feed Horn.

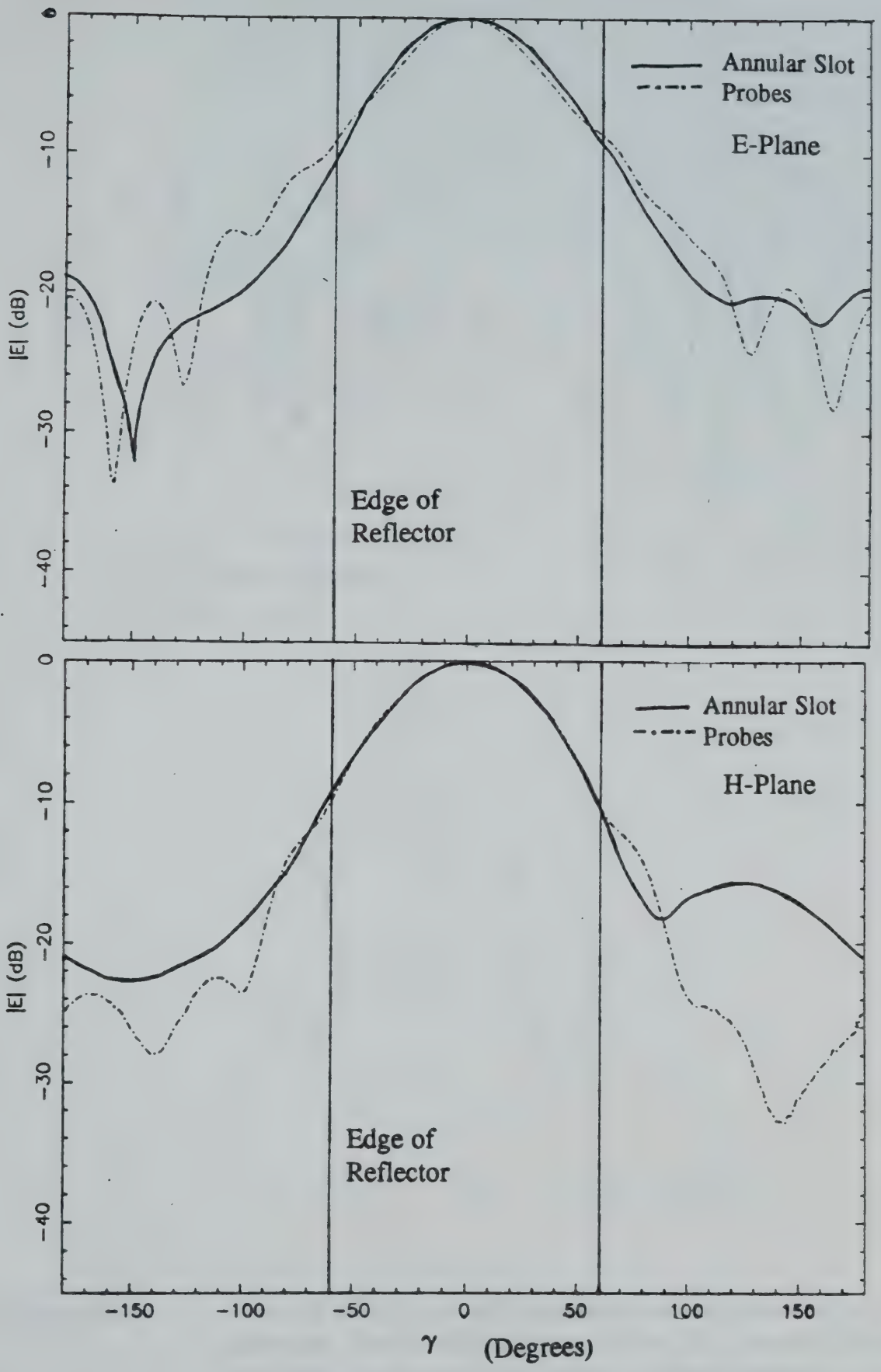

Figure 5.2.3 Measured Feed Patterns of the Annular Slot and the Existing Feed at 408 MHz.

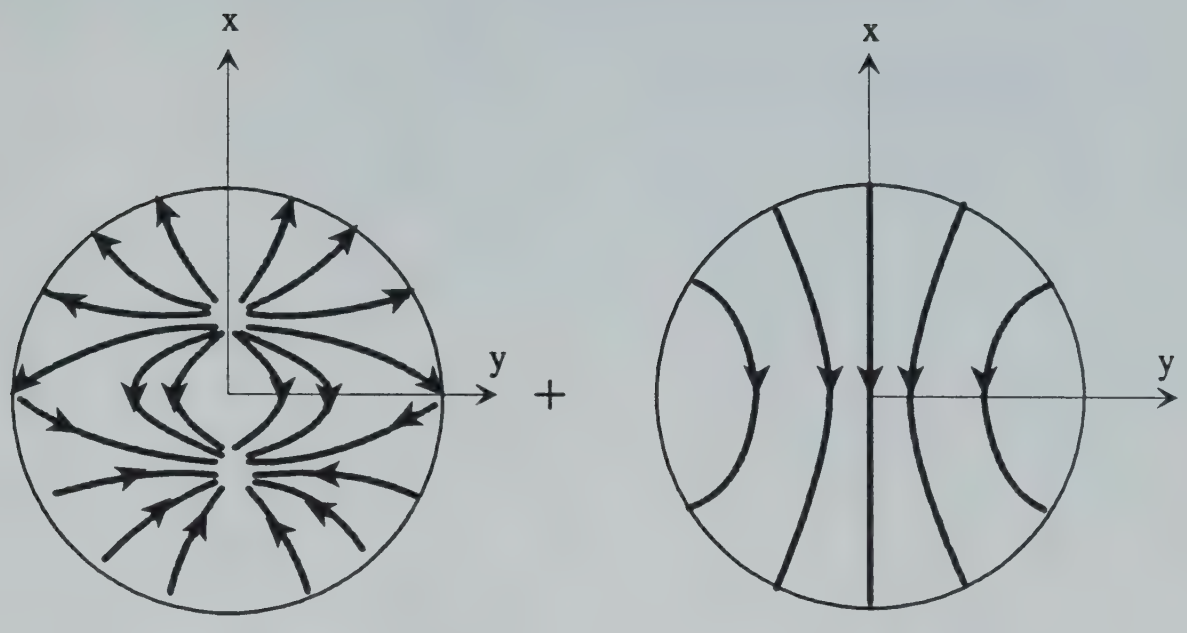

TM_{11} (f_c=429 MHz)
Mode is present because waveguide is small.

TE_{11} (f_c=206 MHz)

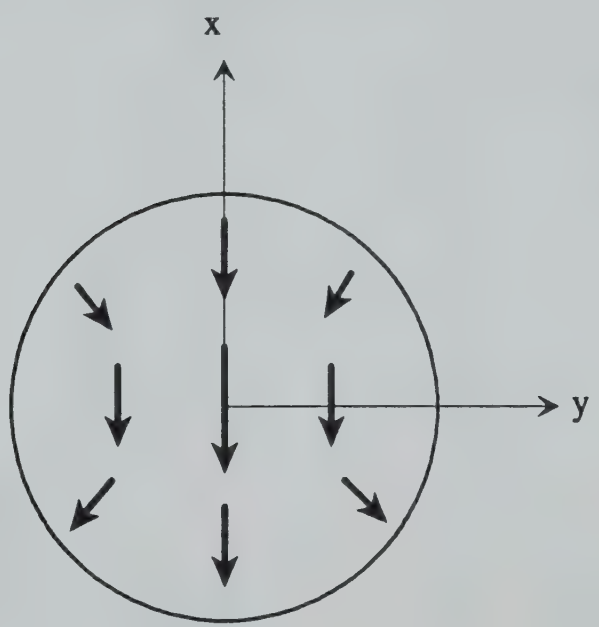

TM_{11} + TE_{11} (Vector Addition)

Figure 5.2.4 The 408 MHz Circular Waveguide Modes present at the Feed Aperture. The cutoff frequency for the TM_{11} mode is just above 408 MHz, but the mode will have an effect because the front circular section of the feed horn is shallow.

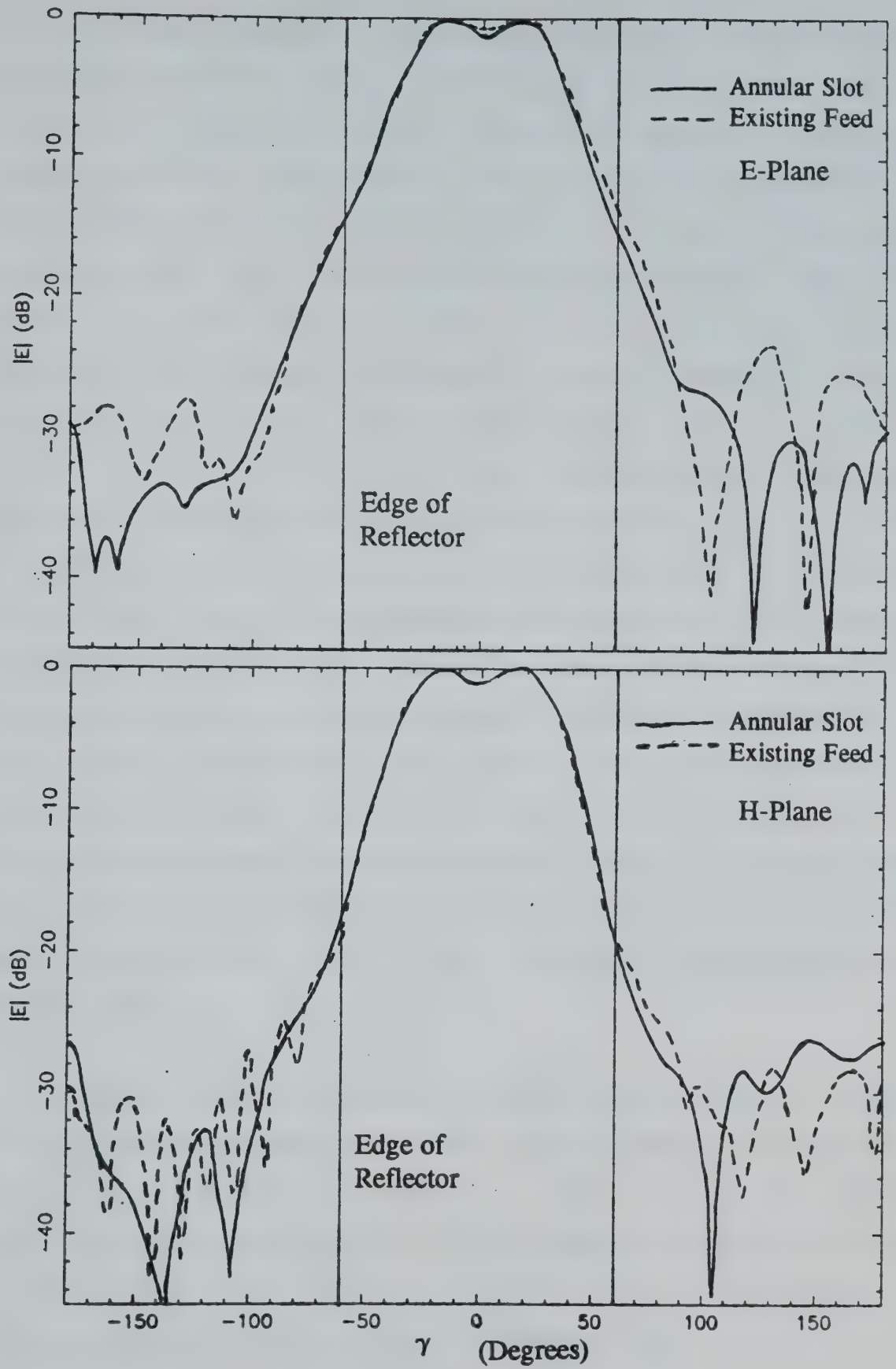

Figure 5.2.5 The Measured Effect of the Annular Slot on the 1420 MHz Feed Pattern.

A first disadvantage is the difficulty in matching to 50 ohm coaxial cable. This is because the distance between the inner and outer conductors of the coaxial waveguide is only 4 cm, and the waveguide impedance is, therefore, quite low. The measured return loss is about 3 dB, and an external matching network is required. There are two ways to overcome the matching problem. The first method involves increasing the width between the inner and outer conductors. With the increase, the probes would be longer and would radiate more efficiently into the waveguide. The second method is to use a "top loading" device. Such a device was constructed as shown in fig. 5.2.6. The device was constructed using a thin strip of brass and a brass sleeve which adjusted the length of the existing probe. The strip was first soldered to the sleeve and then bent to a radius equal to the average radius of the inner and outer conductors of the waveguide. The return loss of 10 dB was achieved by using the "top loading" device. A better return loss was achieved because "top loading" increases the radiation resistance of the probe; that is, larger currents flow at the end of the probe, which effectively results in more radiated power. Increasing the area of the strip would result in a better return loss. The major drawback in using the two methods is that the stronger coupling to the inner conductor of the waveguide would result in high coupling (low isolation) between the adjacent ports.

A second disadvantage is the insufficient distance between the back of the feed horn and the focus box, which houses the front end electronics and feed circuitry. The distance is only 23 cm. This is shorter than the depth of the waveguide feeding the slot. If this solution were to be implemented, it would require some major reconstruction such as lengthening the feed legs and reorganizing the circuitry in the focus box.

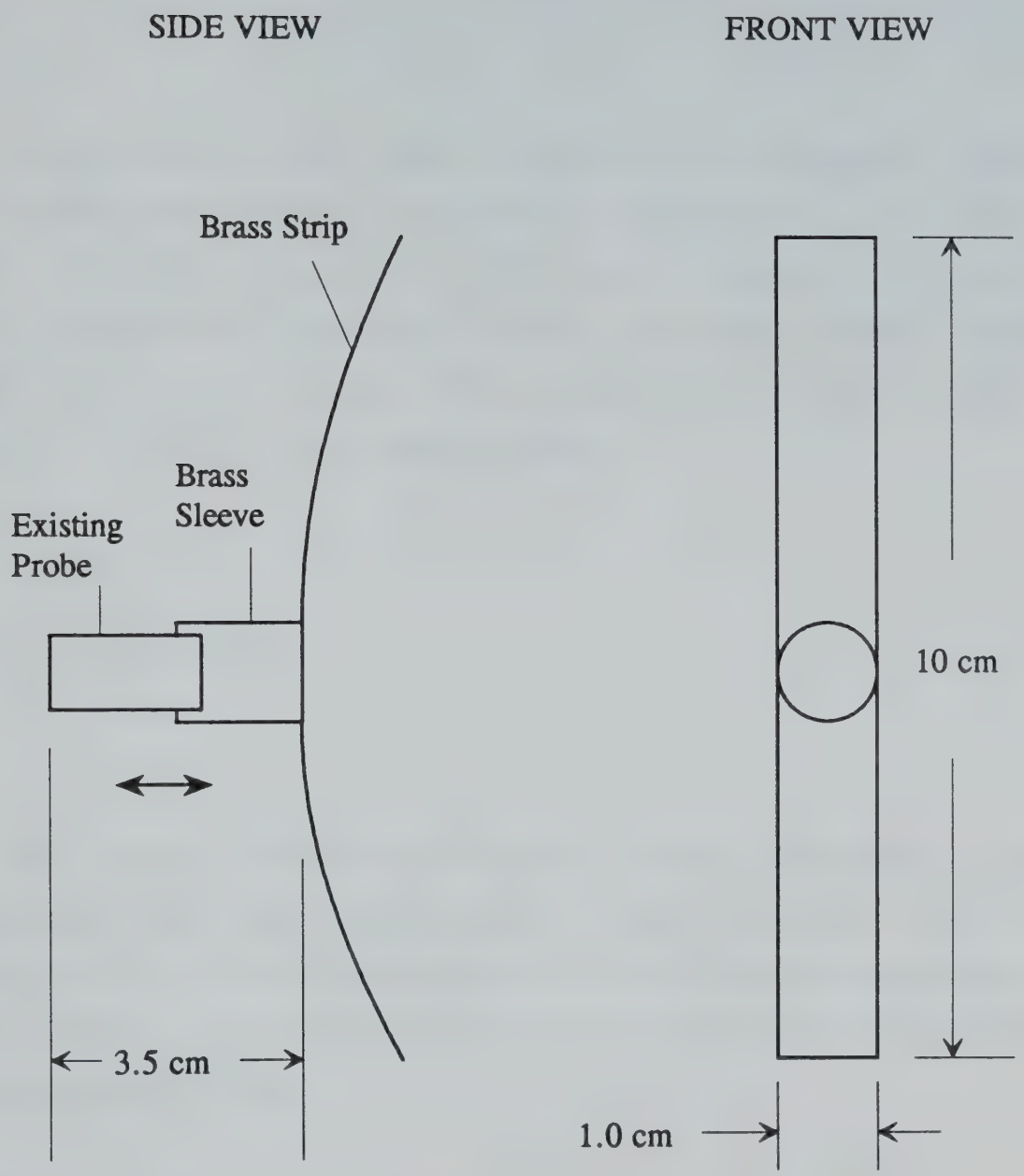

Figure 5.2.6 Details of "Top Loading" the Probe in the Thin Coaxial Waveguide.

5.3 Rectangular Slots backed by Rectangular Waveguide Cavities filled with Dielectric

In this solution, each probe is replaced by a rectangular slot backed by a rectangular waveguide cavity filled with dielectric. The design modification is shown in fig. 5.3.1. The element operates in the same way as a rectangular slot backed by a cavity without the dielectric (Hirokawa, 1989). The waveguide cavity is filled with dielectric to make the slots small enough to fit in the outer coaxial section.

5.3.1 Design Details

The length a of the slot is chosen so that it fits within the physical constraints of the outer coaxial section. A good slot length with a suitable width is 15 cm. Since the slot length is the width of the rectangular waveguide and given that the cutoff frequency for the dominant TE_{10} mode, f_c, is (Montgomery, 1948)

$$\frac{c}{2a\sqrt{\epsilon_r}},$$

the required dielectric constant, ϵ_r, is chosen such that

$$\epsilon_r \geq (\frac{c}{2af_c})^2.$$

Choosing the operating frequency $f_o = 1.2\ f_c$, where $f_o = 408$ MHz, the dielectric constant is $\epsilon_r \geq 8.7$. Therefore $\epsilon_r = 9$ will satisfy the slot length constraint of 15 cm at 408 MHz.

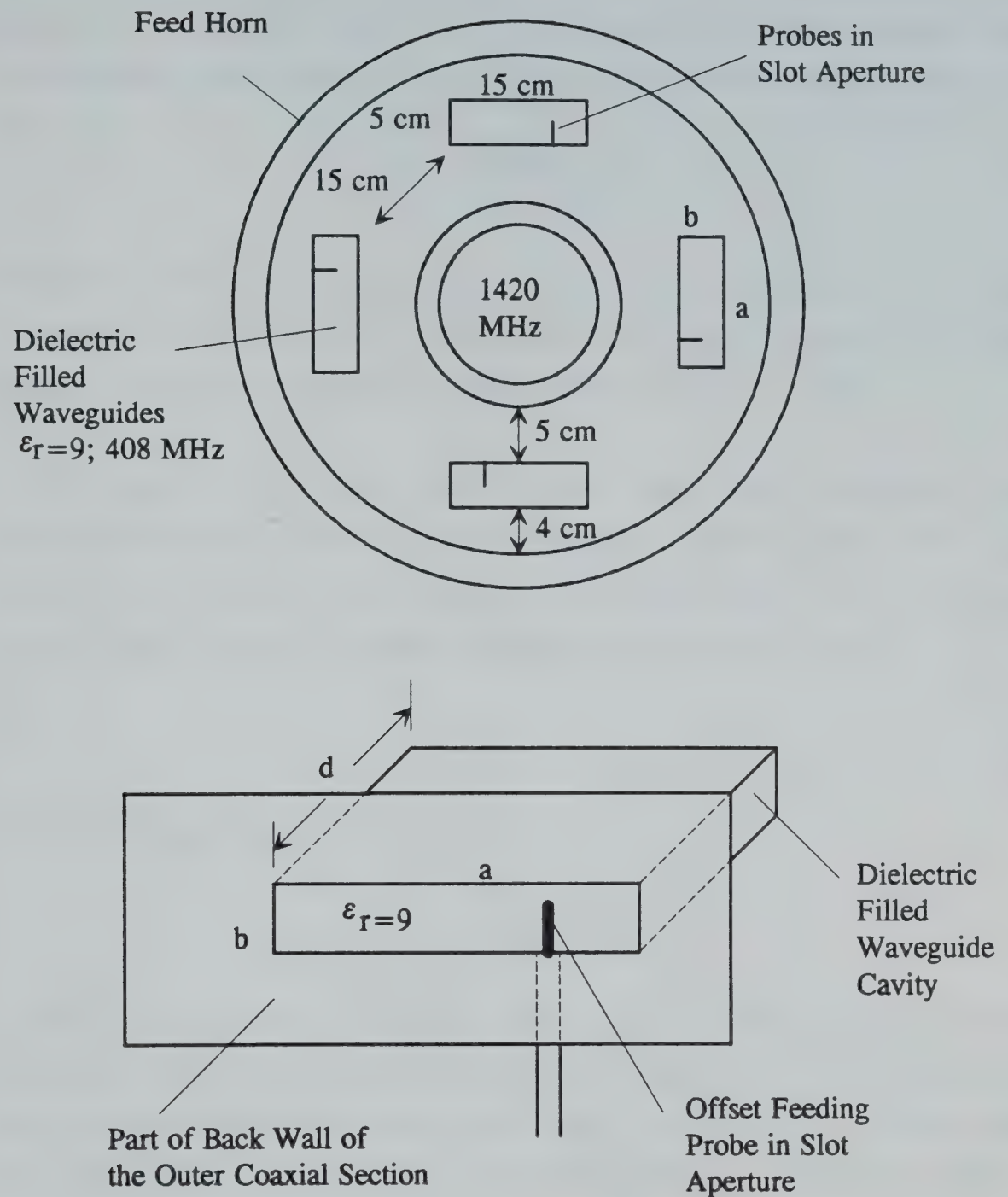

Figure 5.3.1 Slot Orientation and the Dielectric Filled Rectangular Cavity.

The slot is backed by a rectangular waveguide cavity to ensure the slot radiates in one direction only. A probe is located in the slot aperture, and the waveguide cavity depth is $\lambda_g/4$, where λ_g is (Montgomery, 1948)

$$\lambda_g = \frac{\lambda_o}{\sqrt{\epsilon_r - (\frac{\lambda_o}{2a})^2}}.$$

Substituting values, the cavity depth, d, is 10.6 cm. The depth is chosen so that the field produced by the probe at the slot aperture is in phase with the field that is reflected off the back wall of the cavity.

The width b of the slot is chosen so that first, there is sufficient clearance between the slot and the central waveguide ring when the slot is centered between the inner and outer conductors, and second, there is at least one slot length clearance between adjacent slots.(See fig. 5.3.1.)

5.3.2 Exciting the Slots

The slot is excited by a probe located at or near the aperture. It can be excited in two ways depending on the slot width. For narrow slots, the center conductor of the 50 ohm coaxial line is shorted to the opposite side of the slot as shown in fig. 5.3.2. The outer conductor of the coaxial line is clamped to the other side of the slot to prevent any reverse currents from flowing down the outside of the cable. For wider slots, the center pin is left open ended and its length is adjusted, depending on the value of the slot impedance.

The slot impedance is found by relating the slot in an infinite ground plane to a dipole in free space. If the length and thickness of the dipole are the same as the length and width of the slot, the slot is the complement of the dipole (Booker, 1946). Under these conditions, it can be shown that the slot impedance is

$$Z_s = \frac{(377)^2}{4Z_d},$$

where Z_d is the dipole impedance. In our situation, the slot radiates in one direction only, and the ground plane is not infinite. Therefore, the slot impedance must be measured.

Nevertheless, the formula shows that the slot has a high radiation resistance, and the feed point must be offset from the center of the slot to match to 50 ohm coaxial cable. The offset distance is obtained as follows: First, the slot resistance, R_o, is measured at the center. Since the electric field across the slot is sinusoidal with maximum field at the centre of the slot, the input resistance as a function of distance, x', from the centre as shown in fig. 5.3.3 is (Milligan, 1985)

$$R_{in}(x') = R_o \cdot cos^2(\frac{\pi x'}{a}).$$

Essentially, the probe couples to the field strength along the slot. Moving the probe from the center changes the reactance at the aperture and detunes the slot. This changes the resonant frequency slightly, and the change must be compensated by readjusting the depth of the waveguide cavity.

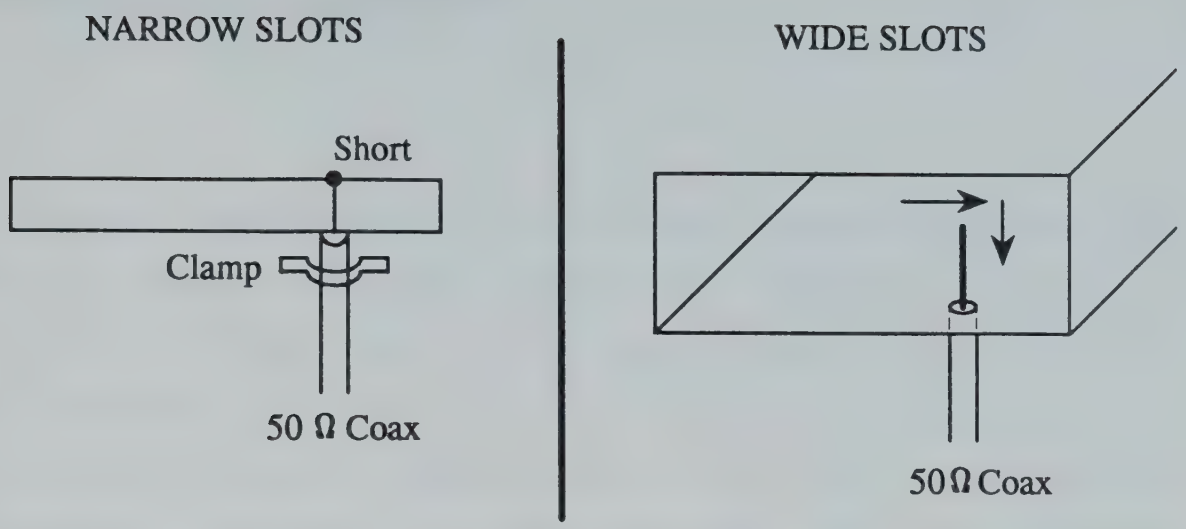

Figure 5.3.2 Coaxial Line to Slot Transitions.

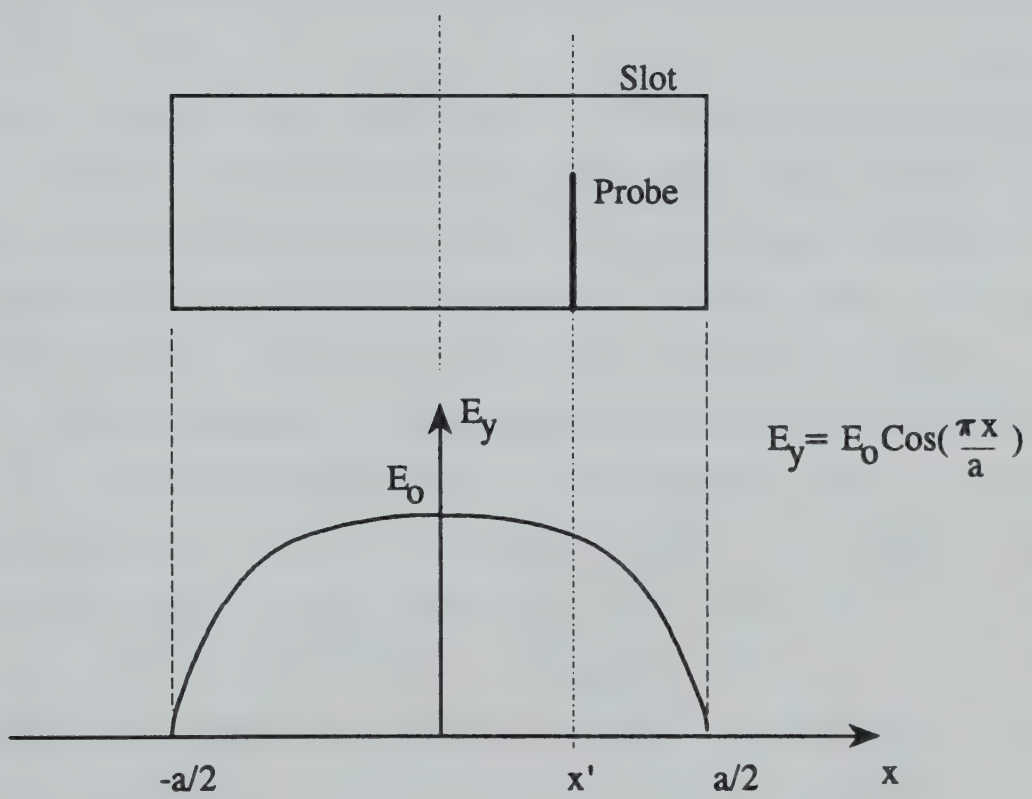

Figure 5.3.3 Calculating the Slot Feed Offset Distance.

5.3.3 Scale Model Construction

All testing was performed on a scale model. The scale model was constructed to operate at 700 MHz. Therefore, the dimensions of the existing feed horn at 408 MHz, except for the metal thickness, were scaled by a factor of 408/700 or approximately 4/7. To ensure strength and rigidity of the scale model, the metal thickness of the full size model was not reduced. The thickness of the metal will not affect the results of the scale model significantly because the thickness is much smaller than a wavelength, even at 700 MHz. The slot and waveguide dimensions that were specified in section 5.3.1 were also reduced in size by the same factor. Only the sections relevant to the scaled 408 MHz operation were constructed; the scaled 1420 MHz waveguide section was not constructed. Also not constructed was the scaled version of the outer choke. The material used in the scale model was aluminum. The spinning process used in the construction of the existing feed was not used in the construction of the scale model. Rather, the inner ring, the outer ring, the back wall of the outer coaxial section, and the rectangular waveguide cavities were connected together using closely spaced screws. All edges were sealed with high quality RF conducting tape to prevent any radiation leakage. A photograph of the scale model is shown in plate 3. The dielectric material used in the rectangular cavities was Emerson and Cumming Eccoflo HiK dielectric powder. The dielectric constant was 9.0 with a loss tangent (dissipation factor) of .0007. The dielectric powder was tightly packed into the rectangular cavities by using a vibrating machine. The cavity was then sealed with a plastic sheet to prevent the powder from leaking out. The results of the tests using the scale model will be discussed in the following sections.

5.3.4 Experimental Results and Discussion

Replacing the probes in the existing feed with slots results in less coupling between adjacent elements. The measured results for the coupling between adjacent and opposing slots and probes are shown in the table in fig. 5.3.4. As expected, the coupling between the adjacent slots is less than that between the adjacent probes. Also, the coupling between the opposing slots is higher than the coupling between the opposing probes. This is because the slots do not couple to each other via the central ring, but rather, they couple to each other by the surface currents flowing on the back wall of the outer coaxial section. The surface currents due to one slot run approximately parallel to the adjacent slots and perpendicular to the opposing slot. The opposing slot should couple highly because the slot interrupts the surface currents. The adjacent slots should couple less because they do not "cut across" the surface current flow. The coupling levels between the adjacent and opposing slots are the same because the length to width ratio of the slot is not too large. Wide adjacent slots interrupt more surface currents than thin adjacent slots, and a long opposing slot interrupts more surface currents than a short opposing slot.

The measured radiation patterns for the slot excited feed horn are shown in fig. 5.3.5. For comparison, the radiation patterns of the existing feed at 408 MHz are shown in the same figure. The feed radiation levels at $\pm$ 60° are -10 dB and -8 dB for the E-plane and H-plane respectively. With respect to the existing feed at 408 MHz, there is no significant reduction in the $\pm$ 60° radiation levels in either plane. This further suggests that any changes made inside the horn do not result in reducing the $\pm$ 60° radiation levels, and any significant reduction must involve increasing the size of the feed. The outer choke was not constructed in the scale model. Therefore, the $\pm$ 60° radiation levels in fig. 5.3.5 for the scale model may be slightly higher than they would be if there was an outer choke.

	Probes At 408 MHz Full Size Existing Feed	Slots at 700 MHz Scale Model
Adjacent Elements	- 8 dB	- 12 dB
Opposing Elements	- 14 dB	- 12 dB

Figure 5.3.4 Isolation Levels for the Probes and Slots.

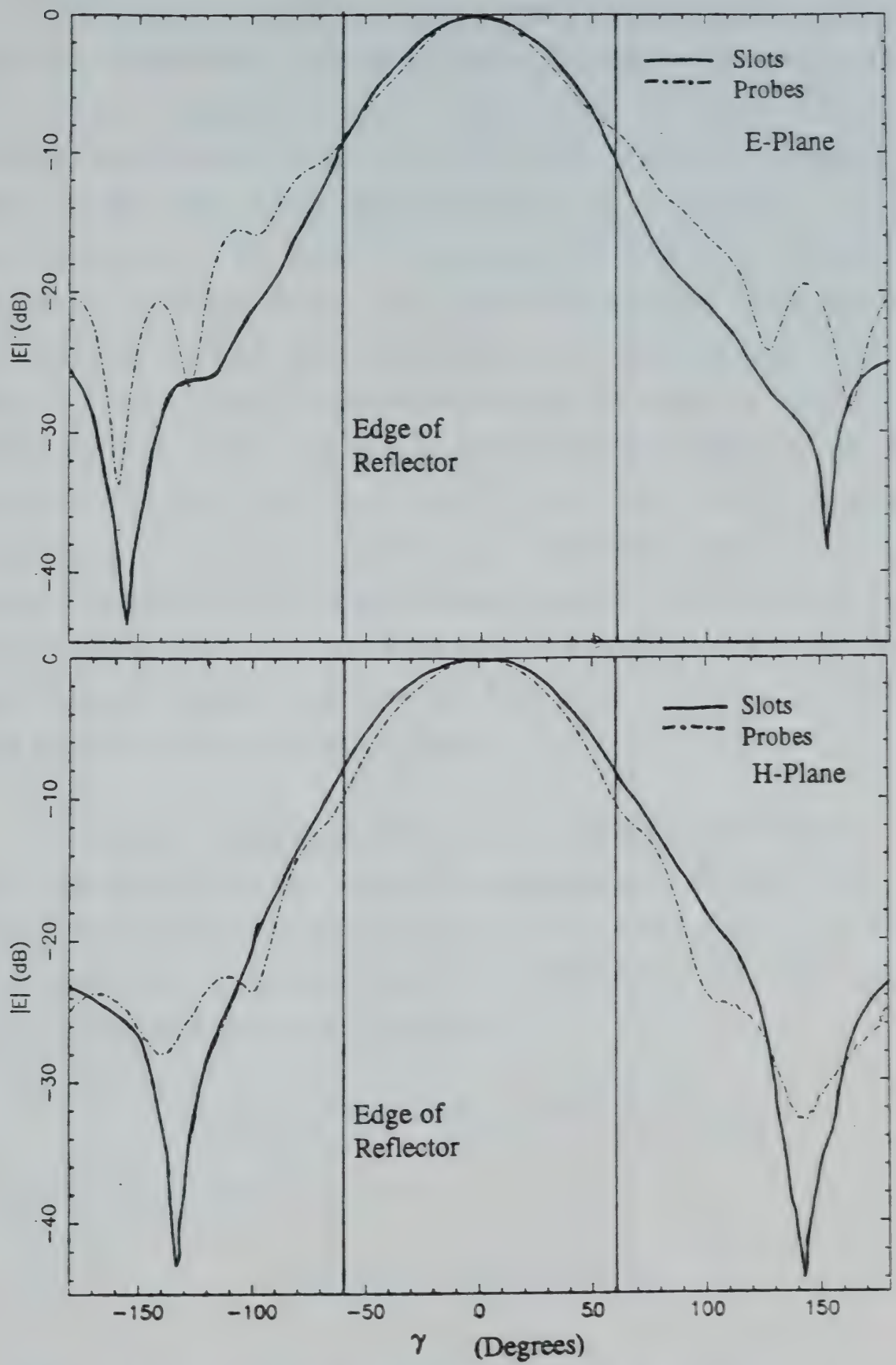

Figure 5.3.5 Measured Feed Patterns for the Slot Excited Feed Horn (Scale Model) at 700 MHz and the Existing Feed at 408 MHz.

Unfortunately, a few disadvantages exist in using the rectangular slots. The first disadvantage is the narrow input impedance bandwidth. The return loss as a function of frequency was measured for one of the slots near 735 MHz and is shown in fig. 5.3.6. The 8 dB return loss bandwidth is 30 MHz. At 408 MHz, this would scale down to 30 $\times$ (408/735) or 17 MHz. The bandwidth of the probes in the present feed horn is 20 MHz. The probes are, therefore, better. The bandwidth reduction would mean that the difference between the input impedance at the operating band edges (408 $\pm$ 2 MHz) and the input impedance at the centre of the band (408 MHz) would be larger than that in the existing feed. However, the degradation in the bandwidth when using the slots would not be as severe as when using the microstrip patches. The bandwidth reduction can be attributed to the use of the high dielectric constant, which increases the antenna quality factor, Q. The bandwidth is proportional to $1/Q$. With a high dielectric constant, most of the fields tend to stay in the dielectric, and hence the stored energy is greater.

The second disadvantage is the cost and weight of the dielectric material. The chosen dielectric material is very expensive. It is also very heavy. The volume of each rectangular cavity is $15cm \times 5cm \times 10.6cm$ or $795cm^3$. The density of the dielectric material is 2.55 g/cm^3. The total mass, M, of dielectric needed for the 4 cavities is

$$M = 4 \times 2.55 g/cm^3 \times 795 cm^3 = 8 \ Kg.$$

The cost for one feed horn is then

$$\$222/Kg \times 8 \ Kg = \$ \ 1,778.$$

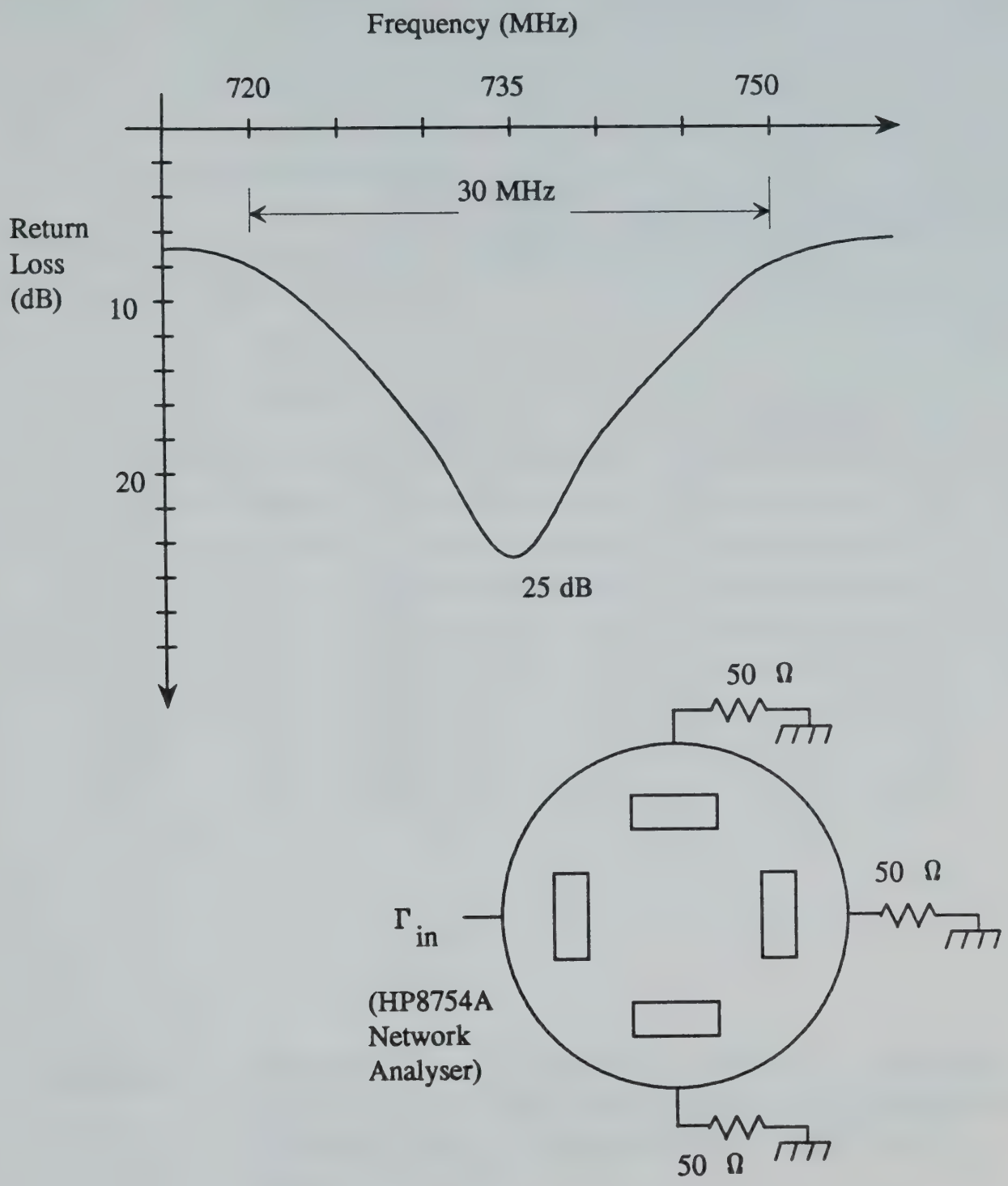

Figure 5.3.6 Measured Input Return Loss at each port for the Scale Model.

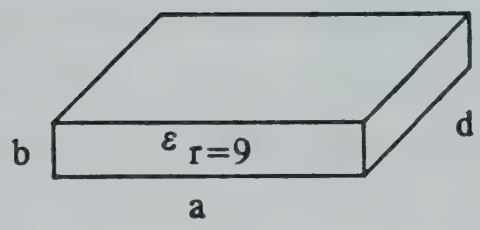

a=0.15m
b=0.05m
d=0.106m

$$f_c = \frac{c}{2\sqrt{\epsilon_r}}\sqrt{(\frac{m}{a})^2 + (\frac{n}{b})^2}$$

TE mode	f_c (MHz)	$d\,\lambda_g$ (1420 MHz)
10	333	1.5
20	667	1.3
30	1000	1.1
01	1000	1.1
11	1054	1.0
21	1202	0.8
40	1333	0.5
31	1414	0.1

Figure 5.3.7 Possible TE modes in the Dielectric Filled Cavity at 1420 MHz. Some of the higher order modes may have a small effect because of the cavity depth; a "virtual short circuit" may exist at the aperture of the cavity.

A third disadvantage is the effect on the 1420 MHz performance. Of all the solutions discussed so far, the slots may have the greatest effect on the 1420 MHz pattern. The $15cm \times 5cm$ slot backed by an $11cm$ deep rectangular cavity filled with the high dielectric constant material allows 1420 MHz TE and TM modes to propagate in the cavity. Since the slots are in a position where the density of the 1420 MHz coaxial TE_{11} mode field lines are high, this mode would be greatly affected. Essentially, the slot cavity combination would act as a mode bandstop filter, and each mode filter would affect a component of the TE_{11} mode existing in the outer coaxial section. Fig. 5.3.7 lists the cutoff frequencies of the TE modes existing in the rectangular cavity at 1420 MHz.

5.3.5 Antenna Losses

It is worthwhile considering the losses that occur in the scale model and how the losses vary with frequency. In other words, what would be the predicted losses in the full size model? The antenna losses consist of both conductor losses and dielectric losses.

Conductor losses are caused by electromagnetic (EM) fields attenuating inside an imperfect conductor. Most of the losses occur when the EM wave attenuates within a distance equal to the skin depth, Δ. The skin depth is (Kraus, 1984)

$$\Delta = \frac{1}{\sqrt{\sigma \pi \mu f}}, \qquad (1)$$

where σ is the metal conductivity, μ is the metal permeability, and f is the operating frequency. By assuming that most of the conductor losses are generated within the skin depth, the losses in a section of metal can be approximately represented by a resistance, R, which is (Meyer, 1984)

$$R = \frac{L}{\sigma W T}, \tag{2}$$

where L is the length of the metal section, W is the width, and T is some thickness. If the thickness is assumed to be approximately equal to the skin depth, it follows immediately that

$$R \propto \frac{L\sqrt{f}}{W}. \tag{3}$$

Therefore, the losses in the full size model operating at 408 MHz would be smaller than the losses in the scale model operating at 700 MHz by a factor of $\sqrt{408/700}$. The length to width ratio of any metal section remains fixed for both models. The conductive losses that actually occur are negligible because the conductivity of aluminum is 38.16 x 10^6 mhos/m. For instance, using equation 2 and substituting the skin depth for the metal thickness, the equivalent resistance for a typical metal section of aluminum at 700 MHz is .009 L/W ohms. This is low compared to the high radiation resistance of the slot.

Dielectric losses are caused by EM fields attenuating in the dielectric material. The propagation constant, γ, for a wave in a lossy dielectric is (Nasar, 1982)

$$\gamma = \alpha + j\beta = j2\pi f\sqrt{\mu\epsilon(1 - jtan\delta)},$$

where α is the attenuation constant, β is the phase constant, $tan\delta$ is the dielectric loss tangent, μ is the dielectric permeability, ϵ is the dielectric constant, and f is the operating frequency. The attenuation constant can be expressed as

$$\alpha = \frac{\sqrt{2\epsilon_r}\pi}{\lambda_o}(\sqrt{1 + tan^2\delta} - 1)^{\frac{1}{2}},$$

where λ_o is the free space wavelength and ϵ_r is the relative permittivity. The fields inside the dielectric will attenuate by the factor $e^{-\alpha' z_\lambda}$, where z_λ is the distance the wave travels in the dielectric in wavelengths, and α' is the modified attenuation constant ($= \alpha \times \lambda_o$).

Therefore the value of the dielectric losses in the scale model will be the same as the value in the full size model because the amount of attenuation depends on the distance travelled in wavelengths. The depth of the cavity filled with dielectric is the same in terms of wavelengths for both models. The losses in the dielectric material can be calculated as follows: Part of the *EM* wave generated at the aperture of the rectangular waveguide travels through the dielectric, reflects off the back wall, and comes back. Since the slot is not non-reflective, diminishing portions of the wave travel back and forth in the cavity. All these portions contribute to the dielectric losses. For the dielectric material in the scale model, α' is 0.0066. The wave will thus attenuate by a factor of 0.998 by travelling a distance of twice the depth of the cavity (z_λ). There will be more attenuation as the wave travels back and forth, but the accumulated loss can be neglected because the attenuation is small.

5.4 Rectangular Slots backed by a Coaxial Cavity

In this solution, the four probes are again replaced by four rectangular slots. However, the slots are backed by a common coaxial waveguide cavity rather than four individual rectangular cavities. For testing purposes, a scale model was designed to operate at 700 MHz and is shown in fig. 5.4.1. The scale model was built by Roman Lipiecki, a machinist in the Electrical Engineering department at the University of Alberta. A photograph of the scale model is shown in plate 3.

5.4.1 Design Details

The physical size of the outer coaxial section imposes a limitation on the slot length. The resonant length of a slot in free space is approximately $\lambda_o/2$, where λ_o is the free space wavelength. A slot of such length will not fit in the present feed horn, and therefore, a dielectric sheet is placed on one side of the slot to reduce its resonant length. The slot now "sees" free space on one side ($\epsilon_r = 1$) and a dielectric sheet such as polyethelyne ($\epsilon_r = 2.4$) on the other side. The effective dielectric constant is then approximately the average of the two, which is $\epsilon_e = 1.7$. The effective dielectric constant may be slightly lower because the dielectric sheet does not fill the half-space on the cavity side of the slot. The resonant length, l_r, of the slot is approximately

$$\frac{\lambda_o}{2\sqrt{\epsilon_e}},$$

and with $\epsilon_r = 2.4$, the slot will fit in the feed horn as long as the slot width is not too large.

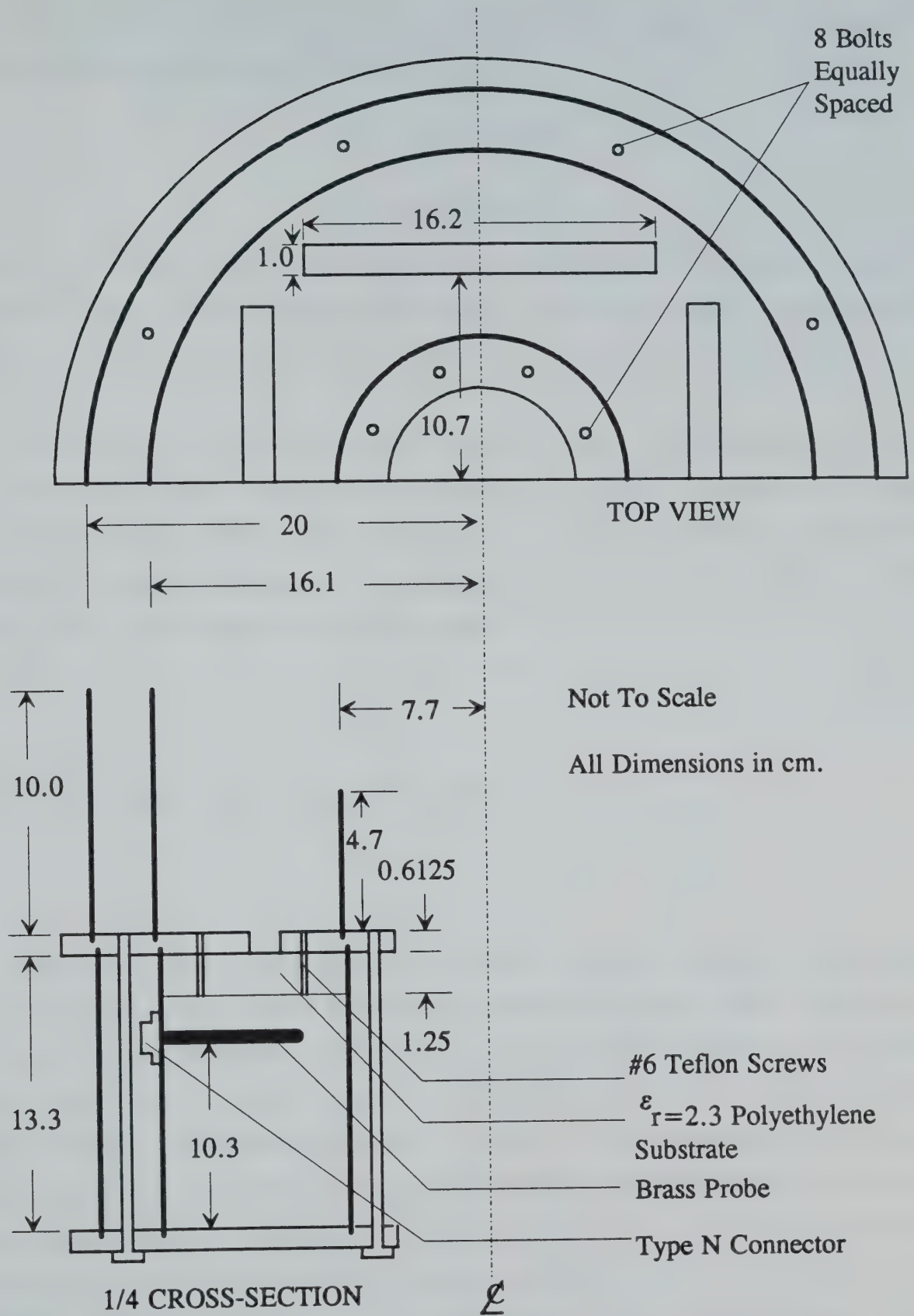

Figure 5.4.1 Scale Model Design of the Slot Excited Feed Horn. The slots are backed by a common coaxial waveguide cavity.

To force the radiation to occur in one direction only, the slot is backed by a $\lambda_g/4$ coaxial waveguide cavity, where

$$\lambda_g = \frac{\lambda_o}{\sqrt{1-(\frac{\lambda_o}{\lambda_c})^2}};$$

$$\lambda_c = \pi(a+b),$$

where λ_c is the cutoff wavelength of the waveguide. Dimensions a and b are the inner and outer radii respectively and are the same as the radii of the inner and outer conductors of the outer coaxial antenna section.

The slots are excited by short probes, which are placed just behind the dielectric sheet. The radiation from the probes is sufficient to couple to the slots. The feed horn arrangement can also be viewed as an infinite coaxial waveguide feeding four rectangular irises, with the dominant mode being the coaxial waveguide TE_{11} mode.

5.4.2 Matching and Tuning the Slots

Matching and tuning the slots requires correctly phased input signals to the probes. The correct phasing is achieved by using a ring hybrid. The ring hybrid was realized in microstrip. The substrate was glass-epoxy material that is used in double sided printed circuit board. The printed circuit layout of the ring hybrid is shown in fig. 5.4.2. The feeding arrangement, that includes the antenna and the ring hybrid, is shown in fig. 5.4.3. Only one pair of slots is considered. Considering the other pair as well requires the use of another ring hybrid. The ring hybrid forces the 180° phase shift between the opposing ports and generates the TE_{11} waveguide mode inside the cavity. The slots are then excited 180° out of phase, and the TE_{11} radiation mode is present in the outer coaxial section. A good match exists if there is a low return loss at the input of the ring hybrid.

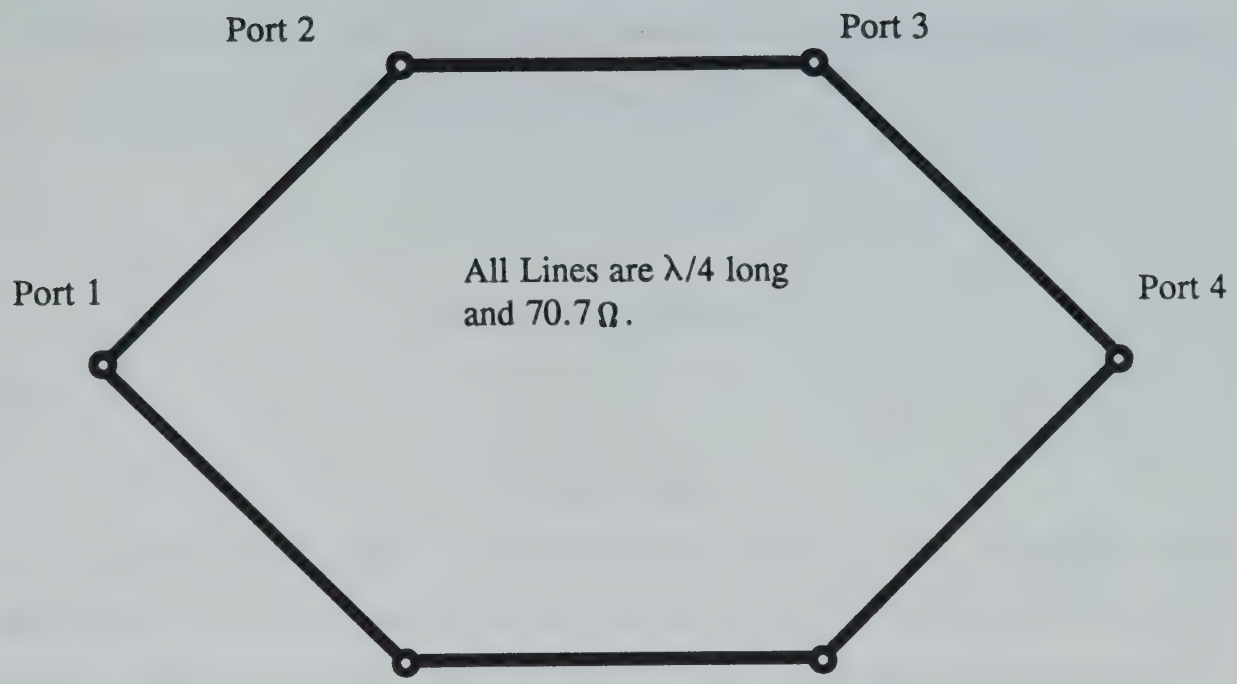

Figure 5.4.2 Printed Circuit Layout for the Ring Hybrid.

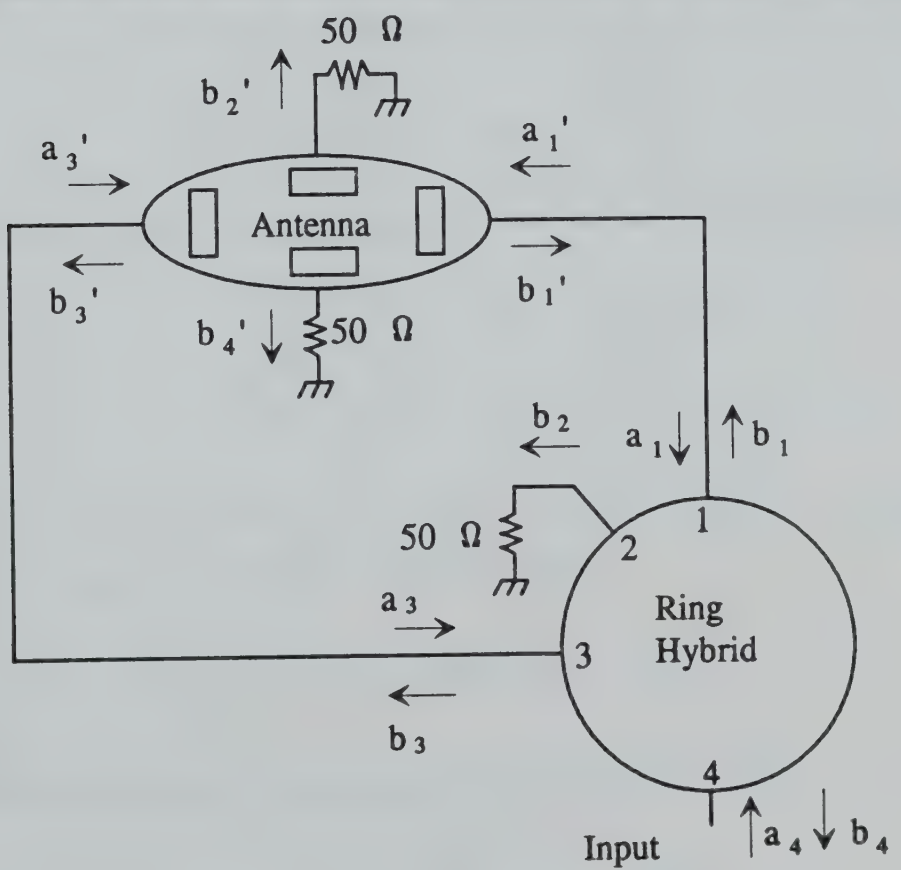

Figure 5.4.3 The Antenna Matching Circuit.

From fig. 5.4.3, the ring hybrid "sees" the antenna as a two port device, and hence, the following condition exists:

$$b_1' = S_{11}a_1' + S_{13}a_3'$$

$$b_3' = S_{31}a_1' + S_{33}a_3',$$

where

$$\begin{pmatrix} S_{11} & S_{13} \\ S_{31} & S_{33} \end{pmatrix}$$

is the S-parameter matrix of the antenna. Ports $1'$ and $3'$ represent the input ports to the opposing slots. The adjacent ports are terminated in matched loads, and therefore $a_2' = a_4' = 0$. The ring hybrid forces the input voltage waves a_1' and a_3' to be equal and 180^o out of phase so that $a_1' = -a_3'$. Under this condition,

$$a_1/b_1 = b_1'/a_1' = (S_{11} - S_{13})$$

$$a_3/b_3 = b_3'/a_3' = (S_{33} - S_{31}).$$

The S-parameter matrix for the ring hybrid is as follows (Gardiol, 1984):

$$\frac{1}{2}j\begin{pmatrix} 0 & -1 & 0 & 1 \\ -1 & 0 & -1 & 0 \\ 0 & -1 & 0 & -1 \\ 1 & 0 & -1 & 0 \end{pmatrix}.$$

By terminating the unused port in 50 ohms ($a_2 = 0$), the reflection coefficient at the input to the ring hybrid becomes

$$b_4/a_4 = \frac{1}{2}(S_{13} + S_{31} - S_{11} - S_{33}), \tag{1}$$

and the isolation between the unused port and the input port is

$$b_2/a_4 = \frac{1}{2}(S_{11} - S_{33} + S_{31} - S_{13}). \tag{2}$$

A low return loss will occur when $S_{13} = S_{31} = S_{11} = S_{33}$, and the probes must be adjusted for this condition. If the minimum return loss does not occur at the desired frequency, the slot length must be readjusted accordingly.

Because of reciprocity, S_{13} is always equal to S_{31}, and S_{11} will equal S_{33} if the probes feeding the slots are adjusted equally. Unequal adjustment will cause S_{11} not to equal S_{33} and will result in power leakage into the unused port. This is evident from equation 2. S_{11} can be made equal or close to S_{13} by varying the probe length and the distance between the probe and the slot. The equality will also ensure a low VSWR at the input ports to the antenna with the phasing network attached.

Equal adjustment of the two probes in the pair is necessary for two reasons. First, power will be delivered to the opposing slots equally, and this will eliminate a primary beam pointing error. Second, the power leakage into the unused port will be a minimum, and this will minimize the system noise temperature. The unused port is terminated with a 50 ohm resistor and can represent a noise source if the ring hybrid is used as part of the antenna feed network. Normal operation of the antenna is achieved by using a 6-port hybrid network, like the one shown in fig. 4.10. This will give the necessary circular polarization at the hybrid inputs. It should be noted that an "unused" port does not exist explicitly in this network, but if the probes are not adjusted equally, power will leak into the 50 ohm isolation resistors that are built into the ladder network as shown in fig. 4.10. In the receiving case, these resistors act as noise sources if the probes are not adjusted equally.

5.4.3 Results from the Scale Model

The following measurements were performed on the scale model: isolation, input return loss, polarization pattern, and radiation patterns. The slots on the scale model were tuned to 730 MHz, and all measurements were done at this frequency.

The coupling levels of the existing feed and the two slot-driven feed solutions discussed in this thesis are shown in fig. 5.4.4. For the slots backed by a coaxial cavity, the isolation is −17 dB between adjacent elements and −6 dB between opposing elements. Comparing the two slot solutions, for the solution with the slots backed by a coaxial cavity, higher coupling occurs between the opposing slots and lower coupling occurs between the adjacent slots. This is because the length to width ratio of the coaxial cavity-backed slots is larger, and coupling occurs both inside and outside the coaxial cavity. If there is good isolation between adjacent slots, and if the opposing slots are tuned and matched by using the method of section 5.4.2, good isolation between the L and R ports of the hybrid network can be achieved. For the scale model, the measured isolation was −26 dB, whereas for the existing feed, the measured isolation was only −14 dB. The isolation may be better than −26 dB because there is a 5° phase error between the adjacent antenna ports of the hybrid network.

The return loss measured at the input to the ring hybrid using the scale model is shown in fig. 5.4.5. The 8 dB return loss bandwidth is about 40 MHz. This scales down to 23 MHz at 408 MHz which is a slight improvement over the present feed. From fig. 5.4.5, the maximum return loss is 25 dB. The VSWR measured at the antenna ports with the phasing network attached (measured as shown in fig. 5.4.6) is 1.2 ± 0.1. A better VSWR at the antenna ports and a better return loss at the ring hybrid

	Probes At 408 MHz Existing Feed	Slots/Reectangular Cavity 700 MHz Scale Model	Slots/Coaxial Cavity 700 MHz Scale Model
Adjacent Elements	- 8 dB	- 12 dB	- 17 dB
Opposing Elements	- 14 dB	- 12 dB	- 6 dB
	Bad	Better	Best

Figure 5.4.4 The Measured Isolation Levels for the Existing Feed at 408 MHz and the two Scale Model, Slot Excited Feeds.

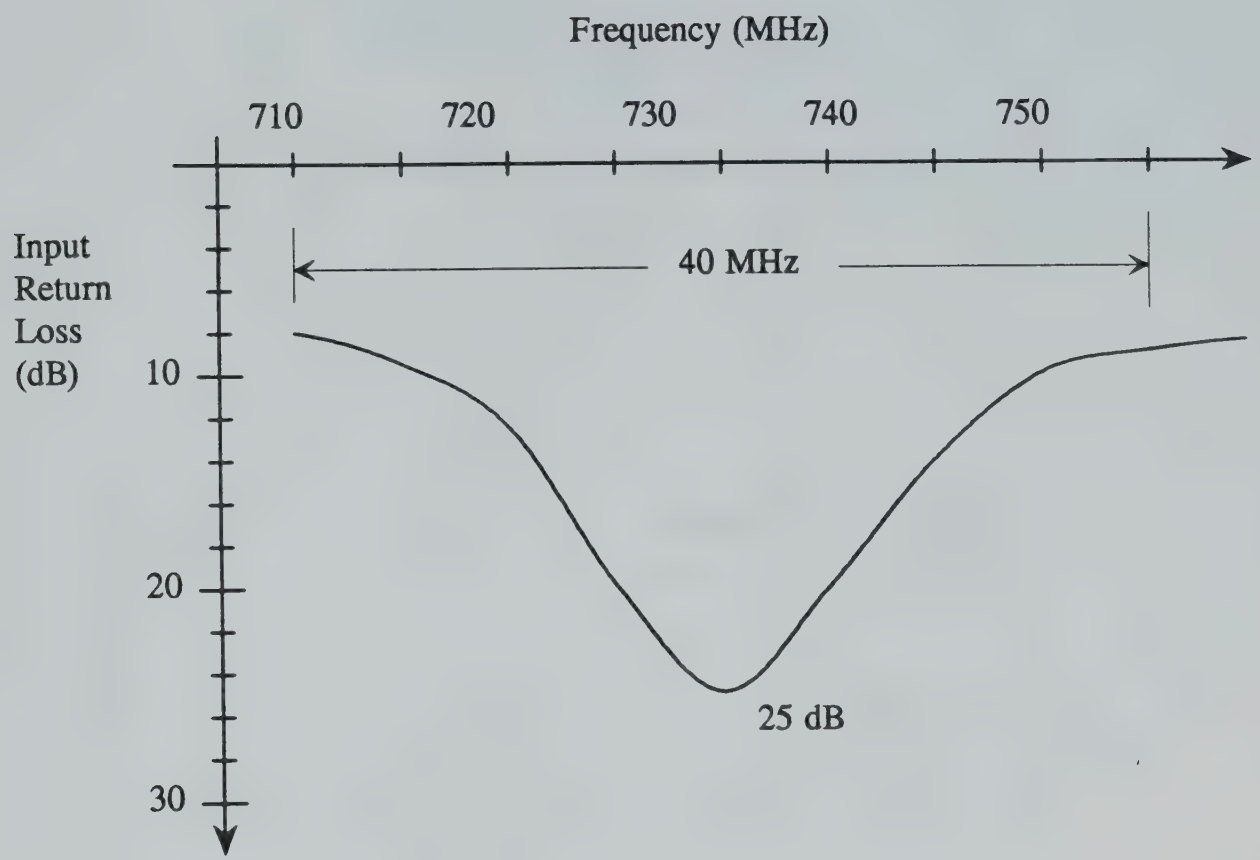

Figure 5.4.5 Return Loss Measured at the Ring Hybrid Input. The measurement was made with the HP8754A Network Analyser.

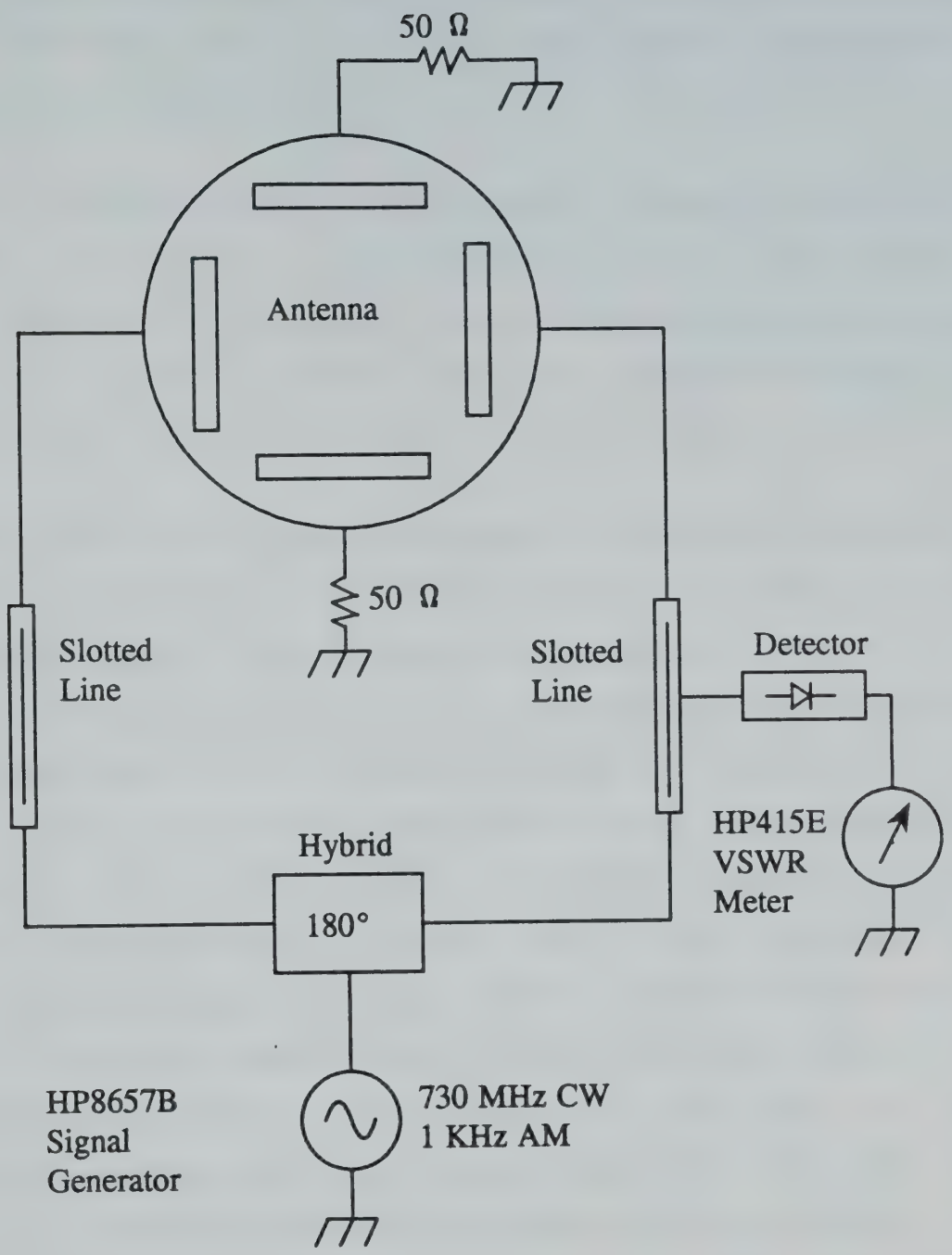

Figure 5.4.6 The VSWR Measuring System.

input can be achieved by varying the probe length and the distance between the probe and the slot. In the scale model, adjustments can only be made in the probe length.

The measured E and H plane radiation patterns for the scale model and the existing feed are shown in fig. 5.4.7. The $\pm$ 60° radiation levels are -8 dB and -9 dB for the E and H plane patterns respectively. As with the two previous solutions, there is no significant reduction in the $\pm$ 60° radiation levels with respect to the existing feed.

The polarization patterns measured on-axis for both the existing feed and the scaled slots are shown in fig. 5.4.8. For the scaled slots, the cross-polarization level is -24 dB, and the axial ratio is 1.14. For the existing feed, the cross-polarization level is -18 dB and the axial ratio is 1.30. The improvement can be explained as follows: For the scaled slots, the distance between the end of the probe and the inner conductor of the coaxial waveguide is about $1.5cm$ to $2.0cm$. In a full size version at 408 MHz, this distance would be scaled up to $3cm$ to $4cm$. In the existing feed, the distance between the end of the probe and the central waveguide ring is only $0.5cm$. The larger distance in the modified feed design results in a lower probability of obtaining a large tuning error, which means less chance of feeding the antenna ports with incorrect amplitudes and phases. For instance, for the feed modification, the change in tuning frequency, Δf, as a function of the change in probe length, Δx, is 2 MHz/mm. For the existing feed, Δf/Δx is 8.8 MHz/mm (Kim, 1988). Therefore, for a slight change in probe length, the change in the input impedance from the nominal value of 50 ohms is smaller with the feed modification than with the existing feed.

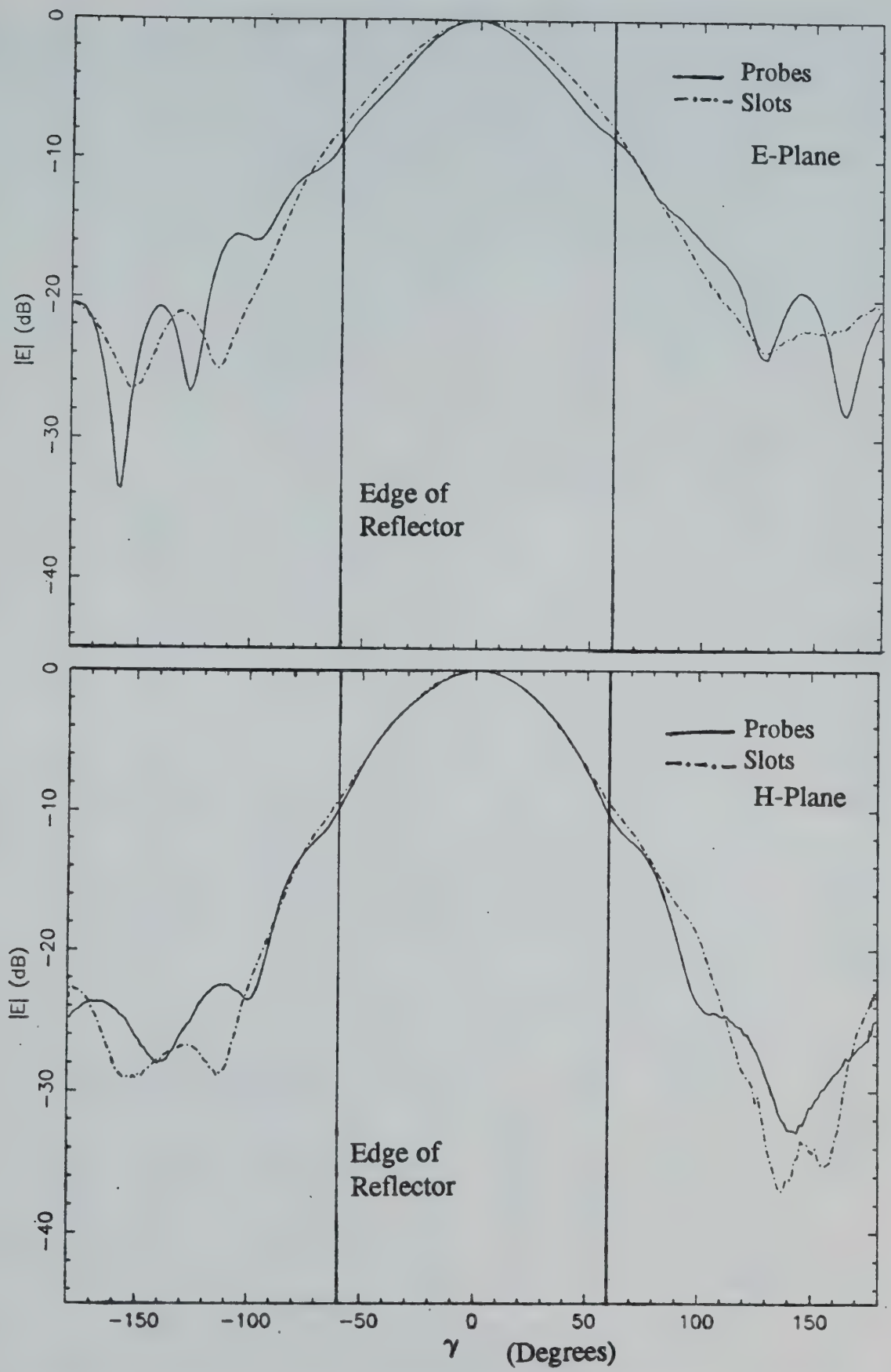

Figure 5.4.7 Measured Feed Patterns for the Scale Model Slot Excited Feed at 730 MHz and for the Existing Feed at 408 MHz.

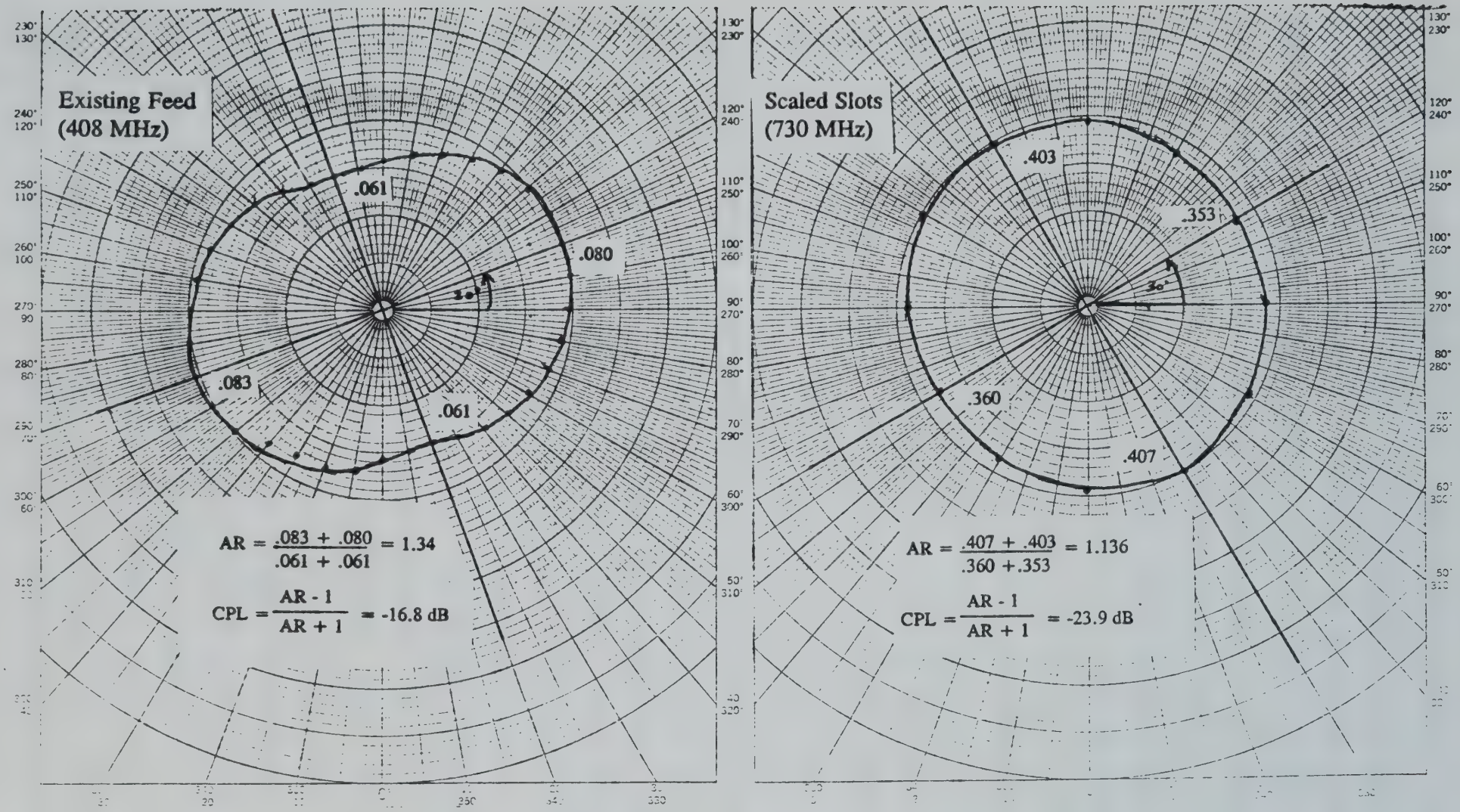

Figure 5.4.8 The Measured Polarization Pattern (on axis) of the Existing Feed and the Scaled Slots.

The cross-polarization of the coaxial cavity feed horn itself is actually lower than -24 dB. There are two sources of error that prevent the measured level from being lower. The first is the 6-port hybrid network. The measured average phase difference between adjacent ports in the hybrid network, which was used at 730 MHz, was $\approx 5^o$. From the graph in fig. 4.14, a 5^o phase error and zero amplitude error result in a cross-polarization level of about -27 dB. The second source of error is the antenna range (fig. 4.21), where the measurement was performed. To test the range, both vertically and horizontally polarized signals were transmitted and received using two dipoles. The ratio of the received vertically polarized signal to the received horizontally polarized signal was 1.10 at 730 MHz. This causes a cross polarization level of -26 dB even if there is no error in the hybrid network. The two sources of error combine to give a cross polarization level of -24 dB.

For the coaxial cavity feed horn, good isolation between the L and R ports, and low power dissipated due to the ohmic losses result in a high radiation efficiency. The power dissipated due to the ohmic losses was measured as follows. The feed aperture was covered with a metal sheet, and three antenna ports were terminated with short circuits. Therefore, no radiation leakage was possible. The return loss was measured at the unterminated port to determine the ohmic losses. For example, the power absorbed by the "covered" antenna or the power dissipated due to the ohmic losses is related to the input return loss; for example, higher ohmic losses will increase the input return loss. It should be noted that this measurement does give an accurate value of the ohmic losses. Covering the antenna with a metal sheet changes the fields behind the feed aperture and also detunes the feed. However, the return loss can still be measured over a broad bandwidth (i.e. 30 MHz) to determine if the ohmic losses in the feed modification are higher or lower than the ohmic losses in the existing feed. The return loss measured was 0.8 dB for the existing feed and 0.2 dB for the

modified feed. Therefore, the ohmic losses in the modified feed are lower. The measured isolation efficiency for the feed modification is 0.9975 (−26 dB isolation between the L and R ports of the hybrid network). The measured isolation efficiency for the existing feed is 0.962 (section 4.2). Therefore, the radiation efficiency for the feed modification is higher than that in the existing feed, and a reduction in the system temperature can thus be achieved.

5.4.4 Working at 408 MHz

Operating at 408 MHz requires increasing the dimensions of the scale model by a factor of 7/4. The metal thickness is not scaled because it was chosen to ensure the strength and rigidity of the scale model. The metal thickness will not be a factor as long as it is kept much smaller than the operating wavelength (e.g. less than $.01\lambda_o$).

The full size model can be constructed in two ways. One way is to construct it in the same way as the scale model (see fig. 5.4.1). The second method involves a spinning process like that used in constructing the present feed horn. In the two cases, the metal thickness surrounding the slots will be different, with the first method using the thicker metal; the resonant frequency of the slot also depends on the thickness of the metal surrounding the slot (Katehi, 1990).

The procedure for finding the exact slot length at 408 MHz is as follows. First, the slots are cut to the length given by the formula in section 5.4.1. Because of the metal thickness and the approximate value for the effective dielectric constant, ϵ_e, the measured resonant frequency will be higher than the desired frequency. Next, another set of slots are cut to a slightly different length, and the resulting resonant frequency is measured. The exact slot length for the desired operating frequency can then be found using the two measured points by interpolating or extrapolating. If the measured frequency is within $\pm$ 2 MHz of the desired frequency, the probe lengths can be readjusted accordingly for a reduction of approximately 5 dB in the input return loss.

5.4.5 Increasing the Bandwidth and Reducing the Probability of Tuning Errors

One of the disadvantages of this solution is the small return loss bandwidth at the input of the ring hybrid. A good match at the input requires $S_{11} = S_{13}$. However, this only occurs at one frequency. In addition, the hybrid gives $a_1' = -a_3'$ only at one frequency. Overall, this results in a bandwidth not too much better than the present probes. The bandwidth can be increased by increasing the width of the slots. This will increase the amount of radiated power and decrease the amount of stored energy in the coaxial waveguide cavity. Increasing the width of the slots, however, will affect the performance at 1420 MHz and will increase the coupling levels between adjacent slots. As shown in section 4.2, a narrow bandwidth would still mean that tuning errors are possible with slight changes in the probe lengths. Although the feed modification is better than the existing feed in terms of probe sensitivity, one way to reduce the sensitivity or the construction tolerances further would be to fix the probe lengths. This can be done by replacing the probes with a printed circuit mounted on the back of the dielectric sheet inside the coaxial cavity as shown in fig. 5.4.9. The printed circuit would consist of four copper strips in place of the four probes.

Replacing the adjustable probes by a printed circuit will reduce the chance of tuning errors. It will also reduce the chance of having unequal opposite probe lengths. As mentioned previously, unequal probe lengths cause power leakage into the unused port of the ring hybrid. The measured fraction of input power leakage as a function of the difference between the probe lengths is shown in fig. 5.4.10. This would no longer be a problem with the printed circuit.

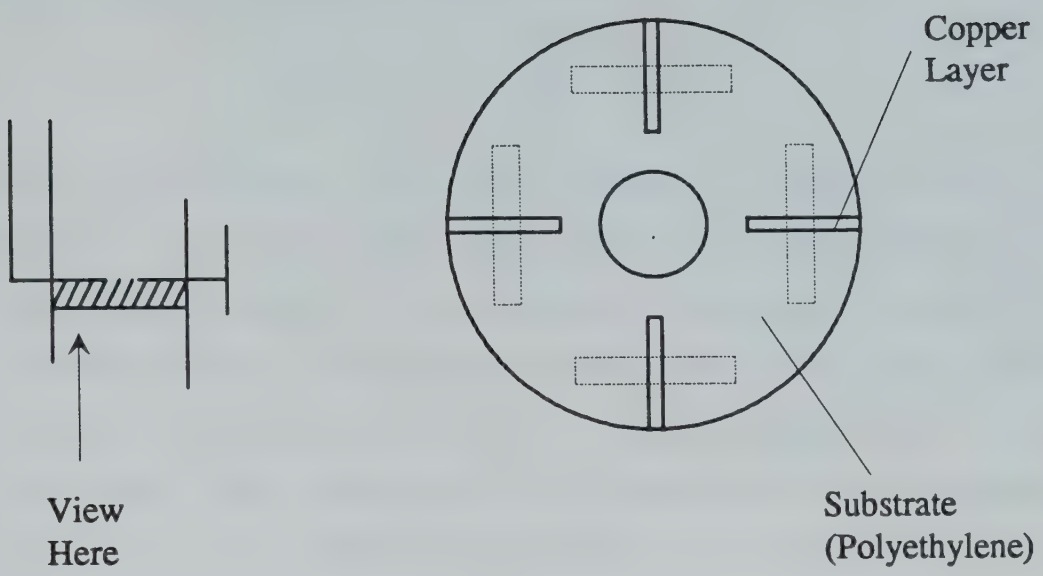

Figure 5.4.9 Replacing the Probes with a Printed Circuit.

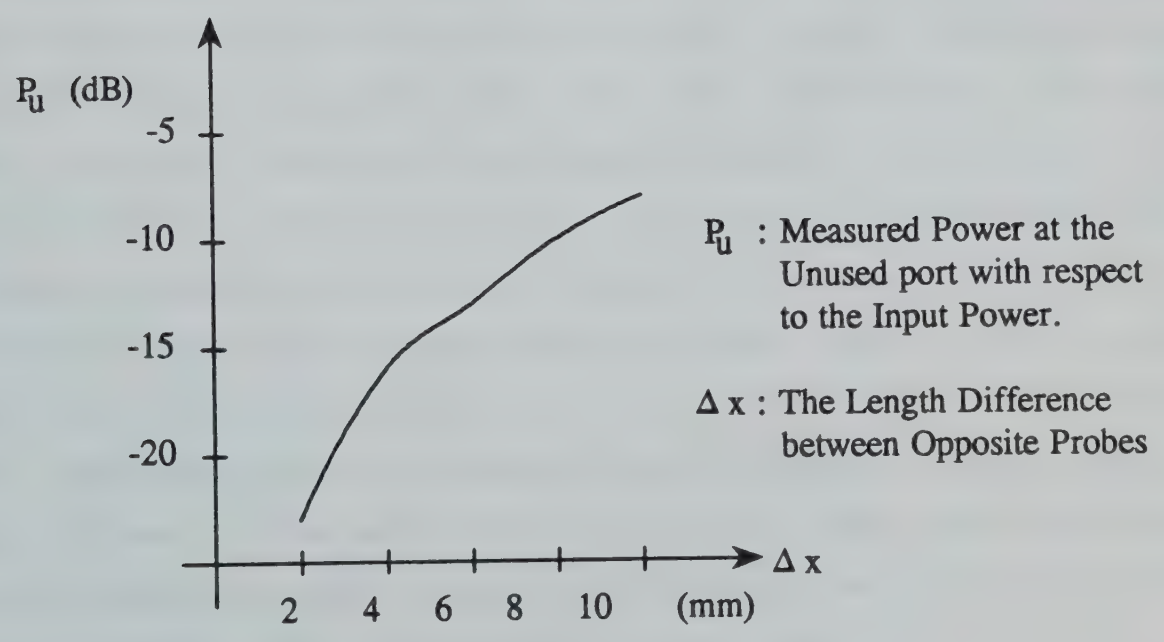

Figure 5.4.10 The Measured Isolation at the Unused Port of the Ring Hybrid versus the Length Difference between Opposite Probes.

5.4.6 Effect on 1420 MHz Performance

Another disadvantage to the slots backed by a coaxial cavity is the possible effect on the 1420 MHz performance. At 1420 MHz, the coaxial TE_{11} mode will be affected by the four slots that present an inductive reactance backed by the 22.6 cm deep coaxial cavity. The guide wavelength in the coaxial waveguide at 1420 MHz is approximately equal to the free space wavelength. The cavity depth is approximately one wavelength at 1420 MHz, and from transmission line theory, the short circuit at the end of the cavity appears as a short circuit near the aperture. The inductance at the plane of the back wall of the outer coaxial section is loaded by this small impedance, and therefore, the effect on the 1420 MHz pattern should be small.

Another way of predicting the effect on the 1420 MHz performance is by noting the slot orientation with respect to the 1420 MHz surface currents flowing on the back wall of the outer coaxial section. From fig. 5.4.11, one pair of slots runs approximately parallel to the direction of the surface currents. This pair will have little effect on the 1420 MHz performance because the slots do not interrupt the surface currents and also because the slots are in a region where the surface current density is small. The other pair of slots, however, cuts across the direction of the current flow. This pair is also in a region where the surface current density is large. However, if the slot width is kept much smaller than the operating wavelength, the effect on the 1420 MHz performance should be small. The slot width is 2cm, which is $0.1\lambda_o$ at 1420 MHz.

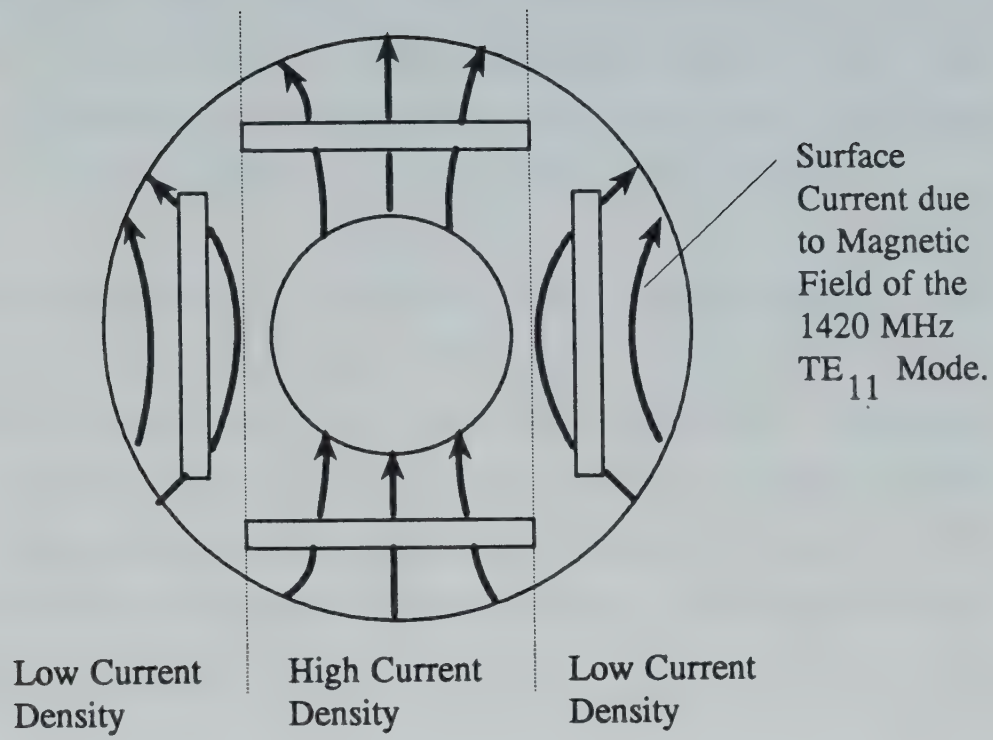
Surface Current due to Magnetic Field of the 1420 MHz TE_{11} Mode.
Low Current Density
High Current Density
Low Current Density

(From N.Marcuvitz, 1951)

Figure 5.4.11 Slot Orientation and 1420 MHz Surface Currents flowing on the back wall of the outer coaxial section.

The scale model does not include the scaled version of the 1420 MHz feed, and therefore, the direct effect on the 1420 MHz pattern could not be measured; the high frequency in the scale model would be 1420 MHz $\times$ (700/408) or 2.436 GHz. Instead, the following measurement was done to determine the probable effect on the 1420 MHz performance.

A signal was transmitted at 2.436 GHz and received through a low frequency port of the scale model; the other three ports were left unterminated. The power level at the receiving end was compared to the power level received using the same antenna as the one used at the transmitting end. The measurement was repeated using the existing feed in which the high frequency was 1420 MHz. The high frequency antennas were well matched E-plane rectangular horns. The results are summarized in fig. 5.4.12.

In the existing feed, it has been shown that the 408 MHz probes have minimal effect on the 1420 MHz performance (Veidt, 1984), yet from the figure, the power received at the 408 MHz port when transmitting a 1420 MHz signal is only 9 dB lower than the power level received using a 1420 MHz antenna. In the scale model, the power level received at the low frequency port when transmitting at 2.436 GHz is 16 dB lower than the power level received using a 2.436 GHz antenna. Since the power received through the low frequency port when transmitting at the high frequency is lower for the slots than it is for the probes, the effect of the slots on the 1420 MHz performance would probably be minimal.

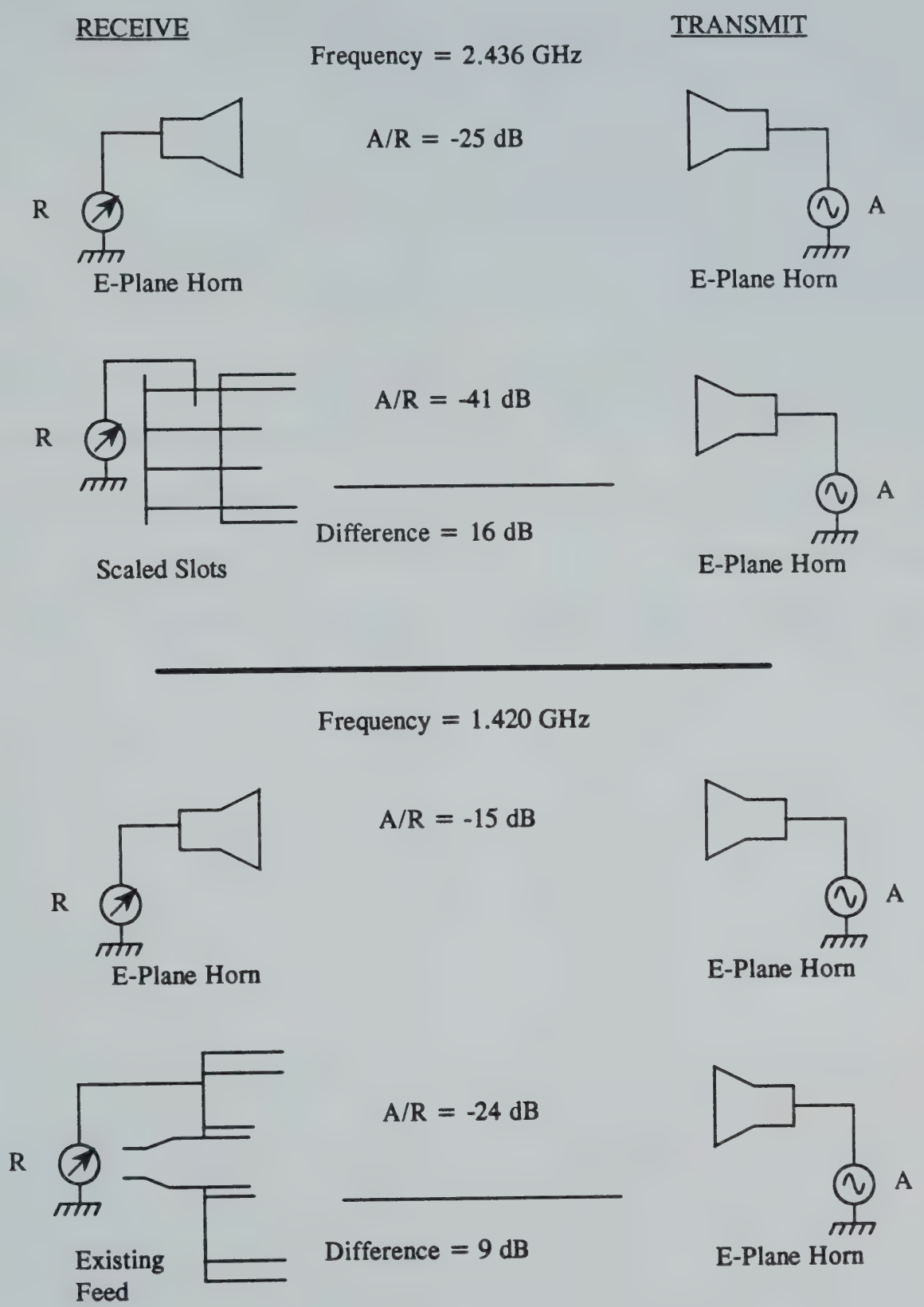

Figure 5.4.12 Measuring the Effect on the 1420 MHz Performance.

Plate 3

These photographs show the feed modifications that were built in an attempt to improve the performance of the existing feed at 408 MHz. The first row from left to right shows the top view and the side view of the annular slot modification. The second row shows the rectangular slot modification in which each of the four slots is backed by a rectangular cavity filled with dielectric. The third row shows another rectangular slot modification, but the slots are backed by a common coaxial waveguide cavity.

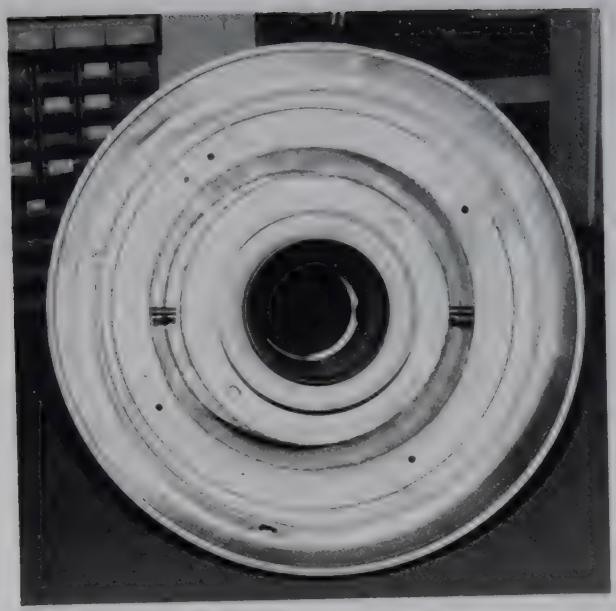

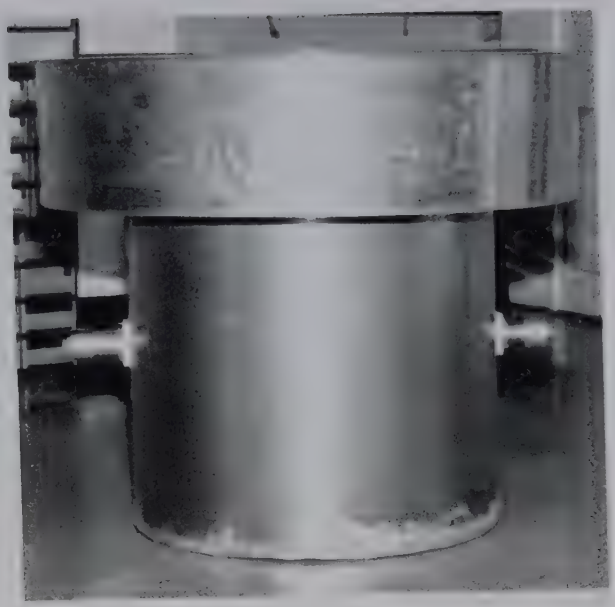

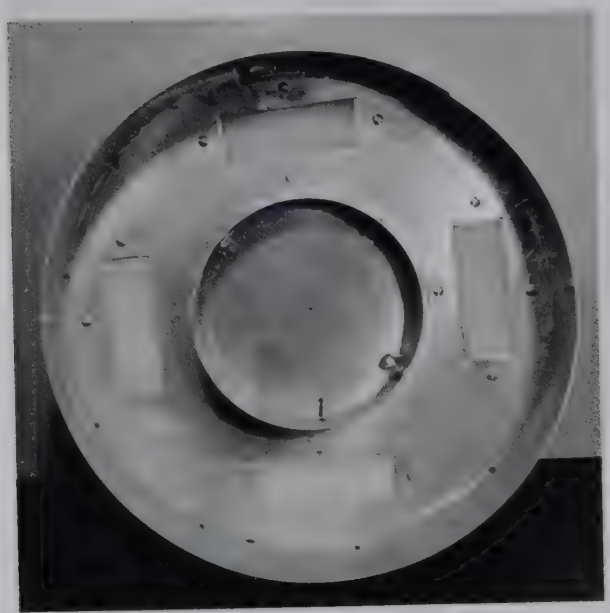

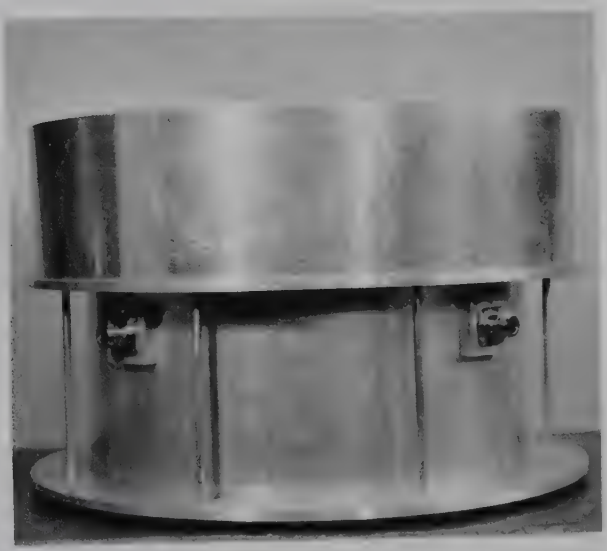

5.5 Sharpening the Primary Beam at 408 MHz

Reducing the sidelobes in the secondary pattern at 408 MHz requires a sharper main beam in the feed pattern. This is necessary to reduce the spillover and the high edge illumination. The results from the previous sections show that it was not possible to reduce the $\pm$ 60^o radiation levels significantly. Therefore, other attempts were made by simulating feed modifications using the Multi-Body Electromagnetic Scattering (MBES) software program, which was developed at the University of Manitoba. The program uses a numerical procedure known as the Method of Moments (Harrington, 1968). The Method of Moments will be explained before presenting the results of the simulations.

5.5.1 Method of Moments

The Method of Moments is a numerical procedure that facilitates solving for the unknown current distribution over the conducting body under consideration.

First, an integral equation is derived. A known source excitation near the body impresses an electric field, $\mathbf{E}^i_{tan}$, tangential to the body. The resulting currents, $\mathbf{J}$, that flow in the body produce an identical tangential scattered field, $\mathbf{E}^s_{tan}$, with opposite polarization to the impressed field. This satisfies the boundary condition. The total electric field at any point in space is the sum of the scattered field and the excitation field. Referring to figure 5.5.1, the integral equation is

$$\mathbf{E}^i_{tan} = -\mathbf{E}^s_{tan} = jw\mathbf{A} + \nabla\Phi,$$

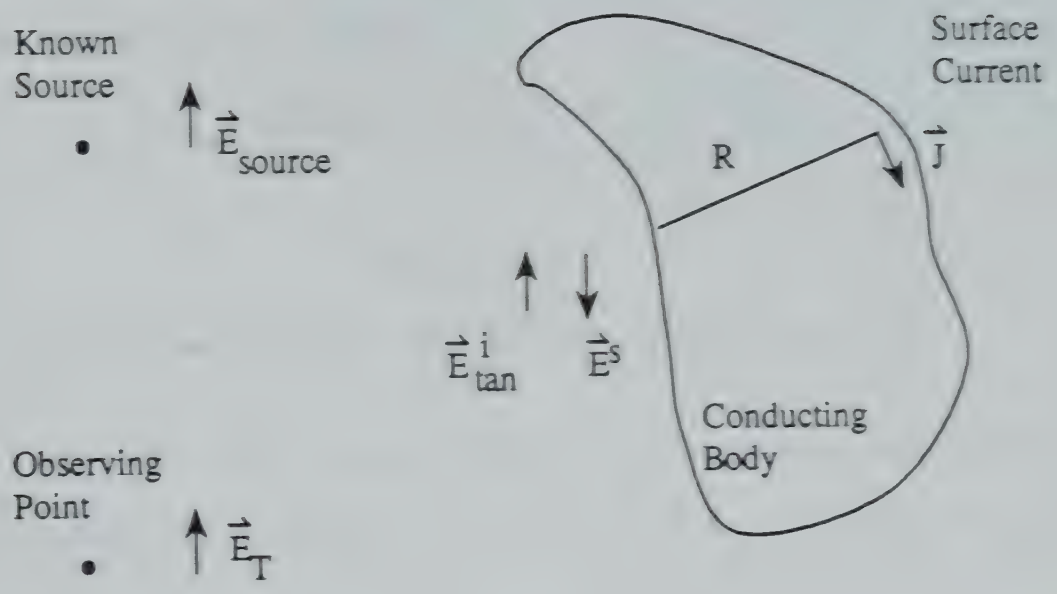

$\vec{E}^{i}_{tan}$: Due to Known Source

$\vec{E}^{s}$: Due to Surface Current

$\vec{E}_T$: Due to $\vec{E}^{s}$ and $\vec{E}_{source}$

Figure 5.5.1 Geometry for Deriving the Integral Equation.

where $\mathbf{A}$ and Φ are the magnetic vector potential and electric scalar potential respectively and are defined as follows:

$$\mathbf{A} = \mu \oiint_S \mathbf{J} \frac{e^{-jkR}}{4\pi R} ds,$$

$$\Phi = \frac{-1}{jw\epsilon} \oiint_S (\nabla \cdot \mathbf{J}) \frac{e^{-jkR}}{4\pi R} ds.$$

The integral equation then reduces to

$$\mathbf{E}^i_{tan} = \oiint_S [jw\mu\mathbf{J} + \frac{j}{\omega\epsilon} \nabla(\nabla \cdot \mathbf{J})] \frac{e^{-jkR}}{4\pi R} ds,$$

or

$$\mathbf{E}^i_{tan} = L(\mathbf{J}),$$

where L is the linear operator that operates on the current $\mathbf{J}$.

The conducting body is then divided into N segments, and by assuming an unknown current distribution of $\mathbf{J} = \sum_{n=1}^{N} I_n \mathbf{J}_n$, the integral equation reduces to

$$\sum_{n=1}^{N} I_n L(\mathbf{J_n}) = \mathbf{E}^i_{tan},$$

where (I_1, I_2,...,I_N) are the unknown current coefficients, and $\mathbf{J}_n$ is the basis function. The basis function is localized to one or two segments, depending on the type of function. The operation, L($\mathbf{J}_n$), still involves a differentiation-integration process, but the process is simplified by operating on a basis function.

The integral equation contains N unknowns, and therefore, a set of testing functions, ($\mathbf{W}_1$, $\mathbf{W}_2$,..., $\mathbf{W}_N$), are introduced to enforce the boundary condition, ($\mathbf{E}^s_{tan}$ + $\mathbf{E}^i_{tan}$) = 0, at N discrete points. The boundary condition at each point is satisfied by forming the inner product between the testing function and both sides of the integral equation at each point. The equation then reduces to

$$\sum_{n=1}^{N} I_n < \mathbf{W}_m, L(\mathbf{J}_n) > = < \mathbf{W}_m, \mathbf{E}^i_{tan} >, \qquad \text{where m=1, 2,..., } N,$$

and where the inner product is defined as follows:

$$< \mathbf{a}, \mathbf{b} >= \oint_S (\mathbf{a} \cdot \mathbf{b}) ds.$$

If the testing function is the Dirac delta function, then

$$\sum_{n=1}^{N} I_n L(\mathbf{J}_n)_m = \mathbf{E}^i_{tan}|_m, \qquad \text{where m=1, 2,..., } N.$$

Since there are now N unknowns and N equations, the unknown current coefficients can be determined using matrix methods.

Inaccuracy of the moment method occurs when the boundary condition is satisfied only at N discrete points and not continuously across the surface. If the testing function is the delta function, $\mathbf{E}_{tan} = 0$ at N points and $\mathbf{E}_{tan} = \mathbf{E}^s_{tan}$ = residual $\neq 0$ at other points. To minimize the residuals, the number of segments must be increased, or another testing function that is a bit more continuous than the delta function must be used. Therefore, increasing the accuracy involves more computation time because more segments are used or because a more complex testing function is used in the evaluation of the inner product.

Once the current coefficients are known, the total electric field can be evaluated as the sum of the scattered field due to the currents flowing over the body and the field due to the source excitation.

5.5.2 Software Simulations

The aim of the simulations was to test modifications which might narrow the beam of the feed at 408 MHz. The feed pattern was also calculated at 1420 MHz to see if there was any effect on the original 1420 MHz feed pattern. The cross-sectional shape of the feed horn is shown in fig. 5.5.2. The additions are shown by the dotted lines. Four different modifications are shown and are labelled as the "0° flange", "45° flange", "90° flange", and "extra ring". At 408 MHz, the feed radiation levels at ± 60° for the E and H planes were computed and compared to the levels using the feed without the modifications. The results are shown in fig. 5.5.2.

From the table, adding the "90° flange" sharpens the H plane beam but broadens the E plane beam. Because the modification causes considerable aperture blockage, it will not be considered further.

Adding the "45° flange" results in a conical horn. Even though the dimensions are not optimized for maximum directivity, a slight narrowing of the beam is still evident. At ± 60°, there is a 1.5 dB reduction in the H-plane and a 0.6 dB reduction in the E-plane. The narrowing of the beam is due to the size increase in the radiating aperture. The price paid for implementing this modification is three-fold. First, as shown in fig. 5.5.3a), the E and H plane patterns at 1420 MHz are no longer equal in the main beam. Some regions in the inner part of the reflector are illuminated at higher levels than other regions, reducing the aperture efficiency. Second, the 408 MHz phase-center has shifted toward the reflector surface because the plane of the feed aperture has shifted toward the reflector surface. Since the 1420 MHz phase-center is fixed at the focus of the paraboloid, more defocussing will occur at 408 MHz with this modification than with the existing feed. As a result, there will be a slight increase in

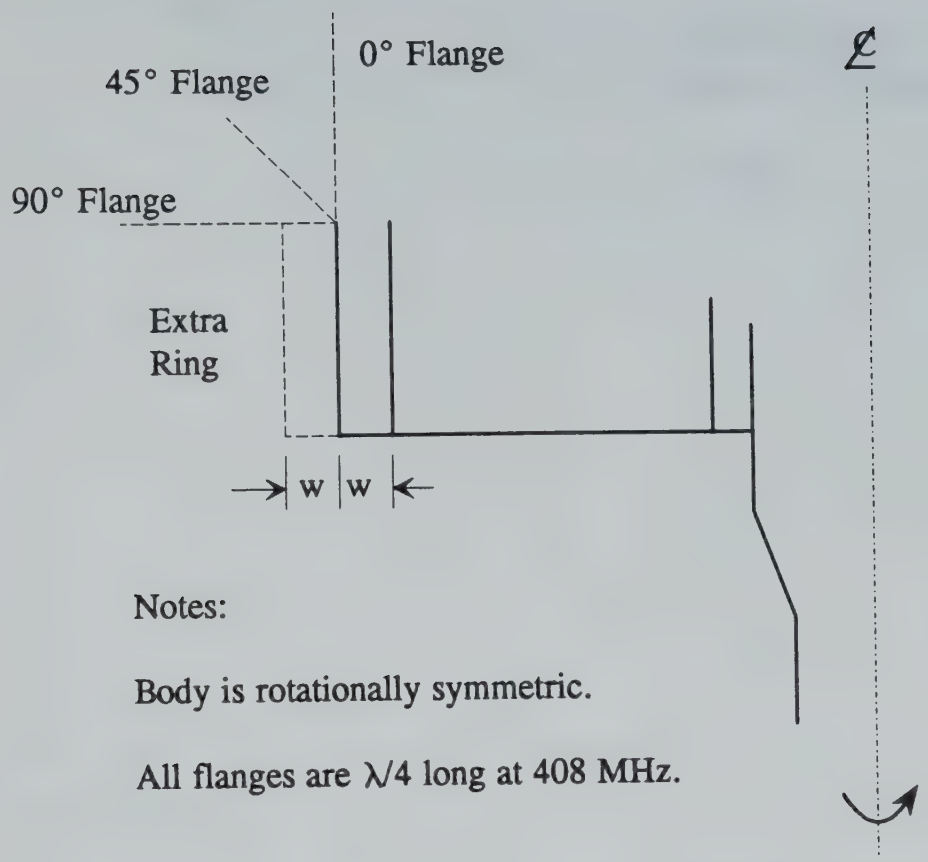

Design Modification	Reduction of the 60° Radiation Levels (dB)		Backlobe Level (dB)
	E-Plane	H-Plane	Reduction
0° Flange	1.1	0.9	2.7
45° Flange	0.6	1.5	4.3
90° Flange	-0.9	1.2	0.4
Extra Ring	0.7	0.9	12.6

Figure 5.5.2 Possible Feed Modifications and Predicted Results of the Modifications at 408 MHz.

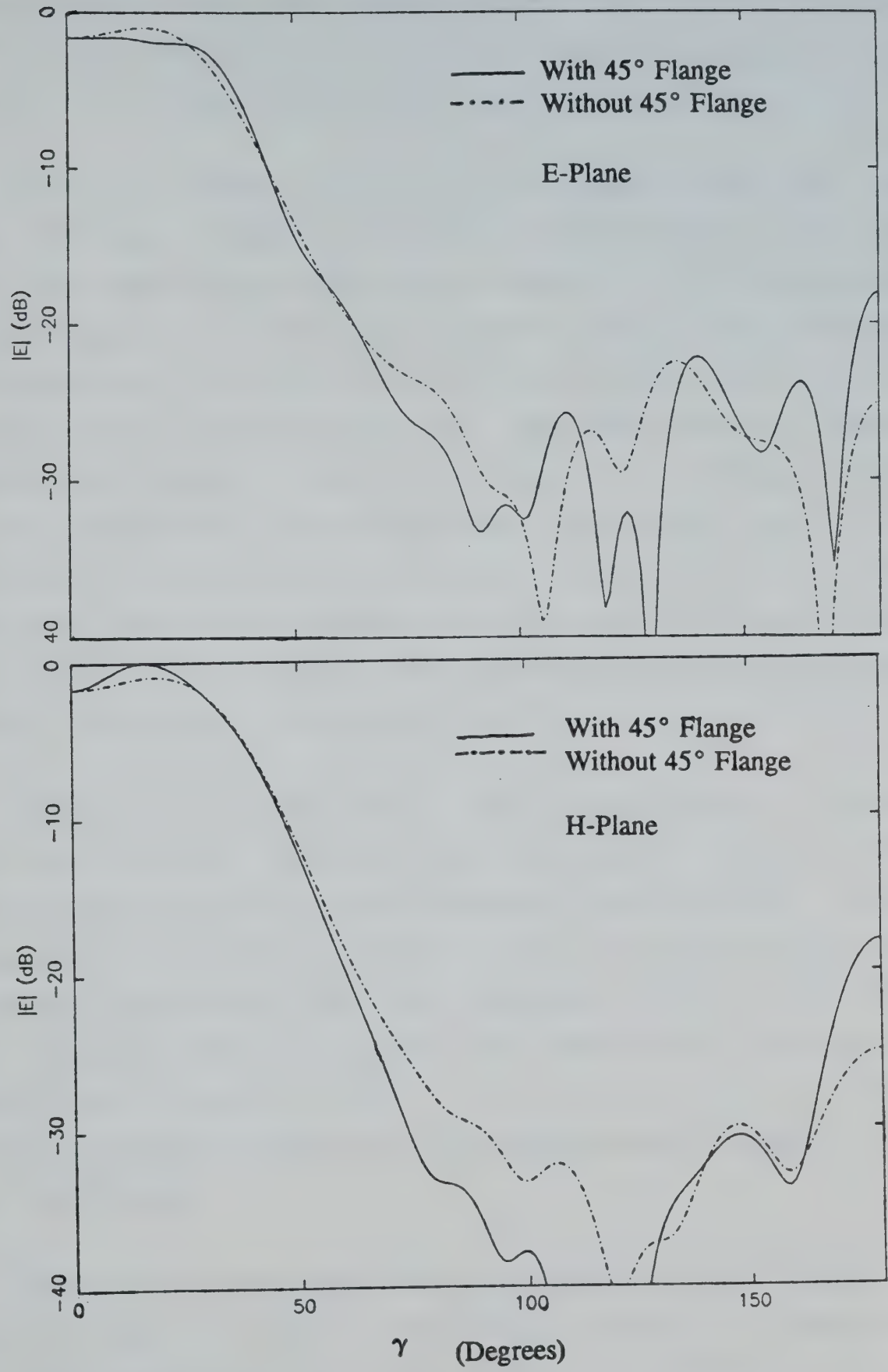

Figure 5.5.3(a) Predicted Effects on the 1420 MHz Feed Pattern due to the "45° Flange" shown in figure 5.5.2.

the first sidelobe level in the reflector pattern. Third, the size increase in the radiating aperture results in more aperture blockage, although it is not as bad as the blockage with the "90° flange" modification.

Adding the "0° flange" is the same as extending the outer choke. Here again, the beam is slightly narrower in both planes. This is evident from the 1 dB reduction in the feed radiation levels at ± 60°. The directivity increases slightly because effectively, a shroud is placed around the probes. The effects on the 1420 MHz pattern are shown in fig. 5.5.3b). First, the tapering and the roll-off occur too early. Again, this reduces the aperture efficiency and increases the effective percentage aperture blockage. Second, the feed sidelobes are higher at 1420 MHz. For example, there is a 10 dB increase in the backlobe level as well as a general increase in the sidelobe level. Third, the defocussing effect at 408 MHz will be greater than the effect with the "45° flange" modification because the plane of the feed aperture will be closer to the reflector surface.

Adding the "extra ring" results in the best performance at both 408 MHz and 1420 MHz. The second outer choke reduces the outer surface currents further, reducing the feed sidelobes at both frequencies. The feed radiation levels at ± 60° are reduced by 0.8 dB, and the backlobe level is reduced by 12.6 dB at 408 MHz. From fig. 5.5.3c), the 1420 MHz main beam is not affected, the general feed sidelobe level is lower, and the backlobe level is reduced by about 5 dB. The only drawback is the slight increase in aperture blockage, but the blockage is small compared to the other modifications.

Of the three modifications, the "45° flange" and the "0° flange" violate the physical or design constraints set in section 4.3. Consequently, these two modifications have drastic effects on the performance at 1420 MHz with very little improvement in the ± 60° radiation levels at 408

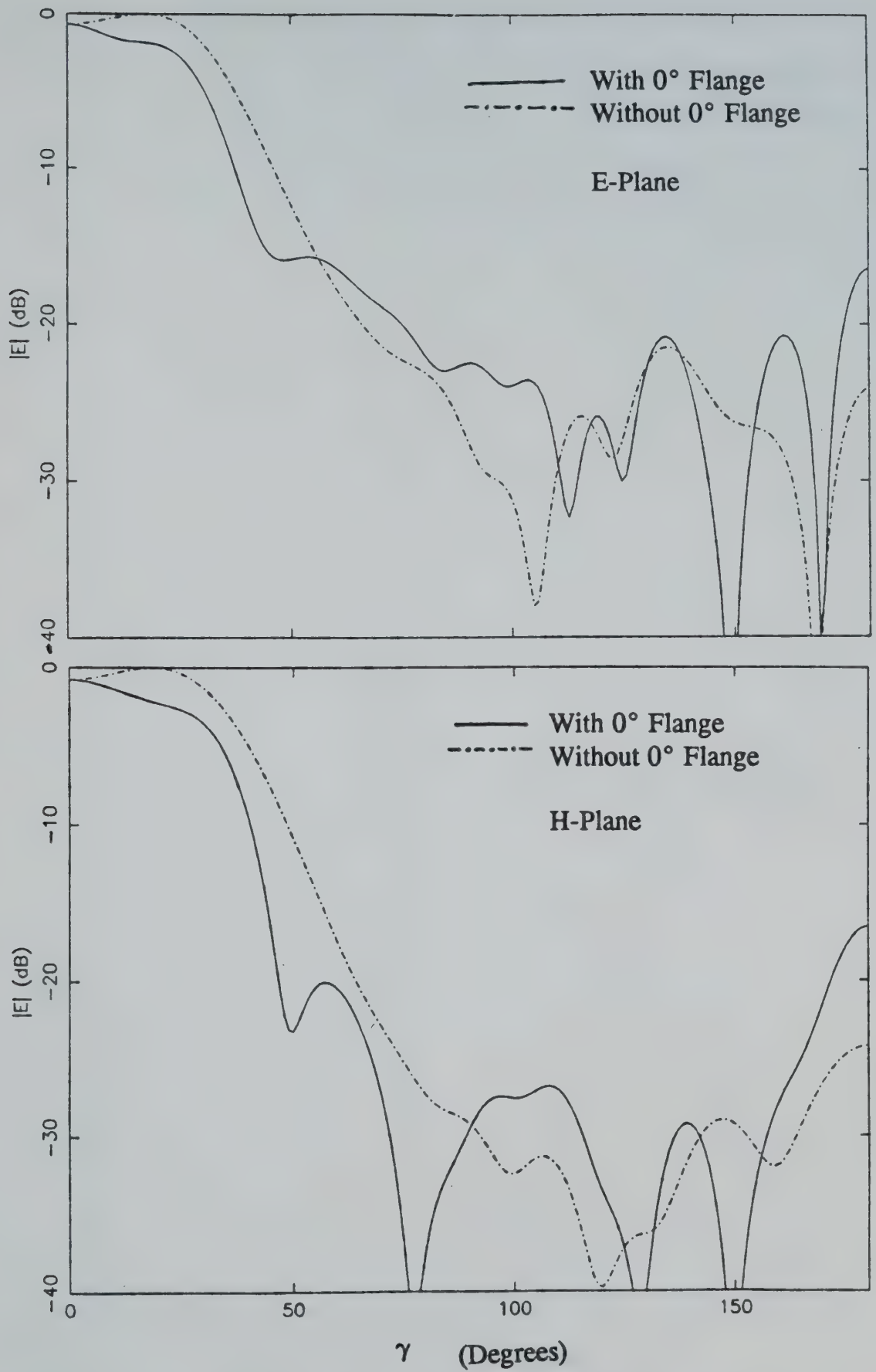

Figure 5.5.3(b) Predicted Effects on the 1420 MHz Feed Pattern due to the "0° Flange" shown in figure 5.5.2.

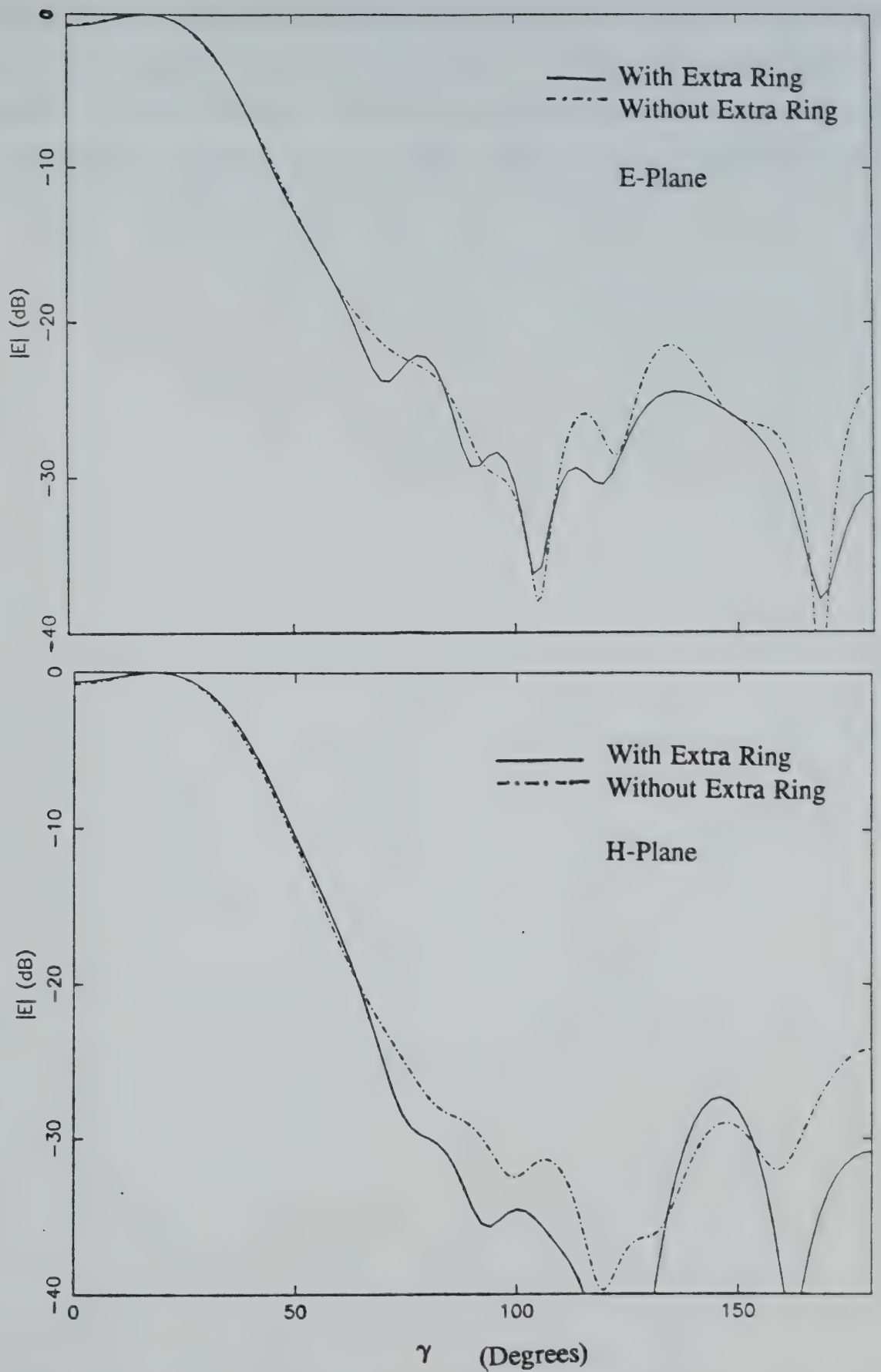

Figure 5.5.3(c) Predicted Effects on the 1420 MHz Feed Pattern due to the "Extra Ring" shown in figure 5.5.2.

MHz. On the other hand, adding the extra ring or extra choke does not violate the physical constraints and does not affect the 1420 MHz performance. The feed patterns at both frequencies have improved, but there is no significant reduction in the $\pm$ 60° radiation levels at 408 MHz because the critical dimensions of the feed remain the same.

5.6 The Middle Ground Option

It is worthwhile considering a possible design to achieve a narrow beam in the feed patterns at the expense of full optimization at 408 MHz or 1420 MHz. Full optimization requires a $2J_1(x)/x$ field distribution in the feed aperture. (See section 4.1 for the definition of x). At present, the feed is optimized at 1420 MHz. To increase the aperture efficiency and to reduce the spillover further, an extra ring can be added at the expense of some aperture blockage. Specifically, adding a third ring to approximate the $2J_1(x)/x$ function up to and including the second lobe at 1420 MHz would increase the feed diameter from 54 cm to 76 cm (ignoring the outer choke), and the aperture blockage would increase from 0.4 % to 0.7 %. This is illustrated in fig. 5.6.1. If the feed is optimized at 408 MHz, the feed diameter would increase to 1.9 m, and the aperture blockage would increase to 4.3 %. The diameter of the feeding circular waveguide would be 46 cm, and the feed legs would have to be changed to support the larger feed size. Therefore, optimizing only at 408 MHz is impractical for the reflector size in question.

However, it may be possible to achieve some middle ground at the expense of some aperture blockage and a slight degradation in the performance at 1420 MHz. This involves adding a third ring. The radius of the ring would be in the range from 38 cm to 51 cm. The smaller radius is chosen to be the radius of the third ring in the full 1420 MHz optimization. The larger radius is chosen to be the radius of the first ring in the full 408 MHz optimization. From figure 5.6.1, locating the third ring in the middle ground option at 45 cm is a suitable compromise. The edge illumination at 408 MHz and 1420 MHz for the "middle gound" option can be predicted by first assuming that a $2J_1(x)/x$ field distribution exists in the feed aperture at both frequencies and then taking the Fourier transform of the field

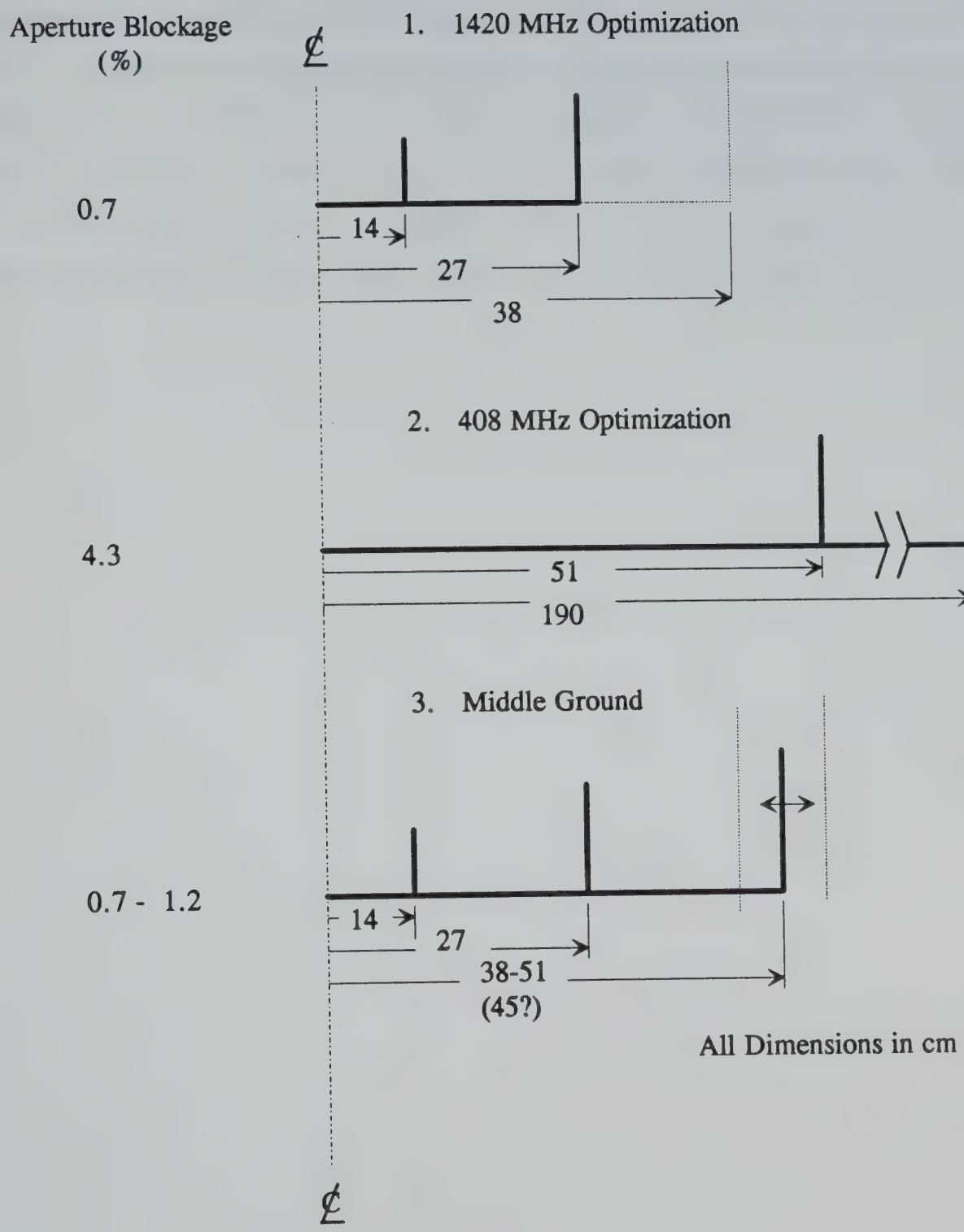

Figure 5.6.1 The Middle Ground Solution.

distribution to get the feed pattern. The edge illumination and the aperture blockage as a function of the radius of the third ring are shown in fig. 5.6.2. As shown in the figure, the aperture blockage increases from the existing 0.4 % to 1.0 %, and the edge illumination at 408 MHz decreases from the existing −9 dB to −12 dB. The increased aperture blockage may be a small price to pay for the reduced system temperature because of the reduced spillover and edge illumination at both 408 MHz and 1420 MHz.

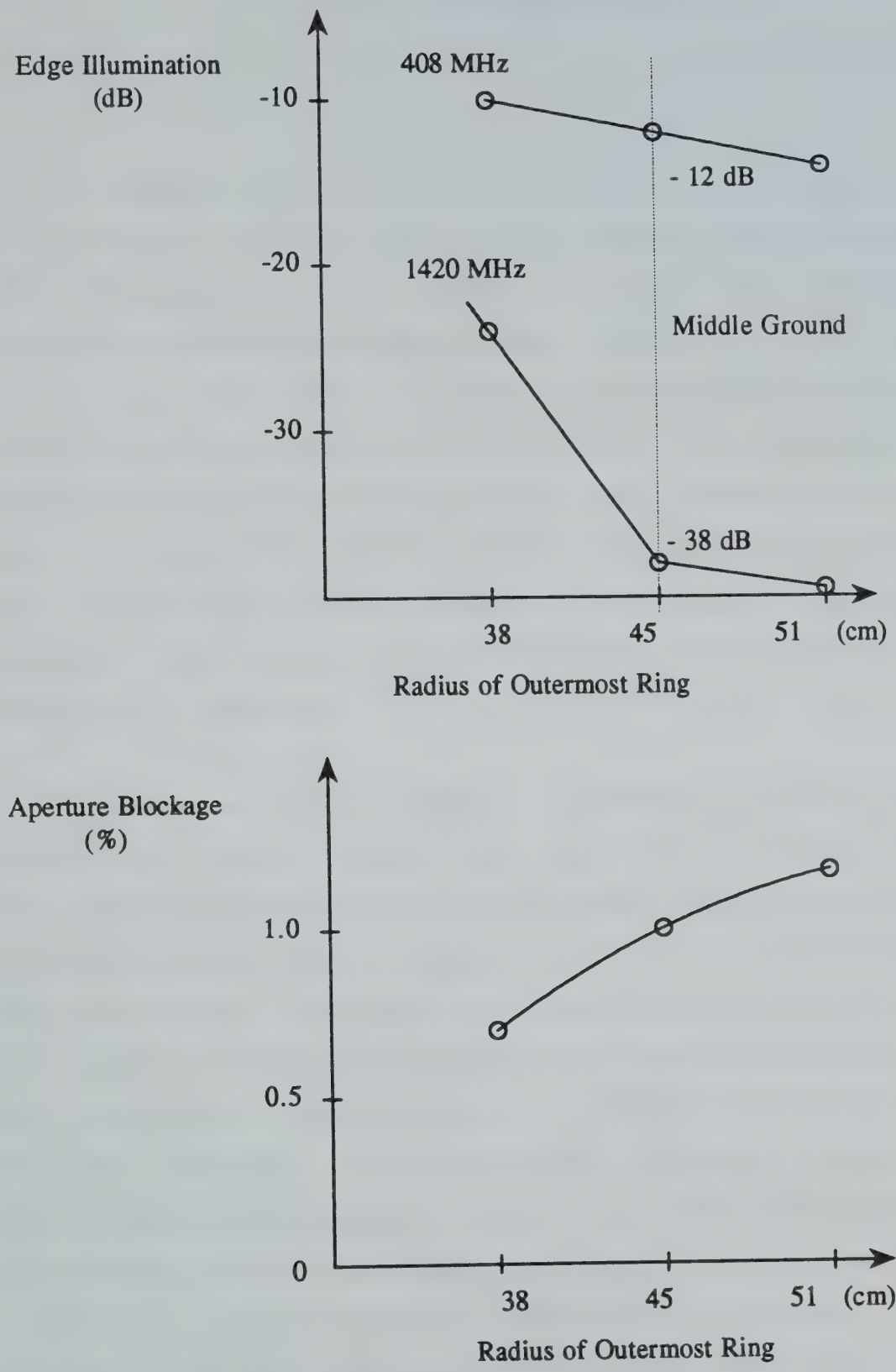

Figure 5.6.2 The Predicted Edge Illumination and Aperture Blockage for the Larger Feed.

6. CONCLUSIONS

The radiation pattern of the 9m paraboloid in the Synthesis Telescope was measured to establish the magnitude of the sidelobe problem at 408 MHz. Measuring the pattern required a suitable antenna range, transmitter, receiver, and a data logging system. Chapter 2 described the major components in detail. The transmitter was remotely activated from a control building located near the receiving antenna. The transmitter supplied enough power for the necessary dynamic range required for the measurement. The power level and the antenna position were logged into a computer at the control building as the receiving antenna was steered. After further computer processing, a 408 MHz radiation pattern of the 9m paraboloid was obtained.

The measured radiation pattern was presented in chapter 3. The measured pattern was in reasonable agreement with the software prediction. The disagreements were due to various effects not taken into account in the software such as surface roughness and scattering of direct feed radiation by the struts. The antenna solid angle calculated from the measured data agreed with the antenna solid angle calculated from other sources, such as the CAS A radio source and the NEC−REF software, to within 8 %. The discrepancy is satisfactory because half of the measured pattern was estimated when calculating the solid angle from the measured data. The measured pattern at 408 MHz was compared to the measured pattern at 1420 MHz, and the comparison showed that the sidelobes at 408 MHz were much higher than the sidelobes at 1420 MHz. One way to reduce the sidelobes was to narrow the beam in the feed pattern at 408 MHz.

In chapter 5, feed modifications were implemented in an attempt to narrow the beam of the feed at 408 MHz. The four solutions in sections 5.1 to 5.4 show that the broad beam in the feed pattern at 408 MHz cannot be narrowed by replacing the probes with other exciting elements. The feed modifications simulated using the MBES software program in section 5.5 show that the beam could not be narrowed without violating the physical constraints set in section 4.4. Therefore, the only way to reduce the sidelobe levels in the reflector pattern at 408 MHz is to remove the physical constraints and compromise the ideal performance at 1420 MHz.

By optimizing the feed at 1420 MHz, other feed problems were created at 408 MHz. Most of the problems were solved by one of the four solutions in sections 5.1 to 5.4. Figure 6.01 summarizes the measured electrical characteristics for each solution. If some parameters of a particular solution were not measured, the solution was rejected because of the performance of the other parameters.

Three solutions were rejected. From the table, the microstrip solution was rejected because it was difficult to attain the necessary bandwidth without making the patch too thick. Also, the spurious radiation of the fringing fields from the sides with opposite polarization would have degraded the feed polarization performance and would have increased the coupling between the adjacent elements. The annular slot solution had good radiation characteristics such as similar E and H plane patterns, but was rejected because it was difficult to match the probes in the thin waveguide to 50 ohm coaxial cable. Matching would have been possible if the annular slot was wider, but poor isolation between the adjacent probes would have existed. The solution with the rectangular slots backed by cavities filled with dielectric was rejected because of the narrow bandwidth, the cost of the dielectric material, and the predicted effect on the 1420 MHz performance. The rectangular slots backed by a coaxial cavity was the best solution. It was chosen because it exceeded most of the electrical characteristics

Electrical Specification	Probes	Microstrip	Annular Slot	Rectangular Slots Rectangular Cavity	Rectangular Slots Coaxial Cavity
1.) Input Return Loss (dB)	30	-	3	25	25
2.) 6 dB Return Loss Bandwidth (MHz)	20	15	-	17	23
3.) Isolation Levels (dB)					
Adjacent Ports	- 8	-	-	- 12	- 17
Opposing Ports	- 14	-	-	- 12	- 6
L - R Ports	- 14	-	-	-	- 26
4.) Cross Polarization Level (dB)	- 17.6	High because of fringing fields	-	-	- 24
Axial Ratio	1.30	-	-	-	1.15
5.) $\pm$ 60° Radiation Levels (dB)					
E - Plane	- 9	-	- 10	- 10 (without outer	- 8
H - Plane	- 10	-	- 9	- 8 choke)	- 9
6.) Cost	low	depends on substrate	low	high because of ϵ_r - 9 material	low
7.) Radiation Efficiency (%)	low	-	-	-	high
8.) Effect on 1420 MHz Performance	minimal	depends on patch thickness	minimal	large; cavities support large number of modes at 1420.	probably minimal

Figure 6.01 Comparison of the Feed Modifications discussed in Sections 5.1 - 5.4.

of the existing feed. Compared to the existing feed, the isolation between adjacent elements of the antenna and the isolation between the L and R ports of the hybrid network are better, the cross polarization is lower, and the radiation efficiency is higher. The effect on the 1420 MHz performance is probably minimal.

Replacing the present feed with the new solution does not solve the sidelobe problem at 408 MHz. The beam in the feed pattern is still broad and high spillover and high edge illumination still exist. The desired reduction in the system temperature is not achieved by reducing the reflector sidelobes but is achieved by the higher radiation efficiency. Therefore, the new feed represents an improvement.

References

Adler, R., 1946, "A Study of Locking Phenomena In Oscillators", Proc. IRE., Vol 34, pp. 351–357.

Anderson, M.D., Landecker, T.L., Vaneldik, J.F., Routledge, D., 1991 "The Far Sidelobes and Noise Temperature of a Small Paraboloidal Antenna Used for Radio Astronomy", Radio Science, in press.

Anderson, M.D., 1990, "Reducing Antenna Noise in a Synthesis Telescope and An Observation of an HII Region", M.Sc. Thesis, University of Alberta, Edmonton.

Anderson, M.D., 1987, D.R.A.O. Application Software.

ARRL, 1988, "The ARRL Antenna Book", 15th Ed., Newington, Conn.

Balanis, C.A., 1982, "Antenna Theory Analysis and Design", Harper and Row, New York.

Booker, H.G., 1946, "Slot Aerials and their relation to Complementary Wire Aerials", JIEE (Lond.), pt IIIA, no. 4, p. 93.

Bracewell, R.N., Thompson, A.R., 1973, "The Main Beam and Ringlobes of an East-West Rotation Synthesis Array", Astrophysical Journal, Ap. J. 182, p. 77.

Christiansen, W.N., Högbom, J.A., 1985, "Radio Telescopes", 2nd. Ed., Cambridge University Press, Cambridge.

Chew, W.C., 1982, "A Broad–Band Annular–Ring Microstrip Antenna", IEEE Trans. Antennas and Propagation, AP–30, pp.918–922.

Fomalont, E.B., Wright, M.C.H., 1984, "Interferometry and Aperture Synthesis", Galactic and Extra–Galactic Radio Astronomy, Verschuur, G.L., Kellermann, K.I. (eds.), Springer–Verlag, New York, Ch. 10.

Gardiol, F.E., 1984, "Introduction to Microwaves", Artech–House, Dedham, MA.

Harrington, R.F., 1968, "Field Computation by Moment Methods", Robert E. Kreiger Publishing Company, Malabar, Florida.

Hewlett–Packard Application Note 920, "Harmonic Generation Using Step Recovery Diodes and SRD Modules".

Higgs, L.A., 1987, D.R.A.O. Application Software.

Hirokawa, J., Arai, H., Goto, N., 1989, "Cavity–backed Wide Slot Antenna", IEE Proc., Vol. 136, Pt. H, No. 1, pp. 29-33.

Howell, J.Q., 1975, "Microstrip Antennas", IEEE Trans. Ant. and Prop., AP-23, pp. 90-93.

James, J.R., Hall, P.S., Wood, C., 1986, "Microstrip Antenna Theory and Design", IEE Electromagnetic Wave Series 12, Peter Penguins Ltd., London, U.K.

Jull, E.V., 1981, "Aperture Antennas and Diffraction Theory", IEE Electromagnetic Wave Series, 10, Peter Peregrinus Ltd., Sterenge, U.K.

Katehi, P.B., 1990, "Dielectric-Covered Waveguide Longitudinal Slots with Finite Wall Thickness", IEEE Trans. Antennas and Propagation, Vol. 38, No. 7.

Keller, J.B., 1962, "Geometrical Theory of Diffraction", J. Opt. Soc. of America, vol. 52, no. 2, pp. 116–130.

Kim, K.T., 1988, "A Radio Continuum Study of the Coma Cluster of Galaxies", Ph.D. Thesis, University of Toronto, Toronto, Ontario.

Koch, G.F., 1973, "Coaxial Feeds for High Aperture Efficiency and Low Spillover of Paraboloidal Reflector Antennas", IEEE Trans. Antennas and Propagation, AP–21, pp. 164-169.

Kraus, J.D., 1984, "Electromagnetics", 3rd. Ed., McGraw–Hill, New York.

Kraus, J.D., 1986, "Radio Astronomy", 2nd. Ed., Cygnus Quasar, Powell, Ohio.

Kraus, J.D., 1988, "Antennas", McGraw–Hill, New York.

Kurokawa, K., 1973, "Injection Locking of Microwave Solid State Oscillators", Proc. IEEE, Vol. 61, No. 10.

Landecker, T.L., Anderson, M.D., Routledge, D., Smegal, R.J., Trikha, P., Vaneldik, J.F., 1991, "Ground Radiation from Feed Support Struts: A Significant Source of Noise in Paraboloidal Antennas", Radio Science, in press.

Marcuvitz, N., 1951, "Waveguide Handbook", Radiation Laboratory Series, McGraw–Hill, Toronto.

Meyer, G., 1984, "Analog Integrated Circuits", 2nd. Ed., Wiley, New York.

Milligan, T.A., 1985, "Modern Antenna Design", McGraw–Hill, New York.

Montgomery, C.G., Dicke, R.H., Purcell, E.M., 1948, "Principles of Microwave Circuits", Radiation Laboratory Series, McGraw–Hill, Toronto.

Mott, H., 1986, "Polarization in Antennas and Radar", Wiley, New York.

Narasimhan, M.S., Raghavan, K., Ramanujam, P., 1983, "GTD Analysis of the Radiation Patterns of a Prime Focus Paraboloid with Shroud", IEEE Trans. Antennas and Propagation AP–31 pp 792–794.

Nasar, S.A., 1982, "Introduction to Electromagnetic Fields", McGraw–Hill, New York.

Paciorek, L.J., 1965, "Injection Locking of Oscillators", Proc. IEEE, Vol. 53, pp. 1723–1727.

Peters, L.Jr., Kilcoyne, T.E., 1965, "Radiating Mechanisms in a Reflector Antenna System", IEEE Trans. on Electromagnetic Compatibility, EMC–7, No. 4, pp. 368–374.

Roscoe, D., Shafai, L., Ittipiboon, A., "Circularly Polarised Travelling–Wave Printed Line Antennas", Electronic Letters, Vol. 25, 21 August, 1989.

Ruddock, R.C., Chang, Y.C., 1982, "Numerical Electromagnetic Code – Reflector Antenna Code", ElectroScience Laboratory, The Ohio State University.

Rusch, W.V.T., 1984, "Forward Scattering from Cylinders of Triangular Cross Section", IEEE Trans. Antennas and Propagation, AP−32, p. 1011.

Rusch, W.V.T., Sorensen, O., Baars, J.W.M., 1982, "Radiation Cones from Feed-Support Struts of Symmetric Paraboloidal Antennas", IEEE Trans. Antennas and Propagation, AP−30, pp.786−789.

Ruze, J., 1968, "Feed Support Blockage Loss In Parabolic Antennas", Microwave Journal, Vol. 11, No. 12, pp. 76−80.

Saleh, A.A.H., 1981, "Planar Multiport Qaudrature−like Power Dividers/ Combiners", IEEE Trans. Microwave Theory Techniques, MTT−29, p. 332.

Sanford, G.G., 1978, "Multiple Resonance Radio Frequency Microstrip Antenna Structure", U.S. Patent 4070676.

Satoh, T., Endo, S., Matsunaka, N., Betsudan, S., Katagi, T., Ebisui, T., 1984, "Sidelobe Level Reduction by Improvement of Strut Shape", IEEE Trans. Antennas and Propagation, AP−32, pp. 698−705.

Scheffer, H., 1971, "Improvements in the Development of Coaxial Feeds for Paraboloidal Reflector Antennas", Proc. of the 5th European Microwave Conference, pp. 46−50.

Silver S., 1949, "Microwave Antenna Theory and Design", Radiation Laboratory Series, McGraw−Hill, Toronto.

Thompson, A.R., Moran, J.M., Swenson, G.W., 1986, "Interferometry and Synthesis in Radio Astronomy", Wiley, Toronto.

Vaneldik, J.F., 1981, "The Main 693 or 695 MHz Oscillators for The Phase−Locked Upper and Lower Sideband Generators", D.R.A.O. Internal Report.

Veidt, B.G., 1984, "A 408 MHz Synthesis Radio Telescope", M.Sc. Thesis, University of Alberta, Edmonton.

B45932